Magnetic vortex dynamics nanostructures

Benjamin Pigeau

0pt0.4pt

UNIVERSITÉ DE PARIS-SUD

UFR Scientifique d'Orsay

Thèse de Doctorat

présentée pour obtenir
le grade de Docteur en sciences
de l'UNIVERSITÉ PARIS SUD, ORSAY

Spécialité:
Physique de la matière condensée

par

Benjamin Pigeau

MAGNETIC VORTEX DYNAMICS IN NANOSTRUCTURES

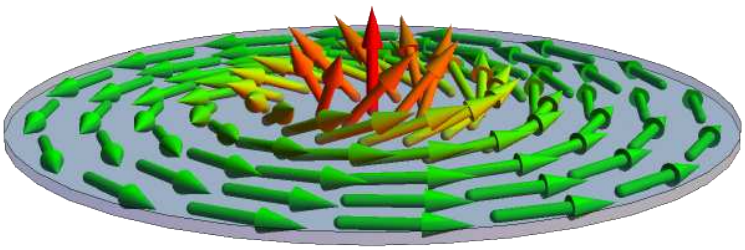

Soutenue le 17 decembre 2012 au CEA Saclay devant le jury composé de :

Rapporteurs	MM.	Christian Back
		Olivier Fruchart
Examinateurs	M.	André Thiaville
	M	Konstantin Guslienko
	M.	Joo-Von Kim
Directeur de thèse	M.	Olivier Klein
Invité	M.	Grégoire de Loubens

Contents

Remerciements

Une thèse est une plongée abrupte d'un jeune étudiant impatient de découvertes dans la réalité de la recherche scientifique. Il faut y conduire sa barque sur un océan tantôt d'huile, tantôt tumultueux.

Je tient particulièrement à remercier le trio de marin confirmé qui m'a soutenu pendant ces trois années passées au Service de Physique de l'Etat Condensé. En premier lieu mon directeur de thèse, Olivier Klein, qui a su entretenir ma motivation et développer mon sens physique grâce à ses connaissances, son intérêt écléctique pour tout les domaines de la physique et ses idées audacieuses. Vient ensuite Grégoire de Loubens, avec qui j'ai eu le plaisir de travailler au quotidien. Son sens de l'humain (et de la Physique) m'à 'eté précieux ainsi que son optimisme communicatif devant toutes les tempêtes. Enfin Vladimir Naletov, physicien doté d'une grande expérience et capable de résoudre TOUT les problèmes dans n'importe quel domaine, grâce à un sens pratique extraordinaire.

Je voudrai aussi remercier Claude Fermon, qui dirige le Laboratoire Magnétisme et Oxydes au sein duquel j'ai effectué cette thèse, ainsi que tout les chercheurs du groupe qui m'ont acceuilli chaleureusement et fait partagér leur expérience. J'ai pu aussi profiter de l'ambiance si propice du SPEC et je tient à remercier son directeur, Eric Vincent, ainsi que tout ses membres.

Plus directement, j'ai été entouré d'une équipe de thésards, post-docs et stagiaires particulierement joyeuse et amicale. Merci donc à Landry, Aurélie, Phuong-anh, Saskia, Abbas, Christian, Rémy, Damien, Ruben, Paolo, Sébastien, Olivier... pour leur soutien inconditionnel.

J'ai aussi eu la chance de développer et en partie construire une expérience, tâche dans laquelle j'ai été grandement soutenu par les membres de l'atelier mécanique du laboratoire. Je tient à souligner ici le grand professionnalisme et les qualités humaines de Gérald Le Goff, Grégory Cannies, Vincent Padilla, Dominique Duet, Pascal Sénat et Philippe Forget (entre autres).

Au cours de cette thèse, j'ai pu profiter de nombreuses et fructueuses collaborations scientifiques. Cela m'a permis de réaliser que mes travaux s'inscrivaient dans une communauté de recherche dynamique. Je voudrai remercier les professeurs Konstantin Guslienko, Andrei Slavin et Vassil Tyberkevich pour leur assistance sur la modélisation théorique de la dynamique d'onde de spin. Les échantillons utilisés pendant ce travail sont le fruit d'une collaboration avec les universités de Nancy et de Würzburg (Allemagne) et je remercie chaleureusement K. Mitsuzuka, S. Andrieu, F. Montaigne, A. Riegler, F. Lochner, G. Schmidt et L.W. Molenkamp pour leur maitrise de la nano-fabrication. Enfin, j'ai pu profiter de l'aide experte de Hervé Hurdequint et de Jamal Ben Youssef sur les aspects résonance ferromagnétique; de Nicolas Vukadinovic, Fabrice Boust et Alexei Khvalkovskiy pour les simulations micromagnétiques; d'André Thiaville et d'Anne-Lise

Adenot-Engelvin pour les nanoparticules magnétiques; enfin de Vincent Cros et Nicolas Locatelli sur la dynamique de vortex.

De façon à vider mon cerveau de ses trop plein et rester en forme, j'ai eu la chance de pratiquer la course à pied presque chaque midi durant ces trois annés. Je remercie chaleureusement la formidable équipe de course à pied du CEA Saclay avec qui j'ai passé de si bon moments: merci Philippe (x2), Gilles, Pascal, Laurent, Marc (x2). Enfin, j'ai réussi à garder mon équilibre global grâce à ma femme Areta qui m'a toujours soutenu.

Chapter 1

Introduction

1.1 Motivation

Recent progress in the growth of high quality thin films of ferromagnetic materials combined with progress in modern nano-lithography techniques has renewed interests in the study of magnetisation dynamics. From a fundamental point of view, spin wave excitations can now be studied in individual nanostructures with a complex spatially non-uniform ground state. This progress also opens up the possibility to control and manipulate the magnetisation of small objects.

These objects are of great interest for the data storage and information processing, where one of the challenges is to be able to control efficiently the magnetisation state of magnetic nanostructures. The reversal of the magnetic configuration implies a trade-off between energy and speed. In this case resonant processes could be of great help as they efficiently bring the system out-of -equilibrium [7, 1, 117]. The challenge here is to identify the normal spin wave modes of the system in a complex ground state which govern the magnetisation dynamics. More recently, it was demonstrated that information processing and data storage could be achieved by using these spin waves themselves. The idea being to transfer and manipulate the energy storage in each of the normal modes. The new field of magnonics involves the study of the collective properties of periodic magnetic nanostructures and tries to understand the spin waves propagation and interactions in order to manipulate them in a controlled manner [81, 73].

In parallel to these developments, the idea to take advantage of the spin degree of freedom in the transport properties has emerged. The ground breaking discovery of giant magneto-resistance(GMR) [8, 14] in 1988 (Nobel Prize in Physics 2007 to Albert Fert and Peter Grünberg) followed by tunnel magneto-resistance (TMR) [96] has launched the field of spintronics [142]. These discoveries led to the development and commercialisation of several applications, especially in the fields of magnetic data storage and field sensors [97, 3, 36, 103], bio-compatible sensors [45] and magnetic random access memories (MRAM) [24]. In a conventional spintronic device, electrons pass through a polarising magnetic layer with electronic transport properties that are anisotropic with respect to the direction of the electron spin. The spin-polarised electrons are scattered by the free magnetic layer, producing a spin torque on its magnetisation. Therefore, it becomes possible to manipulate the magnetisation with a spin polarised current instead of magnetic fields. The recent trends in spintronics are aimed at exploiting this transfer of spin angular momentum from the conduction electrons to the magnetisation of a metallic magnetic

nano-object [13, 123]. This momentum transfer results in a torque that is very efficient in driving large amplitude magnetisation oscillations [75, 64] that generate microwave signals in the frequency range of 0.28 to 65 GHz [38, 17]. The potential of these microwave spintronic devices, or spin transfer nano-oscillators (STNOs), derives from their large and fast frequency tuning, high modulation speed and very high level of integration. Nevertheless, in order to exploit the potential of STNOs their spectral coherence and emitting power have to be improved. This goal requires a precise understanding of their spin wave spectra.

For nanostructures the ground state adopts a complex spatially non-uniform configuration because of the inherent competition between exchange and dipolar energies. The ground state depends on the nature of the magnetic material (mainly through the spontaneous magnetisation M_s and the exchange constant A) and on the geometrical properties, the dot radius R and the dot thickness L. A rich variety of nonuniform micromagnetic states (vortex, onion, in-plane buckling, etc.) has been reported and their respective stability area was delimited within a phase diagram in the plane (thickness, radius) [94].

From a dynamic point of view, the vortex state is particularly interesting. The vortex state is the stable magnetic configuration of soft ferromagnetic platelets. It exists in a certain range of dot sizes $L > l_{ex}$ and $R \gg l_{ex}$ relative to the exchange length $l_{ex} = \sqrt{A/M_s^2}$ of the magnetic material of which the dot is made [54, 29]. While the magnetisation dynamics of most non-uniform states listed above usually leads to a very complex spin wave spectrum [9], the dynamics of the vortex state, thanks to its high symmetry, leads to a greatly simplified signature. In particular, the lowest energy mode, isolated at low frequency, corresponds to the vortex core gyration around the disc centre. The typical frequency of this mode can be several gigahertz below the frequency of the other higher order normal modes of the system. It turns out that such a large energy gap is very important for approaches, which aim at allowing a selective enhancement of a single dynamical mode by current-induced spin transfer phenomena [109]. Moreover, the linewidth of emission of vortex based STNOs was found to be narrow enough to be considered for practical applications [86, 38]. Nevertheless, a lot of effort remains to be done to understand and model the magnetisation dynamics of nano elements in the vortex state.

Another promising way to improve the phase noise of STNOs is to coherently couple them inside a large array [122]. Several mechanisms have been proposed to couple them coherently: microwave current [46], spin pumping [143], spin wave propagation [70, 88] and magneto-dipolar interaction [10]. The latter is the most straightforward because it exists naturally, but it has hardly been studied in the case of complex ground state. The simplest possible system to study this collective magnetisation dynamics under the influence of the dipolar coupling is a pair of nano-discs in the saturated state. It is one of the very few systems where the dynamical dipolar coupling can be calculated analytically with high accuracy.

We shall emphasise that, since we are interested in resonant processes and that improving the linewidth of emission of STNOs is a crucial point towards practical applications, we have concentrated our effort in this thesis on the magnetic materials having among the lowest damping (or magnetic dissipation) among electric conductors. One is a half-metallic ordered alloy NiMnSb. This composition belongs to the Heusler family. The second material that we have extensively measured is another ordered alloy of FeV. Like for the NiMnSb, its Gilbert damping constant is around $\alpha \simeq 2 \times 10^{-3}$. In both cases, the

spectroscopic studies were performed on patterned thin films grown by molecular beam epitaxy.

1.2 Experimental methods

A relevant experimental technique has now to be found to measure the spin wave spectrum of such nano-discs. Several experimental techniques are available to measure the magnetisation dynamics:

1. Recent progress in spintronics has allowed the magnetisation dynamics to be measured in metallic nanostructures using the magneto-resistance effect(GMR, TMR). The sensitivity is very high and scales well with the sample size. In a STNO, the mixing of a microwave current with the high frequency spin waves produces a detectable dc voltage [115, 131]. At the opposite, the microwave resistance associated with the auto-oscillation of spin waves in a STNO produces a microwave voltage when mixed with a dc current [75]. This signal can be detected with a spectrum analyser. It is now even possible to detect FMR with the spin Hall effect [40, 111]. Transport measurements have opened up new possibilities to measure the spin wave dynamics in small objects. However, from a fundamental point of view, it is often necessary to understand the dynamics in absence of charge currents since the latter introduces a new interaction in the system.

2. Conventional inductive ferromagnetic resonance (FMR) techniques. The spin waves are detected through their absorption of energy in a microwave cavity. The spectroscopic precision is very high, but the signal to noise ratio of the detector depends critically on the filling factor, which is the ratio of the volume of the sample over the volume of the cavity. It usually prevents to measure single nanostructures since the cavity is sensitive to any spurious magnetic materials of similar volume present within the cavity. The recent development of new FMR setup using micro antennas and coils in order to increase the filling factor are now available to study nanostructures [138].

3. Optical methods: the interaction between light and matter can provide a lot of physical information. Here, the properties of a light beam, for instance frequency or polarisation, are modified after the interaction with a spin wave. Three main methods will be briefly presented here.

   Time-Resolved Magneto-Optical Kerr Microscopy (TRMOKE) involves a 3D vectorial analysis of the time dependent magnetisation [1, 63]. It is thus phase sensitive. It requires pulsed or harmonic field excitations since the measurement is done in the time domain. By focusing the laser beam, a spatial resolution of 300 nm can be achieved. TRMOKE is commonly used to study the transverse component of the precessing magnetisation. The measurements are made in a pump-probe configuration. The laser pulse is synchronised to either a pulse generator or microwave synthesiser that generates a current waveform and hence a magnetic field within a planar waveguide on which the sample is either fabricated or overlaid. The full dynamics of the sample and all three spatial components of the dynamic magnetisation may be recorded simultaneously. By scanning the sample beneath the probe

beam at fixed time delays, time resolved images of the dynamic magnetisation are obtained. Because this technique allows studying the dynamics in the time domain, it is not very suited to study extremely low linewidth resonant process at low frequency, such as the gyrotropic mode, since it leads to very long integration time. Nevertheless, the vortex gyrotropic mode has already been successfully studied using this method [105].

Micro Brillouin Light Scattering (μ-BLS) [106, 69] is a phase insensitive technique for the investigation of propagating and standing spin wave modes. It can directly map the spin wave modes in the wave vectors k-space. No external excitation is required in many materials since BLS has the sensitivity to detect thermal spin waves. The spatial resolution can be as high as few tens of nanometres using near field optics [69]. One drawback of BLS is that it needs quite large difference in scattering energy since it detects Stoke and Anti-Stoke processes. The gyrotropic motion of the vortex core being mostly in the sub-GHz range is thus mostly out-of-reach to this technique.

With the development of synchrotron radiation sources of increasing brilliance, x-ray magnetic circular dichroism (XMCD) [2] has become a popular and powerful tool for the study of magnetic thin film samples. It can also be coupled to photo-electron emission microscopy (PEEM) [139]. Measurements are made near to an absorption edge corresponding to an electronic transition between a filed core state and vacant states close to the Fermi level. XMCD is element specific, since the core level energy is specific to a particular atomic species, and is sensitive to the magnetic moment parallel to the x-ray wave vector. Due to the spin-orbit splitting of the core levels, the application of sum rules allows the spin and orbital moments of a particular ion to be determined. Third generation synchrotrons typically deliver x-ray pulses some tens of ps in duration, with a pulse separation of a few ns and are well suited to pump-probe experiments analogous to those performed in the optical domain. Also the damping time for precessional oscillations of a magnetic material of narrow linewidth typically exceeds the time between successive x-ray pulses. Therefore x-ray ferromagnetic resonance (XFMR) measurements are usually made with a harmonic rather than a pulsed excitation.

One common advantage between these optical techniques is to perform a non perturbative measurement. Nevertheless, the drawback of all the optical techniques is that they require that the structure is on the surface. It is thus not adapted to buried structures underneath the contact electrode.

In this thesis, we decided to use a mechanical detection of the FMR with a ferromagnetic resonance force microscope (f-MRFM)[113, 150], which was constructed in the laboratory. The basic idea is to couple a scan probe technique, the magnetic force microscopy (MFM), with a microwave excitation line. A magnetic nanoparticle attached at the apex of an ultra soft cantilever is coupled to the stray field of the sample. The FMR is excited in the sample by a broadband microwave antenna and the variations of the longitudinal component of the magnetisation ΔM_z produce a force on the cantilever, whose motion is measured optically.

This particular method has several advantages to realise the spectroscopic experiments described above:

1. First of all, this is a scan probe technique, which allow a local detection of the FMR. Moreover, we can take advantage of the stray field generated by the magnetic particle to create a strong local field gradient, which can continuously bias the frequency tuning between nearby objects. This feature will be exploited in chapter 6

2. By choosing the size of the magnetic probe in the same range as the sample, we are able to optimise the filling factor and work at optimal signal to noise ratio. The force detection of the f-MRFM has been shown to be one of the most sensitive. With our particular setup, a resolution of $100\mu_B$ is easily achievable at room temperature with a commercial cantilever. This room temperature sensitivity makes it sufficient to detect the gyrotropic motion of the vortex core in a single dot.

3. The magnetisation dynamics is measured in the continuous wave (CW) configuration. It allows spin wave spectra to be measured in the frequency domain with arbitrary high accuracy. First this approach becomes more efficient for low frequency modes (time domain would require very large windows). More importantly, the energy resolution is here limited by the spectral purity of commercial microwave sources, which is of the order of the Hertz range. Thus the CW approach is the proper method to measure ultra-narrow lines at low frequency, such as the vortex gyrotropic mode. This is also a good means in order to resolve resonances very close in frequency.

4. We have access to the dynamics through the static measurement of ΔM_z. MRFM detects the longitudinal part of the microwave susceptibility (it is thus phase insensitive), which yields the T_1 relaxation time directly. This ability gives a complementary view to all the methods mentioned above which are measuring the transverse part of the magnetisation, and have therefore access to the T_2 relaxation time.

5. The study of the normally magnetised saturated state requires a high polarising field (up to 2 Tesla). Our home made f-MRFM is built with non-magnetic materials, which allow to work under such high fields. MRFM is one of the best sensitive method under large applied field.

1.3 Content of the thesis

In our road-map to characterise the nature of the spin wave modes in a nano-disc, we first give in Chapter 2 the comprehensive theoretical framework used to index properly the excitation spectra in a two-dimensional space with a general analytical formalism. We first explain the identification of the spin wave eigen-modes in the simplest possible geometry: the normally magnetised circular disc. Then in Chapter 3 we apply this analysis to the vortex state. In particular, we develop a framework explaining the non-linear ingredients which will become determinant. In chapter 4, we present the f-MRFM setup and the experimental protocol used to perform spin wave spectroscopy in a nano-disc and the means to calibrate the signal. In chapter 5, we perform unambiguous assignment of the resonance peaks observed in the linear regime of a vortex state under a perpendicular bias magnetic field. This vortex dynamics is also compared to the case where the device is saturated with a large external magnetic field oriented perpendicular to the layers. We

also concentrate on the dynamical reversal of the vortex core through resonant switching. In chapter 6, we study the role of the dipolar interaction between two discs in the saturated state. The coupled dynamics is carefully analysed. This is of great interest for the practical realisation of coupled arrays of STNOs, wich is a promising way to decrease the phase noise of the auto-oscillating mode in STNO.

Chapter 2

Perpendicularly magnetised soft magnetic dots

In order to study the magnetisation dynamics in a ferromagnetic body, a general theory of the spin wave excitations is presented in this chapter. This theoretical treatment is then applied to the case of thin discs in a perpendicularly saturated state of the magnetisation. This magnetic state is of particular importance since it simplifies the theoretical treatment due to the preserved axial symmetry. It will be shown that the dipolar interaction is integrable in this particular case. Finally, the theory of the collective dynamics of two neighbouring saturated discs dipolarly coupled is presented.

2.1 General theory of linear spin wave excitations

A convenient way to find the spin wave eigen modes of a normally magnetised thin disc is to use the general theory of linear spin wave excitations. This theoretical framework is very general and can be applied to many problems and geometry in magnetism. We are very grateful to Vasyl Tyberkevich and Andrei Slavin for this very general formulation of the problem [137, 99].

2.1.1 Equation of motion

The first step in the spin wave spectrum calculation is to define an equation of motion for the magnetisation. Under the assumption that $|\boldsymbol{M}(\boldsymbol{r},t)| = M_s$ is a constant of the motion, the magnetisation dynamics is described by the Landau-Lifshitz equation [82] extended with a perturbation term:

$$\frac{\partial \boldsymbol{M}}{\partial t} = \gamma \boldsymbol{H}_{\text{eff}} \times \boldsymbol{M} + \gamma \boldsymbol{h}(t) \times \boldsymbol{M} \tag{2.1}$$

where γ is the modulus of the gyromagnetic ratio. The last term includes the time dependent perturbation field $\boldsymbol{h}$ which can be a function of the magnetisation distribution $\boldsymbol{M}$. This field is able to describe non-conservative perturbations such as the influence of the Gilbert damping [44] using $\boldsymbol{h} = (-\alpha/\gamma M_s)\partial \boldsymbol{M}/\partial t$, with α the Gilbert phenomenological damping parameter.

The effective field $\boldsymbol{H}_{\text{eff}}$ is the functional derivative with respect to the magnetisation of the continuous magnetic energy density:

$$\boldsymbol{H}_{\text{eff}} = -\frac{\delta \mathcal{W}(\boldsymbol{r})}{\delta \boldsymbol{M}} \tag{2.2}$$

It is composed of the total external applied field $\boldsymbol{H}_{\text{ext}}$ (including the contribution from other sources such as neighbouring discs, f-MRFM magnetic probe..., and therefore possibly spatially dependent) and the magnetic self-interactions which will be included in the operator $\widehat{\boldsymbol{G}}$:

$$\boldsymbol{H}_{\text{eff}} = \boldsymbol{H}_{\text{ext}} - 4\pi \widehat{\boldsymbol{G}} * \boldsymbol{M} \tag{2.3}$$

In the equilibrium state, the effective field $\boldsymbol{H}_{\text{eff}}$ is parallel (at every spatial point) to the local magnetisation direction $\boldsymbol{u}_M$.

The linear tensor self-adjoint operator $\widehat{\boldsymbol{G}}$ describes the internal magnetic self-interactions. This tensor is the sum of several physical components:

1. The magneto-dipolar interaction $\widehat{\boldsymbol{G}}^d$, which is non-local and dominant at long range in small/confined magnetic systems. Its calculation is a purely geometrical problem, but is usually very complex and converges with difficulty in the general case. Some analytical solutions are known in the case of very symmetric bodies such as spheres or ellipsoids. Of particular interest for the following is the saturated state of the magnetisation. If $D(\boldsymbol{k})$ is the Fourier transform of the body shape function [12], the magneto-dipolar interaction is given in the wave-vector representation by:

$$\widehat{\boldsymbol{G}}^d(\boldsymbol{r}) = \int D(\boldsymbol{k}) \frac{\boldsymbol{k} \bigotimes \boldsymbol{k}}{k^2} \exp^{i\boldsymbol{k}.\boldsymbol{r}} d^3\boldsymbol{k} \tag{2.4}$$

where the symbol $\bigotimes$ denotes direct product of vectors.

2. The inhomogeneous exchange $\widehat{\boldsymbol{G}}^e$ dominant at short range, which is given in the wave-vector representation by:
$$\widehat{\boldsymbol{G}}^e = l_{\text{ex}}^2 k^2 \widehat{\boldsymbol{I}} \tag{2.5}$$
where the exchange length $l_{ex} = \sqrt{2J/(4\pi M_s^2)}$ depends on the exchange stiffness constant J of the considered material. $\widehat{\boldsymbol{I}}$ is here the identity matrix.

3. A contribution from the magneto-crystalline anisotropy. It is related to the atomic lattice symmetry of the considered magnetic material. For some cases, the crystalline symmetry can favour one or multiple preferential axis for the magnetisation, which follow the crystal field. Any deviation from this or these preferred orientations will result in an energy cost. As we are using mostly soft magnetic materials, these contributions will be neglected in the following treatment since it introduces a negligible correction in the spin wave eigenmodes calculation.

4. The magneto-elastic interaction which tends to align the magnetisation along or perpendicular to the the axis of mechanical strains. It will also be neglected in this treatment.

5. A surface anisotropy term created by the magnetic discontinuities at the interfaces. This small contribution is neglected as well in the following.

2.1.2 Linear spin wave spectrum

Having defined an equation of motion for the magnetisation, we shall find the dynamical equations for the small (linear) magnetisation excitations. The following ansatz is used to describe the time-dependent, or out-of-equilibrium component of the magnetisation $\boldsymbol{m}$:

$$\boldsymbol{M}(\boldsymbol{r},t) = M_s\big(\boldsymbol{u}_M + \boldsymbol{m}(\boldsymbol{r},t)\big) + \mathcal{O}(\boldsymbol{m}^2) \tag{2.6}$$

Because we consider a ferromagnet, the norm of the magnetisation vector is a constant of the motion, which implies the condition $\boldsymbol{m}.\boldsymbol{u}_M = 0$. In other words, $\boldsymbol{m}$ is the small component of the magnetisation ($|\boldsymbol{m}| \ll 1$) oscillating in the plane transverse to the local $\boldsymbol{u}_M$. This is the key parameter to describe the spin wave eigenmodes.

Substituting $\boldsymbol{m}$ in the equation (2.1) and keeping only the linear terms, a linear equation describing the transverse magnetisation precession at the Larmor frequency is obtained:

$$\frac{\partial \boldsymbol{m}}{\partial t} = \boldsymbol{u}_M \times \widehat{\boldsymbol{\Omega}} * \boldsymbol{m} \tag{2.7}$$

where the sign $*$ denotes the convolution product. The self-adjoint tensor operator $\widehat{\boldsymbol{\Omega}}$ represents here the Larmor frequency:

$$\widehat{\boldsymbol{\Omega}} = \gamma(H_{\text{eff}}\widehat{\boldsymbol{I}} + 4\pi M_s \widehat{\boldsymbol{G}}) \tag{2.8}$$

Here, $\widehat{\boldsymbol{I}}$ is the identity matrix and H_{eff} is the norm of the effective field described in equation (2.3):

$$H_{\text{eff}} = \boldsymbol{u}_M.\boldsymbol{H}_{\text{ext}} - 4\pi M_s \boldsymbol{u}_M.\widehat{\boldsymbol{G}} * \boldsymbol{u}_M \tag{2.9}$$

Considering only linear excitations of the spin system, $\boldsymbol{m}$ is developed in the general eigen-basis representing the spin wave eigenmodes, labelled by ν:

$$\boldsymbol{m}(\boldsymbol{r},t) \approx \sum_{\nu} c_\nu(t)\boldsymbol{m}_\nu(\boldsymbol{r}) + c.c. \tag{2.10}$$

where *c.c.* stands for complex conjugates. In this formulation, $c_\nu(t)$ are the amplitudes of the eigenmodes and $\boldsymbol{m}_\nu(\boldsymbol{r})$ represents their spatial profile. This standard decomposition must be an orthonormal basis, obeying the closure relation:

$$i\langle\overline{\boldsymbol{m}}_\nu.(\boldsymbol{u}_M \times \boldsymbol{m}_{\nu'})\rangle = \mathcal{N}_\nu\delta_{\nu,\nu'} \tag{2.11}$$

where $\overline{\boldsymbol{m}}$ stands for the complex conjugate of $\boldsymbol{m}$, δ is the Kronecker delta function and the bracket denotes the spatial average over the volume of the magnetic body. $\mathcal{N}_\nu$ are normalisation constants of the basis.

Assuming an oscillatory dependence of the spin wave magnetisation vector $\boldsymbol{m}_\nu$ at the eigen-frequencies ω_ν, the eigen-modes, labelled by ν, are solutions of the equation (2.7):

$$-i\omega_\nu\boldsymbol{m}_\nu = \boldsymbol{u}_M \times \widehat{\boldsymbol{\Omega}} * \boldsymbol{m}_\nu \tag{2.12}$$

The main properties of spin wave excitations follow from the eigen-problem equation (2.12) and the fact that the operator $\widehat{\boldsymbol{\Omega}}$ is self-adjoint and real. In particular, if the equilibrium magnetisation along $\boldsymbol{u}_M$ corresponds to a local minimum of the energy, the operator $\widehat{\boldsymbol{\Omega}}$ is positive-definite. The "physical" (positive) eigenfrequencies are then simply given by the formula:

$$\omega_\nu = \frac{\langle\overline{\boldsymbol{m}}_\nu.\widehat{\boldsymbol{\Omega}} * \boldsymbol{m}_\nu\rangle}{\mathcal{N}_\nu} \tag{2.13}$$

The importance of this relation is that the frequencies ω_ν calculated using equation (2.13) are variationally stable with respect to perturbations of the mode profile $\boldsymbol{m}_\nu$. Thus, injecting some trial vectors inside equation (2.13) allows one to get approximate values of ω_ν with high accuracy.

2.1.3 Practical calculation of the eigenfrequencies

A convenient basis $\tilde{\boldsymbol{m}}_k$ in the space of vector functions $\boldsymbol{m}$ is introduced to describe the spin wave modes. This basis should be complete, orthonormal (i.e. all $\tilde{\boldsymbol{m}}_j$ are orthogonal to $\boldsymbol{u}_M$) and should satisfy appropriate boundary conditions at the edges of magnetic body. The dynamical part of the magnetisation is decomposed on this basis using the amplitudes a_k:

$$\boldsymbol{m} = \sum_k a_k\tilde{\boldsymbol{m}}_k \tag{2.14}$$

This equation is substituted in equation (2.12), which is projected on the axis of the magnetisation precession ($\overline{\tilde{\boldsymbol{m}}}_j \times \boldsymbol{u}_M$) and averaged on the magnetic volume V. Equation (2.13) simply means that the eigenfrequencies ω_ν are given by the spatial average of the Larmor operator $\widehat{\boldsymbol{\Omega}}$ weighted by the spatial pattern of the mode profile. In the following, the curly bracket notation denotes the spatial averaging of a quantity weighted by the profile of the spin wave mode:

$$\{\boldsymbol{A}\}_{jk} = \frac{1}{\mathcal{C}_{j,k}}\int\int_V \overline{\tilde{\boldsymbol{m}}}_j(\boldsymbol{r})\boldsymbol{A}(\boldsymbol{r}-\boldsymbol{r}')\tilde{\boldsymbol{m}}_k(\boldsymbol{r}')\,d^3\boldsymbol{r}'d^3\boldsymbol{r} \tag{2.15}$$

where the normalisation constant is:

$$\mathcal{C}_{jk} = i \int_V \tilde{\overline{\boldsymbol{m}}}_j(\boldsymbol{r}).\big(\boldsymbol{u}_M \times \tilde{\boldsymbol{m}}_k(\boldsymbol{r})\big) d^3\boldsymbol{r} \tag{2.16}$$

This yields the homogeneous system of equations (for different j) for the coefficients a_k:

$$\sum_k \Big(\omega - \{\widehat{\boldsymbol{\Omega}}\}_{jk}\Big) a_k = 0 \tag{2.17}$$

The eigenfrequencies ω_ν can be found from the condition of vanishing determinant of the previous system: $\det(\omega - \{\widehat{\boldsymbol{\Omega}}\}_{jk}) = 0$. The stability of this method with respect to the variation of the mode profile allows the calculation of the eigenfrequencies using typically only a few appropriate basis functions $\tilde{\boldsymbol{m}}_j$.

In order to find the spin wave eigenfrequencies, the problem reduces to the calculation of the average value of the Larmor operator along the diagonal:

$$\{\widehat{\boldsymbol{\Omega}}\}_{jj} = \gamma \left[\Big(\{\boldsymbol{u}_M.\boldsymbol{H}_{\text{ext}}\}_{jj} - 4\pi M_s \{\boldsymbol{u}_M.\widehat{\boldsymbol{G}} * \boldsymbol{u}_M\}_{jj} \Big) \widehat{\boldsymbol{I}} + 4\pi M_s \{\widehat{\boldsymbol{G}}\}_{jj} \right] \tag{2.18}$$

In case of elliptical precession of the magnetisation, one needs thus two separate equations (2.18) for the values of ω for each Cartesian [76] one proportional to $m_x^2/(m_x m_y)$, the other to $m_y^2/(m_x m_y)$. The product of these two equations is independent of the ellipticity, leading to a general Kittel like formula.

2.1.4 Spin wave damping

The spin wave decomposition of equation (2.10) can be introduced in the Landau-Lifshitz equation, leading to the following linear differential equation for the spin wave amplitudes c_ν:

$$\frac{dc_\nu}{dt} = -i\omega_\nu c_\nu \tag{2.19}$$

In absence of damping, the mode spectrum is just a Dirac distribution centred at ω_ν. The actual amplitudes of the modes are in fact intrinsically linked to the magnetic dissipation, which induces a finite linewidth $\Delta\omega_\nu$ in the measurements. The Gilbert damping describing the intrinsic magnetic dissipation in the material can be introduced in the non-conservative perturbation field $\boldsymbol{h}(t)$ of equation (2.1). It has the form of a linear operator, allowing $\boldsymbol{h}(t)$ to depend on the magnetisation distribution:

$$\boldsymbol{h}(t) = \widehat{\boldsymbol{L}} * \boldsymbol{m}(t) \tag{2.20}$$

where the influence of the Gilbert damping $-(\alpha/\gamma M_s)\partial\boldsymbol{M}/\partial t$ is given by:

$$\widehat{\boldsymbol{L}} * \boldsymbol{m} = i\frac{\alpha}{\gamma} \sum_\nu \omega_\nu [c_\nu(t)\boldsymbol{m}_\nu - c.c] \tag{2.21}$$

Then, introducing the decomposition of the eigen-basis (equation 2.10) in the Landau Lifshitz equation (2.1) and using the orthogonality relations, one can obtain the following equation for the spin wave amplitude:

$$\frac{dc_\nu}{dt} = -i\omega_\nu c_\nu - \Gamma_\nu c_\nu \tag{2.22}$$

Assuming that there are no degenerate modes, the spin wave damping rate is then given by:

$$\Gamma_\nu = \alpha\omega_\nu \frac{\langle \overline{\boldsymbol{m}}_\nu . \boldsymbol{m}_\nu \rangle}{\mathcal{N}_\nu} \tag{2.23}$$

The spin wave amplitude c_ν simply follow the equation of motion of a damped harmonic oscillator.

From equation (2.23) the relaxation rate coincides exactly with the intrinsic damping α only if the magnetisation precession is circular because in this case $\mathcal{N}_\nu = \langle \overline{\boldsymbol{m}}_\nu . \boldsymbol{m}_\nu \rangle$. It will be shown in the following section that this is the case of the radial spin wave modes in normally magnetised discs: the damping rate reduces to $\Gamma = \alpha\omega$. Therefore, $\Delta\omega/2\omega = \alpha$ will be experimentally verified, where $\Delta\omega$ is the measured linewidth.

2.2 Normally magnetised thin disc

The general theory developed in the previous section can now be applied to the particular case of a normally magnetised thin ferromagnetic disc.

2.2.1 The proper eigen-basis

In order to solve this problem, a proper eigen-basis decomposition (equation (2.10)) has to be found to describe the spin wave modes in a perpendicularly magnetised disc. Since the frequencies calculated using equation (2.13) are variationally stable with respect to perturbations of the mode profile $\boldsymbol{m}_\nu$, the real magnetisation profile of the modes will be replaced by appropriate trial vectors $\boldsymbol{m}_\nu$ in order to calculate the approximate eigenfrequencies accurately. The trial vectors should obey some simple properties:

1. They must form a complete basis in the space of vector functions $\boldsymbol{m}$ and obey the closure relation equation (2.11).
2. The vectors of this orthonormal basis must be locally orthogonal to $\boldsymbol{u}_M$.
3. Because we consider a finite size system, the vectors should satisfy appropriate boundary conditions at the edges of the magnetic body.

In practice, the spin wave eigen-basis will be imposed by the symmetry of the magnetic system. A perpendicularly magnetised disc exhibits an axial symmetry. This symmetry is described by the operator rotation around the z axis $\widehat{\boldsymbol{R}}_z$. It is assumed that the boundary conditions follow this symmetry, i.e. the pinning at the edges of the disc is homogeneous. The operator describing a rotation around the axis z at the Larmor frequency obviously commutes with the rotation operator: $[\boldsymbol{u}_z \times \widehat{\boldsymbol{\Omega}}, \widehat{\boldsymbol{R}}_z] = 0$. But this statement remains valid when the precession is orthogonal to $\boldsymbol{u}_M$: $[\boldsymbol{u}_{eff} \times \widehat{\boldsymbol{\Omega}}, \widehat{\boldsymbol{R}}_z] = 0$. Moreover, since the disc is homogeneously saturated, the magnetisation is considered uniform across the disc thickness and the problem reduces to a two-dimensional system.

The spin wave eigenmodes $\boldsymbol{m}_\nu$ are then described in the disc plane (ρ, ϕ); they are by definition also eigenfunctions of the operator $\widehat{\boldsymbol{R}}_z$ corresponding to a certain integer azimuthal number l. This defines their behaviour under the azimuthal rotation ϕ around the axis z:

$$\frac{\partial \boldsymbol{m}}{\partial \phi} - \boldsymbol{u}_z \times \boldsymbol{m} = -i(l-1)\boldsymbol{m} \tag{2.24}$$

The radial profiles of the eigenmodes being described by the functions $\psi_l^{(1,2)}(\rho)$, two classes of solutions corresponding to counter-rotating waves in the azimuthal direction are found for the equation (2.24):

$$\boldsymbol{m}_l^{(1)} = \frac{1}{2}(\boldsymbol{u}_x + i\boldsymbol{u}_y)e^{-il\phi}\psi_l^{(1)}(\rho) \tag{2.25a}$$

$$\boldsymbol{m}_l^{(2)} = \frac{1}{2}(\boldsymbol{u}_x - i\boldsymbol{u}_y)e^{-i(l-2)\phi}\psi_l^{(2)}(\rho) \tag{2.25b}$$

Mathematically, the spin wave eigenmodes should be linear combinations of the two solutions. Physically, the coupling mechanism between the two types of waves is the inhomogeneous dipolar interaction. If only the lowest energy modes are considered, this interaction can be neglected, and the right-polarised form of equation (2.25) will be our unique solution. In practice, the error in the eigenfrequencies is of the order of $4\pi\gamma M_s(L/R)^2$, which is small compared to the lowest modes splitting induced by the constrained geometry.

We now have to find an appropriate set of radial functions $\psi_l(\rho)$ to calculate the spin wave spectrum using equation (2.13). Until this point, the treatment is exact, but the calculation of the real radial functions involves to solve complicated integro-differential equations. Our approximation consists of using a reasonable set of known mathematical trial functions.

The Bessel functions of the first kind $J_l(x)$ correspond to our problem since they have the appropriate radial and azimuthal symmetry. Moreover, they reproduce well the strong pinning of the magnetisation at the lateral boundaries introduced by the magneto-dipolar interaction [56].

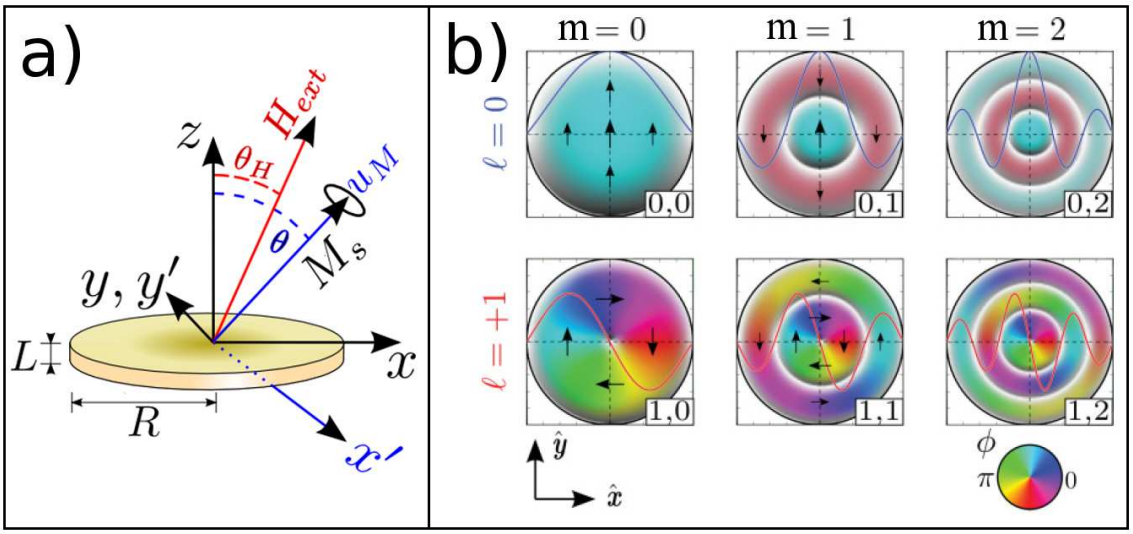

Figure 2.1: a) Parametrisation of the ferromagnetic thin disc: the external magnetic field H_{ext} (including all contributions) is tilted by the angle θ_H, and the equilibrium magnetisation is along the effective field unit vector $\boldsymbol{u}_M$. b) Spatial representation of the Bessel function $J_l(k_{l,m})$ for different values of the azimuthal mode index l (by row) and radial mode index m (by column).

Therefore, we use radial profiles of the form $\psi_l(\rho) = J_l(k_{l,m}\rho)$. The eigenmodes wave numbers $k_{l,m}$ are determined from the pinning conditions at the disc boundary. For very

thin discs, this pinning is found to be almost complete [56], and this quantity is defined as $k_{l,m} = \kappa_{l,m}/(R+L)$, where $\kappa_{l,m}$ is the mth root of the Bessel function of the lth order. The integer radial number m is introduced to label the number of nodes in the radial profile across the disc. The spatial profile of such functions is presented on the figure 2.1b, with the rows corresponding to the azimuthal index l and the columns to the radial index m. The phase (or direction) of the magnetisation precession $\phi = \arg(\boldsymbol{m}_\nu)$ is displayed in colour code using the hue, while the amplitude $|\boldsymbol{m}_\nu|^2$ is given by the brightness.

One can easily identify the $(l = 0, m = 0)$ mode as the "uniform" mode: the magnetisation precesses in-phase uniformly in the disc. The first azimuthal mode $(l = +1, m = 0)$ corresponds to a spin wave that is rotating around the disc in the same direction as the Larmor precession. The corresponding phase is in quadrature between two orthogonal positions and this mode has a node at the centre of the disc (the nodal positions are marked in white). Then, increasing the index m results in an increase of the number of nodes in the radial direction.

2.2.2 Calculation of the eigenfrequencies

Now that a convenient eigen-basis has been chosen to decompose the spin wave modes, we can solve the equation (2.13) and find the eignfrequencies. The indices of the modes ν are replaced by the set l, m. By replacing in the equation (2.25), the magnetisation of the normal eigenmode (l, m) is given by:

$$\boldsymbol{m}_{l,m}(\boldsymbol{r}, t) = \frac{1}{2}(\boldsymbol{u}_x + i\boldsymbol{u}_y)e^{-il\phi}J_l(k_{l,m}\rho) \tag{2.26}$$

Equation (2.18) defining the eigenfrequencies spectrum can be solved using the adapted spin wave profile of equation (2.26): this is the magneto-exchange approximation.

$$\omega_{l,m} = \gamma\left[\left(\{\boldsymbol{u}_M.\boldsymbol{H}_{\text{ext}}\}_{l,m} - 4\pi M_s\{\boldsymbol{u}_M.(\widehat{\boldsymbol{G}}^d + \widehat{\boldsymbol{G}}^e) * \boldsymbol{u}_M\}_{l,m}\right)\widehat{\boldsymbol{I}} + 4\pi M_s\{\widehat{\boldsymbol{G}}^d + \widehat{\boldsymbol{G}}^e\}_{l,m}\right] \tag{2.27}$$

In this particular case, the curly bracket averaging reduces to:

$$\{\boldsymbol{A}\}_{l,m} = \frac{1}{\mathcal{C}_{l,m}}\int_{\boldsymbol{\rho}<R}\int_{\boldsymbol{\rho}'<R} J_l(k_{l,m}\rho)\boldsymbol{A}(\boldsymbol{r} - \boldsymbol{r}')J_l(k_{l,m}\rho')\; e^{il(\phi'-\phi)}\; d^2\boldsymbol{r}'d^2\boldsymbol{r} \tag{2.28}$$

where the normalisation constant is:

$$\mathcal{C}_{l,m} = \int_{\boldsymbol{r}<R}\Big(J_l(k_{l,m}\rho)\cos(l\phi)\Big)^2 d^2\boldsymbol{r} \tag{2.29}$$

The first term of equation (2.27) concerning the external field reduces to $\boldsymbol{H}_{\text{ext}}.\boldsymbol{u}_M$ since this polarising field is spatially homogeneous. If an extra non-homogeneous external field is added to the disc, such as stray fields created by the f-MRFM probe or neighbouring discs, it must be weighted by the mode profile and spatially averaged.

2.2.2.1 The static dipolar self-interaction

The second term of equation (2.27) represents the static magnetic self-interactions. In the case of homogeneously magnetised body, the inhomogeneous exchange contribution to the

static self-interaction is strictly zero and the second term of equation (2.18) reduces to the magneto-dipolar contribution. The magneto-dipolar interaction can be expressed in a more suitable form in terms of the demagnetising tensor $\widehat{\boldsymbol{N}}(\boldsymbol{r})$. The two mathematical formulations are linked by the following expression for the demagnetising tensor elements:

$$N_{i,j}(\boldsymbol{r}) = \boldsymbol{u}_i(\boldsymbol{r}).\widehat{\boldsymbol{G}}^d * \boldsymbol{u}_j \tag{2.30}$$

where $\boldsymbol{u}_{i,j}$ are unit vectors along the directions i, j. The calculation of this tensor is in general non trivial because of the non-locality of the problem.

Nevertheless, the case of a ferromagnetic disc of radius R and thickness L, or more generally a cylinder, whose magnetisation is fully saturated was solved analytically [126]. Because of the axial symmetry, the values of the tensor $\widehat{\boldsymbol{N}}$ are better expressed in the cylindrical coordinates (r, z) and we introduce the reduced units $\zeta = z/R, \tau = t/(2R), \rho = r/R$:

$$N_{zz}(r,z) = +\frac{1}{2}\left\{s_{\zeta,\tau} I_0(\rho,\alpha_-) + I_0(\rho,\alpha_+)\right\} \tag{2.31a}$$

$$N_{zr}(r,z) = -\frac{1}{2}\left\{I_1(\rho,\alpha_-) - I_1(\rho,\alpha_+)\right\} \tag{2.31b}$$

$$\begin{aligned} N_{rr}(r,z) = &+\frac{1}{4}\left\{s_{\zeta,\tau} I_2(\rho,\alpha_-) + I_2(\rho,\alpha_+) - 2H_{\tau,\zeta} I_2(\rho,0)\right\} \\ &-\frac{1}{4}\left\{s_{\zeta,\tau} I_0(\rho,\alpha_-) + I_0(\rho,\alpha_+) - 2H_{\tau,\zeta} I_0(\rho,0)\right\} \end{aligned} \tag{2.31c}$$

where the notations $\alpha_- = |\zeta - \tau|$ and $\alpha_+ = |\zeta + \tau|$ are respectively the distance (in reduced units) with the bottom and top surface of the cylinder. The function s and H design respectively the Sign and Heavisde functions:

$$s_{x,y} = \begin{cases} +1 & \text{if } x < y \\ -1 & \text{else} \end{cases}$$

$$H_{x,y} = \begin{cases} 1 & \text{if } x > y \\ 0 & \text{else} \end{cases}$$

The integrals I_i have the following expressions:

$$I_0(\rho,\alpha) = s_{1,\rho}\frac{1}{2}\Lambda_0(\beta,\kappa) - \frac{k\alpha}{2\pi\sqrt{\rho}}K(k) + H_{1,\rho} \tag{2.32a}$$

$$I_1(\rho,\alpha) = \frac{1}{\pi k\sqrt{\rho}}\left\{(2-m)K(k) - 2E(k)\right\} \tag{2.32b}$$

$$\begin{aligned} I_2(\rho,\alpha) = &\frac{2\alpha}{\pi k\rho^{3/2}}E(k) - (\alpha^2+\rho^2+2)\frac{\alpha k}{2\pi\rho^{5/2}}K(k) \\ &- s_{1,\rho}\frac{1}{2\rho^2}\Lambda_0(\beta,\kappa) + \frac{H_{1,\rho}}{\rho^2} \end{aligned} \tag{2.32c}$$

where

$$m = k^2 = \sin^2\kappa = \frac{4\rho}{(\rho+1)^2+\alpha^2}, \tag{2.33a}$$

$$\beta = \arcsin\left(\frac{\alpha}{\sqrt{(\rho-1)^2+\alpha}}\right). \tag{2.33b}$$

$K(k)$ and $E(k)$ are the complete elliptic integrals of the first and second kind and Λ_0 is the Heuman's Lambda function.

The above expressions are valid everywhere in space. If the magnetisation is aligned with the unit vector $\boldsymbol{u}_M$, the magnetic field induction at every point in space (inside or outside the sample's volume) simply obeys the formula:

$$\boldsymbol{B}(r,z) = \boldsymbol{H}_{\text{ext}} + 4\pi M_s \left\{ \Theta(r,z) - \widehat{\boldsymbol{N}}(r,z).\boldsymbol{u}_M \right\}, \tag{2.34}$$

where Θ is a function equals to 1 inside the cylindrical volume and 0 otherwise:

$$\Theta(r,z)_{x,y} \quad = \quad \begin{cases} 1 & \text{if} \quad r < R \text{ and } |z| < t/2 \\ 0 & \text{else.} \end{cases}$$

Therefore, the magneto-static contribution can be expressed in the form:

$$-4\pi M_s \{ \boldsymbol{u}_M.\widehat{\boldsymbol{G}}^d * \boldsymbol{u}_M \}_{l,m} = -4\pi M_s \{ \boldsymbol{u}_M.\widehat{\boldsymbol{N}}.\boldsymbol{u}_M \}_{l,m} \tag{2.35}$$

This is the self-demagnetising field created by the static magnetisation.

2.2.2.2 The dynamic dipolar self-interaction

The last term of equation (2.27), except the exchange contribution that is straightforward, contains the dynamic magneto-dipolar self-interaction, which represents the depolarisation field of the spin wave mode on itself. This term is really non local since it involves also the non diagonal components of the dipolar Green operator $\widehat{\boldsymbol{G}}^d$. No general expression of this term is available, but an analytical formula was derived for $l = 0$ modes in the case of a strictly perpendicularly magnetised disc. It involves the N_{xx} component of the demagnetising tensor because the oscillating part of the magnetisation is identified to this term in the linear regime:

$$\{\widehat{\boldsymbol{G}}^{\text{d}}\}_{0,0} = \{N_{xx}^{\text{self}}\}_{0,0} = \frac{1}{\mathcal{C}_{0,0}} \int_{V_i} d^2\rho dz J_0(k_{0,0}\rho) \int_0^R du \frac{\partial N_{xx[u,L]}(\rho,z)}{\partial u} J_0(k_{0,0}u) \tag{2.36}$$

where the quantity in the second integral is the magnetic stray field produced at the spatial position $\boldsymbol{r}$ by a cylindrical tube of width du, radius u, and thickness L, homogeneously magnetised along $\boldsymbol{u}_x$ by $J_0(k_0 u)$. This term should not be confused with the eventual static contribution $\{N_{xx}\}_{l,m}$ which has the form of equation (2.28).

To derive this formula, we have taken advantage of the axial symmetry of the $l = 0, m = 0$ mode, which leads to $\{N_{xx}^{self}\}_{0,0} = \{N_{yy}^{self}\}_{0,0}$. This is no longer the case for higher order modes having azimuthal indices different from zero: they present an ellipticity. Nevertheless, the previous expression can be extended to the general case using:

$$\{N_{xx}^{\text{self}}\}_{l,m} = \{N_{xx}^{\text{self}}\}_{0,0} \sqrt{\frac{k_{l,m}}{k_{0,0}}} \tag{2.37}$$

Notice that an approximate expression has been derived by Kalinikos and Slavin [71] for the lowest spin wave branch of platelet shape bodies with uniform magnetisation across the film thickness [76]:

$$\{\widehat{\boldsymbol{G}}^{\text{d}}\}_{l,m} = G_{l,m}^{\perp} \boldsymbol{u}_z \boldsymbol{u}_z + (1 - G_{l,m}^{\perp})(q_l \boldsymbol{u}_x \boldsymbol{u}_x + (1 - q_l)\boldsymbol{u}_y \boldsymbol{u}_y) \tag{2.38}$$

where:

$$G^{\perp}_{l,m} = \frac{2\pi R^2 \Lambda_l}{\mathcal{C}_{l,m}} \int_0^{\infty} \left(\frac{k J_{l-1}(kR) J_l(k_{l,m}R) - k_{l,m} J_{l-1}(k_{l,m}R) J_l(kR)}{k^2 - k^2_{l,m}} \right)^2 \left(\frac{1 - e^{-kt}}{kt} \right) k dk \tag{2.39}$$

Here $\Lambda_l = 1/2$ for anti-symmetrical modes and $\Lambda_l = (1 + \Delta_{l,0})/2$ for symmetrical modes. $q_l = 1/2 \pm \Delta_{l,1}/4$ for symmetrical/anti-symmetrical modes, respectively. The term $\Delta_{l,m}$ represents the ellipticity of the mode l, m.

2.2.2.3 Equilibrium configuration

The equilibrium configuration of the magnetisation vector $\boldsymbol{M}(\boldsymbol{r})$ has to be defined precisely. From an experimental point of view, it is very difficult to align precisely the applied field $\boldsymbol{H}_{\text{ext}}$ with the normal of the disc plane $\boldsymbol{u}_z$. In the real experiments a slight misalignment is always present, which needs to be taken into account in the model.

The first basic principle to understand any equilibrium state is the following: the magnetisation unit vector $\boldsymbol{u}_M$ is always aligned with the local effective field $\boldsymbol{H}_{\text{eff}}$ in the magnetic sample. This field can be locally very different from the applied field $\boldsymbol{H}_{\text{ext}}$, as sketched on the figure 2.1a.

In this model, the static magnetisation is considered fully saturated and homogeneous in the disc volume. The equilibrium orientation of the magnetisation $\boldsymbol{M}(\boldsymbol{r}) = M_s \boldsymbol{u}_M$ is given by the condition that the volume averaged effective field $\langle \boldsymbol{H}_{\text{eff}} \rangle = \langle \boldsymbol{H}_{\text{ext}} + \boldsymbol{H}_{\text{ex}} + \boldsymbol{H}_{\text{d}} \rangle$ is aligned with the direction $\boldsymbol{u}_M$. If θ_H is the angle between the applied field and the disc normal $\boldsymbol{u}_z$, the equilibrium angle θ_M for the magnetisation is given by the positive root of the equation:

$$H_{\text{ext}} \ \sin(\theta_M - \theta_H) + 2\pi M_s \sin(2\theta_M) \Big[\langle N_{xx} \rangle - \langle N_{zz} \rangle \Big] = 0 \tag{2.40}$$

where $\langle N_{xx} \rangle, \langle N_{zz} \rangle$ are the averages over the dot volume of the demagnetising tensor elements. This result is illustrated by the sketch of figure 2.1a.

Solving numerically the previous equation leads to the equilibrium configuration of the magnetisation, once the precise geometry of the dot and the field angle are known. The starting point for the dynamical spin waves spectrum calculation is a uniform state of the magnetisation oriented along $\boldsymbol{u}_M$. Namely: $\boldsymbol{M}(\boldsymbol{r}) = M_s(1, \theta_M, \phi)$ in a spherical frame. The azimuthal angle ϕ is determined by the external field orientation. But there is no explicit dependence on ϕ in this model because of the axial symmetry of the discs considered here. For instance, $\phi = 0$ in the figure 2.1a.

Notice that all the spatial mode profiles introduced in the previous section preserve the rotation invariance symmetry for a perfectly perpendicularly magnetised disc. If the magnetisation is tilted by θ_M, the actual radial profiles of the modes are distorted. We make the assumption that the decomposition on the Bessel functions remains a good approximation for the mode profiles if this angle is small. It was shown [76] that the discrepancy between a realistic simulation and the calculation becomes too important if the angle of the applied field is larger than $\theta_H = 5\hat{A}^{\circ}$. In that sense, the validity of the following calculation of the spin wave eigenfrequencies is restricted to small deviation of the applied field from the perpendicular.

2.2.2.4 The Kittel like formula

Taking into account the tilt of the external field and using the previous notations, the following terms are defined:

1. The total internal field:

$$\{H_{\text{eff}}\}_{l,m} = H_{\text{ext}}\cos(\theta_M - \theta_H) + \{\boldsymbol{H}_{\text{inh}}.\boldsymbol{u}_M\} - 4\pi M_s\{\boldsymbol{u}_M.\widehat{\boldsymbol{N}}.\boldsymbol{u}_M\}_{l,m} \tag{2.41}$$

where H_{ext} is the norm of the external polarising field and $\boldsymbol{H}_{\text{inh}}$ is a spatially inhomogeneous field, created for instance by the f-MRFM probe. The demagnetising field is projected in the local frame of the magnetisation:

$$\{\boldsymbol{u}_M.\widehat{\boldsymbol{N}}.\boldsymbol{u}_M\}_{l,m} = \frac{1}{2}[\{N_{zz}\}_{l,m}(\cos 2\theta_M + 1) - \{N_{xx}\}_{l,m}(\cos 2\theta_M - 1)] \tag{2.42}$$

2. The total exchange field:

$$\{H_{\text{ex}}\}_{l,m} = 4\pi M_s l_{ex}^2 k_{l,m}^2 \tag{2.43}$$

In order to take into account the tilt of the magnetic field, an equation for the eigenfrequencies has to be written for each Cartesian axis, because the magnetisation precession of all the modes become elliptical (in practice $\{N_{xx}^{self}\}_{l,m} \neq \{N_{yy}^{self}\}_{l,m}$). This leads to the general expression for the eigenvalue of arbitrary index:

$$\begin{aligned}\frac{\omega_{l,m}^2}{\gamma^2} =& \left(\{H_{\text{eff}}\}_{l,m} + \{H_{\text{ex}}\}_{l,m} + 4\pi M_s\{N_{x'x'}^{\text{self}}\}_{l,m}\right)\times \\ & \left(\{H_{\text{eff}}\}_{l,m} + \{H_{\text{ex}}\}_{l,m} + 4\pi M_s\{N_{y'y'}^{\text{self}}\}_{l,m}\right)\end{aligned} \tag{2.44}$$

Notice that in this equation, the contributions from the dynamical dipolar self-interaction $\{N_{x'x'/y'y'}^{self}\}_{l,m}$ have to be projected on the new axis $x^{'}, y^{'}$ (see figure 2.1a).

The finite-size effects due to the restriction of the magnetic volume are clearly seen in this calculation. The magneto-dipolar interaction becomes dominant in such discs and the magnetostatic spin wave modes are quantised due to the boundary conditions. Compared to a continuous film, the degeneracy between the eigenfrequencies is lifted. The splitting between eigenmodes increases when the geometrical dimensions are reduced. Experimentally, it is very interesting to measure discs with sub-micron radii, to avoid the non linear coupling between modes when their frequencies are too close [34].

2.2.3 Amplitude and linewidth of the eigenmodes

It was shown in equation (2.22) that the intrinsic amplitude of the spin wave modes depends on the damping rate Γ. Experimentally, the spin waves will be excited with a microwave magnetic field. Therefore, the measured amplitude depends on the overlap between the perturbation field and the symmetry of the mode.

2.2.3.1 Overlap integral with the excitation

Because we are interested in measuring the eigenmode amplitude when excited by an external perturbation field, we should define this field first. The microwave field created by the antenna (see chapter 4 for details) is linearly polarised and spatially homogeneous, at least at the scale of the disc:

$$\boldsymbol{h}_{\mathrm{rf}}(t) = h_{\mathrm{rf}} \cos(\omega_0 t)\boldsymbol{u}_x \tag{2.45}$$

This field has to be added to the perturbation term equation:

$$\boldsymbol{h}(t) = \boldsymbol{h}_{\mathrm{rf}}(t) + \widehat{\boldsymbol{L}} * \boldsymbol{m}(t) \tag{2.46}$$

An extra term appears in the equation of motion of the oscillator:

$$\frac{dc_{l,m}}{dt} = -i\omega_{l,m}c_{l,m} - \Gamma_{l,m}c_{l,m} + i\gamma h_{l,m} \tag{2.47}$$

In this equation, the last new term is very important: this is the driving term relating the coupling efficiency of the microwave field. Assuming that there is no degenerate modes, it is given by the overlap integral between the excitation field symmetry and the excited mode profile:

$$h_{l,m} = \frac{\langle \overline{\boldsymbol{m}}_{l,m}.\boldsymbol{h}_{rf} \rangle}{\mathcal{N}_{l,m}} \tag{2.48}$$

In a sense, the symmetry of the microwave field imposes the selection rules for the excited modes in the linear regime. It can be easily shown that the uniform microwave magnetic field we are using can only excite $(l = 0, m)$ spin wave modes. In order to excite azimuthal $(l \neq 0, m \neq 0)$ spin wave modes, a field with an orthoradial symmetry should be used, as it was demonstrated in reference [99] with an rf current flowing vertically through the disc.

2.2.3.2 Relationship with the f-MRFM measurement

The resolution of equation (2.47) is straightforward and we shall concentrate on the physical parameter measured by the f-MRFM. Here, the probe couples to the stray field created by the longitudinal part of the magnetisation, and the signal is given by the variation of this quantity averaged on the disc volume, $4\pi\langle \Delta \boldsymbol{M}.\boldsymbol{u}_z \rangle$. One can derive an approximate expression of this quantity, for an arbitrary microwave pulsation frequency ω_0, under the approximation that the only relevant coefficients in the damping matrix are the diagonal terms,

$$4\pi\langle \Delta \boldsymbol{M}.\boldsymbol{u}_z \rangle \approx 4\pi M_s \sum_{l,m} \frac{\gamma^2 |h_{l,m}|^2}{(\omega_0 - \omega_{l,m})^2 + \Gamma_{l,m}^2} \mathcal{N}_{l,m} \tag{2.49}$$

The force detected by the f-MRFM cantilever is then proportional to the product $\langle \Delta \boldsymbol{m}.\boldsymbol{u}_z \rangle = \Delta M_z$ with the probe field gradient g_{zz}, as will be explained in chapter 4.

In conclusion, the theoretical calculation of the spin wave eigenmodes in a perpendicularly magnetised disc provides access to the set “frequency, amplitude, linewidthâ for the full spectrum. This allows the spectrum measured by our f-MRFM methods to be reproduced analytically. Quantitative information about the material parameters as well as the physics of the system can be extracted from this comparison [76, 99].

2.3 Coupled dynamics of two neighbouring discs

Once the dynamical behaviour of a single disc is well described, we can consider the interesting case of a pair of them. This is a first step toward the study of the collective dynamics of wide arrays of magnetic discs. Notice that the case of two magnetic discs saturated in the plane and separated by a metallic spacer was already treated [37]. In the problem we will study here, the two discs saturated out-of-plane can be placed either on top of each other or closely packed laterally. The most important point is their magnetic mutual isolation: even if they stand close from each other, they are clearly separated by a non magnetic layer or by vacuum.

Therefore, the only coupling mechanism allowed between the discs is mediated by the magneto-dipolar energy. If the two discs are close enough, the overlap between their dipolar stray field can lead to a collective dynamics of the magnetisation.

The geometry of the problem is defined as follows: the two discs of identical radius R and thickness L, labelled by 1 and 2, are separated by s edge to edge (lateral configuration) or z_0 centre to centre (vertical arrangement). The individual, or uncoupled, spin wave eigenfrequencies $\omega_{l,m}$ of each disc are now defined as ω_1 and ω_2 . Initially, the discs will be considered magnetised fully out-of-plane (i.e. $\theta_H = \theta_M = 0$). The influence of a tilted magnetisation in the collective dynamics will be discussed at the end.

2.3.1 Influence of the magneto-dipolar coupling

The static magnetic interaction in equation (2.18) now comprises cross terms. To avoid any confusion, the different terms will be labelled by indices corresponding to both discs $(i, j) = 1, 2$.

In a first time, we shall consider the effect of the static dipolar coupling. The calculation of the eigenfrequencies $\omega_{1,2}$ will be modified by the static dipolar field radiated by the neighbouring disc. The dipolar self-interaction for the disc i, already taken into account, can now be noted $\{N_{zz}^{i\to i}\}_{l,m}$. The new cross term, corresponding to the static dipolar field from one disc j averaged on the precession profile of the other one i is:

$$\{N_{zz}^{j\to i}\}_{l,m} = \frac{1}{\mathcal{C}_{l,m}} \int_{V_i} N_{zz}(\boldsymbol{r}_{j\to i}) \Big(J_l(k_{l,m}\rho)\cos(l\phi) \Big)^2 d^2\boldsymbol{r} \tag{2.50}$$

where the term $\boldsymbol{r}_{j\to i}$ depends on the geometry. For two discs on top of each other, $\boldsymbol{r}_{j\to i} = (\rho, z+z_0)$ while for the lateral configuration, $\boldsymbol{r}_{j\to i} = (\sqrt{(2R+s)^2 + \rho^2 - (2R+s)\rho\sin\theta}, z)$. This term must be added to the total internal field of equation (2.41).

A new cross term also appears in the dynamic magneto-dipolar interaction. This parameter is very important since it is responsible for the dynamic dipolar coupling between discs. Even though the calculation of this term is in general non trivial, an analytical formula has been derived for the $l = 0$ modes:

$$\{N_{xx}^{\text{cross},ji}\} = \frac{1}{\mathcal{C}_{0,0}} \int_{V_i} d^3\boldsymbol{r}\, J_0(k_{0,0}\rho) \int_0^R du \frac{\partial N_{xx[u,L]}(\boldsymbol{r}_{j\to i})}{\partial u} J_0(k_{0,0}u) \tag{2.51}$$

The general form of this term is similar to the self term of equation (2.36), except the position $\boldsymbol{r}_{j\to i}$ of the second disc.

With these additional contributions arising from the magneto-dipolar coupling, the individual frequencies $\omega_{1,2}$ of each discs can be renormalised to find the coupled frequencies.

2.3.2 Coupled equation of motion and collective dynamics

In both geometries, the dominant coupling mechanism is the magnetic dipolar interaction since there is no "magnetic" contact between discs. The possibility to couple the discs through spin currents [143, 98] is neglected here. The perturbation theory leading to the dynamical equation (2.19) can be extended to the case of coupled discs by adding the coupling cross terms described in equation (2.51). Denoting the spin wave amplitude in both discs by $c_{1,2}$, and neglecting the damping term in a first approximation, one can get:

$$\frac{dc_1}{dt} = -i\omega_1 c_1 + i\gamma h_{2\to1} c_2 \tag{2.52a}$$

$$\frac{dc_2}{dt} = -i\omega_2 c_2 + i\gamma h_{1\to2} c_1 \tag{2.52b}$$

The cross terms that couple these equations are given by:

$$h_{i\to j} = \frac{4\pi M_s}{\mathcal{N}_j} \langle \overline{\boldsymbol{m}}_j . \widehat{\boldsymbol{G}^{\mathrm{d}}} * \boldsymbol{m}_i \rangle_{V_j} \tag{2.53}$$

and its symmetric form, inverting the discs labels $(i, j) = 1, 2$.

Thus, $h_{i\to j}$ is the demagnetising stray field produced by the dynamic magnetisation of the jth disk projected along the local dynamical magnetisation vector inside the ith disk and averaged over its volume. The overlap defined in this equation is maximum if one consider modes having the same wave number in each disc [47]; in the following only the coupling between similar modes will be considered. In that sense $\overline{\boldsymbol{m}}_j$ and $\boldsymbol{m}_i$ correspond to the dynamical magnetisation in each discs but with the same set of mode indices (l, m). This dynamical field, which drives the coupling, is of course an in-plane rotating field that is able to couple to the magnetisation's dynamical part. Therefore, it is easily related to the cross terms of the dynamic magneto-dipolar self-interaction. In the case of two discs on top of each other, this field is isotropic since $N_{xx} = N_{yy}$, and

$$h_{i\to j} = 4\pi M_s \{N_{xx}^{\mathrm{cross},ij}\} \tag{2.54}$$

But in the case of two discs placed side by side, the axial symmetry is broken and:

$$h_{i\to j} = 2\pi M_s \left(\{N_{xx}^{\mathrm{cross},ij}\} + \{N_{yy}^{\mathrm{cross},ij}\} \right) \tag{2.55}$$

In order to be solved, this simple system of linear ordinary differential equations can be written in matrix form:

$$\frac{d}{dt}\begin{pmatrix} c_1 \\ c_2 \end{pmatrix} = -i\widehat{\boldsymbol{A}}\begin{pmatrix} c_1 \\ c_2 \end{pmatrix} \text{ where } \widehat{\boldsymbol{A}} = \begin{pmatrix} \omega_1 & -\gamma h_{2\to1} \\ -\gamma h_{1\to2} & \omega_2 \end{pmatrix} \tag{2.56}$$

The eigenvalues $\omega_{A,B}$ are found by diagonalising the central matrix $\widehat{\boldsymbol{A}}$ in equation (2.56) using the identity: $det(\widehat{\boldsymbol{A}} - \omega\widehat{\boldsymbol{I}}) = 0$. The eigenfrequencies, corresponding to the anti-binding (A) and binding (B) modes are then given by:

$$\omega_{A,B} = \frac{\omega_1 + \omega_2}{2} \pm \sqrt{\left(\frac{\omega_1 - \omega_2}{2}\right)^2 + \left(\frac{\Omega}{2}\right)^2} \tag{2.57}$$

where the coupling strength is:

$$\Omega^2 = \gamma^2 h_{1\to2} h_{2\to1} \tag{2.58}$$

Because the coupled system is composed of two magnetic oscillators, two coupled modes diagonalise the problem. The magnetisation precession occurs in both discs during the coupled modes with the main following characteristics: equal frequency $\omega_{A,B}$ and fixed phase difference. An interesting analogy is done on figure 2.2 with the energy diagram of a two levels molecules having a bounding and an anti-bounding state.

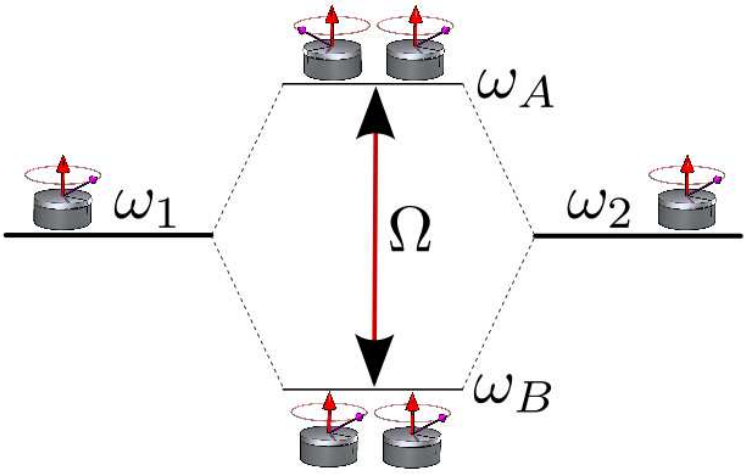

Figure 2.2: Analogy between a two level molecule and the effect of the dipolar coupling on two magnetic oscillators. The magneto dipolar interaction hybridises the system in two binding and anti-binding coupled modes separated in frequency by the dynamical splitting Ω.

In the case of lateral neighbouring discs, the mode with the lowest frequency is the binding mode B, which corresponds to an in-phase precession in both discs: this is an acoustic mode. In the second, or anti-binding mode A, the magnetisation is precessing with a π phase difference between discs: this is an optical mode. The modes frequencies experience an anti-crossing, and the coupling strength Ω (which is a frequency), is simply the frequency splitting between coupled modes at the exact tuning ($\omega_1 = \omega_2$).

Considering two discs on top of each other, this hierarchy is inverted: the anti-binding mode A has the lowest frequency. Indeed, the sign of the dynamical magneto-dipolar interaction is negative. This results from the symmetry of the disc stray field, which forms closed loops of iso-fields. Therefore, the field $h_{i\to j}$, that was positive for neighbouring discs, is now negative. Consequently, the out-of-phase precession of the magnetisation is favoured by the cross dipolar interaction.

The amplitudes $C_{A,B}$ of the coupled modes corresponds to the eigenvectors $\boldsymbol{x}$ of the matrix $\widehat{\boldsymbol{A}}$, calculated with the equation: $(\widehat{\boldsymbol{A}} - \omega_{A,B}\widehat{\boldsymbol{I}})\boldsymbol{X}_{A,B} = 0$. These amplitudes are of course linear combinations of the uncoupled amplitudes, the weight corresponding to the hybridisation of the coupled modes:

$$C_A = c_1 + \frac{\omega_1 - \omega_A}{\gamma h_{2\to1}} c_2 \tag{2.59a}$$

$$C_B = \frac{\omega_2 - \omega_B}{\gamma h_{1\to2}} c_1 + c_2 \tag{2.59b}$$

From an experimental point of view, the critical parameter is the ratio of hybridisation in the two coupled discs. This parameter can easily be related to the force acting on the

f-MRFM cantilever (see chapter 6), for instance. For each coupled mode, this ratio is given by:

$$\left.\frac{c_i}{c_j}\right|_{\omega_{A,B}} = \left(\frac{(\omega_i - \omega_j) \mp \sqrt{(\omega_i - \omega_j)^2 + \Omega^2}}{\Omega}\right)^{\mp 1} \tag{2.60}$$

This equation allows to confirm the symmetry of the coupled modes. For clarity, it will be assumed that the system is placed at the anti-crossing ($\omega_1 = \omega_2$).

In the case of lateral neighbouring discs, in equation (2.60) ,the anti-binding A mode has $c_i = -c_j$, a precession with equal hybridisation weight between the two discs but precessing with a π phase difference. At the opposite, the binding mode B has $c_i = +c_j$ which denotes an in-phase precession. As explained previously, this symmetry is inverted in the case of stacked discs.

2.4 Conclusion

In this chapter, a very general theoretical calculation of the linear spin wave spectrum in a ferromagnetic body was developed. Assuming a conservative dynamics of the magnetisation, its motion was described by the Landau-Lifshitz equation. Taking carefully into account the magnetic interactions (magneto-dipolar, exchange, crystalline anisotropy...), a general expression for the spin wave eigenfrequencies was derived. Moreover, the dissipative phenomena could be introduced in order to calculate the spin wave amplitude and relaxation rate.

This general framework was then applied to the case of a nano disc perpendicularly magnetised to the film plane, which corresponds to the geometry chosen in this thesis. The first important point of this calculation was to treat properly the magneto-dipolar and exchange interactions which becomes dominant in such small magnetic volume. It was done thanks to the demagnetising tensor formulation, which provides an analytical solution of the problem for saturated magnetic bodies. The second point was to find a relevant eigen-basis on which to decompose the spin wave modes. This basis is discrete and the quantised wave vectors are given by the boundary conditions. Moreover, the axial symmetry of the disc has imposed the Bessel functions for describing the radial profiles of these modes. Finally, the key for the calculation of the eigenfrequencies was to average the effective field over the dot volume taking into account the mode profile. It led to a Kittel-like equation for the spin wave frequency. As a result of the magnetic confinement in such discs, the spin wave spectrum is quantised, which will be verified experimentally in chapter 5. Experimental studies of a normally magnetised configuration allows quantitative access to fundamental parameters such as saturation magnetisation M_s, actual radius of the disc, gyromagnetic ratio γ and damping α.

Once the spectrum of a single disc was calculated, we have addressed the problem of the collective magnetisation dynamics in multiple neighbouring discs coupled by the dipolar interaction. For instance the collective dynamics of similar modes excited in neighbouring discs is very interesting. The case of two discs was treated here, revealing the dominant role of the dynamical dipolar interaction in the apparition of two coupled modes. The striking feature of the collective dynamics, the dynamical splitting between coupled modes, was calculated. This theoretical description will be verified experimentally in the chapter 6.

With the problem of the saturated state treated, we can focus our study on unsaturated states, and in particular the vortex state. The general theory developed in the beginning is still valid in this case, the challenge being to take properly into account the dipolar interaction. Indeed the static magnetisation now depends strongly on the spatial position. But it will be shown in chapter 3 that the global axial symmetry is conserved which allows interesting analogies in the treatment of the spin wave spectrum compared to the saturated state.

Chapter 3

The magnetic vortex: static properties and dynamics

In this chapter, a detailed theoretical description of the vortex state will be given. In a first part, different models of this particular spatial distribution of the magnetisation are reviewed. The static magnetic properties of vortices in nanostructures are explored, in particular the stability as a function of the geometry of the dot and versus external applied fields. The second part will be focused on the dynamical excitations in the vortex state. The gyrotropic mode and higher order spin wave modes will be modelled as well as their mutual interactions.

3.1 Introduction to the vortex state

The vortex structure is widespread in nature. This is usually a configuration of the matter that allows an efficient dissipation of energies. It involves various physical parameters such as wind or water velocity in turbulent flows (Von Karmann alley), superconducting order parameter in superconductor of type II, electrical charges in eddy currents, matter density in black holes...and magnetisation in two dimensional ferromagnets.

All these phenomena have in common a structure where the involved physical parameter is curling around a central singularity. The energy should diverge at this point, but the centre of the vortex, the so-called core, regularises this divergence by its particular structure.

Two-dimensional ferromagnets are of particular interest for us, this thesis being focused on the study of very thin ferromagnetic nano-structures, such as discs. The first study on magnetic vortices was done by E. Feldtkeller and H. Thomas who calculated their micromagnetic structure [42]. Magnetic vortices have been intensively studied by Kosterlitz, Berezinsky and Thouless in the 70's as a particular topological solution of the phase transition in the XY model [78]. This general model describes the interactions of classical magnetic moments confined in a plane; it can be applied either to ferro/antiferromagnetism or any spin physics such as helium 3 and polymers. Vortices can be formed to reduce the energy of the system, interacting in pairs of vortex-antivortex for example. They can be seen as topological defects whose structure cannot be reduced to a uniform or continuous state by any finite transformation. They are stable under certain conditions that are reviewed in the following.

3.1.1 Vortices in two dimensional ferromagnets

In ferromagnets, the magnetic moments responsible for the magnetism are strongly coupled by the exchange interaction. The spin system presents a phase transition and exhibits an ordered state below the Curie temperature. The vortex structure is a soliton exhibiting a curling spin structure in the XY plane around a central region where magnetic moments are pointing out of plane to avoid creating a singularity. This two dimensional topological defect is characterised by three "topological charges".

- The *Vorticity* q: This is a very general quantity related to the topology of the magnetic moments curling in the XY plane. If $\boldsymbol{S}(\boldsymbol{r})$ is the spin field of the 2D ferromagnet, the vorticity measures the total angle with respect to a given direction through which the vector $\boldsymbol{S}(\boldsymbol{r})$ turns in a circular contour around the a core [91]. The quantity q, an integer multiple of 2π, it is also known as the winding number. As can be seen in figure 3.1, positive q are related to vortex structures and negative q to anti-vortices. In this thesis, only vortices with vorticity equal to $\pm$ 1 will be considered.

- The *Polarity* p: It defines the relative orientation of the magnetic moments inside the vortex core with respect to the plane of the ferromagnet. This quantity can only be $p = \pm$ 1.

- The *Chirality* C: This quantity completes the vorticity by giving the sense of rotation of the spin vector $\boldsymbol{S}(\boldsymbol{r})$ in a circular contour around the vortex. It can be clockwise or counterclockwise, so $C = \pm$ 1.

To describe the properties of ferromagnetic thin films, the easy-plane ferromagnet model has been introduced. This is the classical two dimensional model of Heisenberg magnetic moments with an in-plane magnetic anisotropy which tends to maintain the magnetic moments in the plane. The vortex state is a particular unstable solution of this model [67] corresponding to a magnetic defect in the spin texture. This model has given a first insight on magnetic vortices, but it will be shown in the following that this structure can be stabilised in laterally confined structures, such as dots.

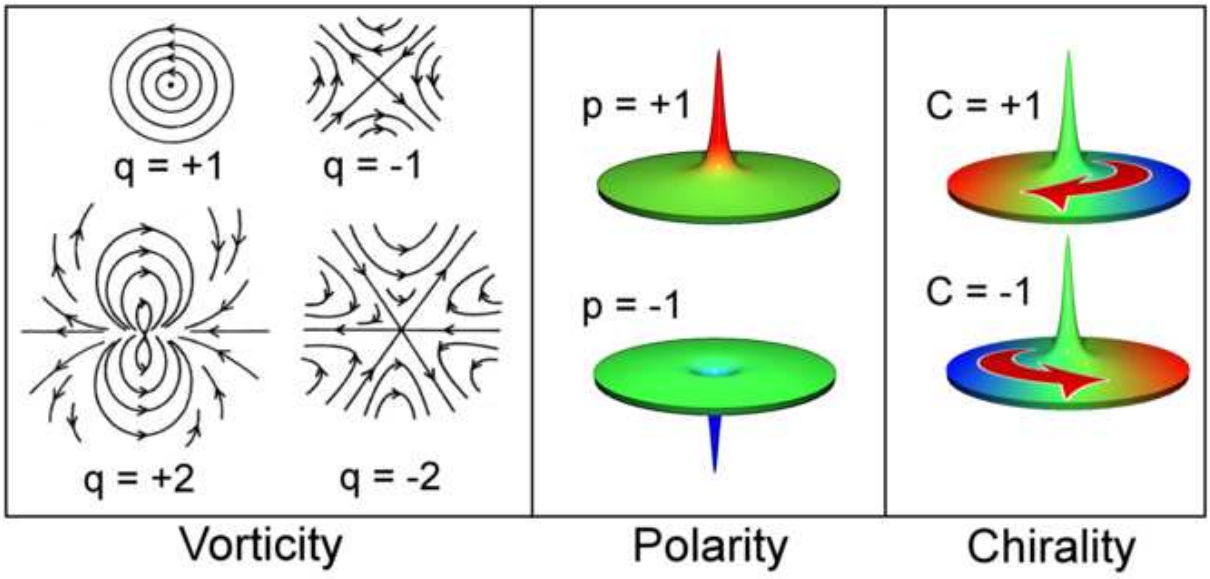

Figure 3.1: Topological "charges" of a ferromagnetic vortex: Vorticity (or winding number, from Mermin [91]), Polarity and Chirality.

3.1.2 Vortices in cylindrical soft magnetic dots

The samples studied in this thesis are discs of few tens of nanometres of thickness and below 1 micron in diameter. The materials considered are soft ferromagnets, i.e., without or with a small magneto-crystalline anisotropy. The remanent magnetisation arrangement in a soft sample depends on the interplay between the magneto-dipolar and exchange energies. If the lateral size of the magnetic object is reduced, the role of exchange energy becomes more important and the magnetisation tends to be uniform. But for larger particle sizes, some non uniform states, or domains of the magnetisation can appear, such as the vortex state. The magnetic anisotropy is dominated by the shape anisotropy created by the demagnetising field. The exchange length, giving the range of the exchange interaction between ferromagnetic magnetic moments, is typically 10 nanometres for ferromagnetic materials. The two dimensional approximation is valid for these samples since no magnetic inhomogeneity can form at this thickness scale. But the radius being larger than this typical length, the magnetic remanent ground state of such discs is a vortex for a wide range of size.

In such discs, the vortex state stability can be roughly understood as follows: the magnetisation curls in the plane of the disc to minimise the dipolar energy by reducing the surface charges. At the centre, few magnetic moments point out-of-plane in a radius comparable to the exchange length to minimise the exchange and dipolar energies. Using

these simple considerations, the diagram of stability of the vortex state with respect to the aspect ratio (radius over thickness) of the disc can be calculated (see figure 3.3).

3.2 Static properties of a confined magnetic vortex

In this section, different ways to describe the magnetic vortex are presented. Using these models, the vortex stability in soft ferromagnetic discs can be calculated. The influence on the vortex state reversal of external magnetic fields, applied either in or out of the disc plane, is described.

3.2.1 Review of vortex modelisation

Let us consider a vector $\boldsymbol{M}$ describing the magnetisation of the vortex. The thickness dependence of $\boldsymbol{M}$ is neglected, and the reduced magnetisation in the disc plane $\boldsymbol{\rho} = (x, y)$ is defined as:

$$\boldsymbol{m}(\boldsymbol{\rho}, t) = \frac{\boldsymbol{M}(\boldsymbol{\rho}, t)}{M_s},\ |\boldsymbol{m}| = 1 \ \text{ and } M_s \text{ is the saturation magnetisation.} \tag{3.1}$$

This vector is parametrised locally by the polar angles $\Theta(\boldsymbol{\rho})$ and $\Phi(\boldsymbol{\rho})$ which are solutions of the Landau-Lifshitz equation of motion for the magnetisation. The three components of the magnetisation can be written using the circular symmetry of the system:

$$m_x + i m_y = \sin\Theta(\boldsymbol{\rho}) e^{i\Phi(\boldsymbol{\rho})}, \quad m_z = p\cos\Theta(\boldsymbol{\rho}) \tag{3.2}$$

The position $\boldsymbol{\rho}$ of the vector $\boldsymbol{m}$ in the disc plane is given in cylindrical units by the coordinates $(\chi,\ \rho)$.

The curling state of the magnetisation around the vortex core is modelled by introducing a constraint on the polar angle Φ, which is always orthogonal to the angle χ:

$$\Phi(\chi, \rho) = q\ \chi + C\ \frac{\pi}{2} \tag{3.3}$$

where q and C are the vortex winding number and chirality defined previously. This formula is given for any position in the disc plane and remains valid if the vortex structure is deformed by any applied field. An expression for the polar angle Θ is less obvious because of the non uniformity of the vortex core structure.

The simplest description of the vortex core has been given by Belavin and Poliakov [11] for extended 2D films, i.e. considering only the exchange energy with respect to the edges of the system. The core structure, described as a soliton, with a radius R_c is given by:

$$\tan\left(\frac{\Theta}{2}\right) = \left(\frac{Rc}{\rho}\right)^{|q|} \tag{3.4}$$

In the discs we are considering here, the edge magneto-static energy may become important due to the lateral confinement. Taking this parameter into account, a first ansatz was proposed by Usov [133] describing a rigid vortex core at the centre of the disc:

$$\sin\Theta(\boldsymbol{\rho}) = \frac{2\rho R_c}{R_c^2 + \rho^2} \ \text{ if } \ \rho < R_c \quad \text{and} \quad \Theta(\boldsymbol{\rho}) = \frac{\pi}{2} \ \text{ if } \ \rho > R_c \tag{3.5}$$

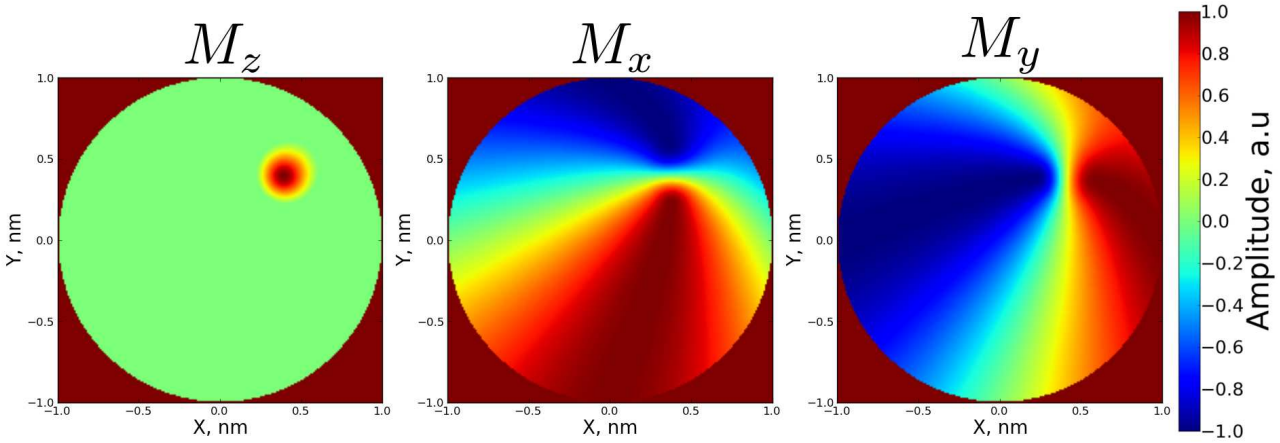

Figure 3.2: Three components of the vortex magnetisation $\boldsymbol{M}$ *along calculated within the "two vortex" ansatz. The model is able to take properly into account a shift of the vortex core from its equilibrium position.*

The vortex core, which has an out of plane Lorentzian shape, is separated from the rest of the disc. Its radius R_c can be calculated by minimising the exchange and magneto-static energies in the dot.

For further description of the static and dynamical properties of the vortex, a more detailed description of the core is needed. To perform calculations, the model should be able to describe the vortex shifted from its equilibrium position in a continuous manner. The disc plane is here parametrised by the Cartesian coordinates x and y, while the vortex core position is given by the set (X, Y). Taking into account the axial symmetry and two dimensionality of the problem, we introduce dimensionless variables, following [54].

$$\zeta = \frac{x + iy}{R}, \quad \bar{\zeta} = \frac{x - iy}{R} \tag{3.6}$$

The reduced vortex core position is given by:

$$s = \frac{X + iY}{R}, \quad \bar{s} = \frac{X - iY}{R} \tag{3.7}$$

with R the radius of the disc. The magnetisation of equation (3.2) can be rewritten as:

$$m_x + im_y = \frac{2w(\zeta, \bar{\zeta})}{1 + w(\zeta, \bar{\zeta})\bar{w}(\zeta, \bar{\zeta})}, \quad m_z = \frac{1 - w(\zeta, \bar{\zeta})\bar{w}(\zeta, \bar{\zeta})}{1 + w(\zeta, \bar{\zeta})\bar{w}(\zeta, \bar{\zeta})}, \quad \boldsymbol{m}^2 = 1 \tag{3.8}$$

The zeros of the complex function $w(\zeta, \bar{\zeta})$ give the position of the soliton's centres. This function should take into account the magnetic charges created on the disc's sides when the vortex core is shifted. It is convenient to express it as follows:

$$w(\zeta, \bar{\zeta}) = f(\zeta) \quad \text{if} \quad |f(\zeta)| < 1 \tag{3.9}$$

$$w(\zeta, \bar{\zeta}) = \frac{f(\zeta)}{|f(\zeta)|} \quad \text{if} \quad |f(\zeta)| \geqslant 1 \tag{3.10}$$

3. The "*Rigid vortex model*" describes the shifted vortex without any deformation of the core. It satisfies the exchange boundary conditions and allows therefore magnetic charges to form on the dot surfaces when the core is shifted. Introducing the relative core radius $c = R_c/R$ and core centre displacement in the dot $s = \sqrt{X^2 + Y^2}/R$, the model, equivalent to the equation (3.5) from Usov for $s = 0$, is given by:

$$f(\zeta) = \frac{i}{c}(\zeta - s) \tag{3.11}$$

The model allows simple analytical calculations of the vortex energy, in particular when a magnetic field is applied in the plane of the disk, moving the core and therefore inducing surface magnetic charges. This model has two disadvantages: the core boundary at $r = R_c$ is abrupt leading to a underestimation of the magnetic energies. Because the modelled core remains rigid when it is shifted from the centre of the disc, this model is not suitable for dynamical calculations which involves core deformations.

4. The "*double vortex*" model allows the deformation of the vortex core. This function involves two vortices, one of them being a virtual one outside of the disc. It satisfies the magnetostatic boundary conditions $\boldsymbol{M}.\boldsymbol{n} = 0$ (with $\boldsymbol{n}$ the vector normal to the surface) on the disc side borders: no magnetic charges are taken into account. The ansatz is the following:

$$f(\zeta) = \frac{1}{c}\left[iC\zeta + \frac{a - \bar{a}\zeta^2}{2}\right] \tag{3.12}$$

where the parameter a is related to the core displacement as $a = -2is/C$.

This model takes into account the ingredient of the core deformation that is necessary to describe the vortex low frequency dynamics. It will also be used to understand the stability of the vortex state when varying the dot aspect ratio.

3.2.2 The vortex magnetic energies

Using the previous models of the vortex structure, it is possible to calculate the total magnetic energy of this system.

Following the notation of section 3.2.1, the vortex magnetic energies can be expressed with a 2D continuous model for the magnetisation [58]. Three types of energies are taken into account.

1. The exchange energy, arising from the non-uniformity of the vortex structure.

The exchange energy is given by the general expansion:

$$W_{ex} = A \int_{dot} d^3\boldsymbol{r} \Sigma_\alpha (\boldsymbol{\nabla} m_\alpha)^2 \tag{3.13}$$

where A is the exchange constant of the material. Using the cylindrical symmetry of the discs considered here, this equation can be expressed normalised in unit of $M_s^2 V$:

$$w_{ex} = \frac{W_{ex}}{M_s^2 V} = \frac{1}{2\pi}\left(\frac{R_0}{R}\right)^2 \int d^2\boldsymbol{\rho}\left[\left(\frac{d\Theta}{d\rho}\right)^2 + \frac{\sin^2\Theta}{\rho^2}\right] \tag{3.14}$$

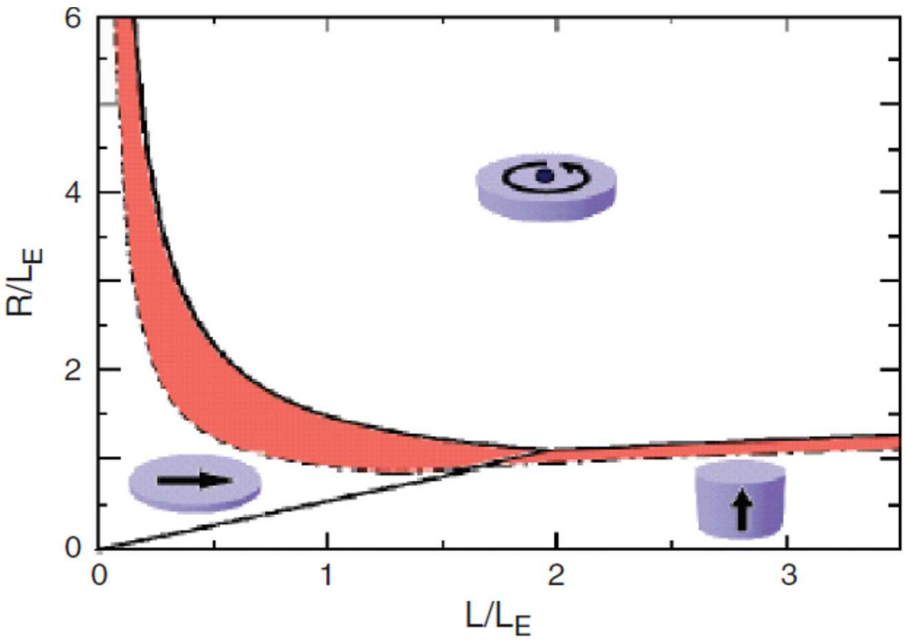

Figure 3.3: Diagram of stability of the vortex state (from [54]) when varying the dot radius R and thickness L (L_E is the material exchange length). The red area is a region of bi-stability.

where $R_0 = \sqrt{2A/M_s}$ is the exchange length and V the volume of the dot.

2. Then, because we consider confined structures, the magneto-static (or dipolar) energy needs to be taken into account.

The magneto-static energy includes the non local dipolar interactions. This energy is usually introduced as a Zeeman term $W_m = \frac{1}{2}\boldsymbol{M}.\boldsymbol{H_m}$ created by the magneto-static or demagnetising field H_m. If the long range dipolar interactions are introduced by the dipolar Green's tensor $\hat{\boldsymbol{G}}^d(\boldsymbol{r})$ already introduced in the chapter 2, this field is given by:

$$\boldsymbol{H}_m(t,\boldsymbol{r}) = -4\pi \int \hat{\boldsymbol{G}}^d(\boldsymbol{r}-\boldsymbol{r}').\boldsymbol{M}(t,\boldsymbol{r}')\ d^2\boldsymbol{r}' \tag{3.15}$$

where the integral is taken over the disc surface. $\hat{\boldsymbol{G}}^d$ is difficult to calculate in the particular case of the vortex.

An alternative way to formulate the problem is through the demagnetising tensor. The magnetisation, composed of magnetic "dipoles" interacting together, produces a self demagnetising stray field. The geometry of the dot and its magnetisation configuration are modelled in a demagnetising tensor $\hat{\boldsymbol{N}}$, and the dipolar field is then $\boldsymbol{H}_m(\boldsymbol{r}) = -4\pi M_s \hat{\boldsymbol{N}}(\boldsymbol{r})$. The calculation of the demagnetising tensor in the vortex state is still a complicated problem.

Finally, the magnetic inhomogeneities can be modelled as magnetic "charges" $\sigma(\boldsymbol{r})$, in the volume, the faces and the side of the dot. The volume charges are neglected in this two dimensional model. The magneto-static energy is the energy of interaction between these charges over the sample upper and bottom surfaces:

$$W_m = \frac{1}{2}\int dS \int dS' \frac{\sigma(\boldsymbol{r})\sigma(\boldsymbol{r}')}{|\boldsymbol{r}-\boldsymbol{r}'|} \tag{3.16}$$

3. The Zeeman energy if an external field is applied. In particular, an in plane field along the X direction will displace the vortex core in the Y direction because of the orthogonality between the core magnetisation and the field direction. Taking this property into account, all the magnetic energies are also calculated as a function of the reduced core position s.

The Zeeman energy is simply the interaction between the magnetisation and any external magnetic field $\boldsymbol{H}_{ext}$:

$$W_Z = -\int_V \boldsymbol{M}(\boldsymbol{r}).\boldsymbol{H}_{\text{ext}} d^3\boldsymbol{r} \tag{3.17}$$

Only discs made of soft magnetic materials are considered here, they have no or little magnetocrystalline anisotropy and therefore the anisotropy energy can be neglected.

3.2.2.1 Vortex stability diagram at remanence

When the lateral size of a thin disc is comparable to the exchange length, there is a competition between the vortex state and the saturated state with the magnetisation in the dot's plane. At the opposite, if the disc thickness is increased, the out-of-plane saturated state will be favoured. When the radius and thickness of the dot are varied, the boundaries between these three states correspond to lines of equal magnetic energy. Nevertheless, a metastable state can continue to exist even when its configuration is not favourable, and regions of bi-stability can be defined.

For each dot aspect ratio L/R, the total vortex magnetic energy is compared to the energy of the other uniformly magnetised states (in-plane and out-of-plane). Assuming that the lowest energy configuration is preferred, the diagram of stability of the vortex state can be calculated.

Without any applied field, the Zeeman energy plays no role and the vortex core remains at the centre of the disc. Therefore, the magneto-static energy is related to the magnetic charges located on the dot faces ($\sigma(\boldsymbol{r}) = (\boldsymbol{M}.\boldsymbol{n})_{\text{faces}}$). There are no charges on the dot sides since the axial symmetry is not broken.

The problem reduces to an Euler equation which minimises the total magnetic energy [133, 52] ($W = W_{ex} + W_m$). This complicated equation can be reduced in a simpler form considering dots of small aspect ratio $\beta = L/R$, but it is still difficult to solve it analytically. However, the Usov's ansatz, corresponding to the centred vortex core is a good approximation if the radius of the core is smaller than the dot radius. This model allows to calculate the iso-energy lines between the three possible magnetic states. They correspond to the black solid lines in the figure 3.3.

The calculation of the bi-stability regions, corresponding to the red area in the figure 3.3, is more complicated, because their boundaries are lines where the vortex state becomes really unstable. When this stability threshold is crossed, a mode of the vortex develops leading to the apparition of a saturated state. It is possible to identify this mode, for both transitions (vortex to out-of-plane [52] and vortex to in-plane magnetisation [90]).

Qualitatively, at remanence the vortex state is stable in soft thin magnetic cylinder with lateral size greater than the exchange length. If the the cylinder is too flat, i.e the

aspect ratio is too small and if the radius is larger than the core radius, the magnetisation is saturated in the plane. If the dot is too thick, the magnetisation is saturated along the cylinder axis. Finally, if the lateral size becomes too large, several multi-domains may appear.

3.2.2.2 Vortex stability under applied magnetic field

By choosing discs with aspect ratios β compatible with the vortex state, the influence of both in-plane and out-of-plane dc magnetic fields is investigated. The main effect of a magnetic field is to deform the vortex structure, eventually leading to its annihilation. The in-plane field basically breaks the axial symmetry of the static vortex resulting in the formation of magnetic charges on the disc sides. The selected model should take those charges into account. To understand this phenomenon, two ingredients are needed: a model of the vortex allowing the core to be displaced and vortex energies written as a function of the core position in the dot.

1. The magnetic field is applied in the plane of the dot.

   The effect of such a field is to displace the vortex core in the perpendicular direction to minimise the Zeeman energy of the in-plane curling domain. The process is driven by the growth of the in-plane domain parallel to the applied field. This produces magnetic charges located on the disks sides whereas the surfaces charges remain unchanged. The "rigid vortex" model is well adapted because it reproduces this behaviour. The total vortex energy is then calculated with this model taking into account the core position s in the dot. The core equilibrium position s_0 is obtained by minimising this energy [58, 51]. The core position is related to the static in-plane magnetic susceptibility χ_s:

   $$s_0 = \chi_s(\beta, R)\frac{H_{ext}}{M_s} \quad \text{where: } \chi_s = \left[2\pi F_1(\beta) - \frac{1}{2}\left(\frac{R_c}{R}\right)^2\right]^{-1} \tag{3.18}$$

   With, $J_n(x)$ being the Bessel function of the first first kind:

   $$F_n(\beta) = \int_0^\infty \frac{dt}{t} f(\beta t) J_n^2(t) \quad \text{and: } f(x) = 1 - \frac{1 - e^{-x}}{x} \tag{3.19}$$

   Using the same method, the dot averaged magnetisation can be calculated:

   $$\langle \boldsymbol{M} \rangle_V = \chi_s(\beta, R).\boldsymbol{H}_{\text{ext}} \tag{3.20}$$

   The hysteresis loop of the vortex versus the in-plane field can be calculated within this model. Of particular interest are the nucleation H_n and annihilation H_{an} fields of the vortex. Displaced by the field, the vortex core is finally expelled from the disc and replaced firstly by a so-called "C" state and then by the in-plane saturated state for high field values. The annihilation field is approximately defined as the field for which the core is located at the disc boundary (or $s_0 = 1$): $H_{an}(\beta, R) = M_s/\chi_s(\beta, R)$. This is a good approximation, even if the real annihilation process involves some instability. The nucleation field case is more complicated: the process is incoherent, and the polarity of the nucleated core is random. In a real disc,

the nucleation will occur on a defect at the boundary, whose magnetisation will most likely define the core polarity. The nucleation fied H_n will be defined as the field where the in-plane saturated state becomes unstable. This gives a good approximation of the real value, even if in reality the nucleation of the vortex core occurs preferentially in defects of the disc sides, which can slightly vary the real H_n value. The calculation follows the reasoning developed to define the boundary of the vortex state stability at remanence. The magnetic field replaces the lateral dot size as an adjustable parameter, and the threshold is defined as the apparition of the lowest vortex mode that destabilises the magnetisation of the "C" state. The proposed nucleation field is [58]: $H_n(\beta, R) = M_s\ 4\pi[F_1(\beta) - F_2(\beta) - \frac{1}{\pi}(\frac{R_0}{R})^2]$.

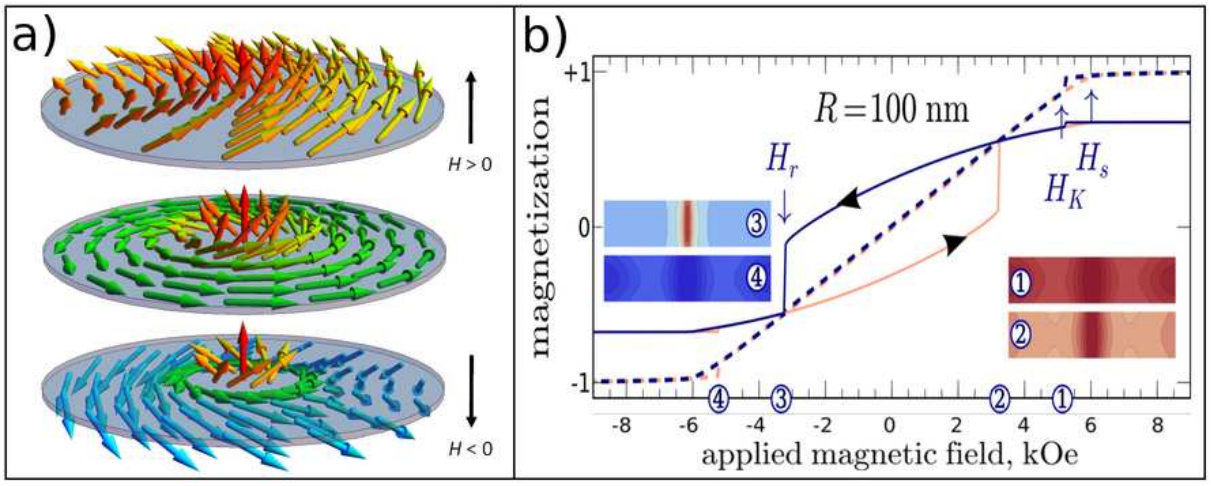

Figure 3.4: a) Sketch of the vortex magnetisation under a perpendicular bias field. The magnetisation in the disc plane follows the field direction, lifting the degeneracy of the two core polarity $p = \pm 1$. b) Numerically calculated field dependence of the static magnetisation of a NiMnSb disc (thickness $t = 44$ nm, radius $R = 100$ nm). The solid lines show the averaged magnetisation over the core only (a cylinder of about 15nm in diameter). The insets show the spatial distribution of M_z at four progressively decreasing values of H [32].

2. The magnetic field is applied perpendicular to the dot plane.

   The main effect of an out-of-plane magnetic field is to cant the curling in-plane structure of the vortex. In the so-called "cone state", the magnetic moments lying in the plane at remanence are tilted out-of-plane in the direction of the field by the Zeeman interaction, as sketched on the figure 3.4a. The curling state is conserved (keeping $\Phi = q\ \chi + C\ \frac{\pi}{2}$ valid and the axial symmetry) but the symmetry with respect ot the disc plane is broken by the core polarity. Two cases have to be considered:

   - The field is parallel to the core polarity. This case is referred as the parallel state (P) or $p = +1$ state in the following.
   - The field is anti-parallel to the core polarity. This case is referred as the anti-parallel state (AP) or $p = -1$ state.

   When the perpendicular field exceeds the saturation field $H_s \simeq 4\pi M_s \langle N_{zz} \rangle$ ($\langle N_{zz} \rangle$ is the out-of-plane demagnetising tensor component averaged on the dot volume), the

magnetisation is fully saturated out-of-plane. In a first approximation, the angle $\Theta(\boldsymbol{\rho}) = M_z(\boldsymbol{\rho})/M_s$ which parametrises the magnetic moments out of the core ($\Theta = 0$ at remanence) is evaluated as $\cos(\Theta) = H_z/H_s$ using the standard electromagnetic boundary conditions. It varies linearly with the bias field.

Two particularities have to be considered to have a more realistic description of the perpendicular field action on the vortex. First of all, the lateral size of the core R_c depends on the field strength. At remanence, the expression for the vortex core radius evaluated by Konstantin Guslienko from the vortex energies minimisation is the following [53]:

$$R_c(0) = 0.68R\left(\frac{L}{R}\right)^{1/3} \tag{3.21}$$

From the calculations made by B.A. Ivanov [67], it seems that the size of the vortex core is linear with H_z. When the field is applied parallel to the core polarity, its lateral size is increased as H_z reaches the saturation H_s. At the opposite, when the field is applied anti-parallel to the core, its volume is narrowed until it is energetically more favourable for the polarity to be reversed. The core and out-of-core magnetisation have indeed an opposite orientation which represents an exchange and Zeeman energy cost. When the energy cost of this strongly localised inhomogeneity equals the energy of a Bloch point, a Bloch point is created and reverses the core polarity by passing across the disc thickness. This process occurs at a given perpendicular field strength, defined as the static core reversal field H_r. The so-called Bloch point is defined by the following property: for any closed surface surrounding the point, the magnetisation vectors on this surface cover the surface of the unit sphere exactly once [127] .

Figure 3.4b summarises the influence of a perpendicular field. The field dependence of the magnetisation is simulated for a NiMnSb magnetic disc of 200 nm in diameter and 44 nm thick using a micromagnetic code developed by F. Boust and N. Vukadinovic [18]. Both the total magnetisation (dashed lines) and the magnetisation of the core (solid lines) present an hysteretic behaviour. First of all, the transition between the vortex and the saturated state at H_s is continuous while at the opposite, since there is no symmetry breaking. At the opposite, the vortex nucleation is abrupt and occurs at a lower field H_k. This is the sign of a mechanism driven by an instability. In a strictly two dimensional model, this hysteresis should not occurs, again because of the preserved axial symmetry. Taking the thickness into account may favour the perpendicularly saturated state. Finally, the vortex is nucleated from the disc side, in a process comparable to the in-plane nucleation.

The core magnetisation presents a strong hysteresis because of the stability of the polarity until the static reversal at H_r. It should be noticed that the hysteresis due to the core has a small influence on the total magnetisation, dominated by the tilted in plane magnetic moments.

In the case where a combination of in and out-of-plane magnetic fields is applied on the dot, the total magnetic energy including both deformations of the vortex have to be calculated to define the core equilibrium position s_0 and the nucleation/annihilation fields, which still has to be done.

3.3 Spin wave excitations of the vortex state in soft micron sized discs

The vortex is a ground state with a rich excitation spectrum. As in any magnetic system, high frequency spin waves can be excited, but dots in the vortex state present two interesting characteristics. The magnetic structure is confined, which leads to the discretisation of the spin wave spectrum (or eigen-modes), already seen in the saturated state in chapter 2. Moreover, the peculiarity of the vortex state, especially the presence of the core, allows the appearance of an unconventional dynamics at low frequency.

3.3.1 Equation of motion

Similarly to the saturated state, the dynamical properties of the magnetisation are solutions of the Landau-Lifshitz equation [82] extended with a non-conservative perturbation term presented equation (2.1) in chapter 2.

The early calculations on the vortex state excitations have been done using the classical 2D Heisenberg hamiltonian with an in-plane anisotropy [144, 66] to model the energy. This hamiltonian neglects the dipolar interaction, which is well adapted for continuous thin film. This is no longer valid in restricted geometry, like dots, since the dipolar energy is dominating over the other energies. This part of the hamiltonian is more complicated to treat since it involves the non local magneto-dipolar interactions. Approximations are developed in the following to model this contribution to the total energy in the vortex state.

The linear excitations are modelled as small deviations of the static vortex magnetisation, obtained by a linearisation of the equation of motion. Due to the axial symmetry of the system, trial functions composed of Bessel functions are introduced to describe the behaviour of the polar angle $\Theta(\boldsymbol{\rho}, t)$ and $\Phi(\boldsymbol{\rho}, t)$ of the magnetisation. Solving these equation gives a set of eigen-modes corresponding to radial and azimuthal spin waves rotating in the plane around the vortex core. These excitations are the continuation of the saturated state eigenmodes, but their dynamics is disturbed by the presence of the vortex core.

But another low frequency mode, corresponding to a motion of the whole vortex also exists. This mode is of particular interest in the micron sized discs we are considering.

3.3.2 The gyrotropic mode

In laterally confined structures such as discs, the vortex core can be seen as "trapped" in a potential that forces it to stay at the centre. If the core is moved away from its equilibrium position, for example by a magnetic field, it will experience a restoring force against this motion. As a result, when the field is turned off, the core gyrates at a given frequency in an iso-energy orbit around the disc centre. This is the so-called gyrotropic mode. Actually, when the field is turned off, because of damping process (magnetic relaxation in the material), the core goes back to its equilibrium position in a spiral motion.

To describe this mode, the vortex core is considered as a "soliton" or domain wall, propagating in the disc. Assuming this approximation, the motion of the core can be described by the Thiele equation [65].

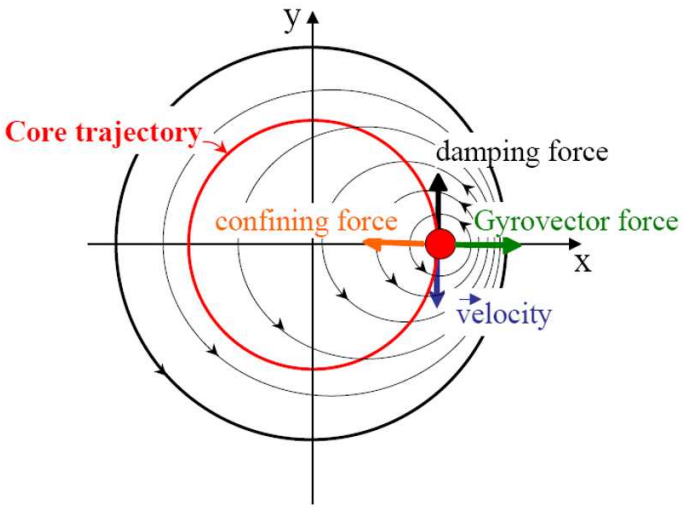

Figure 3.5: Sketch of the magnetic forces driving the gyrotropic mode in a disc (the core is represented by the red dot).

3.3.2.1 The Thiele equation

The main idea introduced by Thiele is to treat the vortex core motion as the one of a domain wall by introducing a set of collective variables for the core position in the disc plane $\boldsymbol{X}(\boldsymbol{\rho}, t) = (X, Y)$ [128]. It is assumed that equation (3.3.1) is applicable and that the core structure can be deformed during the motion. Therefore, the shifted vortex is described in a first approximation by the following travelling wave ansatz [92]:

$$\boldsymbol{M}(\boldsymbol{\rho}, t) = \boldsymbol{M}\Big(\boldsymbol{\rho} - \boldsymbol{X}(t), \dot{\boldsymbol{X}}(t)\Big) \tag{3.22}$$

The equation (3.3.1) can be linearised and rewritten with this ansatz leading to the Thiele equation of motion:

$$\bar{\bar{M}}\ddot{\boldsymbol{X}} - \boldsymbol{G} \times \dot{\boldsymbol{X}} - \bar{\bar{D}}\dot{\boldsymbol{X}} + \boldsymbol{F} = 0 \tag{3.23}$$

The first "mass" term is an inertial like term taking into account the out-of-equilibrium core deformation induced by the interactions with higher order spin waves. The shape of the core depends explicitly on its velocity. The mass tensor has the components:

$$M_{i,j} = \frac{1}{\gamma^2} \int d^2\boldsymbol{\rho} \left(\frac{\partial \Theta}{\partial X_i} \frac{\partial \Phi}{\partial \dot{X}_j} - \frac{\partial \Theta}{\partial \dot{X}_j} \frac{\partial \Phi}{\partial X_i} \right) \tag{3.24}$$

This tensor is symmetric for cylindrical dots and its value can be evaluated to $M \simeq (3/2)L/\gamma^2$ [55]. A numerical apllication using the typical parameter of the materials used in this thesis gives $M \simeq 10^{-20}$g. This term gives a relatively small contribution to the gyrotropic mode frequency and is usually neglected in calculations.

The second term is a force arising from the vortex non uniform magnetisation. The gyrovector, which is a topological charge $\boldsymbol{G} = -G.\boldsymbol{e}_z$, directed perpendicular to the disc plane, is responsible for the vortex core oscillation:

$$\boldsymbol{G} = \frac{M_s}{\gamma} L \int d^2\boldsymbol{r} \ \sin\Theta(\nabla\Phi \times \nabla\Theta) \tag{3.25}$$

It can be calculated by integration over the core profile; using any model of the vortex, it is evaluated as $G = 2\pi qpLM_s/\gamma$ (L is the dot thickness). The sign of the gyrovector is imposed by the vortex core polarity p. Therefore the sense of rotation of the core during the gyrotropic motion follows a right-hand rule relatively to the polarity. It is completely independent of the vortex chirality C.

The third term is a damping force opposed to the gyroforce, responsible for the return to equilibrium of the shifted vortex core. The tensor $\bar{\bar{D}}$ models the magnetic relaxation:

$$D_{i,j} = -\alpha \int d^2\boldsymbol{\rho} \left(\frac{\partial\Theta}{\partial x_i}\frac{\partial\Theta}{\partial x_j} + sin^2\Theta \frac{\partial\Phi}{\partial x_i}\frac{\partial\Phi}{\partial x_j} \right) \tag{3.26}$$

This tensor is diagonal for a cylindrical dot and can be calculated with the rigid vortex model [53]:

$$D = -\frac{\alpha\pi M_s L}{\gamma}\left[2 + \ln\frac{R}{R_c}\right] \tag{3.27}$$

The last term $\boldsymbol{F}$ corresponds to the other internal and external forces acting on the vortex core. The main intrinsic force is a restoring force created by the magneto-static charges formed by the shifted core. This force is equivalent to an energy potential confining the core in the middle of the disc. The force exerted by the external spatially uniform applied field (continuous $\boldsymbol{H}_{\text{ext}}$ and microwave $\boldsymbol{h}_{\text{rf}}$) can also be taken into account. This last term can be expressed with the potential energy as: $\boldsymbol{F} = -\partial W(\boldsymbol{X})/\partial \boldsymbol{X}$.

The two vortex model, which describes well the core shifted in the disc, is used to calculate the total potential energy. The magneto-static energy is modelled as an harmonic potential with the stiffness constant κ and the Zeeman energy is calculated using the averaged in-plane projection of the magnetisation $\langle \boldsymbol{M} \rangle_v$. The potential energy, normalised by $M_s^2 V$ is given by [58]:

$$w(\langle \boldsymbol{M} \rangle_v) = \frac{W}{M_s^2 V} = w(0) + \frac{\langle \boldsymbol{M} \rangle_v^2}{2\chi_s} - \langle \boldsymbol{M} \rangle_v . \frac{H_{ext}}{M_s} + \mathcal{O}(\langle \boldsymbol{M} \rangle_v^4) \tag{3.28}$$

where $w(0)$ is the vortex potential energy when the core is at the centre of the disc. The static susceptibility, already calculated in section 3.2.2.2 with the rigid vortex has to be evaluated within the double vortex model [50]:

$$\chi_s = \left[9\left(4\pi F_v\left(\frac{L}{R}\right) - \left(\frac{R_0}{R}\right)^2\right)\right]^{-1} \quad \text{where: } F_v(x) = \int \frac{dt}{t}\left(1 - \frac{1-e^{-x}}{x}\right)\left[\int_0^1 d\rho\rho J_1(\rho t)\right]^2 \tag{3.29}$$

The energy of the shifted vortex can then be written as:

$$W(\boldsymbol{X}) = W(0) + \frac{\kappa \boldsymbol{X}^2}{2} + \mu[\boldsymbol{u}_z \times (\boldsymbol{H}_{ext} + \boldsymbol{h}_{rf})].\boldsymbol{X} + \mathcal{O}(\boldsymbol{X}^4) \tag{3.30}$$

where $\mu = (V\xi C M_s)/R$. The parameter ξ takes the value 2/3 for the two vortex model.

All the forces contributing to the gyrotropic motion of the vortex core are sketched in the figure 3.5. The vortex core, represented as a red dot, gyrates around an equilibrium orbit, defined by the balance between all the magnetic applied forces.

The linear dynamical part of the magnetisation $\boldsymbol{m}$ during the gyrotropic motion is plotted in the figure 3.6. This is the spatial profile of the magnetisation precession in the gyrotropic mode corresponding to a particular position of the core around the disc centre. It can be noticed that even though the precession is mainly concentrated around the core, all the vortex structure is involved in the gyrotropic mode.

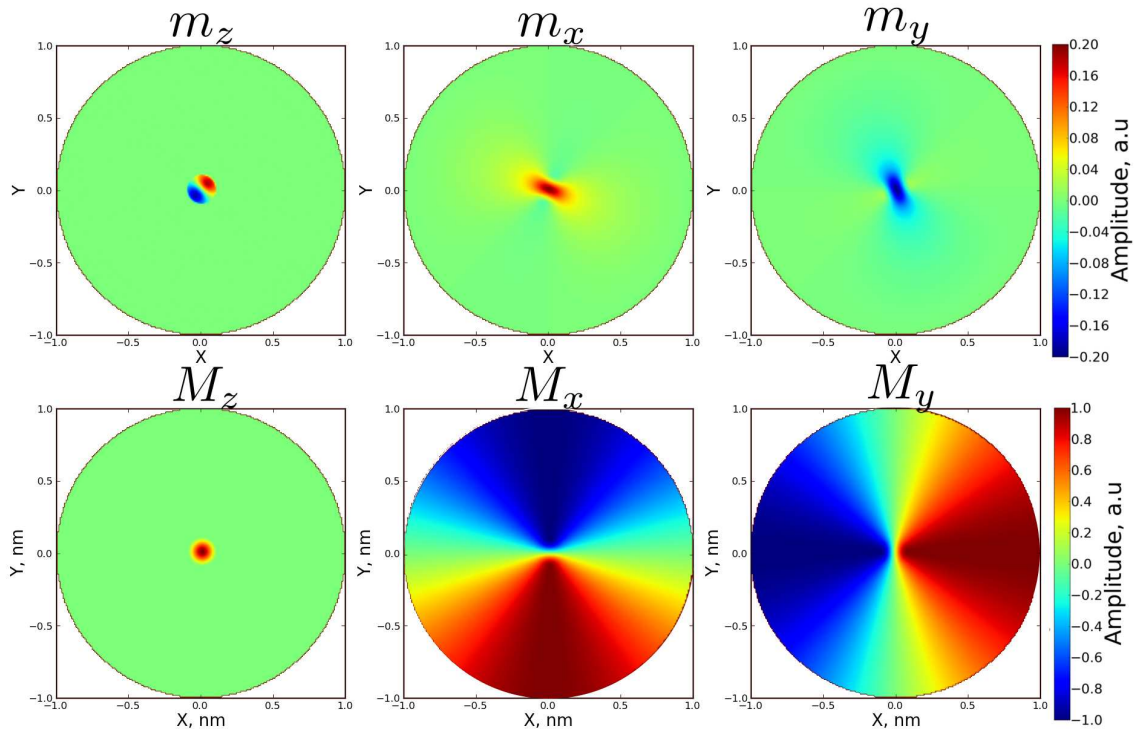

Figure 3.6: Dynamical part of the magnetisation $\boldsymbol{m}(t) - \boldsymbol{m}(0)$ for the gyrotropic mode in the linear regime (first row) compared to the static magnetisation of the vortex $\boldsymbol{M}$ (second row). The effect of the core displacement affect the magnetisation in the whole disc (Notice the difference of scale between the two rows).

3.3.2.2 Different approximations for the eigen-frequency

The resolution of the Thiele equation can be done using various methods [49]; one particular case is presented in Appendix A. Solving the Thiele equation as presented gives access to the gyrotropic mode frequency in the linear regime. In the first calculation done by Konstantin Guslienko, only the gyroforce and the confining potential are taken into account as the main contributions to the mode dynamics. Equation (3.23) becomes rather simple, and the gyrotropic frequency at zero field is given by the ratio $\omega_G(0) = \kappa/G$, which leads to [50]:

$$\omega_G(0) = \frac{1}{2}\gamma M_s \frac{\xi^2}{\chi_s} \simeq \frac{20}{9}\gamma M_s \frac{L}{R} \tag{3.31}$$

The last expression is a good approximation for thin enough discs with radius larger than the exchange length.

The first correction to this frequency is given by the magnetic dissipation. As developed in appendix A, the gyrotropic frequency is then given by:

$$\omega_G(0) = \frac{\kappa|G|}{G^2 + D^2} \tag{3.32}$$

Taking into account the deformation of the vortex core during its motion is equivalent to consider an effective mass of the vortex [92]. More precisely, this vortex mass arises from the interaction of the core with the azimuthal spin waves modes [55]. The Thiele equation is extended to the second order with an inertial term. This introduce a second

correction to the frequency given by:

$$\omega_G^{'}(0) = \omega_G(0)\left[1 - \frac{3\ \omega_G(0)}{4\pi\gamma M_s}\right] \tag{3.33}$$

3.3.2.3 Influence of a perpendicular field

The case of a magnetic field applied perpendicular to the vortex plane is of fundamental importance for the present work since the experimental setup used in this thesis imposes such a field. A new Zeeman term has to be added to the energy of the system in the Thiele equation.

The static structure of the vortex is distorted, as described previously in section 3.2.2.2. The in-plane magnetisation of the vortex follows the perpendicular field and is tilted out-of-plane. The gyrotropic frequency which is strongly dependent on the magnetisation configuration will therefore depend on the field H_z.

Using a continuous approach, and solving the resultant equations numerically, B.A. Ivanov found the dependence of the gyrotropic mode with the perpendicular field as well as the static reversal field [67]. But a fully analytical method can be developed using simple arguments.

The dependence of ω_G can be calculated in a first approximation, assuming that the variation of the core size can be neglected. The gyrotropic frequency is given by $\omega_G(H_z) = \kappa(H_z)/G(H_z)$, with the field dependent vortex stiffness and gyrovector. Outside of the core, the magnetisation is tilted out-of-plane by the polar angle defined by $\cos\ \theta = H_z/H_s$. The gyrovector, defined equation (3.25) at remanence, is then given by:

$$G(H_z) = G(0)\Big(1 - p\ \cos\theta\Big) \tag{3.34}$$

Geometrically speaking, this is the solid angle covered by the magnetisation on the unit sphere [127]. The main contribution to the energy is given by the dipolar interaction. The demagnetising tensor is modified compared to the remanent case which modifies the vortex confining potential. It can be seen as magnetic charges created by the out-of-plane magnetic moments. The field dependent vortex stiffness is then:

$$\kappa(H_z) = \kappa(0)\sin^2\theta \tag{3.35}$$

Using the formulation of equations (3.35) and (3.34), the field dependant gyrotropic frequency can be derived [32]:

$$\omega_G(H_z) = \omega_G(0)\left[1 + p\frac{H_z}{H_s}\right] \tag{3.36}$$

In the case of core polarity $p = -1$ opposed to the applied field, this formula is valid only if the perpendicular field is lower than the static reversal field: $H_z < H_r$. Indeed, for perpendicular field higher than H_r the anti-parallel polarity is unstable.

3.3.2.4 The Dynamical reversal

One of the main and outstanding non linear effects of the gyrotropic motion is the dynamical vortex core reversal. This effect has a very different origin compared to the static

core reversal described in section 3.2.2.2. After an early theoretical prediction by Y. Gaididei [43], it was first shown by the team of B. Van Waeyenberge that a short burst of in-plane microwave field at the gyrotropic frequency could reverse the core polarity at remanence [134]. This new core reversal phenomenon was also achieved applying a spin polarised current [145, 146] and was observed in micromagnetic simulations [62]. The core reversal was also achieved by exciting higher order spin wave modes, strongly coupled to the gyrotropic mode [72, 149, 21, 147, 72].

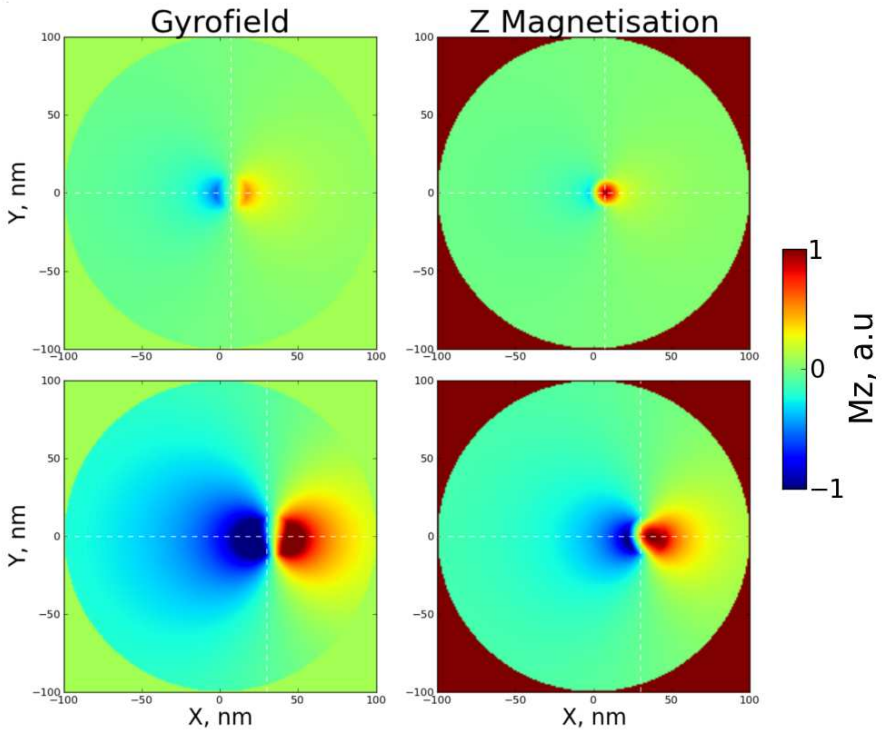

Figure 3.7: Calculations showing the dynamical gyrofield created by the core motion and its effect on the longitudinal magnetisation: the formation of a negative dip next to the core. The core position (related to its velocity) is close to the centre in the upper row and shifted at $\approx R/2$ for the lower row.

The mechanism of this reversal can be understood by a detailed analysis of the core deformation during the gyrotropic motion. The vortex mass introduced in the Thiele equation is a way to understand it phenomenologically. But it is possible to describe the physical origin of this deformation by writing the equivalent field created by the gyrotropic motion [145].

During the core gyrotropic motion, the magnetisation included within the core orbit rotates by $360\hat{A}^\circ$ at every turns. Along the line between the core and the dot centre, the time derivative of the magnetisation is very strong. Moreover, this term increases with the vortex velocity $\boldsymbol{v} = \dot{\boldsymbol{X}}$ as $\dot{\boldsymbol{m}} = -(\boldsymbol{v}.\boldsymbol{\nabla})\boldsymbol{m}$. The magnetisation moving rapidly near the core produces an effective internal field, the gyrofield h_z, directed along $\boldsymbol{u}_z$ and opposed to the core polarity [57]:

$$h_z = -\frac{1}{\gamma}\frac{(\boldsymbol{m}\times\dot{\boldsymbol{m}})_z}{(m_z+p)^2} = -\frac{\left[\tan(\frac{\Theta}{2})\right]^{2p}\dot{\boldsymbol{\Phi}}}{\gamma} \tag{3.37}$$

This field of dynamical origin, concentrated near the core toward the dot centre, deforms the magnetisation and is responsible for the core dynamical profile $m_z(\boldsymbol{r}, t)$. As a consequence, a negative dip in the magnetisation is created near the core and its size depends on the core velocity. The effect of this gyrofield is calculated on the figure 3.7, presenting the field of equation (3.37) and its Zeeman influence on the magnetisation for two increasing core velocities, i.e. core position or gyration raduis. This dynamical deformation of the core was already observed experimentally, as shown on the figure 3.8a. At $H_{ext} = 0$, it is possible to estimate the maximal value taken by the gyrofield, near the core, as $\max(h_z) \simeq (\omega_G(0)/\gamma)|\boldsymbol{X}|/R_c$. The magnetic core profile becomes unstable roughly when $\max(h_z)$ is sufficient to form a dip of magnetisation $m_z(dip) \simeq -1$ opposed to the core. The dip is a pair vortex/anti-vortex of equal amplitude and opposed to the core [134, 62]. The anti-vortex is instantaneously annihilated with the vortex core because of topological reasons. The only structure that remains is the negative dip with $m_z = -1$, which is a vortex core of opposed polarity. This scenario is summarised in figure 3.8b.

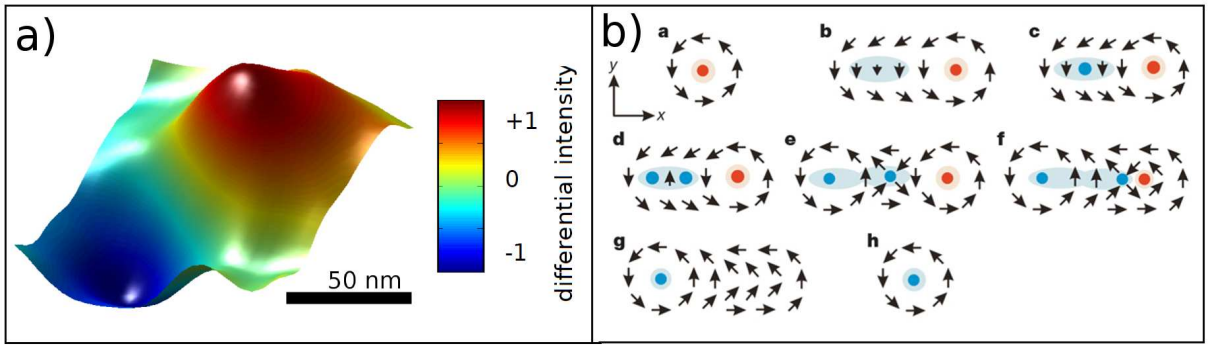

Figure 3.8: a) Three-dimensional representation of the experimentally observed vortex core dynamical profile by high-resolution time-resolved X-ray microscopy (from reference [135]). The core is in red while the dynamical deformation is in blue. b) Schematic description of the core reversal mechanism: the arrows represent the in plane magnetisation, the red dot is the vortex core while the blue dot is the dynamical dip opposed to the core (from reference [134]).

The phenomenon is driven by the core velocity during the gyrotropic motion, and the position of the core when $\max(h_z)$ reaches -1 actually corresponds to a critical speed of the vortex. This critical speed at which the dynamical reversal occurs is the radial velocity of the core $v_c = \boldsymbol{\omega} \times \boldsymbol{X_c}$, with $\boldsymbol{X_c}$ the solution of the equation $\max(h_z) = -1$. An evaluation of this quantity at zero field gives [85]:

$$v_c(0) \simeq \eta\ \gamma \sqrt{A_{ex}} \tag{3.38}$$

The gyrofield responsible for the reversal mostly arises from the short range exchange interaction inside the core structure, which is insensitive to the dot geometry and magnetisation. Here $\eta = 1.66$ is a universal constant independent from the (soft and thin) material parameters. A material with easy plane plane magnetic anisotropy K can be considered, leading to a renormalised critical velocity [74]:

$$v_c(0) \simeq \eta\ \gamma M_s \sqrt{\frac{2\pi A_{ex}}{2\pi M_s^2 + K}} \tag{3.39}$$

Once the critical speed, typically a few hundreds of meters per second, is reached, the core reversal occurs in a few picoseconds followed by an intense emission of spin waves

that relax the energy stored in the vortex-antivortex system. The core is then damped and comes back to its equilibrium position in a spiral motion [15].

This formulation of the critical speed is only valid at remanence and should be modified to include the influence of a perpendicular field. The velocity v_c depends on the magnetic structure of the vortex and simulations have shown a quasi linear dependence with H_z [74, 148]. The core becomes unstable with an opposite field and is statically reversed at $H_z = H_r$. Assuming that the critical velocity reaches 0 at the static reversal field, its dependence can be described as:

$$v_c(H_z) = v_c(0)\left[1 - \frac{H_z}{H_r}\right] \tag{3.40}$$

3.3.2.5 Non linear gyrotropic motion

All the frequencies for the gyrotropic mode were calculated in the linear regime, i.e. as a response to a small microwave perturbation. But the last section on the dynamical reversal has shown the importance of the non linearities to explain the core deformation. To understand properly the core reversal, the non linear mechanism has to be understood.

The non linearity is an intrinsic property of magnetic systems, since the LLG equation governing their dynamics is essentially non linear [4]. The physical reason for the apparition of non linearities when the excitation strength is increased is the interaction between different spin waves modes. For the particular case of the gyrotropic motion, the mode involving the vortex core strongly interacts with the azimuthal spin waves modes [68, 60]. Taking into account in details these complicated scattering mechanism is impossible, nevertheless the main physics can be captured by introducing some reasonable non-linearities in key parameters [49, 39].

For the case of a disc, the first non linearity is introduced in the vortex confining potential, mainly defined by the magneto-static energy term. The Zeeman contribution needs to be extended as well since the vortex is driven by an external microwave field. The last energy term defined in equation (3.30) can be split in two. The magneto-static energy term is extended to the second order:

$$W_m(\boldsymbol{X}) = W(0) + \frac{\kappa \boldsymbol{X}^2}{2} + \frac{\beta \boldsymbol{X}^4}{4} + \mathcal{O}(\boldsymbol{X}^6) \tag{3.41}$$

and the Zeeman term is modified as well to take into account a non linear response to the excitation field:

$$W_Z(\boldsymbol{X}) = [\boldsymbol{u}_z \times (\boldsymbol{H}_{ext} + \boldsymbol{h}_{mw})].\boldsymbol{X}[\mu - \delta|\boldsymbol{X}|^2] + \mathcal{O}(\boldsymbol{X}^3) \tag{3.42}$$

The non linearity of the gyrotropic mode appears to be essential when the core orbit exceeds $|\boldsymbol{X}| > 0.13R$ [19]. If the driving field is increased, three stationary orbits can be found, and the shape of the resonance line becomes asymmetric: this is the foldover bifurcation [49]. This foldover experienced by the resonance peak is due to the non linear frequency shift of the gyrotropic resonance. A shift toward low frequency is supported by many experimental measurements [26, 136], including ours (see figure 5.6 of chapter 5); but taking only into account the previous non linear terms leads to a positive frequency shift. The system should be dominated by an other source of damping. Our experimental

results, presented in the chapter 5, suggest that the damping term is itself non linear [107]. It was then proposed to extend the damping term as follows [118]:

$$D' = D + D_1|\dot{\boldsymbol{X}}|^2 \tag{3.43}$$

with D being the linear damping term previously introduced. A non linear red shift of the gyrotropic resonance frequency can be explained within this model by choosing a proper phenomenological parameter D_1. Nevertheless, more investigations have to be done on this topic in order to validate this scenario.

An interesting phenomenon arising from this non linear coupling between the gyrotropic mode and higher order spin waves is the possibility to reverse the core. Indeed, it has been shown that the core polarity can be reversed by exciting particular spin wave modes in the non linear regime. For instance, a non linear coupling between azimuthal spin wave modes and the gyrotropic mode can reverse the core [72, 80]. Moreover, radially symmetric spin wave modes excited by an ou-of-plane microwave field could lead to a polarity switching [149, 21, 147, 72].

3.3.3 Higher order modes in the vortex state

At higher frequency, other modes exist, consisting of spin waves over the vortex ground state [59, 68]. The symmetry of the dots considered here is reflected on the spin wave dynamics. Similarly to the perpendicularly saturated case, the boundary conditions induces a quantisation of the spin wave spectrum. The theoretical treatment is very similar to the chapter 2. The spectrum is composed of radial and azimuthal modes developing in the vortex plane. The main difference being the vortex core located at the disc centre and the static azimuthal symmetry of the magnetisation.

3.3.3.1 Radial spin waves

Let first consider the spin excitations having only a radial symmetry: $(l = 0, m)$. Similarly to the case of a dot saturated out-of-plane, which have the same symmetry, radial spin waves develop in the disc plane, consisting on a radially varying angle of precession [21, 140]. In the limit of thin dots (small aspect ratio β), the amplitude of the dynamic part of the magnetisation is well described by Bessel functions [59, 140]. The presence of the vortex core doesn't break the symmetry, but imposes the angle of precession to be null at the centre of the dot. Therefore, instead of the $J_0(\rho)$ function used in the saturated state, the $J_1(\rho)$ function is appropriate since it vanishes for $\rho = 0$.

The wave vector κ_m of the radial spin wave $(l = 0, m)$ is given by the mth root α_m of the equation $J_1(\rho) = 0$, where J_1 is the Bessel function of the first kind with index 1. The spatial component of the eigen-functions modelling the dynamical magnetisation are:

$$m_m(\rho) = C_m J_1(\kappa_m \rho) \quad \text{where: } \kappa_m = \frac{\alpha_m}{R} \tag{3.44}$$

where C_m is the eigen-basis normalisation constant. This is the asymptotic limit for small aspect ratio $\beta \ll 1$, it corresponds to the strong pinning regime. Within this approximation, the set of eigen-frequencies is at remanence given by:

$$\omega_{0,m} = 4\pi\gamma M_s \sqrt{1 - \frac{1 - e^{-\beta\alpha_m}}{\beta\alpha_m}} \tag{3.45}$$

The frequency of the radial modes increases with increasing indices m. Indeed, the wave vector is perpendicular to the local magnetisation: the magnetic energy increases for smaller wave vector, or higher m. Moreover, the frequency dependence under a perpendicular applied field is the same as for the gyrotropic mode [149].

This approximation doesn't take into account the real dipolar pinning conditions for the magnetisation, especially if $\beta > 0.1$. The real intermediate pinning regime deforms the mode profiles. It can be taken into account by defining a new wave vector [54]: $\kappa_m^{'} = \alpha_m^{'}/R$ where $\alpha_m^{'}$ is is the nth root of the boundary equation $R\partial m_m(\rho = R)/\partial\rho + \eta m_m(\rho = R) = 0$ where:

$$\eta(\beta, L) = \frac{2\pi}{\beta\left[4(ln\frac{8}{\beta} - \frac{1}{2}) + (\frac{l_{ex}}{L})^2\right]} \tag{3.46}$$

Compared to the saturated state, the symmetry of the magnetisation background in which the spin wave modes develop is inverted. Out of the core, the magnetisation follows an azimuthal symmetry, while it was axial in the saturated case. Therefore, the selection rules for the excitations of these spin waves are also inverted. To be coupled to the radial modes in the vortex state, the excitation has to follow an azimuthal symmetry. For instance, a microwave field or pulse applied perpendicularly to the plane of the disc would be effective [140].

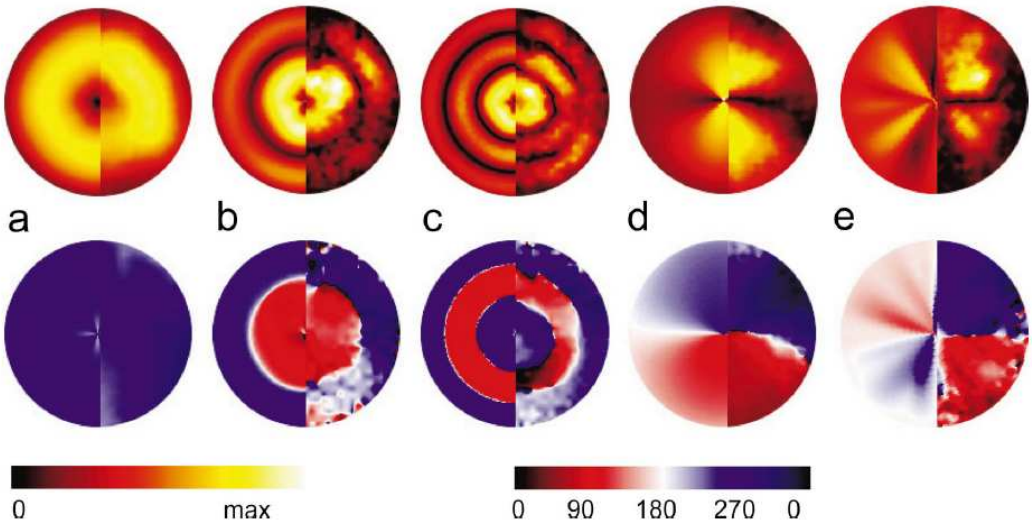

Figure 3.9: From reference [22]: Amplitude (first row) and phase (second row) of the spin wave modes dynamical magnetisation in the vortex state. The modal maps are composed from two half-images: the left from the micromagnetic simulation; the right from a TR-Moke experiment. a), b) and c) correspond to the radial modes ($l = 0, m = 1, 2, 3$); d) and e) correspond to the azimuthal modes ($l = 1, 2, m = 0$).

3.3.3.2 Azimuthal spin waves

Another type of spin wave can be excited, consisting in waves travelling around the vortex core: $(l, m = 0)$. The spatial component of the dynamical part of the magnetisation is now proportional to $\simeq m_l(\rho)\cos(m\phi + \omega_{l,0}t)$. In a saturated dot the azimuthal spin waves with

indices $\pm l$, travelling in the opposite direction, are degenerated in energy. The presence of the vortex core lifts the degeneracy, and also imposes $m_l(\rho = 0)$ to be zero.

The gyrotropic mode strongly interacts with the azimuthal modes by dynamic dipolar coupling [60]. The rotational invariance is broken by the gyrovector and therefore, for a given core polarity, this interaction has a different energy for each travelling spin wave $\pm l$. Following this statement, the waves travelling in the same sense of rotation as the gyrotropic mode have a lower frequency than the phase symmetric one. This coupling is responsible for the apparition of an effective mass of the vortex core in the equation (3.23). At the lowest order (considering only the coupling with the mode ($l = \pm 1, 0$)) this mass is evaluated as $M \simeq 3L/2\gamma^2$ [49].

The equation (3.23) has then two solutions: the first one gives the gyrotropic frequency (equation(3.31)) and the second one leads to the $l = 1$ degenerated frequency. The analytical frequencies of the azimuthal modes are more complicated to calculate than the radial ones. The frequency of the first mode, with $l \pm 1$, has been widely investigated, and is found to be proportional to the dot aspect ratio, $\omega_{n,1} \propto \sqrt{\beta}$ [5]. The splitting between these two modes due to the interaction with the core is then proportional to $\Delta\omega_{n,\pm 1} \propto \beta$ [104]. More generally, the frequency of these azimuthal modes decreases with increasing indices l. At the opposite of the radial modes, the wave vector is now parallel to the local magnetisation and the magnetic energy decreases while the wave vector drecreases. This is of course valid only for magneto-static spin waves.

The selection rules for these modes is also reversed compared to the saturated state and they could be excited only by a spatially homogeneous in-plane microwave field or pulse.

These spin wave modes have been measured by TR-MOKE [22] and the spatial profile and phase of the dynamical magnetisation are displayed for the few first modes in the figure 3.9. This experimental measurement confirms the analytical model developed to model the spin wave in the vortex state.

3.4 Conclusion

The vortex state is found to be the stable ground state of a wide range of unsaturated magnetic nanostructures, such as nano-discs. Even if most of the unsaturated magnetisation states are complicated to tackle, the symmetry of the vortex state is of great help toward a precise description of its properties. Compared to the saturated state in nano-discs described previously, the axial symmetry is conserved, the new ingredient being given by the presence of the vortex core.

This magnetic structure appears to be very stable with respect to the application of static bias fields either in or out-of-plane. Moreover, the precise deformations induced by these perturbation can be calculated analytically.

But the real interest of the vortex state lies in its dynamics. The spin wave spectrum is composed of an atypical low frequency mode, or gyrotropic mode, well separated in energy from higher order modes having a symmetry similar to the saturated case. Its eigenfrequency, only dependent on the geometry of the dot, was calculated as well as its evolution under a perpendicular bias field. The validity of the theoretical description, based on the Thiele equation, will be demonstrated experimentally in chapter 5.

The non linear dynamics of the vortex state is of particular interest. First of all,

the gyrotropic motion driven at high amplitude leads to the dynamical core reversal. The ability to reverse resonantly the vortex core between two stable polarities is very promising for applications in the data storage, as will be shown in the chapter 5. But a strong non linear coupling exists also between the gyrotropic mode and higher order spin wave modes. It is even possible to reverse the core by exciting either azimuthal or radial vortex modes at high amplitude.

This dynamics, and especially the gyrotropic mode, is also promising in realising vortex based STNO's. The collective motion of arrays of vortices dipolarly coupled becomes then a key problem in the optimisation of such devices. The precise theoretical description of this coupled dynamics is maybe one of the challenge in the field and the preliminary results are already promising [124, 125].

It is now important to test the model of the vortex experimentally. The measurable signals, in particular for the gyrotropic mode, are expected to be very small regarding the few amount of magnetisation involved in the dynamics. This requires a sensitive experimental techniques, the f-MRFM, that will be presented in the next chapter.

Chapter 4

Magnetic Resonance Force Microscopy

The sensitivity of magnetic resonance will be used for measuring the spin wave dispersion of our magnetic nano structures. As mentioned in the introduction, the force detection of the ferromagnetic resonance is well adapted to the constraints of our experiments. In this chapter, after an introduction to the idea of force detection of the magnetisation dynamics, the particular setup developed and used in this thesis is presented. Emphasis will be placed on the quantitative link between the measurement and the investigated physical parameters.

4.1 Introduction

In paramagnetic systems, nuclear or electronic spins, the main idea of magnetic resonance is to determine the local spin splitting (or Zeeman) energy of the magnetic moments. The magnetisation is brought out of equilibrium using a small time varying magnetic field, whose frequency is tuned to match energy difference $\hbar\omega$. The Fermi golden rule, calculated with the theory of perturbation dependent on time allows to calculate the resonance frequency ω. For paramagnetic systems, the resonance frequencies are in radio frequency range which leads to very narrow linewidths, since few relaxation channel are available at this frequency. The accuracy of the measurement of the local field is therefore very high. This is a powerful technique to analyse spectroscopically the chemical or magnetic environment of a solid or a liquid. Moreover dealing with narrow linewidths allows to localise the resonance in space and perform three dimensional images. This is the basis of magnetic resonance imaging (MRI), which is now widely used in medicine.

NMR (Nuclear Magnetic Resonance), ESR (Electron Spin Resonance) or FMR (Ferro-Magnetic Resonance) are usually detected via inductive means by a set of tuned coils for low frequencies or microwave resonators coupled to diodes for high frequencies. The small amount of microwave energy that is absorbed by the spin system is proportional to the transverse part of the precessing magnetic moments. But this detection is very sensitive to the filling factor, i.e., the ratio between the volume of the sample and the effective field volume captured by the detectors. This prevents individual or non homogeneous objects to be studied, such as magnetic nanostructures or biological molecules. The idea to use a mechanical detection of the resonance then emerged, the force sensors available being very accurate and possibly adapted to a local detection.

After a first attempt using a mechanical detection by Evans in the 60's [41], the idea of performing Magnetic Resonance Force Microscopy (MRFM) was proposed in the early 90's by John Sidles [120]. He was searching for a reliable and precise technique to determine the molecular structure of biological objects. For this purpose, he wanted a spectroscopic signature to understand the atomic structure of unknown objects. In order to achieve this goal, the atomic resolution is needed with the ability to study individual objects in the three spatial dimensions. The studied objects being fragile and sensible to external conditions, a non-destructive and non-invasive technique was also needed [121]. The development in the 80's of the scanning surface probe techniques such as Scanning Tunnelling Microscopy (STM), Atomic and Magnetic Force Microscopy (AFM/MFM) gives access to a high spatial resolution. The idea is to couple a highly sensitive force sensor like a micrometre sized cantilever to the longitudinal component of magnetic moments, either nuclear or electronic spins. Following the principles of MRI techniques developed for medical applications, the spins precession excited by a microwave field could be localised spatially in a "resonant slice" of the sample by an appropriate field gradient. The force exerted on the cantilever being also proportional to the field gradient, the spatial resolution could be increased by keeping the same signal-to-noise ratio. The sensitivity then becomes independent of the spatial resolution.

The first ESR MRFM signal was detected in Diphenylpycrilhydrazil (DPPH) by Dan Rugar's team in 1992 [113], followed in 1993 by an MRFM image of this molecule [151] and the first NMR MRFM signal in 1994 [114]. The team of Chris Hammel and Phil Wigen has then applied this technique to FMR by measuring resonances of YIG films in 1996 [150].

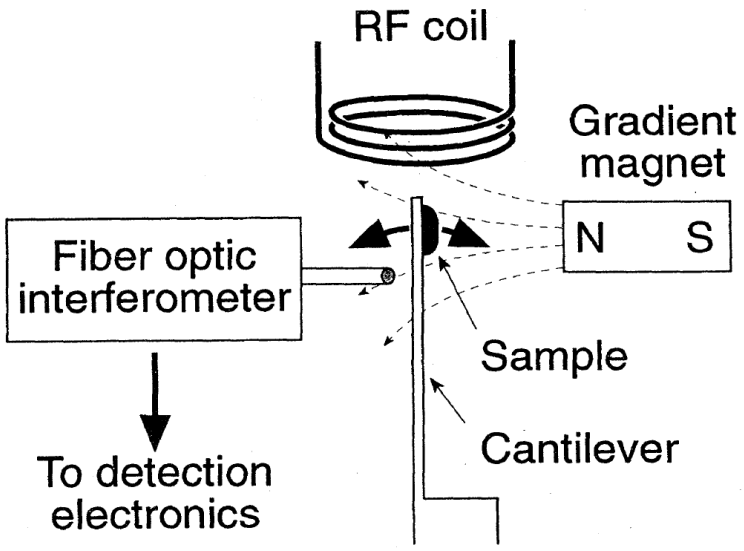

Figure 4.1: Basic principle of the MRFM detection, from J.Sidles [121].

4.2 Magnetic resonance with MRFM

4.2.1 Basic principles

The basic features of the MRFM detection, as proposed by J. Sidles and developed by D. Rugar are sketched in figure 4.1. The sample to be studied is placed at the end of a very soft cantilever. A local field gradient, which can be created by a ferromagnetic nanoparticle or a nanostructured magnetic dot, couples to the longitudinal component of the magnetic moments of the sample. If the field gradient source is fixed, a force proportional to this gradient is applied on the sample and a resultant force is exerted on the clamped cantilever. With $\boldsymbol{B}$ the non homogeneous stray field from the magnetic field gradient source, the force applied on the magnetic moment $\boldsymbol{m}$ of the sample is:

$$\boldsymbol{F} = (\boldsymbol{m}.\boldsymbol{\nabla})\boldsymbol{B} \tag{4.1}$$

The dynamics of the magnetic moments, either precession or cyclic inversion, is then excited with a radio-frequency coil. The resulting variation of the longitudinal component of the magnetic moments will change the static force between the magnetic probe and the sample, and the equilibrium position of the cantilever will change. The relative position of the cantilever is measured at the picometre scale with an interferometric detection.

4.2.2 NMR and EPR

This technique can be applied to the measurement of any kind of magnetic moment. Let us consider the case of nuclear or paramagnetic electron spins, which have only weak self interactions. When these spins are excited by an RF field, because of the static field gradient, only few of them will meet the resonance condition $\omega = \gamma H$. The precession, which gives the MRFM signal, will be spatially localised in a "resonant slice" of the sample, corresponding to an iso-field region. By combining the spatial distribution of the field gradient and the ability to displace the cantilever with an accuracy of a few Angströms,

three dimensional images of the spins distribution can be reconstructed [87, 33]. The amazing sensitivity of force detection was demonstrated in 2004 by the team of Dan Rugar with the detection of a single electronic spin resonance, at low temperature (200 mK) [112]. A better NMR experiment allows to reach a spatial resolution of 4 nanometres with a sensitivity of $\simeq 50$ nuclear spins [33].

4.2.3 Ferromagnetic resonance

The samples that will be considered in this thesis are ferromagnets. The electrons inside these materials are strongly correlated by the exchange interaction. They respond to an excitation as a coupled ensemble, and the concept of local excitation (resonant slice) is no longer valid. This will modify our approach of MRFM, as this was first described in the thesis of Melissa Midzor [93].

4.3 Ferromagnetic resonance with MRFM

In this section, I will describe step by step how the microscope used in this thesis was developed and built. Each important part will be presented with its own characteristics and its role in the measurement process. This is in a way the basic "recipe" to construct an f-MRFM.

4.3.1 The force sensor: a cantilever

The basic idea of the MRFM is to detect the spin resonance phenomenon with a force sensor. The recent progress of micro-fabrication allows to develop very accurate mechanical resonators with reduced dimensions. This gives access to resonators with relatively high reference frequency that keep high quality factors. The case of the cantilever, a simple beam clamped in one side, is of great interest because of its simplicity and its incredible sensitivity. We can define an idealised cantilever as sketched in figure 4.2a), which is approaching the real design of the cantilever that has been used in this thesis (figure 4.2b).

4.3.1.1 Static response

If a static perpendicular force F is applied at the free end perpendicular to the beam, the cantilever will be bent. At this location, the displacement D_{end} of the cantilever is simply [130]:

$$D_{\text{end}} = \frac{F}{k} \tag{4.2}$$

where k is the cantilever spring constant.

4.3.1.2 The cantilever as a natural amplifier: Dynamical properties

In the measurement process, the cantilever acts as a force-displacement transformer. But the cantilever is also a resonator that can be used to increase the signal to noise ratio. In the f-MRFM experiment, a homodyne detection of the of the FMR is performed at the cantilever frequency to gain a factor Q in the signal amplitude, in order to be able to

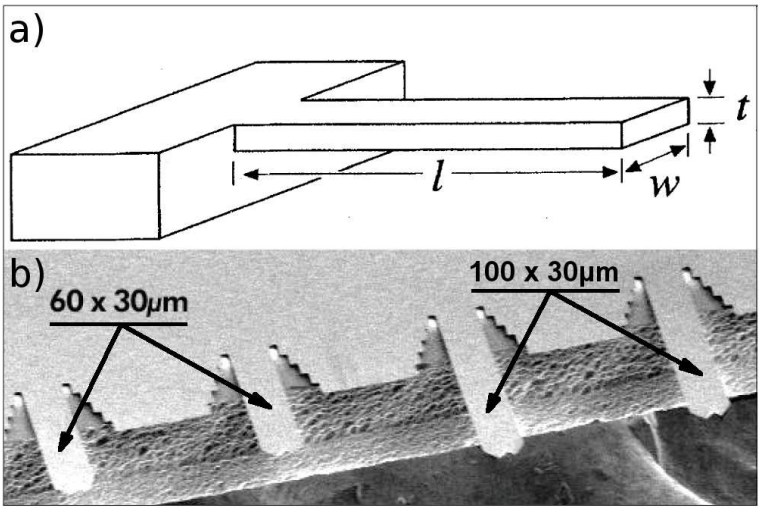

Figure 4.2: a) Modelisation of a simple cantilever, from J.Sidles [121]. b) Set of four cantilevers used in this thesis: Biolever series from Olympus, Asylum research.

measure tiny forces. Another advantage of using the cantilever as a resonator is that the signal can be localised in a narrow frequency range where no other physical process could disturb the measurement, especially mechanical resonances arising from the body of the microscope or noise sources in the detection.

The cantilever is excited with a piezoelectric crystal that is placed under its holder. Excited at its resonance frequency, the amplitude of vibration $A(\omega = \omega_c)$ of the first flexural mode is related to the force applied at the free end of the cantilever as:

$$A(\omega_c) = \frac{Q}{k} \text{ Force} \tag{4.3}$$

The main parameters of this micro-resonator are its resonance frequency ω_c and quality factor Q. Considering the dimensions and the design of figure 4.2a, the frequency of the lowest energy flexural mode is given by [89]:

$$\omega_c = 3.516 \frac{t}{l^2} \Big(\frac{E}{12\rho}\Big)^{1/2} \tag{4.4}$$

with E the Young modulus and ρ the density of the cantilever's material. This frequency can be calculated using more accessible physical parameters such as an effective mass $m^* = \eta \times m$, where η depends on the mode indices, and the stiffness constant k:

$$\omega_c = \sqrt{\frac{k}{m^*}} \tag{4.5}$$

The dissipative phenomena involved in the cantilever dynamics, dominated by surface effects, are not fully understood yet and are phenomenologically modelled by the quality factor Q. We can then define the resonance frequency $\omega_c^{'}$ taking into account this dissipation, in the form of a damped oscillator [25]:

$$\omega_c^{'} = \omega_0 \sqrt{\frac{1 - \frac{1}{4Q^2}}{1 + \frac{1}{4Q^2}}} \tag{4.6}$$

The intrinsic limitation of this force sensor will be given by its thermally activated motion. The phonon modes that propagate in the cantilever due to temperature T can be modelled as a Langevin random force, with the spectral density[121, 25]:

$$S_F = \frac{k}{Q\omega_c} 4k_B T \tag{4.7}$$

where k_B is the Boltzmann constant. The thermal noise $\sigma_x(\omega = \omega_c)$ in the amplitude of vibration x corresponding to the spectral density S_F (see equation (4.7)) is given by:

$$\sigma_x(\omega_c) = \frac{Q}{k}.S_F^{1/2}.\sqrt{B} = \sqrt{\frac{4k_B TQB}{\omega_c k}} \tag{4.8}$$

Taking into account these thermal fluctuations in the equation of motion of the cantilever, we can calculate the minimum detectable force with this sensor, in a detection bandwidth B:

$$F_{\min} = \sqrt{\frac{4k_B TkB}{\omega_c Q}} \tag{4.9}$$

If the measurement is operated at the cantilever resonance frequency, the amplitude of the signal is increased by a factor Q. There are several ways to increase the sensitivity or the "gain" of our cantilever:

- To decrease the minimum detectable force, one needs to decrease the spring constant k and increase the resonance frequency ω_c. But these two parameters are not independent. Experimentally lowering the spring constant is achieved by using a very thin cantilever, but it also reduces its eigenfrequency (see equation 4.4). By lowering the mass of the cantilever, the team of Dan Rugar fabricated an ultra sensitive cantilever with a spring of $k = 0.11 \times 10^{-3}$ N.m^{-1} and a frequency of about 5 kHz [112]. A promising way to decrease the spring constant while keeping very high frequencies is to use Silicon nanowires [100]. These resonators could have frequencies in the megahertz range with a spring constant in the μN.m^{-1} range.

- Increasing the quality factor Q of the resonator. For a mechanical cantilever with the shape we are considering, the thickness seems to be the key parameter. Moreover, the whole microscope is placed under a vacuum of 10^{-6} mbar to avoid the mechanical dissipation due to air viscosity. The quality factor of our cantilever is increased by a factor 200 under vacuum and reaches $Q \geq 2000$.

- Decreasing the working temperature. The microscope can be cooled down to 1.5 K if necessary, which reduces the thermo-mechanical noise. However, most of the experiments of this thesis have been done at room temperature, because the signal to noise ratio is high enough for the FRM signals we are considering.

For our particular setup, we have chosen the commercial cantilever having the lowest spring constant, the Biolever from Olympus. The longest cantilever of the figure 4.2b has been used. It is made of crystalline Silicon Nitride (Si_3N_4) coated by 30 nanometres of gold, and its dimensions are $l = 100$ μm, $w = 30$ μm and $t = 160$ nm. The spring constant is as low as $k = 6.10^{-3}$ N.m^{-1}, and we are working under vacuum to increase the quality factor to about $Q \simeq 2000$. A simple calculation using equation (4.4) gives a frequency

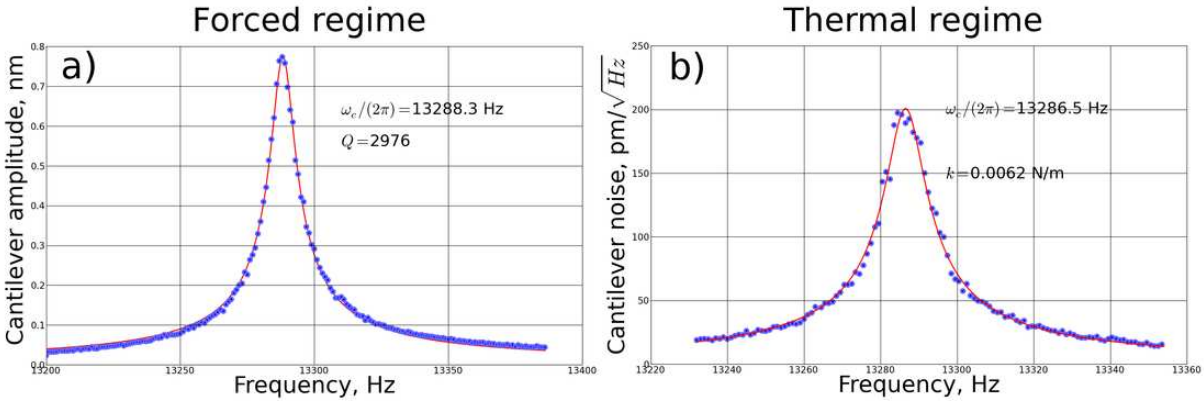

Figure 4.3: a) Resonance curve of the 100 µm Biolever cantilever as a function of the ac voltage frequency applied on the piezo excitation. b) Thermo-mechanical noise of the same cantilever. The eigenfrequency, quality factor and stiffness constant of the cantilever are extracted from the Lorentzian fitting curves (in red). All measurements are done under vacuum (2.10^{-6} mbar) at room temperature (300 K).

around 14 kHz, which gives a minimum detectable force of 0.7 femto-newtons in a one second bandwidth.

A typical resonance curve of the cantilever excited by applying an ac voltage on a piezo actuator is presented on figure 4.3a. The measured resonance frequency (13.3 kHz) is in good agreement with the expected one from equation (4.4) and the Lorentzian shape of the resonance confirms the quality of the oscillator. The thermo-mechanical noise of this cantilever can also be monitored without external excitation around its resonance frequency (figure 4.3b). This corresponds to a thermally activated vibration amplitude of about 200 picometres, which is in good agreement with the noise expected from equation 4.8.

4.3.2 The interferometric detection

4.3.2.1 Generalities

To detect the motion of the cantilever, a very sensitive and local technique is needed. Optical methods are indicated for three reasons:

- Using laser light, the detection beam can be easily focalised on the cantilever free end (i.e a few μm^2), and nearly totally reflected by the gold coating.
- The coupling between the detection and the force sensor is small because the laser beam carries very few energy: the measurement is done without disturbing the motion of the cantilever.
- The intrinsic noise of these methods is always small compared to the cantilever thermo-mechanical noise. Therefore, the total signal to noise ratio is always limited by the cantilever noise.

In our experiment, an interferometric detection has been chosen, because this method gives the highest sensitivity to measure distances, down to the picometre range. The light source is an infrared laser of wavelength $\lambda = 830$ nm which is guided to the cantilever by

a mono-mode optical fibre of 125 μm in diameter. The beam passes through a directional coupler that splits it into two parts. The reference part is directed on a photo-diode, and the other part is focused on the cantilever. The cavity of the interferometer is composed of the cantilever plane and the cleaved end of the fibre. Its mean length, set between 20 and 50 μm, can be tuned. Indeed, the end of the fibre is clamped on a piezo actuator and the cavity length can be varied to obtain interferences in a range of 10 μm. The reflected beam is recombined with the reference in the coupler and a photo-diode monitors the resultant intensity.

The interference fringes are observed in the diode signal by varying the cavity length d. The amplitude of the voltage delivered by the photo-diode can be modelled with the simple formula:

$$A(d) = A_0 \sin\left(\frac{4\pi d}{\lambda}\right) \tag{4.10}$$

where A_0 is the dc offset given by the diode and λ is the laser wavelength. The cavity length is then fixed to be at the maximum of slope in the interference curve, which gives the best sensitivity. A variation of the output amplitude δA is related to a change of the cavity length Δd as:

$$\Delta d = \frac{\lambda\ \delta A}{4\pi A_0 \cos\left(\frac{4\pi d}{\lambda}\right)} \tag{4.11}$$

This distance corresponds to two times the cantilever displacement. The intrinsic noise of this interferometer is given by the shot noise of the photon source. The photon flux exerts a force on the cantilever and the fluctuations of this flux increase the measured cantilever noise [121]. This noise is also related to a "virtual" cantilever fluctuation with equation (4.11) because a fluctuation of δA in the photon source will be interpreted as a cantilever displacement δd in our measurement. This noise is also increased by the extrinsic noise of the photo-diode, which is maintained at constant temperature to avoid fluctuations. In the figure 4.3b), this noise source, given by the baseline of the curve, can be evaluated around the cantilever frequency to $\simeq$ 15 pico-metres. It is important to notice that this noise is about ten times weaker than the cantilever thermo-mechanical noise. The overall noise of the detection setup is limited by the intrinsic noise of the detector.

4.3.2.2 Coupling to the micro-resonator

Exciting the cantilever at its resonance frequency is needed to use it as a resonator. Apart the fact that the amplitude would be too small, a dc measurement is difficult because the cavity length is drifting with time due to thermal expansion of mechanical pieces and relaxation of the piezoelectric crystal. The excitation source will be the actuator that holds the optical fibre. A dc voltage is applied on this piezoelectric crystal to tune the cavity length, and an ac voltage at the cantilever eigenfrequency is superimposed. The whole system vibrates mechanically and the cantilever is excited at resonance.

The eigenfrequency of the cantilever can vary with time during a measurement due to various effects, such as: variation in the heating from the laser beam, variations of the static force applied, eddy current due to the strong magnetic field... To keep a maximum sensitivity, a phase lock loop (PLL) coupled with a lock-in detection is used to maintain the excitation at the cantilever eigenfrequency. The amplitude and phase of the signal

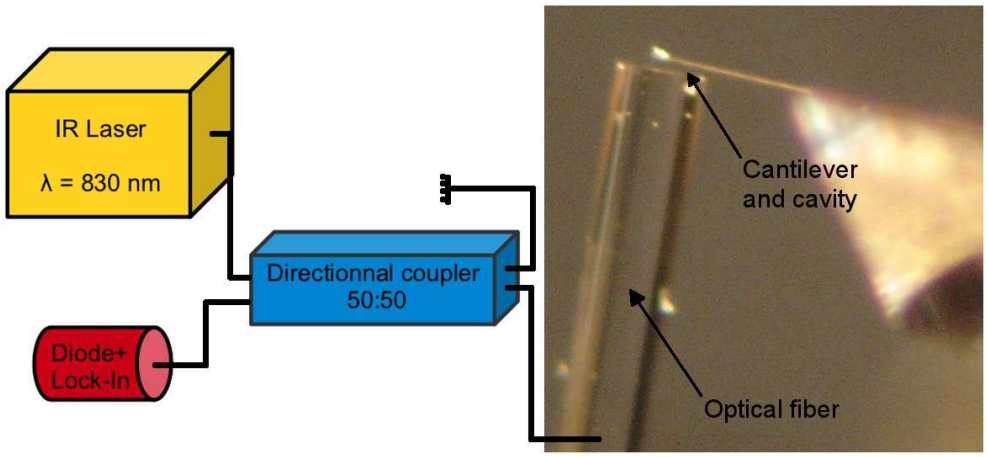

Figure 4.4: Basic scheme of the interferometer used for the cantilever motion measurements. The picture on the right shows the optical fibre (glass tube) placed perpendicularly to the cantilever to form a cavity of length about 25 µm.

from the interferometer diode are demodulated at the cantilever frequency with a lock-in and introduced in the PLL. Three options are then possible to measure an MRFM signal:

- The MRFM signal is given by the *amplitude* at the cantilever frequency. The ac voltage applied on the piezoelectric crystal is kept constant and the PLL adjusts continuously the frequency of this excitation to maintain the cantilever phase in quadrature, which corresponds to the resonance.
- To improve the stability of the measurement, it can be useful to maintain the amplitude of the cantilever constant. This prevents uncontrolled back-action on the sample dynamics and non linear effects at high amplitude. The PLL will adjust the frequency *and the strength* of the ac excitation on the piezo crystal to maintain the amplitude at a defined value (a few nanometres in most of the experiments presented here). The f-MRFM signal is then given by the strength of the excitation, i.e amplitude of the ac voltage.
- Finally, the *frequency shift* of the cantilever can be measured at constant excitation strength.

4.3.3 The field gradient

As equation (4.1) shows, a force is created if the magnetic moments of the sample are coupled to a field gradient. A magnetic particle has been chosen as a field gradient, this particle is attached at the apex of the cantilever and placed over the magnetic sample to be studied. Once placed in stray field of the sample, the magnetic particle will experience the force $\boldsymbol{F}$ of equation (4.1), which will be transmitted to the cantilever and transformed into a measurable displacement.

A spherical magnetic particle has been chosen as f-MRFM probe for several reasons. First of all, it preserves the axial symmetry of the magnetic discs studied in this thesis. Then, the filling factor, which gives the coupling efficiency between the sample and the magnetic particle, can be easily optimised within this symmetry. To maximise this parameter, the sphere should have about the same diameter as the sample [31]. Finally,

a magnetic sphere has no shape anisotropy and its magnetisation follows the local magnetic field. It prevents parasitic torques to develop, which may disturb the motion of the cantilever. As a result of the spherical symmetry, the particle is identified to a magnetic dipole $\boldsymbol{m}_{\text{sphere}} = m.\boldsymbol{u}_{\text{sphere}}$ located at the centre of the sphere, with the magnetic moment $m = \frac{4}{3}\pi R^3_{\text{sphere}} M_s$ where M_s is the saturation magnetisation of material. The stray field of the probe is then given by:

$$\boldsymbol{H}_{\text{sphere}} = \boldsymbol{\nabla}\frac{(\boldsymbol{m}_{\text{sphere}}.\boldsymbol{r})}{r^3} \tag{4.12}$$

The advantage of this geometry is to minimise the perturbation from the sphere in the measurement process. In order to be non invasive, the inhomogeneity of the stray field arising from the sphere at the sample location has to be small compared to the internal field of the sample. Practically, for typical spectroscopic studies, the probe is placed at the vertical of the disc to be studied, between 1 and 2 microns above the disc.

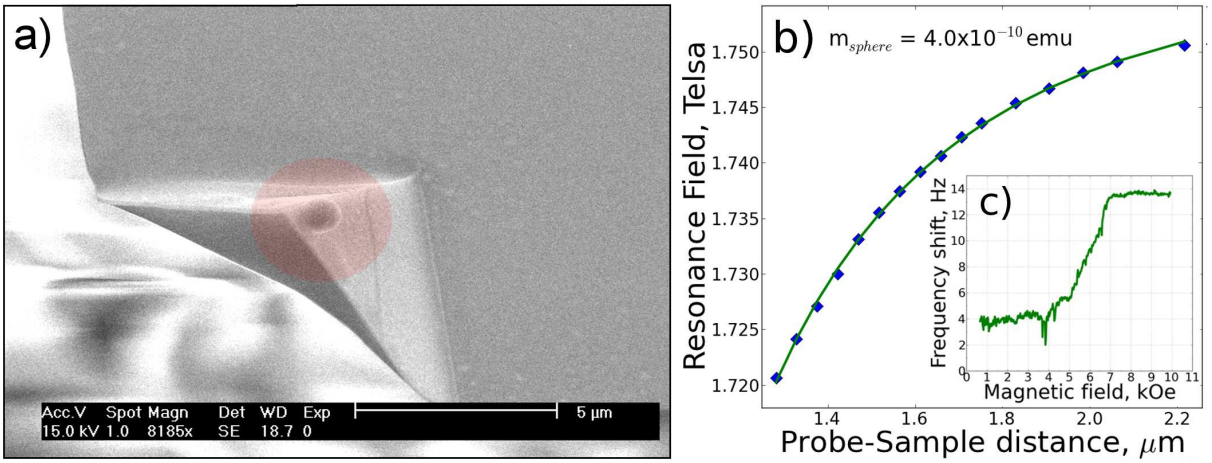

Figure 4.5: a) Scanning electron microscope images of the FeSi magnetic sphere (of diameter $\phi \simeq 800$ nm) glued on the Olympus Biolever's tip. b) Calibration of the magnetic moment of the probe. c) Frequency shift of the cantilever when the probe is placed in the residual field gradient of the perpendicular field. The saturation observed after 6.5 kOe gives an experimental value of the probe saturation field.

4.3.3.1 Nanoparticle fabrication

The choice of the material for the f-MRFM probe was motivated by two arguments. First, to maximise the field gradient to increase the force F. For this purpose, iron was chosen to get the highest possible magnetisation M_s. But crystalline iron has a non negligible crystalline anisotropy. In the same way as the shape anisotropy, it could induce parasitic torques, which we wanted to avoid. To fulfil these conditions, the chosen material is an amorphous alloy FeSi with 3% in mass of silicon. The synthesis is done by spraying the melted alloy into a neutral nitrogen gas beam. Droplets are cooled down very rapidly forming sub-micron particles with a weak crystalline anisotropy. These particles have been studied by the team of Anne-Lise Adenot-Engelvin at the CEA Le Ripault, France. They have evaluated their averaged magnetisation to $M_s = 1.43 \times 10^6$ A.m^{-1}.

Among these soft particles, a sphere of 800 nm in diameter has been selected. A special procedure has been developed to attach the nanoparticle at the apex of the cantilever. The

powder of particles is spread on a silicon wafer and the tip of the cantilever is covered by a tiny amount of epoxy glue. Under an optical microscope, the cantilever can be scanned over the wafer with a micro-manipulator and the proper sphere is simply "fished". The result can be seen on the figure 4.5. The key point is to attach the particle at the very end of the tip to be able to approach it as close as possible from the sample.

4.3.3.2 Calibration of the probe magnetic moment

In order to perform further quantitative measurements, it is important to calibrate the actual magnetic moment of the FeSi particle once it is glued at the end of the cantilever inside the microscope. To do so, we have measured the ferromagnetic resonance of a single FeV disc of 600 nm in diameter perpendicularly saturated (this sample is presented in detail in chapter 6). The measurement is done with the f-MRFM probe placed above the disc centre. The resonance field of the uniform mode ($l = 0, m = 0$, see chapter 2) is given by $\omega = \gamma H_{\text{res}}$. For an excitation at constant microwave frequency, the resonance condition is fulfilled when the sum of the bias field and the probe stray field along the disc normal equals the resonance field $H_z + \boldsymbol{H}_{\text{sphere}}.\boldsymbol{u}_z = H_{\text{res}}$. The experimental procedure is the following:

1. The magnetic probe is placed 1.2 μm above the centre of the FeV disc.

2. The resonance field of the FeV disc is measured at constant frequency for different increasing probe-sample distances.

3. The spherical magnetic probe is identified with a punctual magnetic dipole m_{sphere} placed at its centre. The stray field along the disc normal produced by the probe at the disc location is then simply $\boldsymbol{H}_{\text{sphere},z}.\boldsymbol{u}_z = 2m_{\text{sphere}}/z^3$, with z the distance between the sample and the middle of the sphere.

4. In order to evaluate m_{sphere}, the curve of the resonance field versus the probe sample distance, presented figure 4.5b, can be fitted with the formula:

$$H_{\text{res}} = H_z + \frac{2m_{\text{sphere}}}{(z - z_0)^3} \tag{4.13}$$

The result of the fit, the green curve in the figure 4.5b, leads to an evaluated moment for the sphere of $m_{\text{sphere}} \simeq 4 \times 10^{-10}$ emu.

The SEM image of the particle on the figure 4.5 gives an approximate diameter of 800 nm, which is coherent with the previous magnetisation values.

The saturation field of the sphere can be measured as follows: the frequency shift of the cantilever is measured as a function of the perpendicular field. Mainly because of the residual field gradient in the magnet, a tiny force is exerted on the cantilever. Even if this force is not well understood and calibrated it can be seen on the figure 4.5 that the cantilever frequency saturates. The only physical parameter able to vary with the field in the system is the probe magnetisation. Therefore, the observed saturation gives a measurement of the sphere saturation field, around $H_s \simeq 6.5$ kOe. This is consistent with the expected value for the saturation field of the sphere, which is about $H_s \simeq 4\pi M_s/3 \simeq 6$ kOe. Indeed, the demagnetising factor of a sphere is $N_{zz} = 1/3$. Notice that the choice

of a soft spherical particle implies the impossibility to work without external field and to lose some magnetic moment under its saturation field.

Notice that the probe magnetic moment could be calibrated using a well known field gradient, for instance a coil. This procedure was not performed with the particle used in this thesis, but the results of previous calibrations on bigger spheres of the same material are consistent with the values given above.

4.3.3.3 Quantitative measurement of ΔM_z

In our experiments, the dc external applied field $\boldsymbol{B}_{\text{ext}}$ is directed perpendicular to the sample plane along $\boldsymbol{u}_z$. Therefore, the magnetic sphere is saturated in this direction and is coupled to the longitudinal component of the sample magnetisation M_z. The variation of the force applied on the cantilever is directly related to the variation of this quantity, averaged on the sample volume: $\langle \Delta \boldsymbol{M}.\boldsymbol{u}_z \rangle$. The f-MRFM gives a quantitative measurement of $\langle \Delta \boldsymbol{M}.\boldsymbol{u}_z \rangle$ in the sample.

The equation (4.1) can be rewritten as a function of ΔM_z and taking the probe symmetry into account. If the field gradient of the magnetic probe along $\boldsymbol{u}_z$ is given by $g_{zz}(\boldsymbol{r})$, the force applied on the cantilever is:

$$F.\boldsymbol{u}_{z'} = \int_{V_s} \Delta M_z(\boldsymbol{r}) g_{zz'}(r, z+s) d^2 r dz \tag{4.14}$$

where V_s is the volume of the sample and s is the probe-sample separation. In the real f-MRFM setup, the cantilever is tilted by $15\hat{A}^\circ$ with respect to the xy plane to be sure that the tip is the closest part from the sample. Therefore, the force has to be projected on the axis of vibration of the cantilever $\boldsymbol{u}_{z'}$.

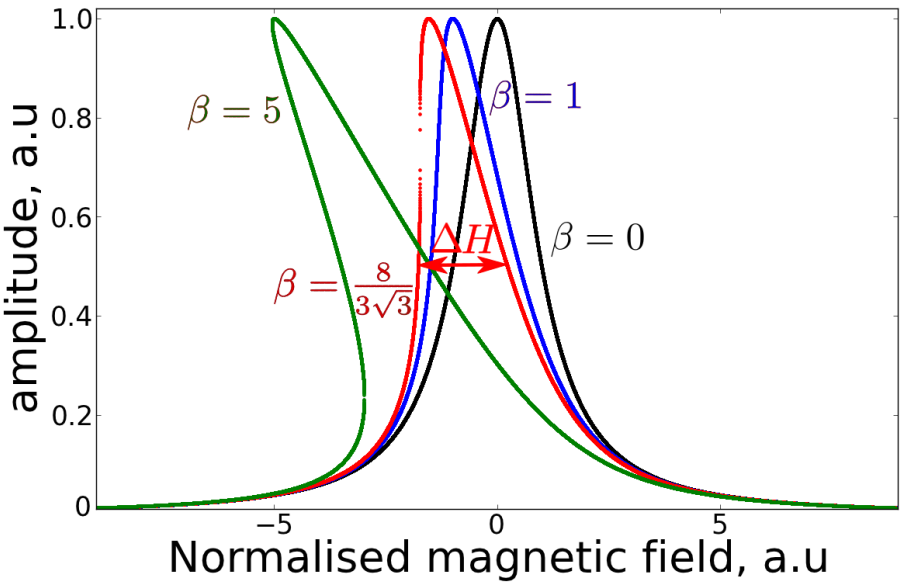

Figure 4.6: Deformation of the resonance lines towards low fields at high microwave power in the non linear regime. The Foldover threshold (red curve) gives a direct calibration of the measured amplitude.

We shall describe below the methodology so that $\langle \Delta \boldsymbol{M}.\boldsymbol{u}_z \rangle$ can be calibrated. This is done by measuring the uniform mode of a perpendicularly magnetised thin disc. In the

non-linear regime, i.e. at high microwave power, the field-sweep line shapes are distorted toward low fields. This is due to the renormalisation of the demagnetising field when the angle of precession of the magnetisation becomes non negligible. The amplitude of the uniform mode is a solution of the equation $[(x+\beta y)^2+1]y=1$ where the linewidth and the amplitude are normalised to one [116]. The coefficient β takes the non linearity into account. The figure 4.6 displays normalised resonance curves plotted with this equation for increasing values of β, which models the increasing microwave power. If the non linear coefficient $\beta=0$, the resonance shape is the pure Lorentzian curve measured in the linear regime. With increasing β, the resonance starts to be deformed towards low fields. There is a critical strength of the rf magnetic field for which the slope of the resonance curve becomes infinite on the low field side of the resonance: this is the foldover threshold, corresponding to the red curve of figure 4.6. It can be seen that at this point, the maximal amplitude of the resonance, which equals the longitudinal change of the magnetisation is [4]:

$$4\pi\langle\Delta\boldsymbol{M}.\boldsymbol{u}_z\rangle=\frac{4}{3\sqrt{3}}\Delta H \tag{4.15}$$

where ΔH is the FWHM linewidth measured in the linear regime. Experimentally, we determine ΔH in the linear regime and we increase the microwave field strength until the vertical tangent in the low field side is measured. Then the maximum of the signal is given by equation (4.15).

4.3.4 The microwave excitation circuit

The MRFM is a powerful tool to detect any change in the magnetisation of a ferromagnetic sample. We now need a reliable and integrated way to excite the magnetisation dynamics and perform spectroscopy. Since the resonances we want to study are in the gigahertz range, a microwave field at these frequencies has to be created in the near field of the sample. The simplest way would be to build a microwave cavity that resonates at a given frequency ω. The external field is then swept to perform the spectroscopy.

4.3.4.1 The micro-stripline

But it is interesting to be able to sweep the microwave frequency. For instance, the structure of the vortex state is very sensitive to magnetic fields and performing the spectroscopy at fixed bias field prevents the static magnetisation to evolve during the measurement. For this purpose, a microwave broadband micro-stripline antenna has been chosen. The idea is to pass a microwave current in a metallic stripline to create an orthoradial microwave field in its surrounding, following Ampere's law.

The constraints for the design are the following:

- Reduced dimensions. The microwave field has to be homogeneous at the samples scale (i.e. a few microns) but its source should be as close as possible from the samples to get the maximum of amplitude and maximise the filling factor. This implies that the antenna implementation should be integrated in the sample fabrication process.

- The standard for electronic systems is to be impedance matched at 50 Ω. The design of the contact pads should approximately follow this standard to minimise

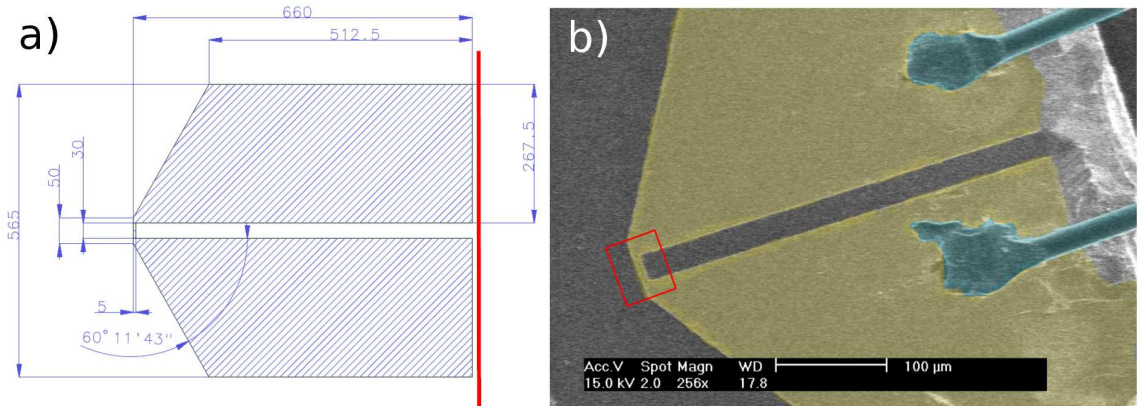

Figure 4.7: a) Design of the microwave stripline antenna; all dimensions are in microns. b) SEM image of the same antenna (with artificial colours). The samples will be located in the shorted end (surrounded in red) where the microwave field is maximum. The microwave lines, connected to the high frequency source are bonded in each electrodes.

the parasitic reflections.

- The microwave end is a short circuit (magnetic field anti-node). It leads to a total reflection at the end.

To fulfil those conditions, the design presented in figure 4.7 has been created. The antenna is defined by lift-off and patterned by e-beam lithography from a 300 nanometres thick gold film, deposited by evaporation. The two electrodes are separated by 30 μm which ensures the 50 Ω matching of the antenna. The flared shape of the electrodes prevents the microwave current to be reflected to the source before the constriction. This microwave current, created by a broadband source (Anritsu synthesiser, 100 kHz to 20 GHz), flows through a constriction that short-circuits the two electrodes of the antenna, as shown in the red square of figure 4.7b. An anti-node of current is created at this location. The constriction is 5 μm wide and 25 μm long and creates an orthoradial microwave field h that is linearly polarised in the direction perpendicular to the stripe. Simulations performed with the Sonnet microwave software have validated the properties of the antenna.

Two locations are possible to place the samples, which are flat discs in this thesis. Over or under the constriction after a thin insulating layer to avoid electrical contact: the sample will experience a linearly polarised in-plane field. Next to the constriction, the sample would be submitted to an out-of-plane microwave field.

Particular attention has been focused on the microwave circuit to avoid losses and resonances in the system. Indeed, to perform experiments where the frequency of the microwave field is swept, the microwave field intensity $|h(\omega_0)|$ delivered by the antenna has to be as constant as possible. We used rigid and semi-rigid coaxial cables adapted to high frequencies and low temperatures; they are connected with SMA connectors. Moreover, the antenna was connected to the coaxial cables through parallel wire bonding. To evaluate the residual losses, the whole microwave line has been characterised with a vector network analyser to quantify the response of the circuit up to 20 GHz.

At the same time, any variation of the microwave intensity has also an influence on the cantilever response. The cantilever used in this thesis is covered by gold to improve the reflection of the laser light for interferometry. Placed in a microwave field, eddy currents

can develop in the gold layer and disturb the cantilever motion. Moreover this gold layer is heated by the absorption of microwave energy. The attenuation of the microwave power in the cables when the frequency increases does not affect the cantilever amplitude, but strong resonances at low frequency interferes with the motion, as seen in figure 4.8. Measuring the cantilever amplitude over the gold antenna without any sample results in a baseline when the microwave frequency is swept. The frequencies of these phenomena corresponding to wavelength in the tens of centimetres, they are attributed to standing wave phenomena inside the semi-rigid cables, between the SMA connectors which are slightly impedance mismatched.

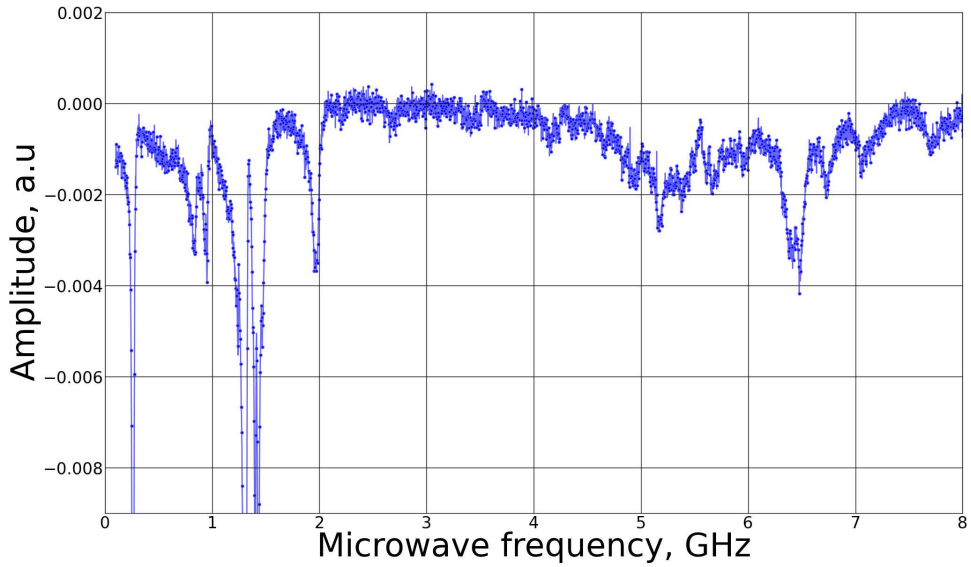

Figure 4.8: Baseline of the amplitude of vibration for the Olympus cantilever over the antenna, without any magnetic sample. The microwave power in -15 dBm and the magnetic sphere is saturated perpendicularly. The resonances are associated to reflections in the microwave circuit.

This baseline arising from the coupling between the f-MRFM detection and the excitation part has to be precisely known and is scalable with the microwave power. It has to be subtracted from the measured signal to obtain the real physical signal from the sample.

4.3.4.2 Modulation of the microwave source

To detect FMR resonances, the variation of the longitudinal component of the magnetisation ΔM_z in the sample is detected via the interaction of the magnetic probe which drives the motion of the cantilever. As explained before, the measurement is done at the cantilever frequency to gain the quality factor Q.

The way to detect resonances is to modulate the microwave excitation field at the resonance frequency of the cantilever. In other words, the microwave source is turned on and off at the cantilever frequency. During the half period when the cantilever is far from the sample, the microwave is turned off, no resonance are excited. Then during the other period, the microwave is turned on and the resonance produces a ΔM_z that will deflect the cantilever. The signal is given by the total amplitude of vibration of the cantilever.

In practice, the Phase Lock-Loop that tracks the cantilever frequency sends a square wave signal in-phase with the cantilever motion to the microwave synthesiser. The mi-

crowave current $I(t)$ delivered by the source is the convolution of a continuous microwave emission with this square wave:

$$I(t) = I_0 e^{i\omega_0 t} \mathrm{sgn}[\sin(\omega_c t)] \tag{4.16}$$

Here I_0 is the microwave intensity, $\omega_0/2\pi$ is the microwave frequency and $\omega_c/2\pi$ is the cantilever frequency.

The cantilever frequency ω_c, around 10 kHz, is far from the Larmor frequency, which lies in the gigahertz range. Notice also that the modulation period $2\pi/\omega_c$ is large compared to the relaxation time T_1 and T_2. Therefore, the f-MRFM measurement is always a static measurement of the magnetisation dynamics.

4.3.4.3 Calibration of the microwave field

Following the calibration of ΔM_z, the amplitude of the uniform rf magnetic field can be calibrated by studying the power dependence of the uniform mode line shape of a perpendicularly magnetised disc. It was pointed out by Anderson and Suhl [4] that the resonance curve at high power should be skewed, due to the static change of the magnetisation M_z, which also shifts the resonance frequency: this is the foldover effect. There is a critical strength of the rf magnetic field h_c (linearly polarised amplitude) for which the slope of the resonance curve becomes infinite on the low field side of the resonance:

$$h_c = 2\Delta H \sqrt{\frac{2\Delta H}{3\sqrt{3}[\{N_{zz}\} - \{N_{xx}\}]4\pi M_s}} \tag{4.17}$$

where ΔH is the linewidth measured in the linear regime and $\{N\}$ are the demagnetising factors defined in chapter 2. Experimentally, the conversion between the microwave current power and the rf field amplitude is measured at the foldover threshold, which gives for our antenna: $h_{rf} = 1.05$ mTesla for $P_{rf} = 0$ dBm.

The linear amplitude of h_{rf} at the sample location (just below the antenna) can also be estimated from Maxwell-Ampere law:

$$h_{rf} = \frac{\mu_0}{w}\sqrt{\frac{P_{rf}}{2Z}} \tag{4.18}$$

where w is the width of the constriction and $Z = 50\Omega$ is the impedance matched to the synthesiser. The estimation given by this method is $h_{rf} = 0.8$ mTesla for $P_{rf} = 0$ dBm. The agreement between the two methods is within 75%, which is already quite good regarding to approximations (losses in cables, frequency dependence, geometry, matching, current density homogeneity, etc...).

4.4 Practical realisation

The main components needed to perform MRFM have been detailed. In this section the scheme to assemble them in a proper manner is explicited.

4.4.1 The static magnetic field

All the samples studied in this thesis are flat magnetic discs. The magnetisation dynamics in these discs have been studied in the perpendicularly magnetised configuration.

To produce the static magnetic field, a superconducting axial magnet, with a room temperature bore access has been used. It consists of a coil of Niobium-Titanium cooled down to 4 kelvin in liquid helium that produces ± 70 kOe in the axis of the bore. An additional shim coil can add ± 1 kOe in the same direction, to perform experiments where the field is swept. The advantage of this setup is to decouple the cryogeny of the microscope and the cryogeny of the magnet, which has then a very low helium consumption.

4.4.2 Cryogeny

The whole microscope sits in a vacuum chamber (see figure 4.9b), which is placed in a helium flow cryostat. The cryostat is introduced in the bore of the superconducting magnet, inside the axial static magnetic field (see figure 4.9a) . As can be seen in figure 4.9b), the vacuum chamber is equipped with windows. The cryostat, from Oxford instruments, has also windows aligned with the vacuum chamber. This allows an optical access to the sample stage, even at low temperatures and high field. A special borescope, which displays the images to a screen, is introduced in front of the cryostat windows inside the bore of the superconducting magnet. The final approach of the cantilever toward the sample, which is a delicate action, can be done once the microscope is closed and cooled down with the help of the borescope.

To cool down the sample, depending on the desired temperature, a helium gas flow is passed around the vacuum chamber at a given pressure. To reach 4 K, liquid helium is introduced, and it is also possible to reach 1.5 K by pumping in the cryostat on the liquid helium. The sample, which is under vacuum, has to be thermalised. The titanium piece (that has a good thermal conductivity) holding the microscope head is connected with copper wire braids to the bottom piece closing the vacuum chamber. This copper piece, selected for its high thermal conductivity, makes the thermal contact between the helium flow chamber and the inner chamber. Finally, the sample temperature can be controlled by resistor elements. With this setup, the working temperature range is between 2 and 300 K.

4.4.3 Piezoelectric displacement stages

The aim of MRFM is to perform images, or at least spectroscopy of individual nano-objects. All the components presented before must be mounted on displacement stages having accuracy better than a nanometre. Two kinds of system are implemented, using piezoelectric crystals. The choice of piezoelectric systems is preferred because of their accuracy and ability to work without large deformation at low temperature. All the specifications given here are valid at room temperature.

- The sample, with the microwave antenna, is placed on a piezoelectric tube, whose Z axis is parallel to the static field. The tube has a nanometre accuracy and can be distorted in the three axis of space. The accessible range is about 25x25 μm in the XY plane and 2 μm in the Z direction. The piezoelectric crystal motion are driven by applying high voltages on its electrodes.

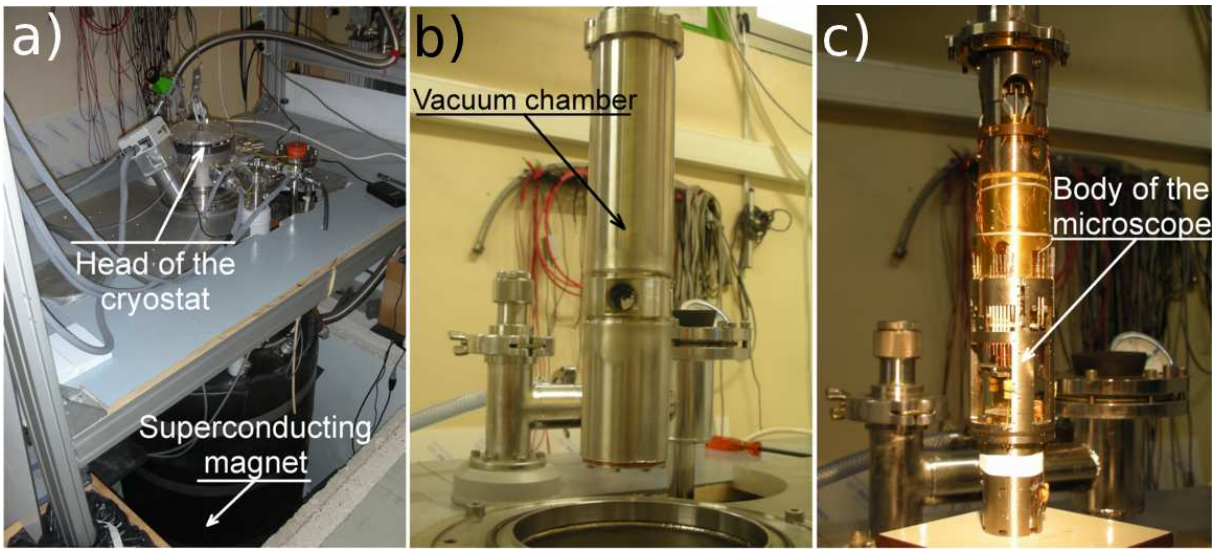

Figure 4.9: Pictures of the MRFM setup used during this thesis. a) The helium flow cryostat is introduced in the superconducting magnet. The vacuum chamber b) that contains the body of the microscope c) sits at the end of the cryostat, in the middle of the magnet's bore.

- The piezoelectric tube holding the sample is mounted on a coarse positioner moving in the Z direction. This is a piezo stack system where an ac voltage is applied between two piezoelectric crystals making them sliding on each other. The accuracy is lower, in the micron range, but the displacement can be as large as 1 centimetre.

- The cantilever holder and the optical fibre are placed upside down with respect to the sample. The cantilever is nearly perpendicular to the static field. This stage of the microscope is suspended on two piezo stacks that displace the cantilever in the X and Y plane.

With this system, the cantilever can be roughly placed over the sample using the three piezo stacks in XYZ. The cantilever and the sample are placed on special holders whose base can be tuned in three points to align them perpendicularly to the static magnetic field. Then a fine tuning is performed with the piezo tube holding the sample. To perform images, the piezo tube is scanned in the proper directions.

To fit in the vacuum chamber, all these pieces are assembled in the body of the microscope, at the bottom of the cryostat (see figure 4.9c). Titanium has been chosen for this piece, because of its strong rigidity. The microwave antenna and the electrodes that drive the piezo stages are connected by cables coming from the top of the cryostat.

4.4.4 Isolation from noise sources

To minimise sources of noise, the whole microscope is well isolated.

- The feet of the aluminium structure that holds the whole microscope are placed in containers filled with fine sand. Those containers are based on the real ground of the building. This avoid low frequency vibration from the surroundings.

- The cryostat, and also the vacuum chamber, are placed on a active anti-vibration system that compensates efficiently vibrations in the tens of Hertz range.

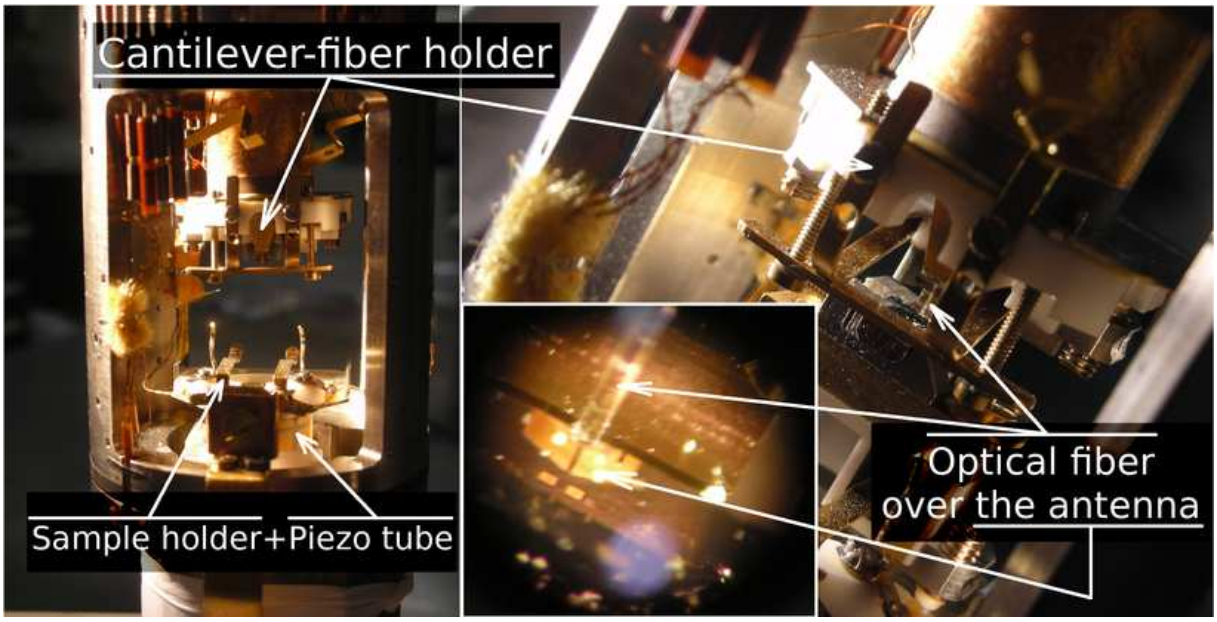

Figure 4.10: Details of the MRFM microscope head presented in figure 4.9 c). The sample holder and the reversed cantilever-fibre holder can be seen on the left, mounted on their piezolelectric positioners. On the right, two detailed views show the position of the fibre over the cantilever with respect to the sample (only the gold microwave antenna can be seen here at this scale).

- The microscope is suspended as a pendulum in the cryostat to be damped by Foucault current when the perpendicular field is turned on.
- The temperature of the laboratory is maintained constant at $21 \pm 1 \hat{A}°\mathrm{C}$ with an air conditioning system. Moreover, the body of the microscope is placed under vacuum in the cryostat and inside the bore of the superconducting magnet. The temperature of the microscope is then very stable. Observed temperature fluctuations are lower than 0.1 K.

4.5 Conclusion

The f-MRFM combines the spectroscopic accuracy of ferromagnetic resonance with a force sensor capable to detect tiny signals. This sensor, being a micro cantilever, is also a scanning probe technique, allowing images of the resonance field in a ferromagnetic sample to be obtained. Moreover, the nature of the measured signal, a field gradient, decouples the sensitivity from the probed magnetic volume. The signal to noise ratio then becomes independent of the spatial resolution. These specifications allow a precise measurement of the FMR in a single nanostructure

The force captured by the couple cantilever-magnetic probe measures directly and quantitatively the variation of the longitudinal component of the magnetisation in the sample. Therefore, with appropriate microwave excitations, an f-MRFM measurement can give access to the whole spin wave spectrum of a magnetic body: frequency and linewidth of the modes, as well as their amplitude.

The stray field created by the magnetic probe could be turned into an advantage: it can be used as a strong and local field gradient. For instance, the spin wave modes of a

magnetic film can be localised in an internal field well created locally by the probe [83, 27].

The practical realisation of this microscope in our laboratory allowed us to adapt it to few particular interesting experimental conditions. The material chosen for its body are non-magnetic, which allow to work with high magnetic fields. The whole design has been oriented to isolate the microscope from all noise sources, such as temperature variation, mechanical vibrations or microwave radiations. Finally, the f-MRFM microscope is included in a helium flow cryostat, which opens up the low temperature regime for FMR experiments.

Chapter 5

Experimental results I: the vortex state

The f-MRFM technique presented in the previous chapter is used to measure the spin wave excitation in the vortex state described in the chapter 3. In particular, the gyrotropic mode is studied as well as the vortex core dynamical reversal. Moreover, the influence of a perpendicular bias field on the vortex dynamics will be highlighted. Finally, the higher order spin wave modes developing in the presence of the vortex core will be measured and labelled.

5.1 Introduction

The magnetic vortex state, previously introduced theoretically as a soliton solution in thin films, and described as a stable configuration in soft ferromagnetic dots of micron radii, has been widely studied experimentally. The first experimental signature of the vortex state has been given by magneto-optical measurements of hysteresis loops on Permalloy (NiFe) discs with applied magnetic fields in the disc plane [29, 94]. This work was followed by a direct observation of the vortex state in Permalloy discs using Magnetic Force Microscopy (MFM) [119], and the core structure was spatially resolved by Scanning Tunnelling Microscopy (STM) [141] as well as its polarity.

During this thesis, two magnetic materials have been investigated: NiMnSb and FeV. Thin films of these ferromagnets have been deposited and later patterned in discs of various diameters, between 1 and 0.1 microns. The dimensions of our dots have been chosen to stabilise a magnetic vortex at remanence, whereas the axial symmetry is well adapted to the f-MRFM detection scheme and simplifies the calculations. The materials chosen are adapted both to vortex dynamics experiments because of their crystalline structure with a low anisotropy and to the ferromagnetic resonance detection with their damping among the lowest reported for metallic ferromagnetic thin films.

The great advantage of our f-MRFM detection will be to study the dynamical properties of single discs, eventually buried under non magnetic electrodes. We have access to a precise spectroscopic measurement of the vortex eigen-modes, without any averaging on an array of discs. Using this peculiarity, the effects of an external magnetic field applied perpendicularly to the discs plane is widely investigated.

In this section, the sample fabrication process is detailed, as well as the intrinsic properties of the materials and the vortex state. The vortex static and dynamical properties are then investigated at room temperature, focusing on the gyrotropic motion and the dynamical reversal under an applied field. Finally, a detailed analysis of the magnetic dissipation in the vortex state is presented.

5.2 Samples preparation

The NiMnSb samples used to study the vortex state were designed in our team, but the whole fabrication was done in Würzburg University in the group of Professor L. W. Molenkamp. For this major contribution to this thesis, I would like to thank Andreas Riegler, Florian Lochner and Georg Schmidt.

The NiMnSb has been chosen to study the vortex state. This is a ferromagnetic half-Heusler alloy, which is metallic. It is supposed to be half-metallic, or hundred percent spin polarised at the Fermi level when grown along a particular crystalline axis [79]. It is therefore a potential candidate as spin filter/injector in future spintronics applications. Moreover its high Curie temperature (730 K) and very low magnetic losses are very interesting for our room temperature f-MRFM experiments.

5.2.1 Thin film growth

The NiMnSb crystallises in a $C1_b$ cubic structure, composed of three superimposed face centred cubic (fcc) latices corresponding to the sites Ni = A(0,0,0), Mn = B($\frac{1}{4}$, $\frac{1}{4}$, $\frac{1}{4}$),

Sb = C($\frac{3}{4}, \frac{3}{4}, \frac{3}{4}$) [6]. The NiMnSb lattice constant is a = 5.903 Å, and the films are grown on a InP wafer which minimises the lattice mismatch, and a 200 nm buffer layer of $(In_{0.53}Ga_{0.47})As$ oriented in the (001) direction.

The growth is realised under ultra high vacuum by molecular beam epitaxy (MBE) in the crystallographic direction (001) [6]. Nickel, manganese and antimony were co-evaporated in the wafer heated at 300Å°C. An in-situ characterisation technique, the reflection high-energy electron diffraction (RHEED), was used to monitor the growth. For this thesis, two different thicknesses of 44 and 20 nanometres were deposited.

5.2.2 Nanostructuring

The nano-structuring of the sample was done by standard e-beam lithography techniques using special resists followed by a dry etching realised by ion-milling. The NiMnSb film is patterned into several discs: the geometry is chosen to ensure a magnetic vortex ground state, as well as for its interesting axial symmetry. The f-MRFM detection, described in the previous section, uses a spherical magnetic probe which does not break the sample symmetry.

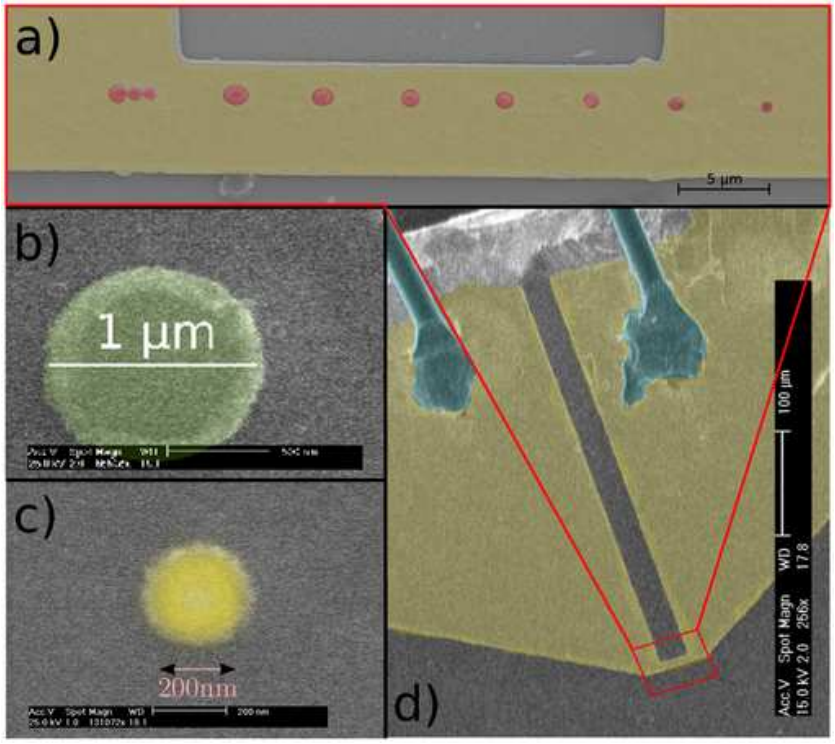

Figure 5.1: NiMnSb sample used to study the vortex state. In a), a scanning electron microscope (SEM) image of the 20 nm thick film patterned in discs of several diameters is presented, while the 44 nm thick film is nanostructured in discs of 0.2 and 1 microns shown in b) and c). The microwave antenna and its constriction under which the discs are located (red square) are presented in d).

As presented in the figure 5.1b and c, the thickest film of 44 nm is patterned in two discs of diameters 1.04 μm and 260 nm. The 20 nm thick film presented in the figure 5.1a is patterned in a series of isolated discs with the nominal diameters 700, 500, 400, 250, 200 175 and 150 nanometres separated from each other by 5 μm. A special design with three

closely packed discs, shown in the left, was produced for a study of the dipolar coupling between neighbouring discs. This study is presented in the chapter 6. This variety of thicknesses and diameters will allow a precise study of the vortex dynamics dependence on the geometry of the dots.

The discs are then covered by a 50 nm thick isolating layer of Si_3N_4, and the microwave antenna, consisting of 300 nm thick gold film patterned by UV lithography, is deposited on top. It can be seen in yellow on the figure 5.1d and figure 5.1a is a zoom of the constriction.

The electrodes of the antenna are finally connected by wire bonding to the microwave source (an Anritsu synthesiser) through adapted coaxial cables. The sample is then introduced in the f-MRFM microscope previously described in chapter 4, and the magnetic tip is placed approximately $\simeq 1.5$ μm above the disc to be studied.

5.3 Sample characterisation

In this section, the general properties of the samples presented below are investigated at room temperature, especially the magnetisation dynamics in both the saturated and vortex states.

5.3.1 Basic magnetic properties

First of all, the magnetic properties of the NiMnSb films have to be determined. A precise characterisation of the saturation magnetisation M_s, the crystalline anisotropy field H_a, the damping parameter α (related to the magnetic relaxation) and the effective gyromagnetic ratio γ is given by cavity FMR measurements. This study was realised on unpatterned thin films, identical to those used for our samples, by Hervé Hurdequint at the Laboratoire de Physique des Solides in Orsay, France.

An analysis of the films in the saturated state is performed to study the resonant field of the uniform spin wave mode versus the angle of the applied field. The results are summarised in the table 5.1.

M_s(emu.cm^{-3})	H_a(G)	α	γ(rad.s^{-1}.G^{-1})	l_{ex}(nm)
550	-1850	2.3×10^{-3}	1.8×10^{7}	11.7

Table 5.1: Fundamental magnetic parameters of the NiMnSb thin films: saturation magnetisation, anisotropy field, damping, effective gyromagnetic ratio and exchange length (from literature [110]).

5.3.2 Eigenmodes in the saturated state

As presented theoretically in the chapter 2, studying the perpendicularly magnetised uniform state is a first step in the understanding of the discs intrinsic properties. This analysis is compared to the study realised on thin films, to confirm that the magnetic properties are conserved in the nanostructures. The difference between the two analysis

being the magnetic confinement inside the discs, the precise diameter of the samples can be evaluated as well.

Typical results are shown in the figure 5.2 for the two different thicknesses and various diameters. On the left, the disc of 1 μm in diameter and 44 nmthick is measured. The spin wave spectrum is acquired by varying the perpendicular field while the magnetisation is excited by an in plane and linearly polarised microwave field. Several modes can be detected and then labelled using the theoretical approach developed in the chapter 2. These modes are described by Bessel functions and labelled with two indices (l, m) corresponding to the number of nodes of the precessing magnetisation in the radial and azimuthal directions, as sketched on the left in colour plots. The most intense mode on the right corresponds to the uniform mode $(l = 0, m = 0)$, and the following modes are radial spin waves $(l = 0, m = 1, 2, 3...)$, whose resonant fields are calculated and shown by ticks under each peak. Only radial modes are excited because there is no overlap between the uniform in plane microwave field and the azimuthal symmetry of the $l \geq 1$ modes.

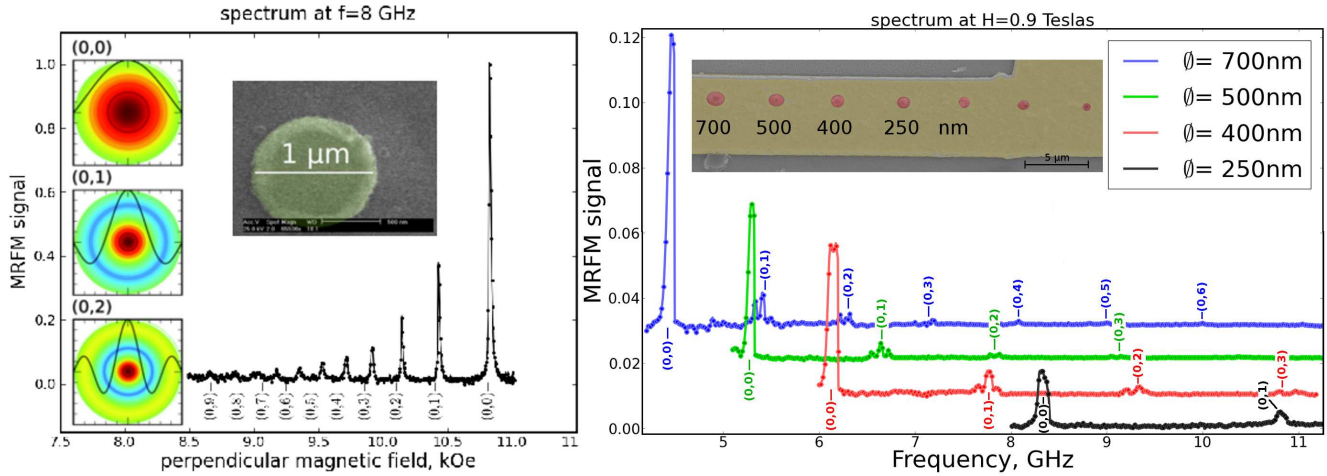

Figure 5.2: MRFM spectrum of NiMnSb discs in the saturated state. On the left, the spectrum at constant frequency is shown for the disc of 1 μm in diameter. The black ticks under each peak correspond to the calculated resonant field of each $(l = 0, m)$ modes. On the right, the spectra at constant field of the series of discs with the thickness 20 nm is shown to highlight the effect of the confinement on the spin waves dispersion.

On the right of the figure 5.2, the four biggest discs of thicknesses 20 nanometres are measured. Here, the spectrum is recorded at constant field by varying the microwave frequency (the offset between the spectra is set for clarity). The same spin wave modes can be seen in the frequency domain. The difference of confinement changes the boundary conditions, resulting in two main effects: the resonance frequencies are increased for smaller radius and the splitting between modes increases as well.

The comparison between these spectra and analytical calculations allows to extract magnetic constants (M_s, γ, α, H_s) for the nanostructures in good agreement with the table 5.1. Moreover, the diameter of the two thickest discs (44 nm) have been found larger than the nominal diameter due to lithography imperfections: 1.04 and 0.26 μm instead of 1 and 0.2 μm respectively. This is consistent with the diameters evaluated on the SEM images.

5.3.3 The vortex state

We display in figure 5.3 the effect of the perpendicular applied field on the magnetisation dynamics. The field goes from +9 kG to -9 kG in order to explore the unsaturated state of the nano discs.

The magnetic probe is placed at 1.4 μm above the disc of 260 nm in diameter and 44 nm thick. The cantilever frequency is directly proportional to the static dipolar force between the sample magnetisation and the sphere. Indeed, the cantilever resonance frequency is proportional to $\omega_c \propto \sqrt{k(z)/m}$, where the effective sping constant depends on the force gradient along z at the altitude z_0: $k(z) = k - \partial_z F_{z_0}$. Panel a of the figure 5.3 shows the frequency of the f-MRFM cantilever when the perpendicular field is varied.

The signal, which is flat until the saturation field at $\pm$ 6 kOe, starts to increase for lower field values meaning that the static force applied on the cantilever decreases. This is the signature of a new, unsaturated, magnetic state identified as a magnetic vortex. This statement is confirmed by a standard magnetic force microscopy (MFM) measurement of the 1 μm disc at remanence, shown in the figure 5.5c. This image was done with a standard MFM whose sharp tip was coated with a magnetic layer and scanned $\simeq$ 30 nm above the sample. The magnetisation is in plane, except at the centre where the vortex core, with an out of plane magnetisation, is seen as a black dot.

Evidence for a vortex state are also given by the dynamical measurements of the figure 5.3, panel b and c. The variation of the longitudinal component of the magnetisation is measured at constant microwave frequency by varying the perpendicular field (the baseline is shifted for each frequency for clarity). At high frequency, panel b, the standard saturated modes already described in the chapter 2 are seen and labelled. But below the saturation field, a new mode appear at low frequency on the panel c, which is attributed to the gyrotropic motion of the core around its equilibrium position. This mode can be measured in all the discs already presented, and its frequency range is consistent with the gyrotropic frequencies calculated in the chapter 3.

5.4 Gyrotropic motion of the vortex core

This section is dedicated to the analysis of the gyrotropic mode in the NiMnSb discs and the consequences of a perpendicular bias field on its dynamics.

Our MRFM technique is well adapted for these experiments for several reasons. First of all, it has ability to measure a single nanostructure with a great spectroscopic accuracy. The symmetry of the gyrotropic mode is also well adapted to our detection, which introduces an axially symmetric perturbation field. It has already been shown [28] that the in plane microwave field generated by our antenna has the good symmetry to excite the gyrotropic mode. A MRFM signal will then be measured if the excited mode profile produces a detectable variation of the longitudinal component of the magnetisation longitudinal component ΔM_z. This is indeed the case for the gyrotropic mode since the dynamical deformation of the vortex core produces a M_z dip opposed to the core polarity proportional to the velocity (see chapter 3, section 3.3.2.4). Finally, the perpendicular applied field keeps a good symmetry for the measurement since it is needed to magnetise the magnetic probe in the z direction.

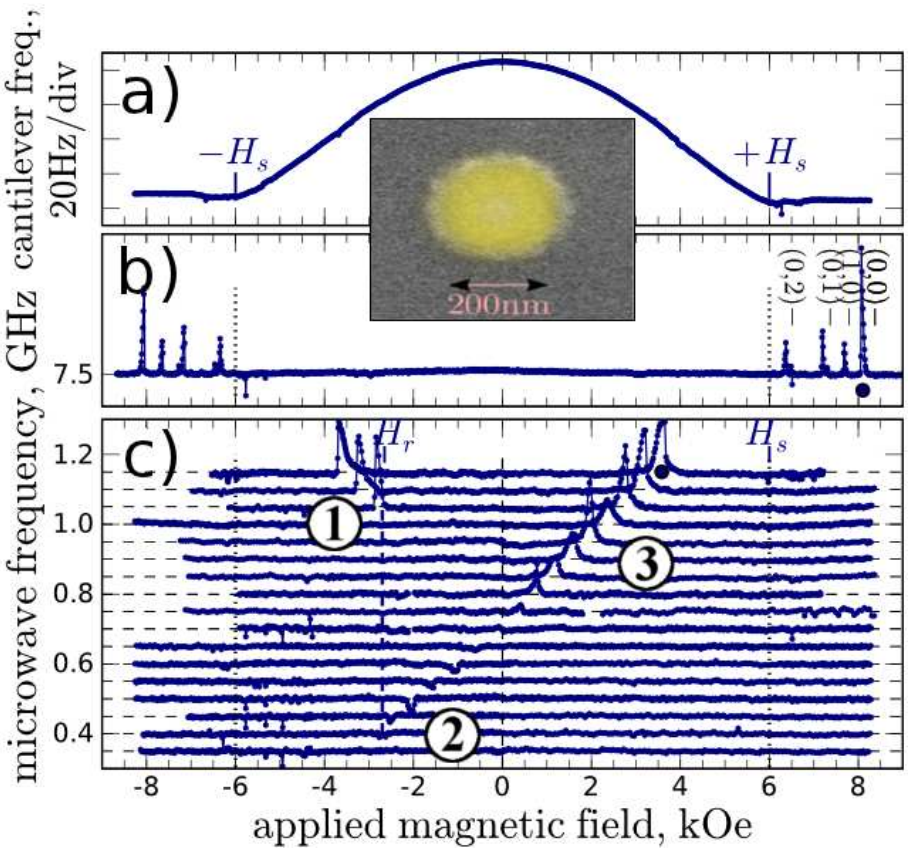

Figure 5.3: a) Cantilever frequency, proportional to the static M_z component over the NiMnSb disc of 260 nm in diameter while varying the perpendicular field. The spin wave spectrum at constant frequency are shown in the saturated (b) and the vortex state (c). The three labelled regions corresponds to the magnetic configurations described in the figure 5.4.

5.4.1 The gyrotropic mode under a perpendicular field

The gyrotropic mode, already presented in the section 3.3.2 of chapter 3, is the lowest energy mode of the vortex dynamics. It consists of a low frequency gyration of the vortex core around the disc centre, that has been observed experimentally [28, 105, 101, 20] and is well described theoretically. All the previous experimental studies on the gyrotopic mode were done at remanence or under a small in-plane field. This study will focus on the effect of a perpendicular magnetic field on the vortex dynamics. As described previously, the vortex structure is deformed by a magnetic field (see figure 3.4 of chapter 3), adding Zeeman energy, modifying the magneto-static energy and therefore the spin waves frequencies.

Let us first describe more precisely the panel c of figure 5.3. All the spectra were measured by saturating the disc above H_s and then by decreasing the field; in that sense, the nucleated vortex core is parallel to the applied field. By following the dynamics when the field is decreased below H_s, a first peak (labelled with a blue dot) appears around 4 kOe for a microwave frequency of 1.2 GHz: this is the gyrotropic mode. It is well separated in frequency from the rest of the spin wave spectrum because of the lateral boundary conditions. Therefore, the measured resonance can only be attributed to the gyrotropic mode.

The resonance frequency of this mode decreases with the applied field until remanence,

which is the first interesting point: the gyrotropic frequency depends linearly on the perpendicular bias field. Then the frequency continues to decrease until $H_r \simeq 2.5$ kOe. The same mode can be followed at negative field, meaning that the vortex core polarity remains stable, but anti-parallel to the field orientation. For lower anti-parallel field values, the gyrotropic frequency jumps on another branch having the opposed field dependence as the previous one, which is the signature of the static core reversal at H_r.

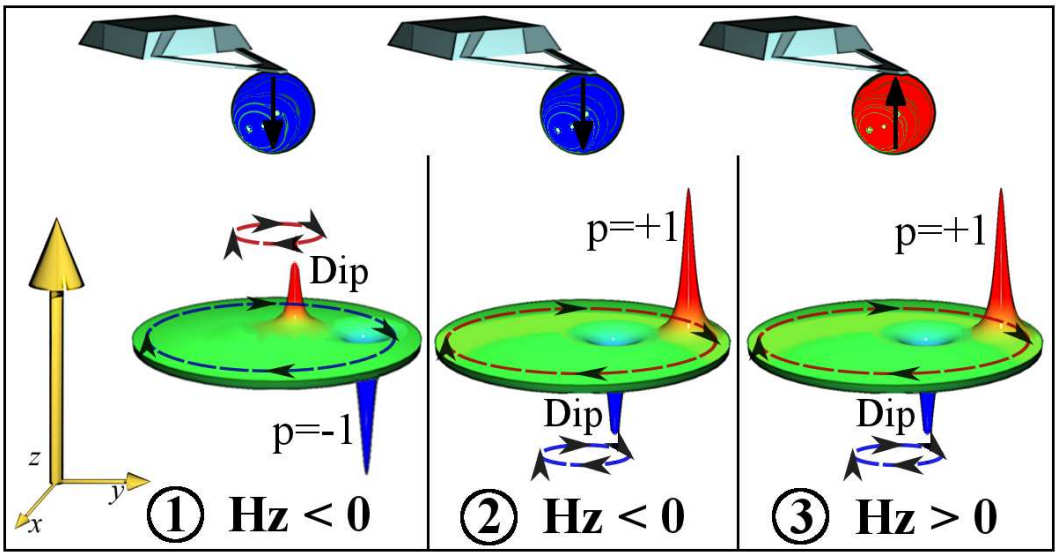

Figure 5.4: Sketch of the magnetisation configuration of the vortex gyrotropic mode coupled to the f-MRFM probe for the three regions labelled in the figure 5.3 (the size of the dynamical dip is exagerated for clarity). The sign and amplitude of the resonance peaks can be understood from these sketches.

The amplitude and sign of the resonance peaks also confirm this scenario. The sign of the peaks is given by the product of the signal ΔM_z and the magnetisation of the MRFM probe. We recall that its magnetisation follows exactly the applied field since it is a sphere without coercivity. Concerning the gyrotropic mode, the measured ΔM_z has two origins:

1. The main contribution is indeed the dynamical dip that forms close to the core during the gyrotropic motion. Its sign is always opposed to the core polarity. This is illustrated by the sketch of the figure 5.4. The f-MRFM measures the difference between the magnetisation of the core at the centre of the disc and the magnetisation of the couple vortex-dip during the gyrotropic motion.

2. Since the f-MRFM measurement is the time average over several precession periods, another contribution to ΔM_z is given by the difference between the configuration with the core at the center and the gyrotropic motion where the core magnetic moment is diluted over a circular orbit. This part is actually small and represents only $\simeq 10$ % of the signal.

In the region labelled ③ on figure 5.3, the magnetisation has the arrangement of the third panel of figure 5.4. The probe magnetisation is parallel to the applied field. The ΔM_z created by the gyrotropic mode having a polarity $p = +1$ parallel to the field is

opposed to the probe magnetisation. The force applied on the cantilever is lowered which increases the amplitude of vibration. Therefore, the signal is positive.

In the region labelled ② on figure 5.3, the magnetisation of the probe is reversed, since the perpendicular field is now negative. But as sketched on the second panel of figure 5.4, the ΔM_z contribution from the gyrotropic mode is unchanged since it has the same polarity. The measured signal is then negative.

Finally, in the region labelled ① on figure 5.3, the probe magnetisation is unchanged. But the vortex polarity has been reversed and the ΔM_z contribution from the gyrotropic mode is again opposed to the probe magnetisation. A positive signal is recovered.

Two main conclusions arise from the perpendicular field dependence of the gyrotropic mode:

- The gyrotropic frequency ω_G varies linearly with the bias field H_z, following two opposite branches depending on the core polarity p. This behaviour was calculated theoretically in the section 3.3.2.3 of chapter 3 as:

$$\omega_G(H_z) = \omega_G(0)\left[1 + p\frac{H_z}{H_s}\right] \tag{5.1}$$

  where $\omega_G(0) \simeq (20/9)\gamma M_s L/R$ is the gyrotropic frequency at remanence.

- The vortex core polarity is stable under an anti-parallel bias field until a threshold field H_r. This value corresponds to the static core reversal described in the section 3.2.2.2 of chapter 3. If the opposite experiment is performed starting from the negative saturation field $-H_s$, a symmetric behaviour is observed, and the core is reversed at $H_r \simeq +2.5$ kOe, as shown on figure 5.5. As can be seen on the figure 5.5, the static reversal field seems to be independent of the disc diameter, even if the saturation field H_s is different. This is confirmed by all the measurements done in the other NiMnSb discs presented previously. As explained in the theoretical part, the static reversal is influenced mostly by the energy stored in the vortex core. In that sense, the disc thickness should be the key parameter that controls H_r [127].

Panels a and b of figure 5.5 compare the experimental values (dots) measured on the NiMnSb discs of 1.04 and 0.26 μm in diameter and the calculations (solid lines) given by the equation 5.1. For each disc, the Kittel mode is measured above the saturation field H_s. Below, a transition occurs indicated by an abrupt change of slope: this is the gyrotropic mode, appearing because of vortex nucleation. The mode can be followed, for example with the blue dots, until the core polarity is reversed at H_r. The frequency then jumps onto the symmetric branch with the opposite slope. The result of the calculation, using the theory of the saturated state, above H_s, and the formula 5.1 above, shown in dashed lines, reproduces well the experimental data.

Performing the same experiment but from the opposite saturation field, with the orange dots, reveals an hysteresis, arising from the asymmetry associated with the core polarity. The vortex structure is deformed by the perpendicular field and the two polarities of the core are no more equivalent. The core polarities symmetric and anti-symmetric to the field have different energies, which is reflected on the gyrotropic frequency. This effect can be seen as an equivalent Zeeman splitting of the gyrotropic frequency. The splitting between the two polarities is then simply proportional to the field H_z:

$$\Delta\omega_{G,\uparrow\downarrow}(H_z) = 2\omega_G(0)\frac{H_z}{H_s} \tag{5.2}$$

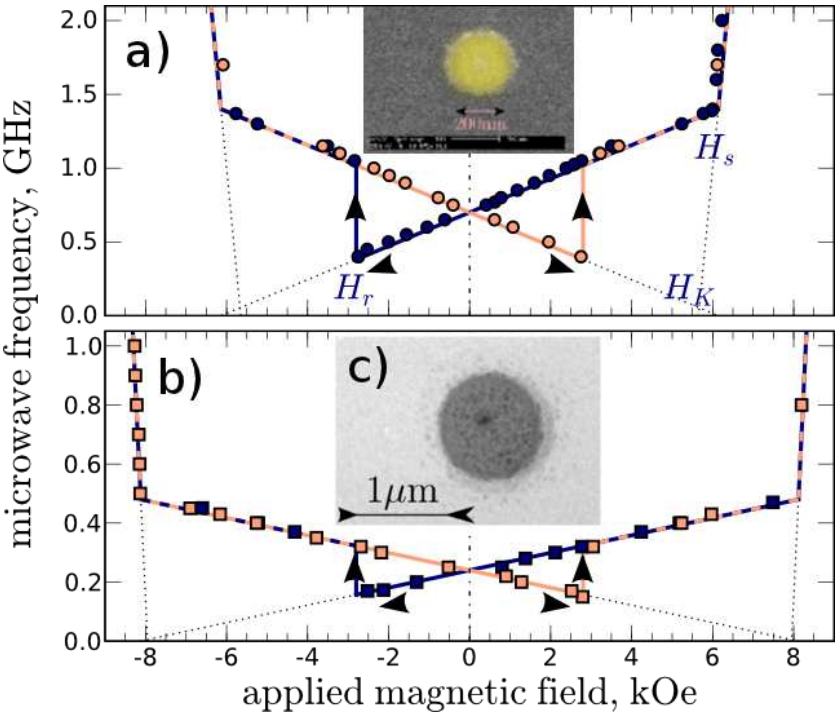

Figure 5.5: Experimental (dots) and calculated (lines) gyrotropic frequency versus applied field for the two discs of 1 μm a) and 0.26 μm b) in diameters and 44 nm thick. The inset c) is a standard MFM image at remanence of the 1 micron disc, revealing the presence of a vortex.

To emphasise this phenomenon, the "Zeeman" diagram of the gyrotropic mode is presented in the figure 5.6. The spectra have been recorded at constant perpendicular field by varying the microwave frequency, for each core polarity. Two examples are shown for the perpendicular fields 0.6 and 1.5 kOe. For the blue curves, the polarity is anti-parallel to the field ($p = -1$), the peaks are negative and therefore the gyrotropic frequency is lower than the value at remanence. In the opposite, for the red curves, the polarity is parallel to the field ($p = +1$) and the gyrotropic frequency is increased. The theoretical frequencies calculated with the formula 5.1 are plotted as the red and blue lines.

To confirm the universality of this phenomenon, the same experiment was done on the NiMnSb sample with the thickness 20 nm. The gyrotropic spectra were recorded at constant perpendicular field. On the figure 5.7, the spectra corresponding to the parallel polarity of the core are shown for each disc with the diameters between 500 and 175 nanometres for different bias fields. The calculated frequencies are superimposed (coloured lines) for comparison.

Two main observations arise from this diagram:

- The gyrotropic frequency is determined by the magnetic confinement, i.e. the aspect ratio of the disc. The smaller the disc, the larger the gyrotropic frequency. This is the evidence that the magneto-static energy plays a dominant role in the "quantisation" of the gyrotropic mode in confined geometries. We emphasise the fact that the gyrotropic motion can be observed in discs with diameters smaller than 200 nanometres.

- The same Zeeman like splitting is observed, the slope of which is mainly determined by the saturation field of the considered disc. The saturation field H_s can be eval-

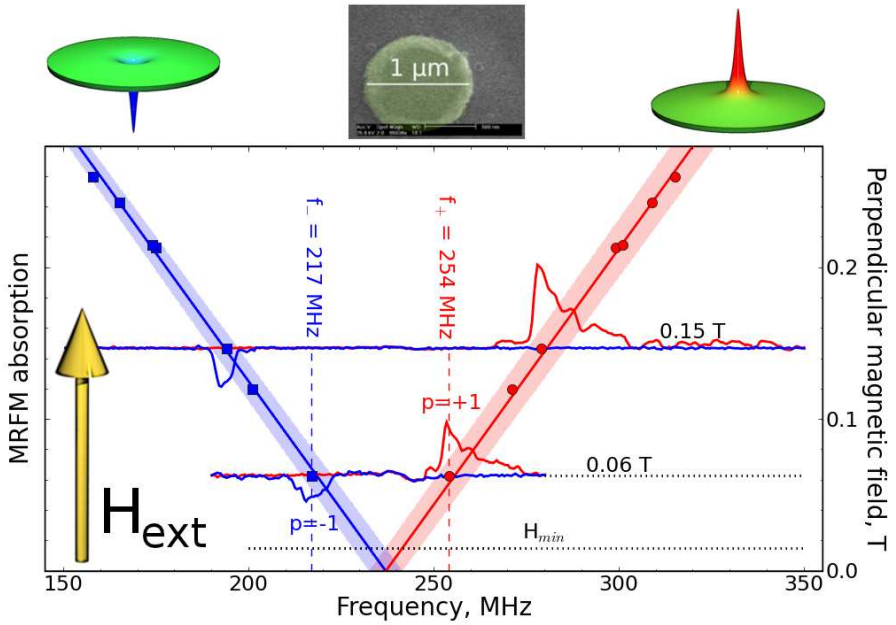

Figure 5.6: Frequency splitting induced by a perpendicular magnetic field between the gyrotropic modes corresponding to the two opposite core polarities $p = \pm 1$. Two spectra, recorded at fixed field by varying the microwave frequency, are presented for each core polarity.

uated as the intersection between the gyrotropic and saturated dispersions, as seen in the figure 5.5a.

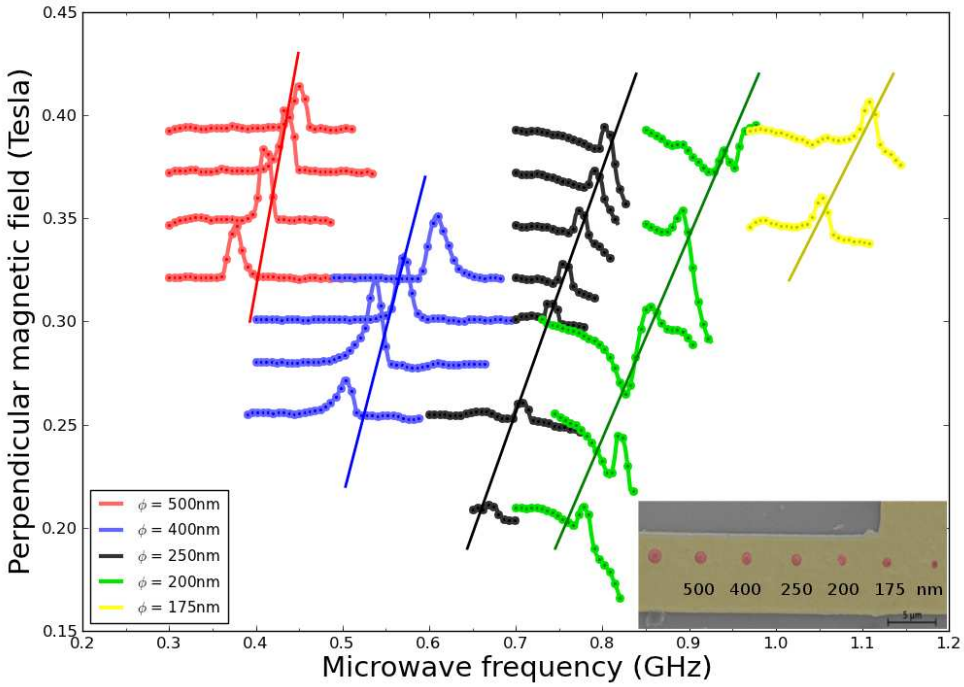

Figure 5.7: Dispersion relation for the gyrotropic mode as a function of the disc diameter for the NiMnSb discs of thicknesses 20 nm with the core polarity parallel to the perpendicular field. The coloured lines are the frequencies calculated using equation (5.1).

5.4.2 The dynamical core reversal

The previous study of the vortex gyrotropic mode was done in the linear regime with a small microwave field which never exceed $\simeq 1$ mT. It is now very important to focus on the most interesting effect of the core non linear dynamics: its dynamical reversal. As already explained in the chapter 3 section 3.3.2.4, when the radius r of the core orbit increases, a distortion of the core profile characterised by the appearance of a tail having the magnetisation direction opposite to that of the original core polarity occurs. The magnitude of this tail depends solely on the linear velocity $V = \omega_g(0)r$ of the vortex core. When the latter reaches the critical speed $V_c \simeq 1.66\gamma\sqrt{A_{ex}}$ at remanence, the core polarity suddenly reverses.

5.4.2.1 Experimental evidences

To begin with, it is crucial to understand the signature of the dynamical reversal in our experiment. The first experimental evidence [134] of this phenomenon was given by time-resolved scanning transmission X-ray microscopy at remanence. After a short and intense microwave pulse, the polarity of the core was determined by the sense of rotation of the core. The f-MRFM technique produces a measurement averaged in time and does not allow this determination. Nevertheless it possible to distinguish the polarity before and after a reversal event using the Zeeman like splitting of the gyrotropic mode, as explained in the previous section (figure 5.6).

To be able to discriminate the core polarity deterministically, it is necessary to choose the static perpendicular magnetic field H_z in such a way that the field-induced gyrotropic frequency splitting exceeds the intrinsic linewidth Δf of the gyrotropic mode. Obviously, H_z should be lower than H_r to avoid a static core reversal. The gyrotropic mode linewidth will be discussed in detail in the section 5.5, but to fulfil this criterion, a field of 1.5 kOe is chosen.

A typical core dynamical reversal experiment is shown in figure 5.8 for the NiMnSb disc of 1 μm in diameter and 44 nm in thickness, with which all this study will be performed. The protocol is the following:

1. The core polarity anti-parallel to the perpendicular field is nucleated at high negative perpendicular field. The field is then decreased and reversed to be +1.5 kOe, where the polarity $p = -1$ is still stable. The first upper spectrum is recorded at low microwave power (-16 dBm), displaying the frequency of the lower gyrotropic mode ($p = -1$ branch).

2. For the second spectrum (in red), the microwave power is increased to -14 dBm and the frequency is scanned from 150 to 350 MHz. The beginning of the $p = -1$ resonance line appears, but the critical speed is reached by the core and its polarity is reversed. Therefore, the frequency of the upper gyrotropic mode ($p = +1$ branch) appears.

3. The same spectrum is repeated with a low microwave power (-16 dBm), to confirm the stability of the $p = +1$ gyrotropic resonance.

4. Finally, the microwave power is increased again and the frequency sweep is done from 350 to 250 MHz. The beginning of the $p = +1$ resonance can be seen, but an

abrupt jump denotes the core reversal. The sweep is performed backward, and the $p = +1$ resonance has disappeared. The spectrum of the first step is then recovered.

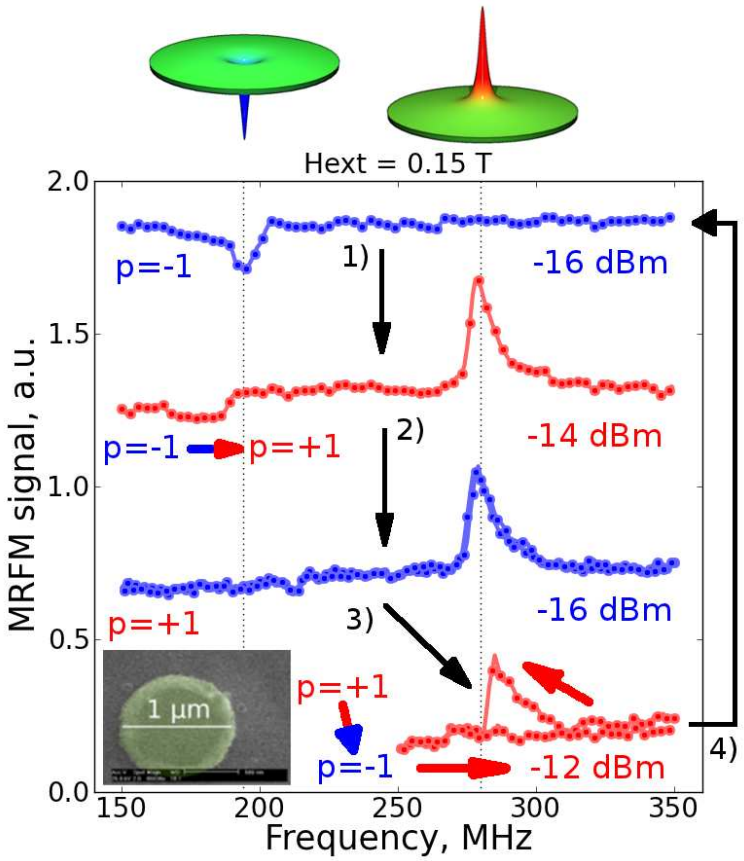

Figure 5.8: Experimental evidence of the dynamical core reversal with the NiMnSb disc of 1 µm in diameter. In this experiment, the perpendicular field is set constant at 1.5 kOe and a continuous microwave excitation is shined on the sample.

In this experiment, we were able to demonstrate the "bi-stability" of the gyrotropic dynamics for $p = \pm 1$, as well as the dynamical reversal of the core polarity. This was achieved by sending a continuous microwave excitation whose power was increased to drive the vortex core over its critical speed.

5.4.2.2 Optimisation of the vortex core reversal

It is clear from this experiment that the reversal process is resonant. Therefore, instead of shining the microwave excitation continuously, a single microwave field pulse applied at the proper ($p = +1$ or $p = -1$) gyrotropic frequency should be sufficient to reverse the polarity. In this section, the design of such efficient microwave pulses is investigated.

The efficiency of a microwave pulse to reverse the core polarity is a function of its frequency, duration and amplitude. To optimise these parameters, a typical reversal diagram is constructed. First of all, a perpendicular bias field of $\mu_0 H_z = 65$ mT is chosen to be able to discriminate the two gyrotropic polarities. Using the same kind of experiment as in the figure 5.8, the resonant gyrotropic frequencies corresponding to the polarity $p = \pm 1$ are measured: $f_- = 217$ MHz and $f_+ = 254$ MHz (see figure 5.6). This

enables a single-shot and deterministic readout of the initial and final core polarity. At the same time the field H_z is low enough to minimise the asymmetry between the two polarities.

The efficiency of both single pulses, from $p = -1$ anti-parallel to H_z to $p = +1$ and from $p = +1$ to $p = -1$ is then investigated. By analogy with the NMR π pulses used to reverse the magnetisation, the microwave pulse that reverse the core polarity $p = -1 \rightarrow 1$ ($p = +1 \rightarrow -1$) is called a Π_- (Π_+)pulse. The chosen protocol is the following:

1. For studies of the reversal Π_- (Π_+) pulses, the initial $p = -1$ ($p = +1$) state is first reset using an initialisation pulse whose result is known to be fully deterministic.

2. A single Π_- (Π_+) pulse of given duration $w = 100$ ns, frequency f and power P is applied through the microwave antenna.

3. The final polarity state is read by a single measurement of the MRFM amplitude at the frequency f_+ (f_-).

4. The result is averaged over 16 Π_- (Π_+) attempts and displayed in colour code at the position (f,P): a pixel coloured in red(blue) marks a successful reversal while the transparency gives the switching probability.

5. The same experiment is repeated for the pulse duration $w = 50$ (orange, light blue) and 20 (yellow, green) nano-seconds, and the resulting diagrams are superimposed.

The result is shown in the panel a of the figure 5.9. One can first notice the clear signature of the frequency splitting introduced by the field H_z: the two symmetric reversal events are well separated in frequency. Nevertheless, the shape of the two reversal areas is very similar because the splitting is too small to create a real asymmetry in the static magnetisation. The resonant character of the reversal process is then revealed by the position of the minimum power needed to reverse the core, marked by red squares in the figure 5.9. It corresponds to a Π_- (Π_+) pulse at the gyrotropic frequency f_- (f_+). If the microwave pulse is detuned from the resonant frequency, its power has to be increased to reach the reversal, since the dynamic susceptibility of the vortex core is lower at this frequency. Finally, if the pulse duration is reduced, more microwave power is needed to reverse the core. This is because the critical velocity, which is the key parameter of the reversal process, has to be reached sooner.

Notice that the presented diagrams have been restricted in purpose to power lower than -4 dBm, while the experiments were performed until higher microwave power. If the strength of the microwave excitation is high enough, the opposite reversal areas start to overlap and the core can be reversed more than once. The shape of the reversal areas becomes very complicated, exhibiting stripes of increasing number of consecutive reversals. The analysis of this region is difficult and we have concentrated our efforts on the low power region of the diagram.

To have a deeper understanding of the reversal mechanism, calculations were performed. The vortex core motion during the gyrotropic mode is well described by the Thiele equation, which allows to calculate the eigenfrequency. But a more detailed analysis is needed to have access to the transient motion of the core before it reaches a steady state orbit. In the reversal mechanism, the core is indeed reversed before reaching a steady orbit. Following the appendix A, the time dependent position of the vortex core

$\boldsymbol{Z}(t) = X + iY$ can be calculated at remanence. Assuming that the asymmetry created by the perpendicular field is negligible, the asymmetry between the core instantaneous velocity $V(t) = \omega_G r(t)$ only depends on the frequency associated to each polarity. Excited by a microwave field of frequency f and power P, it is given by the time derivative of $\boldsymbol{Z}(t)$ [85]:

$$V(t) = \frac{1}{3}\gamma Rh \frac{\sqrt{\Omega^2 + F(\Omega, t)}}{\sqrt{(1-\Omega)^2 + d^2\Omega^2}} \tag{5.3}$$

where $\Omega = 2\pi f/\omega_G$ and:

$$F(\Omega, t) = e^{-2d\omega_G t} - 2\Omega e^{-d\omega_G t}\Big[\cos[(1-\Omega)\omega_G t] - d\sin[(1-\Omega)\omega_G t]\Big] \tag{5.4}$$

The term d is the damping in the vortex state that will be calculated in the section 5.5.

Using this result, a simple numerical simulation is performed to reproduce the experimental diagram of the figure 5.9a with a similar protocol:

1. For each pixel (f, P), the corresponding core velocity at the end of the microwave pulse of duration w is calculated as $V(w)$ with equation 5.3.

2. The reversal threshold is defined by the critical speed calculated by Guslienko, transformed to take the effect of the perpendicular field into account [74]. The vortex core is considered reversed dynamically if:

$$V(w) \geq 1.66\gamma\sqrt{A_{ex}}\left[1 + p\frac{H_z}{H_s}\right] \tag{5.5}$$

3. Following the same colour code, if the core is reversed after the pulse, the pixel (f, P) has a colour corresponding to the pulse duration w, otherwise it is blanked.

The result of this simulation is shown in the panel b of the figure 5.9. To be in quantitative agreement with the experiment, the damping parameter d introduced in the calculation has to be adjusted to d_{forced}, because the experimental value measured in the linear regime is too small. This is due to the strongly non linear dynamics experienced by the vortex core near the reversal threshold, that will be discussed in detail in the section 5.5. Within this adjustment, a reasonable agreement is found between the experiment and the calculation.

We shall now analyse in detail the efficiency of the microwave pulses in order to optimise them. The optimal power needed to switch the core is defined as $P^* \propto h_c(f, w)^2$, where $h_c(f, w)$ is the microwave field amplitude. For each reversal diagram, this optimal power was materialised by red squares in the figure 5.9. If a long resonant microwave pulse is obviously efficient to reverse the core with the minimum power, it is more interesting to define the pulse that costs a minimum of energy. The optimal energy of a pulse is then $E^* = P^* w^*$, where w^* is the optimal pulse duration.

In the figure 5.10b the energy $E = Pw$ released by the microwave pulse is plotted as a function of the pulse duration w using experimental points obtained from the analysis of data sets similar to those presented figure 5.9a. There is a clear minimum in the optimal pulse energy that occurs around $w = 50$ ns. The position of this minimum yields an estimation of the characteristic decay time of the vortex core back to equilibrium.

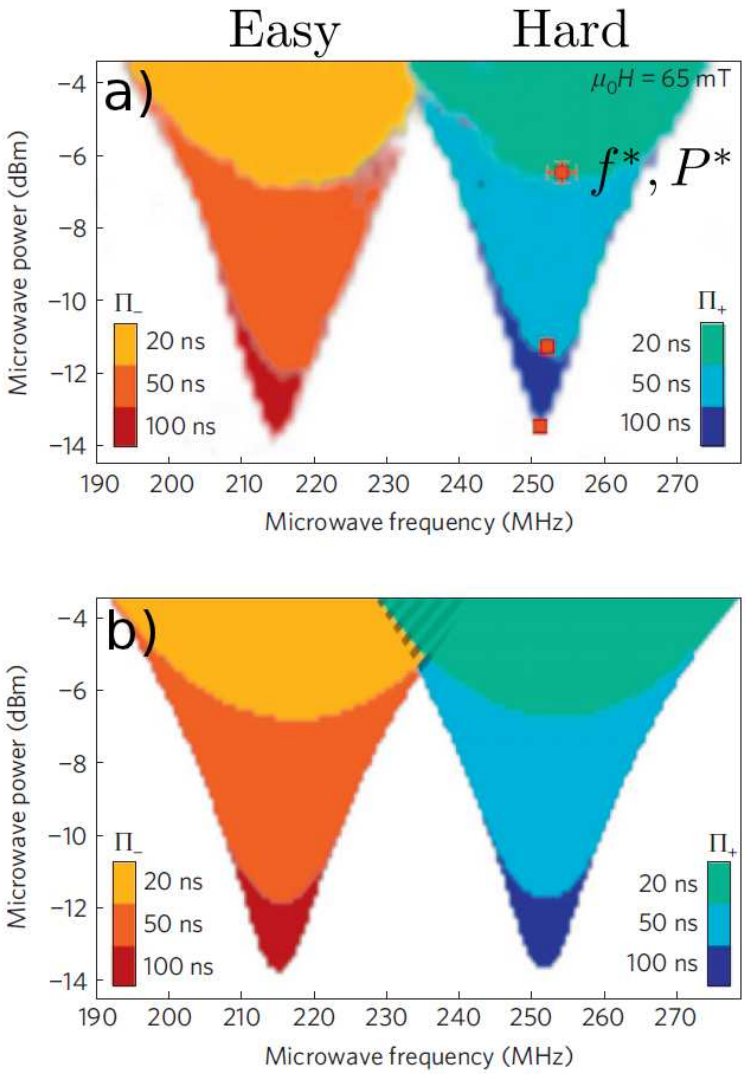

Figure 5.9: a) Diagram comparing the efficiency of microwave pulses of various frequency, duration and power to reverse dynamically the core polarity, performed on the NiMnSb disc of 1 micron in diameter with a bias field of 65 mT. A coloured dot means a successful core reversal event while the transparency gives the switching probability averaged over 16 events. The panel b) is the result of a calculation using the Thiele equation and the critical speed for the core reversal.

The microwave power is concentrated within the linewidth of the mode, which is the most efficient. If the pulse duration exceeds this characteristic time, the vortex-core dynamics reaches steady state before the end of the pulse; that is, the pulse duration is unnecessarily long. In contrast, if the pulse duration is shorter than this characteristic time, some energy is wasted outside the resonance line. In other words, the linewidth of the microwave emission Δf is broadened by the finite temporal size of the pulse w, which is a property of the Fourier transform $\Delta f \propto 1/w$.

This effect can also be seen in the of the optimal frequency f^* plotted in figure 5.10a. The optimal frequency f^* for each pulse duration corresponds to the point of lower power (red squares on figure 5.9a) and should be the gyrotropic frequency. This is true if the pulse length w is longer than this estimated decay time of 50 ns. If the vortex is forced

on a shorter length scale, the optimal frequency shifts toward higher frequencies, as can be seen on the figure 5.10a. This behaviour is a well known characteristic of damped harmonic oscillators.

In order to model this behaviour, the optimal energy is calculated with $E \propto w h_c(f,w)^2$, where $h_c(f,w)$ is calculated with equation (5.3) at $V = v_c$. Minimisation of the energy E with respect to the pulse frequency f yields the dependence on w of the optimal pulse energy E^* plotted in figure 5.10b. With a defined as an experimental conversion factor between the input power in the antenna and the microwave field power h^2, the optimal energy can be written as:

$$E^*(w) = w\frac{h_c^2}{a} = \left(\frac{6dv_c}{a\gamma R}\right)^2 \frac{w}{1 + e^{-2d\omega_G w} - 2e^{-d\omega_G w}} \tag{5.6}$$

Two independent parameters are used to adjust this calculation with the data in 5.10b: the damping ratio d to fit the overall shape (position of the minimum) and the critical velocity V_c to fit the absolute value of the energy. The critical velocity fitted in this calculations is $v_c \approx 190$ ms^{-1}. This value is in good agreement with the expected value of 225 ms^{-1} predicted by the Guslienko's criterion for our NiMnSb disc (see equation (3.38)) of chapter 3).

The continuous lines in figure 5.10b show the dependence of the Energy (from equation (5.6)) with the damping term d. The black curve corresponds to the linear vortex damping (see figure 5.15). The blue curves, for which the best agreement is found with the data, was plotted with a damping parameter $d_{forced} = 0.018$. This value "non linear" was already introduced in the previous calculation of the reversal diagrams.

Within these adjustments, the optimal pulse duration w_{min} corresponding to the minimum energy E_{min} follows from equation (5.6): $w_{min} = 1.26/(d_{forced})\omega_G = 1.26\ \tau_{forced}$. For the blue solid line in figure 5.10b, $d_{forced} = 0.018$, τ_{forced} =35 ns, hence E_{min} is reached for $w_{min} = 44$ ns.

Minimising the energy E with respect to the frequency also allows to deduce the dependence of the optimal frequency f^* with the pulse duration. Using the previous parameters of the damping, the shift of the optimal frequency towards high frequencies observed on figure 5.10b can be well reproduced.

This analysis allows to define an optimal microwave pulse $\Pi_{+/-}$ of duration $w \simeq 44$ ns and frequency f^* that is able to reverse the core, consuming only few pJ. At this optimal point, the corresponding microwave field strength can be evaluated following the analysis of the section 4.3.4 of chapter 4: only $\simeq 2$ Oe of rf field are needed to achieve the core reversal. This has to be compared to the 0.3 kOe needed to reach the static reversal.

This dynamical mechanism allows an efficient and extremely rapid vortex core reversal with a very low energy consumption, because of its resonant nature.

5.4.2.3 Effect of the perpendicular field induced asymmetry

In the previous exploration of the dynamical reversal properties, the bias perpendicular field was only used to create a slight splitting between the $p = +1$ and $p = -1$ states, in order to read unambiguously the vortex core polarity.

The dc bias field is now increased to investigate its effect on the core reversal. The static structure of the vortex is significantly deformed, creating a real asymmetry. The magnetisation that was in-plane at remanence is now uniformly tilted out-of-plane through

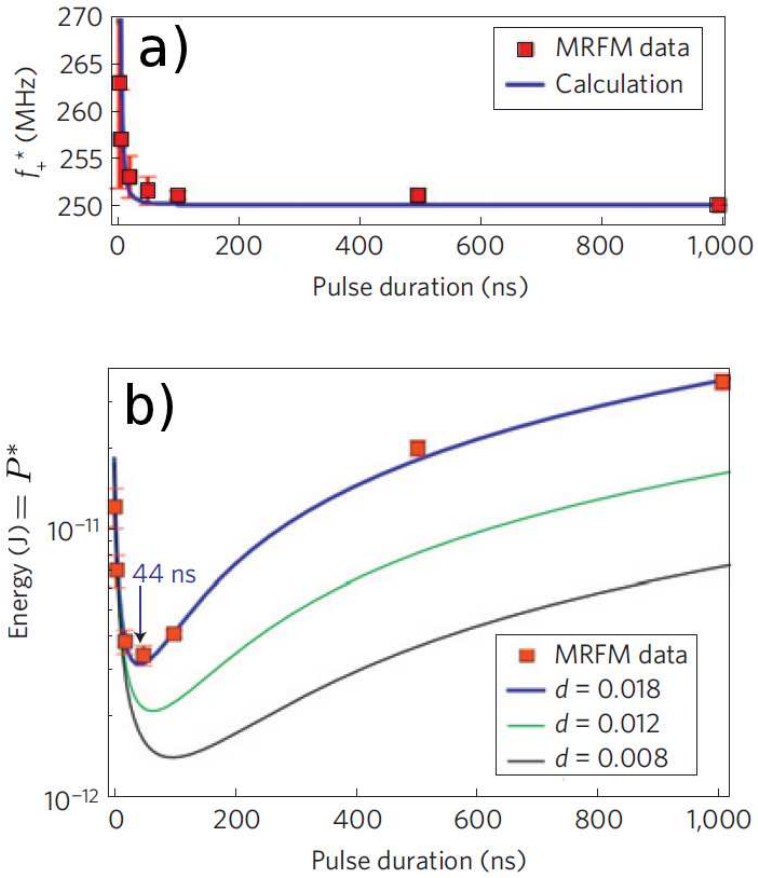

Figure 5.10: a) Optimal frequency of the microwave pulse to reverse the core polarity as a function of the pulse duration. b) Energy carried by the pulse as a function of the pulse duration. The minimum observed corresponds to the vortex characteristic decay time.

an angle $\cos(\Theta) = H_z/H_s$. If the core polarity is parallel to the bias field, the core size is broadened and for the polarity opposed to the field, the core size is narrowed.

This asymmetry should have an effect on the dynamical reversal mechanism since the initial and final states are different. The reversal between the core anti-parallel and parallel to the applied field ($p = -1$ to $p = +1$) is of course energetically favoured, since it is helped by the static field: this is the "easy" reversal. On the contrary, the opposite reversal ($p = +1$ to $p = -1$) ending with an anti-parallel polarity is energetically unfavoured: this is the "hard" reversal.

An analogy with the microwave assisted reversal of the magnetisation (for instance in a nanoparticle) could be done [129]. The polarities of the vortex core form the ground states of a double potential well. To pass from one to the other polarity, the energy barrier has to be overcome by the dynamical reversal process. At remanence, the two ground states are degenerated, but this degeneracy is lifted by the perpendicular field, giving a higher energy to the parallel state $p = +1$. If the energy provided by the bias field equals the barrier, the static reversal occurs.

Following this analogy, the "easy" reversal will always favoured by the bias field, and no significant variations are expected, as will be shown on figure 5.13. We will then focus the study on the hard reversal.

An experiment similar to the previous one presented on figure 5.9 was performed. Only

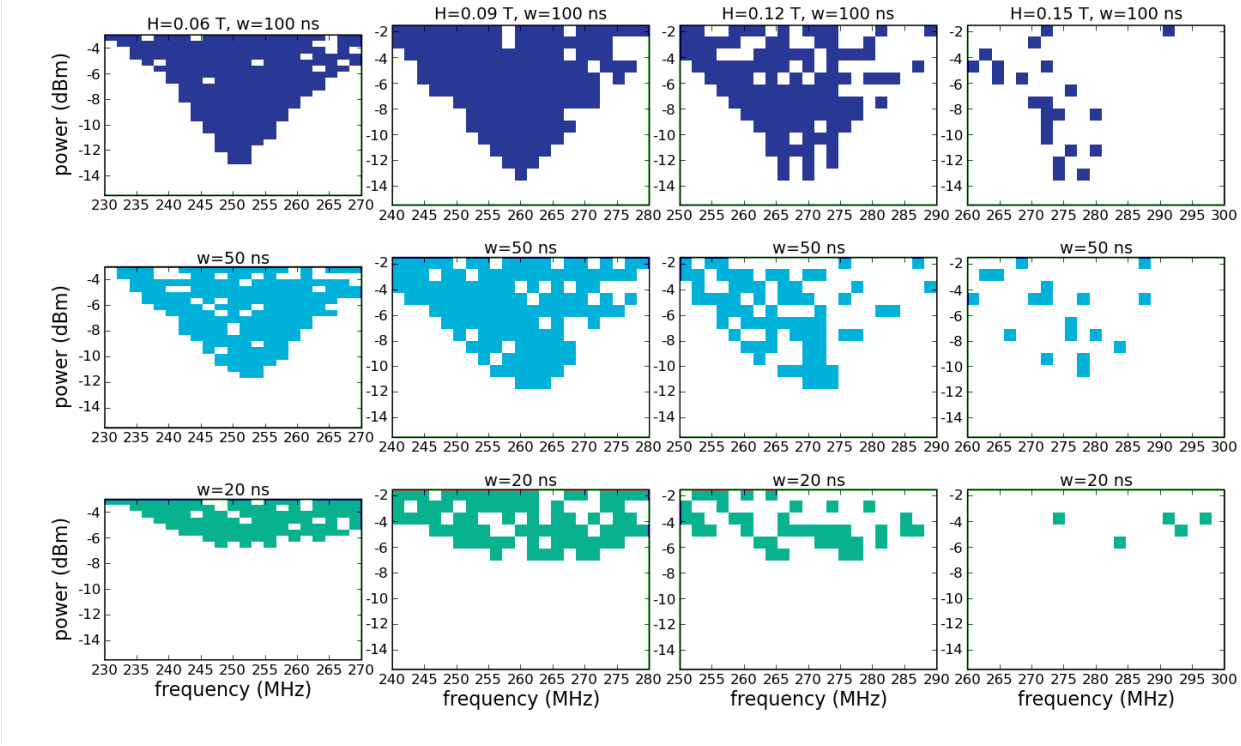

Figure 5.11: Evolution of the core hard reversal diagram of the figure 5.9 (from polarity parallel to anti-parallel to the bias perpendicular field) as a function of the applied perpendicular field. No averaging was performed.

the effect of Π_+ pulses was investigated, but the experiment was repeated with increasing perpendicular fields.

The result is presented in the figure 5.11, where the upper row corresponds to pulse duration $w = 100$ ns, the middle row to $w = 50$ ns and the lower row to $w = 20$ ns. The left column corresponds to a perpendicular field of $H_z = 60$ mT, and the field is increased by 30 mT steps from left to right. In these diagrams, the reversal events are displayed with the same colour code as in the figure 5.9. Notice that the first column corresponds to the right part (Π_+ pulses) of the figure 5.9. In this experiment the pixel size (power and frequency steps) was increased and no averaging were performed, therefore the reversal events looks scattered. However, it is clear that:

- For all three pulse durations, the *minimal power* needed to reverse the core seems to be independent from the perpendicular bias field H_z (around -13, -11 and -6 dBm respectively for each pulse duration).

- The reversal events seem more and more scattered as H_z is increased. The evaluated "*switching probability*" (there is only one event per pixel) roughly decreases as H_z, opposed to the initial polarity, increases. In other words, the global shape of the reversal region is conserved, but the number of reversal events recorded inside decreases while H_z increases, even if their positions seem to be randomly distributed.

To emphasise this phenomenon, the raw experiment of the extreme case is shown on the figure 5.12. The perpendicular field, $H_z = 2.7$ kOe, is chosen to be very close to the

static reversal field (from polarity anti-parallel to parallel) which is $H_r \simeq 2.8$ kOe. The microwave pulse duration chosen here is $w = 100$ ns, and the reversal events are displayed in red/blue.

First of all, the "easy" reversal shown on the panel a, which is greatly favoured by the perpendicular field, does not seem to be affected. The shape of the reversal events area is indeed very similar to the experiment done at lower field, for instance at 65 mT in the left part of figure 5.9. A more quantitative analysis confirms that the "easy" reversal is independent from the perpendicular field. In other words, the deformation of the vortex structure does not affect the "energy scale" of this "easy" switching. This remains true up to the static reversal threshold. From a microscopic point of view, it means that the transient motion of the vortex core, driven by the microwave field, before the reversal is not affected by the bias field H_z.

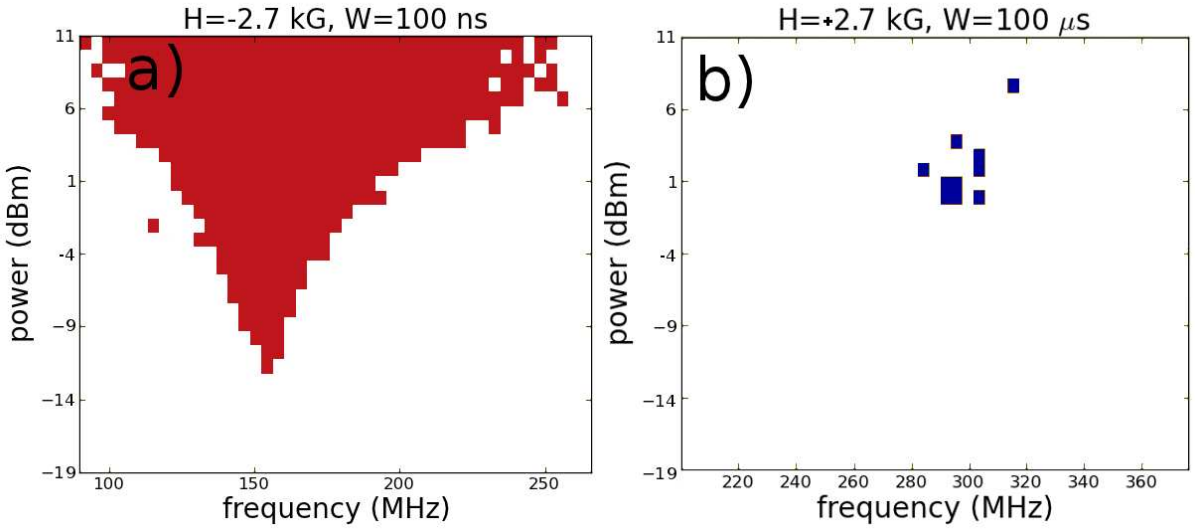

Figure 5.12: Comparison between the "easy" (a) and "hard" (b) reversal diagrams under a bias perpendicular field of 2.7 kOe. The microwave pulse duration w is a) 100 ns and b) 100 μs.

At the opposite, the panel b of the figure 5.12 demonstrates that the hard reversal (leading to a core polarity opposed to H_z) could be achieved, even very close to the static reversal field. To achieve this reversal, the microwave pulse duration was increased up to $w = 100$ μs. Nevertheless, the conclusions from the figure 5.11 remain the same:

- The "hard" reversal presents the same "energy scale" as the "easy" reversal: the shape of the switching events area and the corresponding energy minimum required for the dynamical core reversal are not affected by the increase of the perpendicular field.

- But while switching events are deterministic for the "easy" reversal, these events become probabilistic for the "hard" reversal events.

To illustrate this asymmetric behaviour, we have measured the switching probability by averaging over typically 500 events in the region close to minimal power using the results of experiments similar to those presented in Fig.5.11. The Figure 5.13 shows the evolution of the switching probability of both "easy" and "hard" reversals versus

perpendicular field for different values of the pulse duration (ranging from 20 ns up to 100 μs). The orange-red-brown colour symbols correspond to the "easy" reversal, for which the switching probability is always equal to 1. The deterministic character of these reversal events is thus confirmed. The green-blue-violet symbols correspond to the "hard" reversal, with increasing pulse duration w. The continuous lines are guides to the eye: they are plotted using a Fermi-Dirac like function:

$$P(H_z) = \frac{1}{1 + e^{(H_z - H_0)/\sigma}} \tag{5.7}$$

with the fitting parameters H_0 and σ that depend on w, plotted figure 5.13. The main observation is the following: the shorter the pulse, the lower the *critical perpendicular field* above which the "hard" reversal probability drops below 1. This can be seen in figure 5.13 on the dependence of the parameter H_0, which gives the field where the probability is reduced by a half. Moreover, the slope of the transition tends to increase for longer pulse, as modelled by the parameter σ.

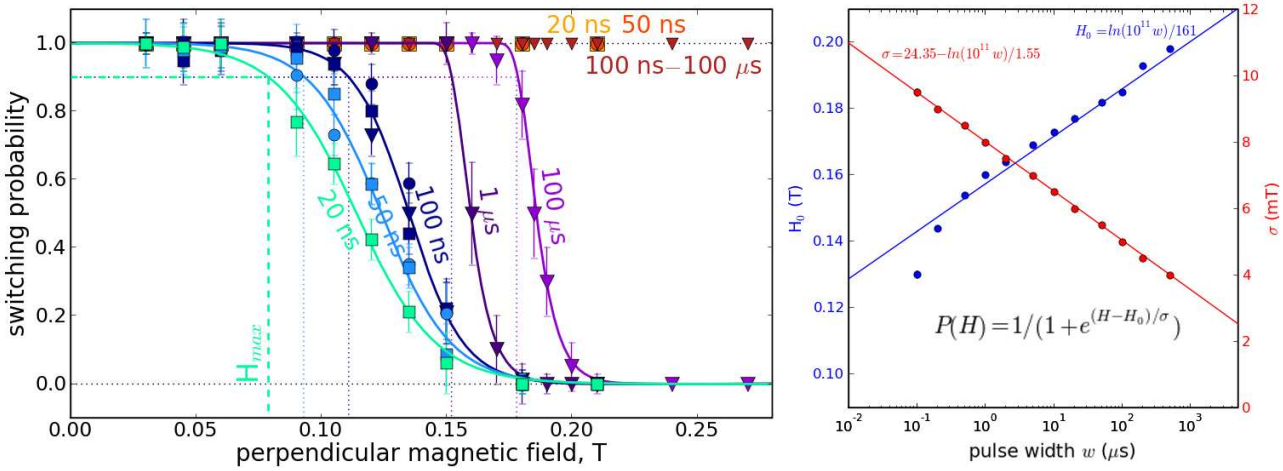

Figure 5.13: Dynamical reversal probability versus the applied perpendicular field for increasing microwave pulse duration. The "easy" switching is represented by orange-red-brown colour symbols while the "hard" reversal are the green-blue-violet symbols. The curves are plotted with a Fermi-Dirac like distribution function, whose adjustable parameters H_0 and σ are plotted on the rigth.

To explain these results, a preliminary phenomenological approach is developed here. The core gyration radius in the gyrotropic mode depends linearly on the microwave field strength h. When the microwave field is increased, the gyration radius increases and a negative dip develops in the surroundings of the core. Roughly, when the out-of-plane magnetisation of this dip reaches $-M_s$, the vortex core reversal occurs. More precisely, this phenomenon happens at a critical core velocity v_c which is universal at remanence [85]. Practically, reaching the reversal means that the vortex core has exceeded a certain critical radius corresponding to $R_c(H_z) = V_c(H_z)/\omega_G(H_z)$. The key here is the dependence of the critical velocity with the bias field [74]. This could explain the fact that the minimum microwave pulse power required to reverse the vortex core is independent of the perpendicular field. It is indeed realistic that the field dependence of $V_c(H_z)$ and $\omega_G(H_z)$ compensate, leaving the critical radius R_c independent from the field H_z. For a given

microwave pulse shape, if the critical radius needed to reverse the core does not depend on the bias field, the strength of the pulse should be the same for all fields.

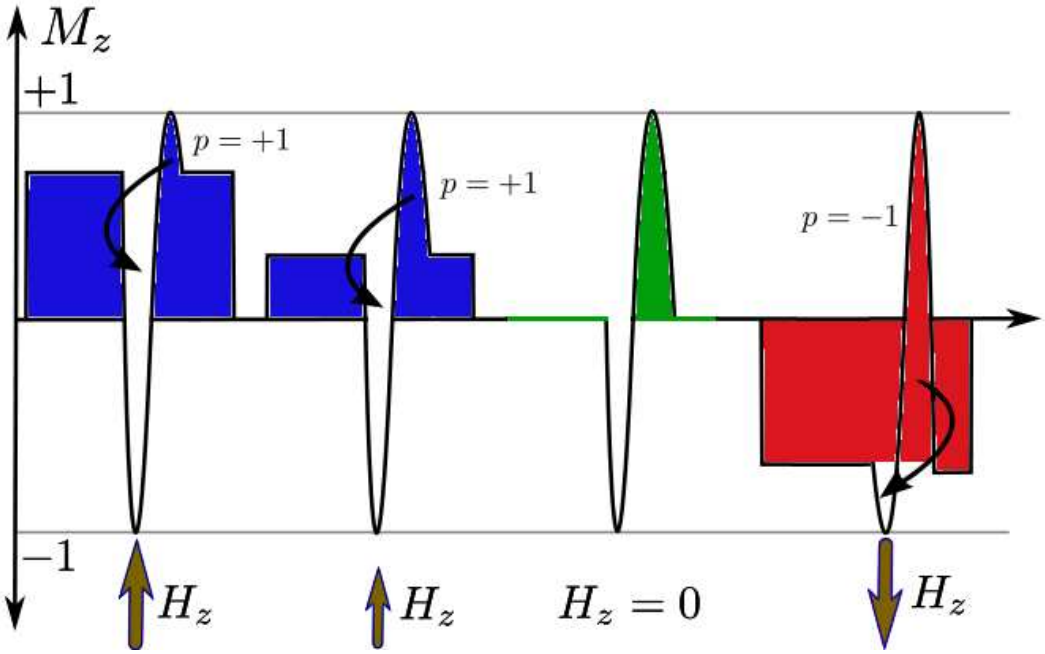

Figure 5.14: Schematic view of the vortex core deformation when the core reaches the critical radius R_c for different perpendicular fields and polarities. The "hard" reversal is sketched in red while the "easy" reversal is in blue.

This result is also supported from the point of view of magnetic energies. In the very simple description of Figure 5.14, the magnetisation of the vortex is sketched at the reversal threshold for different perpendicular field and core polarities. Even if more realistic calculations are needed, it is noticeable that the total exchange energy cost of both the vortex core and the dynamical dip close to the reversal is nearly independent from the field. Therefore, the amount of microwave energy absorbed by the system (the gyrotropic mode) to deform the magnetisation until the reversal should be independent from the initial magnetic configuration induced by the perpendicular field.

Nevertheless, the origin of the probabilistic character for the "hard" reversal remains unknown, and more investigations are needed.

5.5 Magnetic damping in the vortex state

Magnetic dissipation, or damping, is a very important parameter to understand ferromagnetic resonance. The mostly used form was introduced by Gilbert [44] as a damping torque Γ_d with the dimensionless phenomenological parameter α in the Landau-Lifschitz equation of the magnetisation dynamics:

$$\Gamma_d = \frac{\alpha}{M_s} \boldsymbol{M} \times \frac{d\boldsymbol{M}}{dt} \tag{5.8}$$

This term is responsible for the return to equilibrium of the precessing magnetisation toward the internal. Despite a lot of research efforts, the microscopic mechanism responsible for the dissipation in magnetic metals remain are not well described yet.

5.5.1 Linewidth in the linear regime

Nevertheless, it is very important to understand at least experimentally the behaviour of the magnetic dissipation in the vortex state. This is a key parameter that gives a lot of information, for example about the non-linear processes involved in the vortex core reversal.

To begin with, it is important to notice that, contrarily to time resolved experiments, the damping d is not directly accessible in our f-MRFM experiment. It is measured through the *linewidth*, and more precisely the quality factor, of the concerned resonance: $d = \Delta f/2f$. The damping is equal to the intrinsic Gilbert damping α of the material only in the case of the uniform mode in a perpendicularly magnetised thin film (or disc) excited in the linear regime (small oscillation amplitude). In this case, the magnetisation precession is perfectly circular and homogeneous, and one can write: $\alpha = d_{\text{sat}}$. For all other magnetic configurations, the precession is no longer circular and the measured linewidth of the resonance can differ significantly from α.

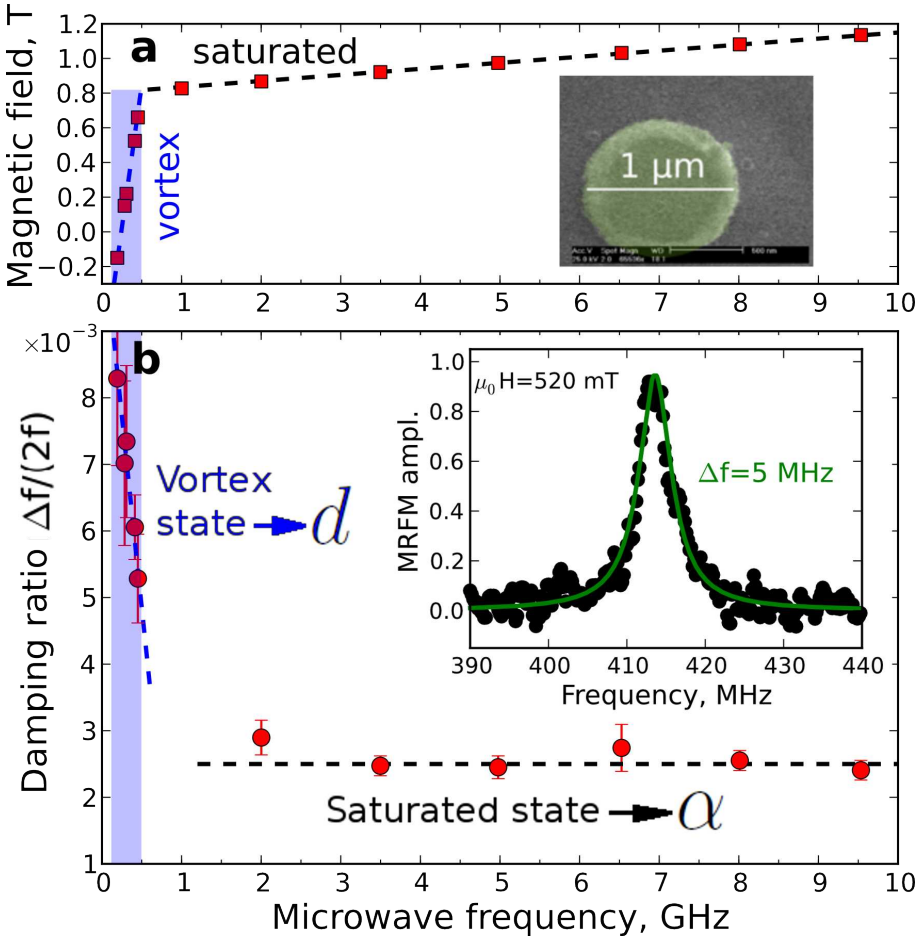

Figure 5.15: a) Resonance field versus microwave frequency for the NiMnSb disc of 1 micron. The abrupt change of slope around 0.8 T marks the boundary between the vortex and the saturated state. b) Comparison between the linewidth of the saturated state and the vortex state corresponding to the points of the panel a). The inset shows a typical resonance line of the vortex gyrotropic mode in the linear regime.

The figure 5.15 presents the different linewidths (actually $\Delta f/2f$, the damping or

inverse quality factor) measured on the NiMnSb disc of 1 micron in diameter. At high frequency (materialised by the dashed line) the linewidth of the perpendicularly saturated state is measured. The value $d_{\text{sat}} = \Delta f/2f = 2.3\ 10^{-3} = \alpha$, constant versus field is found, which confirms the theoretical prediction.

At low frequency (in the blue area) the linewidth of the gyrotropic mode is measured. The gyrotropic resonance line, presented on the inset, is fitted with a Lorentzian function and the linewith at half maximum is extracted, for different perpendicular fields. Because of the complex magnetic structure of the vortex state, the quality factor can be multiplied by a factor 3 at remanence compared to the intrinsic α. The damping term D involved in the Thiele equation of motion was calculated in section 3.3.2.1 of the chapter 3. The effective damping of the gyrotropic mode (in the sense of Gilbert) is related to the Thiele damping by using the rigid vortex model at remanence as follows [53]:

$$d_{\text{vortex}} = -\frac{D}{G} = \alpha\left[1 + \frac{1}{2}\ln\frac{R}{R_c}\right] \tag{5.9}$$

From a mathematical point of view, the factor that multiplies α is a renormalisation due to the non homogeneous vortex structure, taken into account by the Thiele equation. Physically, the particular geometry of the core gyrotropic motion broadens the resonance line. A simple numerical application using a disc radius of $R = 500$ nm and a core radius of $R_c = 10$ nm allows to recover the factor 3 between α and d, observed experimentally. The variation of d with the frequency/perpendicular field is due to the evolution of the core radius, calculated in the section 3.2.2.2 of chapter 3, when the vortex structure is deformed by the bias field. Since the variation of the in-plane magnetisation as well as the size of the core are linear with respect to the perpendicular field, the damping variation should also be linear with H_z. The effect of the variation of the damping parameter on the gyrotropic mode is about 5% for $H_z = Hr$ compared to $H_z = 0$ (whereas the gyrotropic frequency changes by 30%).

In conclusion, the effective linear damping d of the vortex gyrotropic mode, measured through its linewidth, is three times larger than the intrinsic damping α of the NiMnSb at remanence. This renormalisation can be calculated analytically taking into account the non homogeneous structure of the vortex. Finally, the dependence of d on the perpendicular field can be evaluated.

5.5.2 Relaxation time close to the reversal threshold

The analysis of the reversal diagram of figure 5.9, and in particular the calculation of the minimal microwave pulse power E^*_{min} to reverse the vortex core, has provided evidence for a strongly non linear dynamics close to the core reversal. An effective damping d_{forced} has to be introduced to reproduce the experimental data, which is almost 3 times larger than the linear damping d. In this reversal experiment, the gyrotropic core motion is indeed probed with a high microwave excitation field, corresponding to high gyration radius. The magnetisation dynamics is no longer linear at these amplitudes, and this could affect the damping of the gyrotropic mode.

To support the previous measurement and analysis of $d_{forced} = 0.018$, a new experiment, presented on the figure 5.16, was performed in order to really probe the gyrotropic mode decay time close to the reversal threshold. The same perpendicular field of 65

mT is applied on the NiMnSb disc of 1 micron to split the two gyrotropic frequencies corresponding to the core polarity $p = \pm 1$. The experimental procedure is the following:

1. The core polarity is initialised with $p = +1$ ($p = -1$) with a deterministic microwave pulse.

2. A first Π_+ (Π_-) microwave pulse of duration $w = 9$ ns and power $P = -1.8$ dBm is applied with a given frequency f between 160 and 310 MHz. The pulse power is slightly below the minimum power $P^* = -1$ dBm required to reverse the core polarity p for such a short pulse. In practice, the core is driven close to the reversal radius and the microwave is turned off.

3. After a delay τ, which is varied between 0 and 120 ns, a second microwave pulse Π_+ (Π_-) identical to the first one (panels a and b), or with a π phase shift (panels c and d) is applied. In contrast to a single pulse, two pulses separated by a delay can reverse p.

4. The procedure is repeated 10 times for each pixel (f,τ) of the diagrams and the averaged value of the switching events is presented in a blue (red) colour code. Here, a blank pixel means no reversal event.

The striking oscillatory dependence on the pulse carrier frequency and on the delay τ observed in figure 5.16a,b elucidates the phase coherent coupling between the vortex gyrotropic motion and the microwave excitation. During the pulse, the core gyrotropic motion is forced at the microwave frequency. Whereas during the delay τ, the core is damped toward the equilibrium position at its natural gyrotropic eigenfrequency. The core then acquires a phase shift relative to the second microwave pulse. As a result, the efficiency of the second pulse to drive the vortex core to the reversal threshold depends on the microwave frequency and on the delay between pulses in an oscillatory manner (the oscillation period scales as the inverse frequency detuning).

This effect is emphasised by the experiment of the panel c and d where a π phase shift was introduced between the two pulses. The switching regions in the panel a (b) are complementary to these of the panel c (d). Thus, phase control of the microwave excitation can trigger vortex-core switching.

To be more accurate, lets have a closer view to the panels a and b of figure 5.16. When the two microwave pulses are generated at the gyrotropic eigenfrequency ω_G corresponding to the field H_z ($\simeq$ 215 and 250 MHz respectively), the core is always switched for $\tau < 80$ ns. Indeed, there is no phase difference between the core damped motion and the second pulse, which is always efficient. If the pulse frequency is shifted by 15 MHz, a region of low switching probability is observed . The core has roughly acquired a π phase shift with respect to the second pulse, which is less efficient. A region of high switching probability is then recovered when the pulses frequency shift corresponds to a second π phase shift of the core free motion. The opposite effect is observed in the panels c and d, where the phase of the second pulse is artificially shifted by π. Actually, the fringes that are observed are hyperbolas corresponding to $\omega\tau$ =cst.

To extract more details from this experiment, a simple simulation was performed. The philosophy of the calculation is the same as in the figure 5.9b. Using the vortex core position (X, Y) during its transient motion, calculated in the appendix A, the trajectory of the core during the microwave pulse and its decay can be calculated.

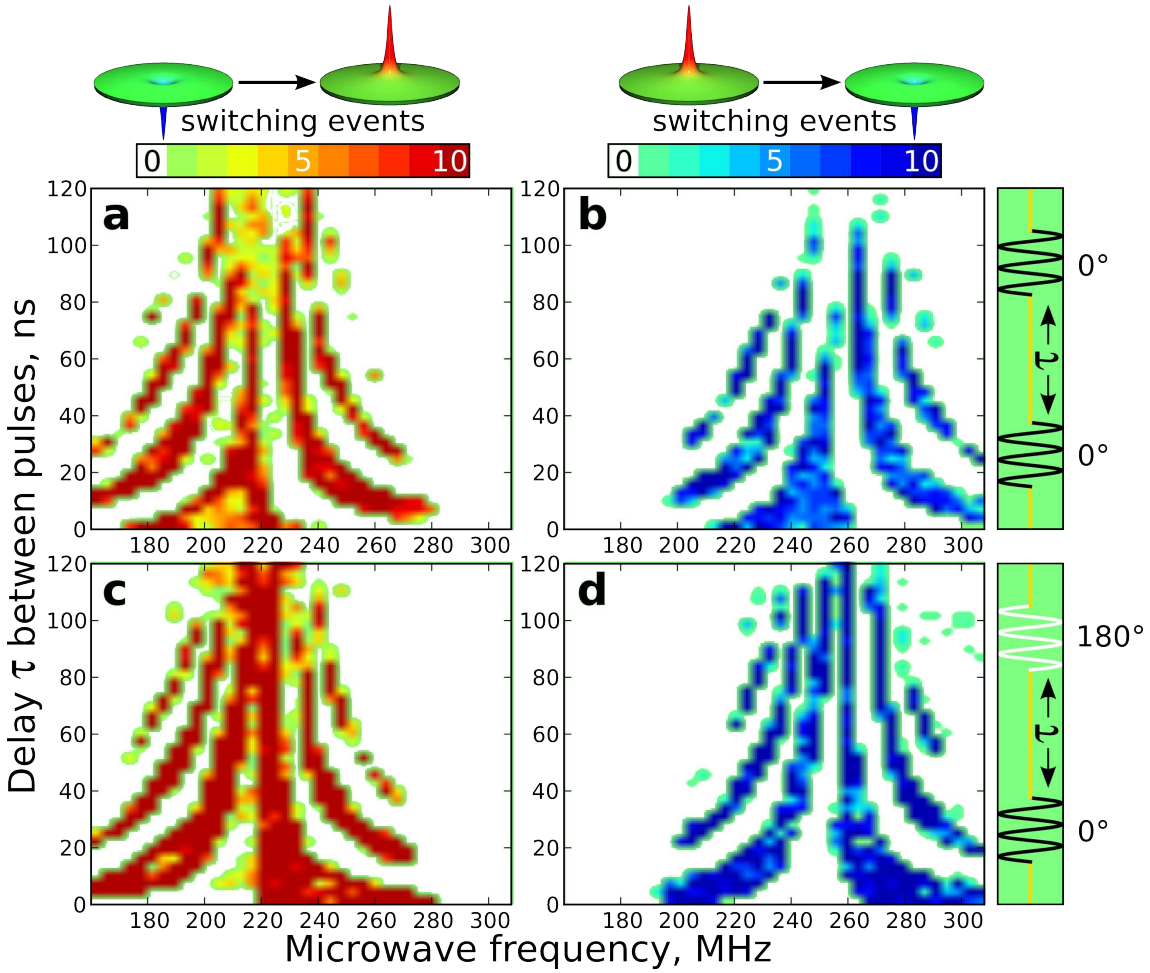

Figure 5.16: Oscillatory dependence of the vortex-core reversal efficiency on frequency and delay between two consecutive pulses. a)-d) Number of switching events out of ten attempts as a function of the delay τ separating the two pulses and of the carrier microwave frequency. The bias magnetic field is $\mu_0 H_z = 65$ mT. The initial polarity state is $p = +1$ in the left-hand graphs (a,c) and $p = -1$ in the right-hand graphs (b,d). As depicted in the right-hand panels, the phase difference between the two microwave pulses is zero in the upper graphs (a,b) and π in the lower graphs (c,d).

The panel b of figure 5.17 presents such trajectories in the disc plane (x, y) after two Π_+ pulses at the gyrotropic f_+. frequency (253 MHz) separated by a 60 ns delay τ. The first microwave pulse drives the core from the centre to the top of the disc, close to the reversal orbit (purple dashed circle): this is the black trajectory. The microwave is turned off and during the delay τ, the core relaxes in a spiral motion back to its equilibrium position, at the gyrotropic eigenfrequency: this is the yellow trajectory. We have then two cases:

1. In the upper graph, the second pulse is applied with the same phase as the first one. Because the microwave frequency is equal here to the gyrotropic frequency, the core motion has the same phase as the second pulse. The coupling to the microwave excitation is therefore in phase and efficient. Then, because the core is not returned to the disc centre during the transient decay, the second pulse amplifies the gyrotropic motion and brings the vortex core over the limit circle (when the second black trajectory crosses the purple star). Consequently, the core is switched

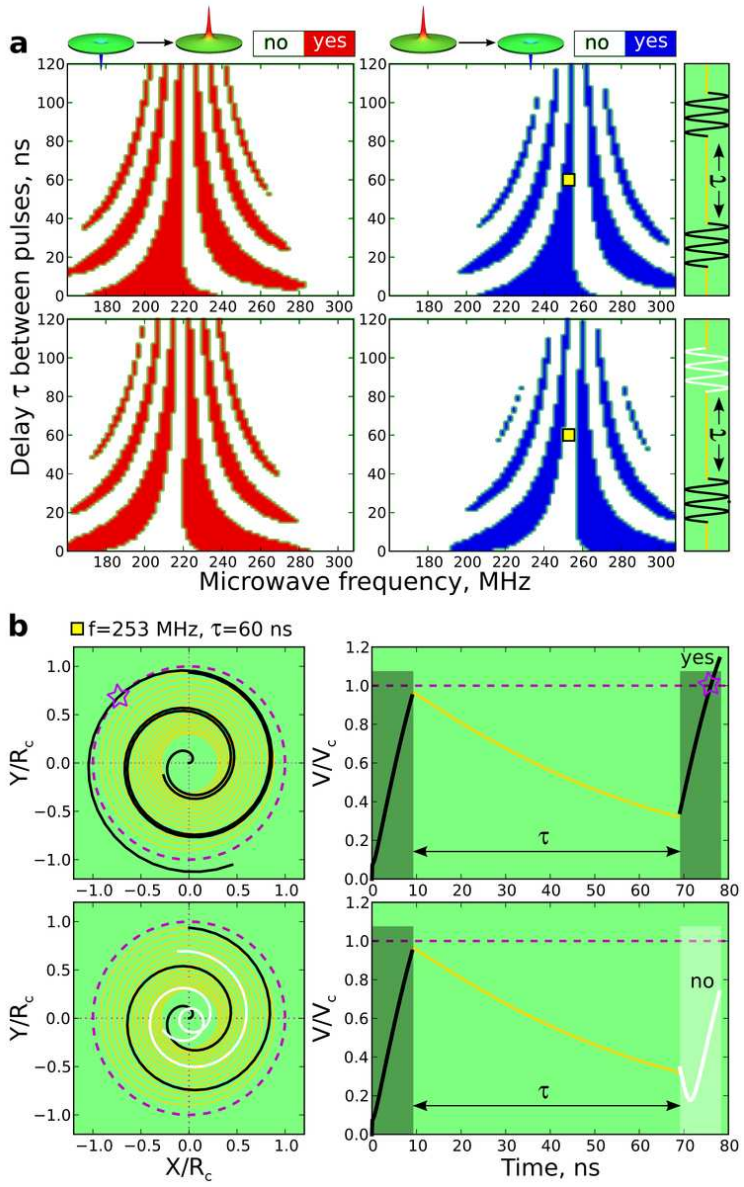

Figure 5.17: a) Numerical calculation of the double-pulse sequences presented in figure 5.16. The best agreement is obtained for a characteristic decay time $\tau_{free} = 53 \pm 6$ ns in the free regime. b) Associated vortex-core trajectory (left) and velocity (right) versus time plotted for two Π_+ pulses with settings $\tau = 60$ ns and $f = 253$ MHz (corresponding to the yellow squares in a). For these settings, the vortex core is reversed when the phase difference between the pulses is equal to zero (top, see star) and not reversed when it is equal to π (bottom).

after the second pulse.

2. In the lower graph, the second pulse is applied with a π phase shift with respect to the first one. When the second pulse is applied, the core first experiences a complicated forced trajectory (in white) to compensate this phase difference. As a result, the core is over-damped before to be accelerated again, and the limit circle could not be reached by the end of the pulse. Consequently, the core is not switched after the second pulse.

By taking the derivative with respect to time, the core trajectories can be converted into speed. The core speed, normalised by the critical speed V_c, is presented during the two pulses process on the right panels of the figure 5.17b. The first pulse brings the core close to the critical speed. The core speed is then slowly decreased during the free decay. Finally, if the second pulse is in phase with the core trajectory, the critical speed is reached and the core is reversed. At the opposite, for the out-of-phase pulse, the core speed is damped in a first time before to be accelerated, and the threshold speed could not be reached.

To perform the simulations presented in the figure 5.17a, the core polarity was initialised to $p = -1$ (on the left) and $p = +1$ (on the right). For both initial polarities, the numerical experiment of the panel b was performed for each pixel (f,τ) and the core was considered reversed if the critical speed was reached by the end of the second pulse.

To be able to reproduce quantitatively the experimental reversal diagrams of the figure 5.16, a non linear damping has to be introduced. A slight asymmetry can be noticed on the four experimental diagrams, which bends the reversal stripes toward the high frequencies. This is again the sign of a non linear dynamics of the core gyrotropic motion close to the reversal threshold. This asymmetry could be reproduced in the simulations with the best agreement by introducing the effective damping $d_{free} = 0.012$.

We recall that in the first reversal experiment of the figure 5.9, the non linear core motion was probed close to the critical speed *forced by the microwave field*, and a parameter $d_{forced} = 0.018$ was introduced to reproduce the data. Here, the gyrotropic motion is again probed close to the reversal but *in the free decay regime* when the core oscillates toward its equilibrium position. This is why the damping fitted here is called d_{free}.

The damping values extracted from the experiments can be converted into decay times that are more physically meaningful: $\tau = 1/d\ \omega_G$. The results are summarised in the following table:

τ_{linear}	τ_{free}	τ_{forced}
80±4 ns	53±6 ns	35±2 ns

Table 5.2: Values of the characteristic gyrotropic mode decay time, calculated from the damping in the linear regime (figure 5.15), in the non linear free regime (figure 5.17) and in the non linear forced regime (figure 5.9).

The analysis of the difference between these values sheds some light on the precise nonlinear nature of magnetic dissipation close to the reversal threshold and on its dependence on the amplitude of the vortex-core motion. This precise measurement of the vortex magnetic damping is actually done for three different core positions (and speed, which is connected) during its gyrotropic motion. In the linear regime, the core is very close from its equilibrium position, the disc centre, and its speed is low. At the opposite, in the forced regime the core is close to its maximal speed V_c and far from the disc centre. Finally, during the free regime the core is probed in between and the fitted damping is somehow the mean of the explored region.

This could be an argument to support the scenario proposed by C.Serpico, presented in the section 3.3.2.5 of chapter 3 and developed in reference [39]. The effective magnetic damping in the vortex state could be a function of the core velocity as $d' = d_{linear} + d_{nl}|\dot{\boldsymbol{X}}|^2$.

It is likely that this assumption could explain part of the non linear red-shift of the gyrotropic resonance line as well.

5.6 The vortex core as a magnetic memory

The magnetic vortex state is a very interesting candidate for designing non-volatile random access memories (MRAM) [30, 84]. We could take advantage of the novel properties described in this chapter to build and optimise such applications [108, 77].

The key idea of such memory is to use the two vortex core polarities $p = \pm 1$ as a magnetic bit, that can be easily read spectroscopically and written via the dynamical reversal. The specific design of an efficient MRAM must satisfy several technical points, which are fulfilled by a vortex based memory.

1. *Non volatility*: The numerical information must be stored as bits and kept in a physical system that is stable in time and versus any perturbations, such as temperature, magnetic fields, chocks... Moreover, the information should be stored in a passive device. The magnetic vortex is the remanent and extremely stable state of micro-discs made of magnetic materials, for example NiMnSb. The core polarity used as a bit is stable over temperature (the Curie temperature of NiMnSb is $T_c = 730$ K) and magnetic fields, since the static reversal field of the core polarity is typically in the tesla range. The core can be expelled from the disc by a smaller in-plane field ($\simeq 0.1 - 0.2$ kOe), but smaller disc's radius stabilise the core since the static susceptibility decreases.

2. *Low energy consumption*: The main advantage of the vortex based memory is the small magnetic volume involved in the data storage. The unit cell is a disc of hundred nanometres in diameter, but the relevant part is the vortex core that is only 10 nanometres in diameter. The writing process, which is the limiting process in terms of energy consumption, only involves the reversal of the core volume, which is very small. The resonant character of the switching reduces the energy cost as well, since a microwave field of only a few Gauss is needed to reverse the polarity of the core. Moreover, it will be shown that the reading process only requires a bias field of the order of the linewidth, that is to say few tens of Gauss.

3. *Integrated fabrication process*: This magnetic memory can easily be realised using the standard planar micro and nano fabrication process: thin film growth and lithography techniques are now well implemented in the industry.

4. *Fast operation time*: A crucial point is to be able to read and write the solid state bits as fast as possible. This is a key advantage of the vortex. The reading process can consist in measuring spectroscopically the core polarity via its gyrotropic frequency. Moreover, the writing is done by flipping the core polarity taking advantage of the resonant dynamical reversal. As shown previously, microwaves pulses at the gyrotropic frequency can switch the polarity in less than 50 ns. This is of course slow, and studies have demonstrated the core reversal with 100 ps pulses [134, 84], the price to pay being more energy consumption.

The proof of concept of our vortex based MRAM will be made with the NiMnSb disc of 1 μm in diameter and 44 nm thick. The disc, which is in the vortex state at remanence,

represents a binary information coded with its core polarity: for example $p = +1$ is the 0 and $p = -1$ is the 1.

Taking advantage of the high dynamical susceptibility of the vortex state, the "read/write" process will be done resonantly using the gyrotropic core motion. Circularly polarised microwave fields could be used to discriminate between the two core polarities, but this field geometry is rather complicated to create. The key idea is to produce a controlled splitting of the gyrotropic frequencies, depending on the core polarity, with a perpendicular bias field. The mechanism of this frequency splitting was explained in detail in the previous section and its value can be evaluated using equation (5.2). To design a practical memory cell it is necessary to choose the static magnetic field H_z in such a way that the field-induced gyrotropic frequency splitting exceeds the linewidth Δf of the gyrotropic mode, which can be approximately expressed as $\Delta f = d\omega_G/2\pi$. Here, d is the damping in the vortex state studied in the section 5.5. Thus, the minimum perpendicular bias field is given by the expression:

$$H_z \geq \frac{1}{2} d H_s \tag{5.10}$$

It is crucial to select a magnetic material with a low damping to minimise the perpendicular field strength. The NiMnSb is well suited with its intrinsic damping $\alpha = 2\ 10^{-3}$. The aspect ratio $\beta = L/R$ could also be increased as this leads to the decrease in the saturation field H_s.

For this specific experiment, the perpendicular field is set to 65 mT. The splitting of the gyrotropic frequencies is presented in the figure 5.18a. The spectra were recorded by the f-MRFM for each core polarity, revealing a splitting of about 40 MHz between f_+ and f_-. It is then very easy, using a simple linearly polarised microwave field, to discriminate between the two core polarities.

The "reading" procedure is illustrated on the figure 5.18c. A weak microwave field is applied to the sample at the frequency f_+, which excites the gyrotropic motion in the linear regime. The microwave frequency chosen corresponds to the $p = +1$ gyrotropic eigen-frequency: $f_+ = 254$ MHz. The signal being given by the f-MRFM cantilever amplitude, the microwave field is here modulated at the cantilever frequency. The result is the following: if a cantilever deflection is measured, the gyrotropic mode with the frequency f_+ is excited and therefore the core polarity is +1 (red dots). At the opposite, if no signal is detected, the gyrotropic motion is not excited at the frequency f_+ and therefore the core polarity is -1 (blue dots).

The writing process in a dot with initial core polarity equal to $p = +1$ is illustrated by figure 5.18b. A strong Π_+ pulse of duration $w = 50$ ns, frequency f_+ and power $P = 100\ \mu$W (corresponding to a microwave magnetic field of $\mu_0 h = 3$ mT), is able to reverse, or "write", the core dynamically, as explained previously. The core reversal is confirmed on the panel b by the change of the MRFM signal after the pulse. A second Π_- pulse at the frequency f_- with the same characteristics reverses the core back to $p = +1$. The process can be repeated without any error since it was shown that the core reversal is deterministic after such pulses. To emphasise the robustness of the procedure, a Π_- (Π_+) reversal pulse is applied to the opposite polarity $p = +1$ ($p = -1$) . As shown in the right part of the figure 5.18b and 5.18c, the polarity remains unchanged after a "wrong" pulse.

The first step towards a real application is to build a dense array of these magnetic discs. To avoid the crosstalk during the "read/write" process of a particular cell, the

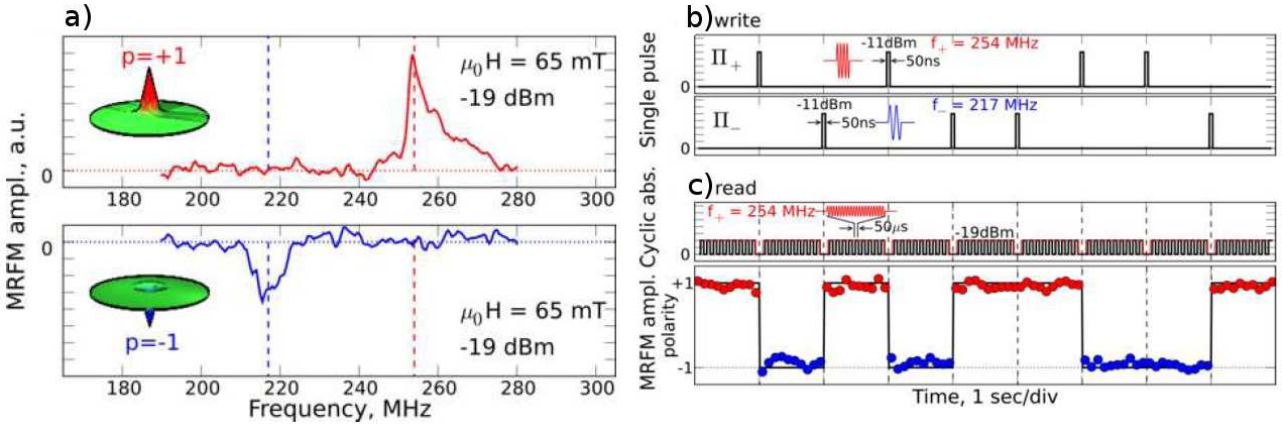

Figure 5.18: a) MRFM spectra of the gyrotropic mode performed by varying the microwave frequency at a fixed perpendicular field of 65 mT. A resulting splitting of 40 MHz is observed between the opposite core polarities. b) and c) "Write" and "read" schemes of the vortex MRAM. The polarity is determined by the f-MRFM amplitude while the core reversal is achieved with short microwave pulses.

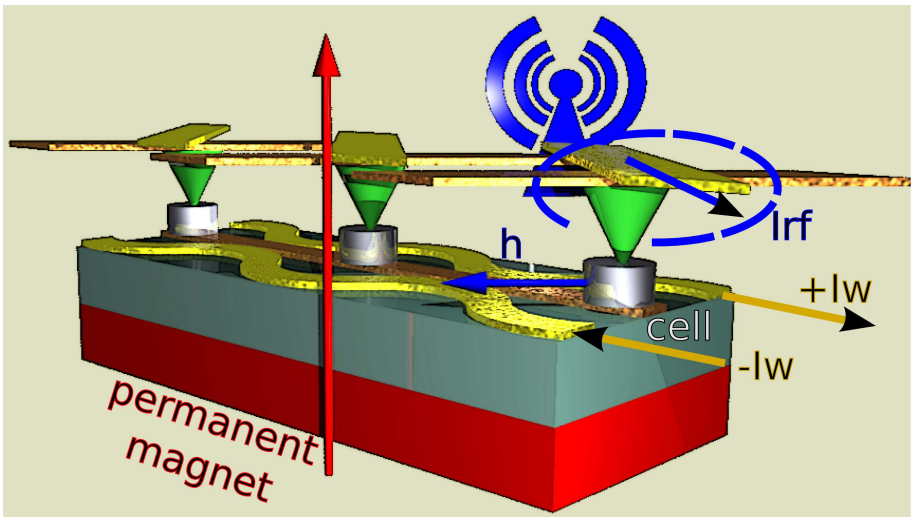

Figure 5.19: Proposed solid state design of the frequency controlled magnetic memory.

discs are placed on a square lattice separated by 10 μm. Moving the MRFM probe to the neighbouring dots during the reading sequence allows one to check that the core polarity in adjacent dots (situated 10 μm away) is unaffected by the core reversal process in the selected dot. This is because the stray field produced by the f-MRFM probe is able to localise the resonance in the dot placed underneath. Thus, it demonstrates that the frequency-selective deterministic manipulation of the binary information can be achieved locally.

Although the 1 μm NiMnSb device can be used as a prototype for the development of a frequency-controlled magnetic memory, a series of improvements can be imagined to make a more practical solid-state variant, presented in figure 5.19. First of all, it would be useful to increase the dot aspect ratio to $\beta = 1$ in order to reduce the dot saturation field H_s, and, therefore, the minimum perpendicular bias magnetic field to $\mu_0 H_z = 5$ mT. In this case, a permanent magnet pinned perpendicularly and placed underneath

the substrate could produce a static field of about 20 mT, sufficient to ensure reliable operation of the memory.

The magnetic discs, arranged in a square lattice, have to be addressed separately. This could be achieved using a combination of dc and microwave current lines (I_{rf} and $\pm I_W$ in the figure 5.19) intersecting on each dots. A dc current of only 5 mA could produce an additional static Oersted field of 10 mT on the discs next to the current line and the gyrotropic frequency inside these discs will experience an additional splitting. The microwave line placed at 90 degrees can then address a single bit with the proper frequency.

The f-MRFM reading and writing process have of course to be replaced by a full solid state method. The reading could be done by local electrical detectors of the absorbed power.

5.7 Higher order spin wave modes in the vortex state

5.7.1 Micromagnetic simulations

The spin wave spectrum of the vortex state is also composed of higher order modes having azimuthal and radial symmetries, as explained in the last section of chapter 3. Interestingly, the gyrotropic mode is coupled to their dynamics. The core reversal can even be achieved by exciting these modes at high amplitude. Therefore, understanding their dynamics is very important.

The transition between the saturated state, described in chapter 2, and the vortex state is well illustrated by the micromagnetic simulations performed in reference [23]. The dynamic susceptibility tensor $\chi_{i,j}(\boldsymbol{r},\omega)$ $(i,j=x,y,z)$ of a permalloy disc ($L=50$ nm, $R=500$ nm) in the vortex state is calculated using a home made software. Due to the rotational symmetry of the element, the in-plane susceptibility is expressed using the circular polarisation basis resulting in two elements $\chi_\pm$ defined as $\chi_\pm = 1/2[(\chi_{xx}+\chi_{yy}) \pm (\chi_{yx}-\chi_{xy})]$. The choice of the in-plane components allows the modes excited to be reproduced with an in-plane uniform microwave field linearly polarised. This quantity is calculated versus the perpendicular field from the saturated state to the vortex state having a polarity $p=+1$. The result is displayed on the figure 5.20.

Above the saturation field (around $H_s = 9$ kOe), the radial modes $(l=0,m)$ described in the chapter 2 are seen in the χ_- component. The azimuthal modes $(l,m=0)$ are not seen since their symmetry doesn't couple to a spatially homogeneous in-plane microwave field. Below H_s, the low frequency gyrotropic mode is identified as $0-$. It has the expected dependence versus field and couples only to χ_- because of the particular sense of rotation of the core.

At higher frequency, several spin wave modes can be seen in the vortex state. They exhibit an opposite dependence with the perpendicular field. In contrast to the saturated state, they correspond to azimuthal modes. The magnetisation of the vortex is curling in-plane and an in-plane excitation field could not couple to the radial modes. The azimuthal modes can travel either clockwise or counter-clockwise around the disc, this is reason why they can be seen in both χ_- and χ_+. Interestingly, the modes having indices $l=\pm1,2...$ are not degenerate in energy, as shown on the figure 5.20 for the modes $1\pm$ and $2\pm$. This is the signature of the non linear interaction with the vortex core, described in the

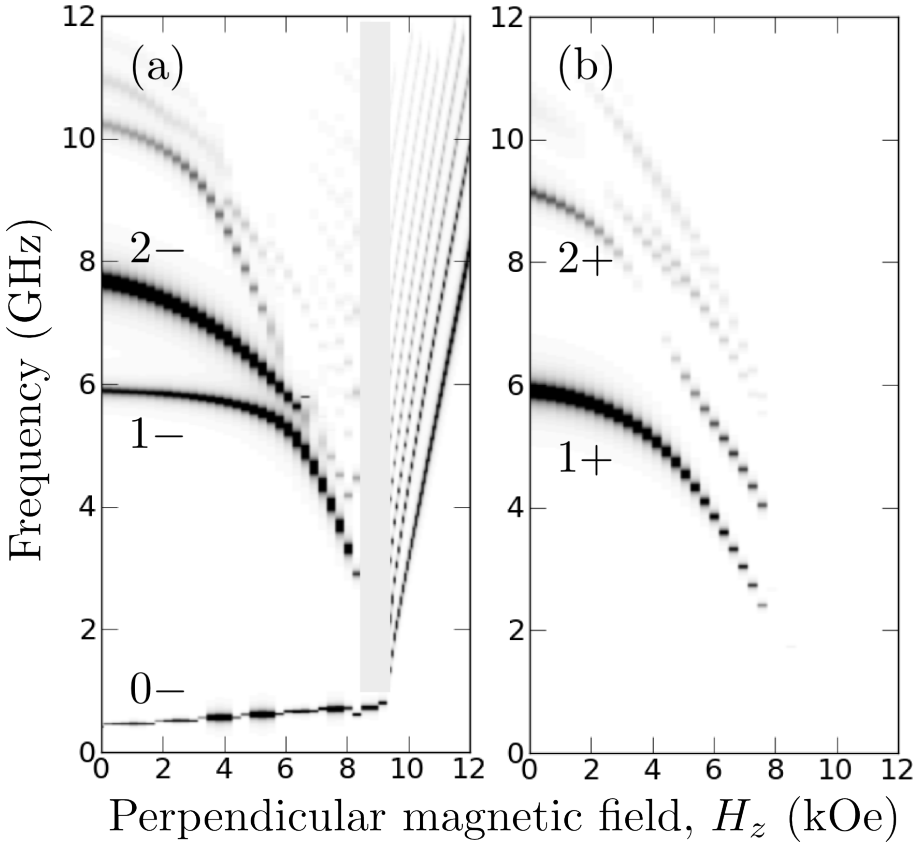

Figure 5.20: In plane dynamical susceptibilities a) χ_- and b) χ_+ for a downward field sweep and a positive field branch ($p = +1$). The high values are in black and the low ones in light gray.

previous section.

5.7.2 Experiments

These modes were experimentally studied by f-MRFM on the NiMnSb disc of 1 μm in diameter and 44 nm thick. As explained in the theoretical section, the spatially uniform microwave field delivered by our antenna has a non zero overlap only with the vortex azimuthal spin wave modes. Only these modes could be investigated in this study, but the f-MRFM gives access to their dependence upon a perpendicular applied field.

Following the numerical simulation presented on the figure 5.20, spectra at constant frequency have been performed by sweeping the perpendicular bias field 10 kOe down to zero field. The raw spectra are presented on figure 5.21a. The saturation field of the NiMnSb disc being $H_s \simeq 8.1$ kOe, we have access to the spin wave spectrum in both saturated and vortex states.

In the saturated state, the microwave excitation only couples to the radial spin wave modes described in chapter 2. The first bright mode is the uniform mode ($l = 0, m = 0$) and the following are the modes ($l = 0, m = 1, 2, 3...$). In the vortex state, the shape and behaviour of the modes are completely different. Their dispersion relation is plotted on figure 5.21b. The lowest frequency mode is the gyrotropic mode, which field evolution follows the predicted dependence. Then, four well resolved higher order modes are seen in the spectrum. The frequency of these modes decreases with the applied field, and goes to

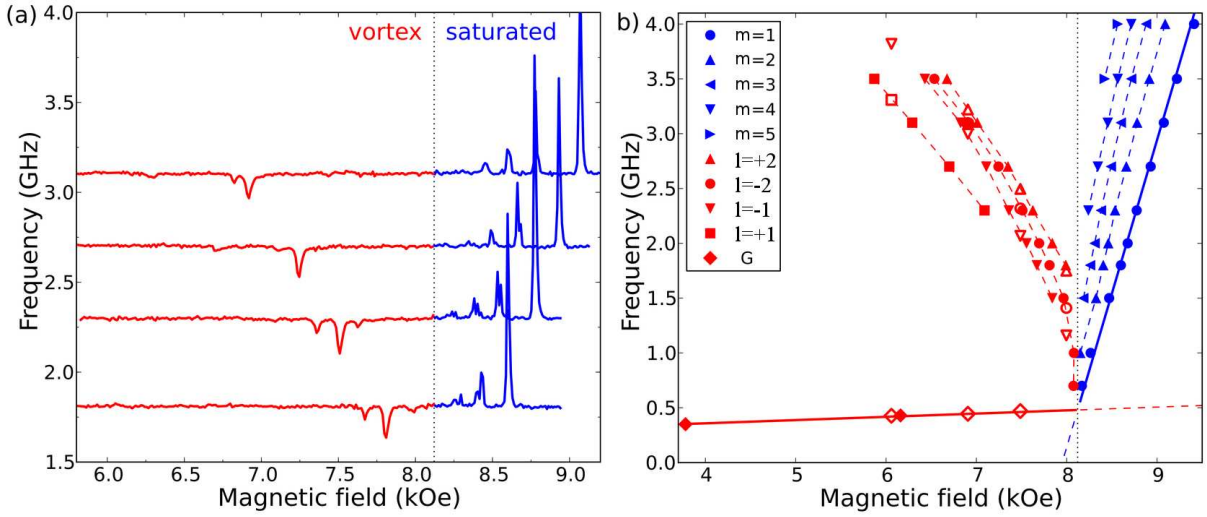

Figure 5.21: a) Resonance spectra on the individual disc of NiMnSb of 1 micron in diameter. The dotted vertical line displays the saturation field $H_s = 8.1$ kOe of the NiMnSb disc, separating the vortex state from the saturated state. b) Dispersion relation of the different spin-wave modes observed experimentally. Solid symbols have been obtained from field-sweep spectra at fixed frequency. Open symbols have been obtained from other frequency-sweep spectra at fixed magnetic field. Solid lines in the saturated and vortex states ($H_z < H_s$) are theoretical predictions, respectively. Dashed lines are guides to the eye.

zero at the saturation field. This negative slope of the frequency-field dispersion relation is related to the decrease of the effective field probed by these modes in the unsaturated state as H_z increases. It should be noted that the f-MRFM signal corresponding to these modes in the vortex state is negative, meaning that the averaged component of magnetisation M_z along the applied field H_z increases at resonance, in contrast to the standard case observed in the saturated state. These modes are identified with the azimuthal spin waves $l = \pm 1$ and ± 2. Contrarily to the simulation presented figure 5.20, the two chirality are excited at the same time. This is because the experimental microwave field, which is linearly polarised, is the sum of two contra-rotating circularly polarised fields.

Even if the frequency of these modes are not well understood yet, there is a clear continuity between the spin wave modes of the saturated state and the vortex state. The static behaviour of the vortex structure under a perpendicular field induces a reversal of the slope $\omega = f(H_z)$ of the modes. Moreover, as predicted by the theoretical analysis and the numerical simulations, the degeneracy of the azimuthal modes is lifted by the presence of the core in the vortex state.

5.8 Conclusion

The experimental results presented in this chapter echo the theoretical description given in the previous chapters. Using the f-MRFM spectroscopy presented in the chapter 4, the spin wave spectrum of isolated NiMnSb discs in the saturated state were measured. The sets of eigenfrequencies could be well reproduced by the theory developed in chapter 2, which allowed us to extract some of the physical parameters of the sample such as discs real diameters, magnetisation, damping...

Switching to the vortex state, the gyrotropic frequency was measured and its simple dependence versus the disc diameter was confirmed. Then we have shown the striking effect of a perpendicular bias field on the gyrotropic dynamics. The degeneracy in frequency between the two polarities $p = \pm 1$ is lifted by the deformation of the vortex and a Zeeman like splitting is observed. It is well explained by the calculation made in chapter 3.

Particular attention was then focused on the non linear dynamics of the gyrotropic mode, leading to dynamical core reversal. After verifying the universality of the critical speed V_c needed to reverse the core, we have demonstrated the ability to switch the core resonantly with a single microwave pulse optimised in energy. The interest of combining the Zeeman like splitting introduced by a bias field and the bi-stability of the core was shown for the future realisation of vortex based magnetic memories. Nevertheless, open questions remains about the evolution of the core reversal under a strong perpendicular field. If the dependence of the critical speed is now understood, the physical origin of the asymmetry between the "hard" and "easy" reversal has to be clarified.

This study of the core reversal was also an opportunity to study in a controlled manner the non linear dynamics of the gyrotropic mode at high amplitude. Using two independent experiments, we have shown that the relaxation time of the mode is increased by a factor 2-3 when it is probed close to the reversal threshold. This feature could attributed to the coupling between the gyrotropic mode and the azimuthal spin wave developing in the vortex plane.

This is why we have finally characterised the the spin waves of higher order in the vortex state. Unfortunately, the symmetry of our microwave excitation can only couple to the azimuthal modes. But we were able to measure the splitting of the modes having opposite indices ($l = \pm 1, \pm 2...$), which is the experimental signature of the coupling with the gyrotropic mode.

Chapter 6

Experimental results II: coupled dynamics of magnetic dots

In this chapter, the role of the dynamical magneto-dipolar interaction in the collective dynamics of coupled magnetic discs is investigated. Pairs of identical FeV nano discs with various separation will be measured by f-MRFM. Evidences of the collective magnetisation dynamics in these nano structures are presented. The role of the geometry in the dynamics of these dipolarly coupled pairs is particularly highlighted. Finally, this analysis is extended to more complicated systems: four neighbouring FeV discs and an asymmetric pair of NiMnSb discs.

6.1 Introduction

The fundamental role of the magneto-dipolar interaction in describing the magnetisation dynamics of magnetic systems was already emphasised in both the saturated and the vortex cases. Its dominant contribution to the calculation of the spin wave spectra of nano objects was introduced in the case of a single disc in the chapter 2 and 3.

But to improve the fundamental understanding of the magnetisation dynamics as well as to realise practical applications, it turns out to be crucial to study arrays of these magnetic nanostructures [137]. By engineering their design, the properties of such arrays do not reduce to the sum of the individual behaviours. The elements are strongly interacting and collective properties are generated. This is, for instance, the purpose of magnonics [81]. The aim of this emerging field of magnetism is to understand and control the spin wave properties in periodically nanostructured magnetic materials. With these structures it becomes possible to control spin waves in order to use them for information processing or data storage applications. Moreover, in the field of spintronics, the synchronisation of spin transfer nano-oscillators closely packed in arrays is also a promising way to improve their spectral characteristics [46, 10].

Among all the coupling mechanisms (spin pumping, spin waves, magneto-exchange...), the magneto-dipolar interaction is a key element to understand interacting magnetic elements since it is a long range interaction. Moreover, regarding the nanometric size and the shape of the elements of the arrays as well as the large magnetisation of the magnetic material commonly used, this interaction becomes dominant.

The static dipolar interaction between each elements of the array obviously shapes the static configuration of the magnetisation in the whole array. But the role of the dynamic interaction is more striking: it allows a collective dynamics to appear in the array. Studying this tiny component is usually difficult from an experimental point of view since it requires to reach a regime where it is dominant. In order to be measured, the strength of the dynamical coupling should exceed both the deviation range of eigenfrequencies between coupled objects and the resonance linewidth.

6.2 Dynamical dipolar coupling in a pair of magnetic nano-disks

The main questions to be addressed would be: how the static interaction modifies the magnetisation of the system and in particular how the dynamical part of the magnetisation of each structure can be coupled to give rise to a collective dynamics.

This problem being non trivial, we decided to perform a preliminary study using only one pair of magnetic discs (single ferromagnetic layer) placed nearby laterally. Moreover, this model system will be first studied in the perpendicularly magnetised state before moving to the vortex state. As explained at the beginning of the chapter 5, the saturated state of one nano-disc is well controlled. The main physics of the dipolar coupling will be explored within this state before exploring more complicated magnetisation arrangement.

As detailed in the chapter 2, the problem of the magnetisation dynamics in two ferromagnetic discs placed in the vicinity of each other was solved analytically. If the frequencies of the magneto-static modes excited in each discs are $\omega_{1,2}$, the collective dynamics is

composed of an anti-binding A and a binding B mode, whose eigenfrequencies are:

$$\omega_{A,B} = \frac{\omega_1 + \omega_2}{2} \pm \sqrt{\left(\frac{\omega_1 - \omega_2}{2}\right)^2 + \left(\frac{\Omega}{2}\right)^2} \tag{6.1}$$

where $\Omega^2 = 4\gamma^2 h_{1\to2} h_{2\to1}$ is the coupling strength, corresponding to the frequency splitting at the coupled mode anti-crossing. The cross term $h_{i\to j}$ represents the demagnetising stray field produced by the oscillating component of the magnetisation in the i-th disk projected along the local deviation vector inside the j-th disk and averaged over its volume.

The key point is to measure accurately the coupling strength Ω between discs, which is the key parameter of the coupled dynamics. Experimentally, this value corresponds exactly to the coupled modes splitting $\omega_A - \omega_B$ at the maximum of the coupling, i.e. when $\omega_1 = \omega_2$.

To realise this measurement, two essential points are needed:

1. Ω has to be maximised and measured. We have to choose a ferromagnetic material for the sample that maximise M_s while keeping a low damping α which produces narrow linewidth. Moreover, the geometry should bring the sample in the strong coupling regime.

2. To find a way to continuously tune and detune the relative resonance frequencies between two nano-discs. As in any standard quantum mechanical experiment on a coupled two levels system, a parameter has to be varied to reach the coupling maximum. Moreover, for long wavelengths, the spin wave eigen-frequencies of our oscillators are very sensitive to small imperfections in the confinement geometry inherently linked to uncertainties of the nano-fabrication process. These frequency differences have to be compensated to perform an accurate measurement.

6.2.1 Magnetic sample

In order to perform this study on dipolar coupling, a new sample was prepared. For this purpose, the dipolar field radiated by the ferromagnetic discs should be increased to maximise the investigated effect: the coupling strength Ω has to be maximised to exceed the resonance linewidth as well as the the deviation range of eigen-frequencies between coupled objects. The demagnetising field $\boldsymbol{H_d}$ of a disc is proportional to its saturation magnetisation M_s and demagnetising tensor $\widehat{\boldsymbol{N}}$: $\boldsymbol{H}_d(\boldsymbol{r}) = -4\pi M_s \widehat{\boldsymbol{N}}(\boldsymbol{r})$. First of all, we could play on the saturation magnetisation M_s.

The chosen material is a ferromagnetic alloy of Iron with 10% of Vanadium (Fe-V). Its saturation magnetisation is very large, around $4\pi M_s = 18$ kG, but the intrinsic magnetic damping is still in the same order of magnitude as the NiMnSb. This is very important for our spectroscopic f-MRFM detection: to be detected, the dynamical coupling Ω has to be larger than the resonance linewidth.

The geometry of the samples can be adapted to maximise the dipolar interaction as well. The dipolar field strength, modelled in the demagnetising tensor, is a pure function of the sample geometry: it only depends on the relative size. In particular, the coupling strength remains unchanged if all the dimensions of the sample are scaled up or down with the same geometrical factor. For instance, the demagnetising tensor of a magnetic disc only depends on its aspect ratio L/R thickness over radius.

Nevertheless, before choosing the final dimensions, intrinsic constraints have to be considered. First, the degeneracy between spin wave eigenmodes must be lifted. It has been shown in the theoretical description of chapter 2 and experimentally in the chapter 5 that the frequency splitting between spin wave modes is strongly dependent on the lateral confinement. In that sense, the lateral size of the discs should be in the micron range to get a sufficient splitting (see for instance the spectrum of figure 6.4). Higher order modes (harmonics of the fundamental mode either along the diameter or the thickness) have weaker dipolar cross-coupling, because their averaged transverse dynamic magnetisation is smaller. As the dimensions of the disc increase, the splitting produced by the confinement between higher order modes decreases. Once this splitting becomes of the order of Ω of the uniform mode, the anti-crossing effect washes out, as the higher order modes will start to cross in the gap region.

Moreover, the measurement of the dynamical coupling requires a magnetic material with a low damping, which means a crystalline material. From a technical point of view, it is very difficult to grow thick Fe-V films with a high crystalline quality. Therefore, the thickness of the discs will be limited to a few tens of nanometres.

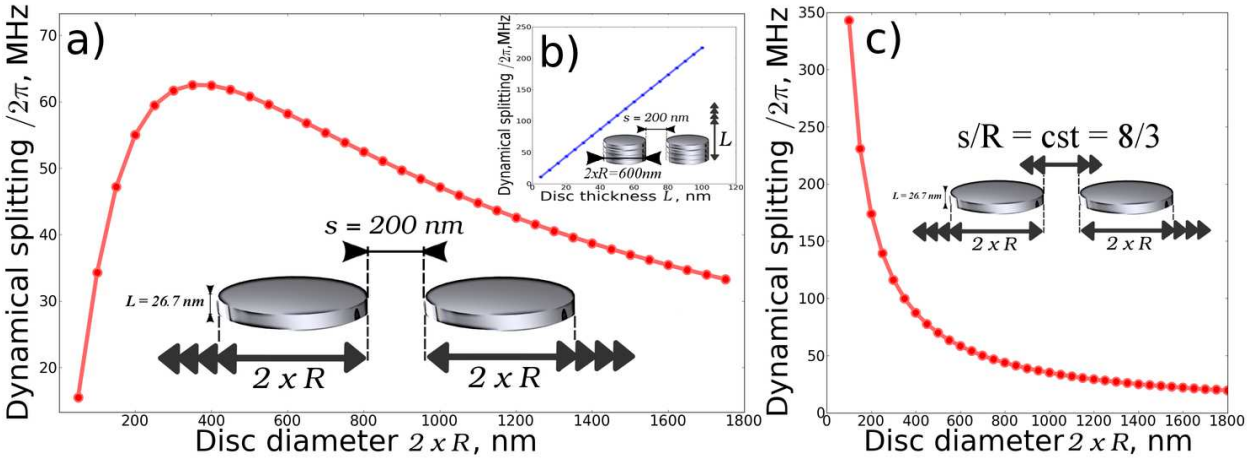

Figure 6.1: Dependence of the dynamical splitting Ω on the geometrical parameters of a discs pair. a) The thickness and the separation are kept constant while the discs diameter is varied. b) The thickness is varied at fixed radius and separation. c) The separation s and radius R are varied with a constant s/R ratio.

Using the theory of the chapter 2 (see equation (2.58)) the geometrical dependence of the dynamical splitting Ω for a disc pair can be calculated for the lowest spin wave mode. First of all the diameter of the discs is fixed at $2 \times R = 600$ nm as well as their edge to edge separation $s = 200$ nm, while the thickness is varied. The figure 6.1b shows that the thickest disc pair has the highest Ω. Nevertheless, we have seen that this parameter is constrained by the material quality required for this experiment. In practice, the Fe-V films we have used are 26.7 nm thick.

We can also play on the disc diameter within a certain range while the disc separation remains fixed at $s = 200$ nm. The figure 6.1a shows that, choosing the previous thickness, there is an optimum in the disc diameter around $2 \times R = 400$ nm. Finally, in the figure 6.1c the ratio separation over radius is kept constant which highlights that, by keeping the thickness constant, Ω is increased if the lateral dimensions are decreased.

One has to keep in mind that the intrinsic frequencies of the two discs must be very

close to be able to see a collective dynamics. In that sense, if the diameter is too small, the intrinsic frequencies $\omega_{1,2}$ could be too dependent of the imperfection of the fabrication process. It is also very important to avoid magnetic contacts between discs, and for lithography reasons, the separation should not be smaller than 100 nm.

Finally a good compromise is met with discs of diameter 600 nm and thickness 26.7 nm, while the pair separation is in the hundreds of nanometres range. As evidenced by the figure 6.1, it ensure a dynamical splitting around 55 MHz, which can be easily measured experimentally.

6.2.1.1 Nano-fabrication

The Fe-V samples were prepared at the University of Nancy and we are greatly indebted to K. Mitsuzuka, D. Lacour, M. Hehn, S. Andrieu and F. Montaigne for this beautiful and very precise work [16, 61, 95].

A 26.7 nm film of Fe-V (10% of V) was deposited by co-evaporation of Fe and V on an MgO(001) substrate by molecular beam epitaxy operating with a base pressure of $8\text{x}10^{-9}$ Pa.

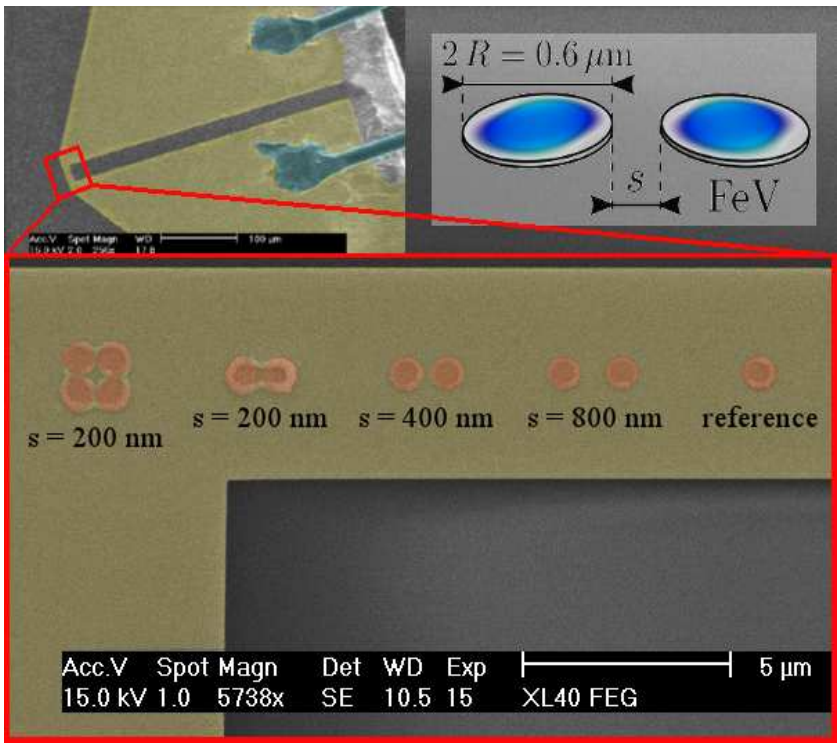

Figure 6.2: Iron Vanadium pairs of discs. The thickness is 26.7 nm for a diameter of 600 nm. Three different edge-to-edge separation s are chosen. The four disc arranged in square are a trial toward more complicated geometry. The yellow stripe is the constriction of the microwave antenna grown on top, as seen on the top inset.

The film is patterned into discs by e-beam lithography and ion milling techniques. As shown on figure 6.2, the geometrical pattern consists in three sets of nearby disks pairs having the same nominal diameter 600 nm but different edge-to-edge separations: s = 200 nm, 400 nm and 800 nm. An empty interval of 3 microns separates each set to avoid cross coupling phenomena. On the right, a single disc of 600 nm in diameter was patterned as

a reference oscillator. Finally, as a trial towards more complicated arrays, four discs with the same diameter arranged in square were prepared on the left.

The discs were then capped with a 50 nm layer of an insulating resist (SiO_2) and the 300 nm thick gold microwave antenna, described in the section 4.3.4 of chapter 4 and shown in the inset of figure 6.2, was patterned on top. This sample, connected to the microwave source, is introduced in the f-MRFM and the magnetic probe is placed above at an altitude of 1.8 microns.

The discs are perpendicularly magnetised (along the $\boldsymbol{u}_z$-axis) by an external field of 17.2 kOe. This field is sufficient to magnetise all the discs in the saturated state. Unfortunately, the external field is slightly tilted in the x direction by the polar angle $\theta_H \simeq 2\hat{A}^\circ$. Our current setup does not allow in-situ correction of this small misalignment. This parameter will be taken into account in the theoretical description of our experiments.

6.2.1.2 Magnetic properties

The magnetic properties of the Fe-V film were studied by cavity FMR, with the same procedure as for the NiMnSb film of the previous chapter. The results are summarised in the following table 6.2.1.2:

M_s(emu.cm^{-3})	H_a(G)	α	γ(rad.s^{-1}.G^{-1})
1353	-500	2×10^{-3}	1.76×10^{7}

Table 6.1: Fundamental magnetic parameters of the Fe-V thin film: saturation magnetisation, fourfold anisotropy field, damping and effective gyromagnetic ratio.

A complete standard MFM study was performed at zero field to investigate the vortex state in these discs [95]. The same Fe-V film was used, but patterned in larger discs of diameter 3.15 microns. An MFM image from this study is presented on the figure 6.3. The vortex structure is well identified in these image while no evident magnetic defects

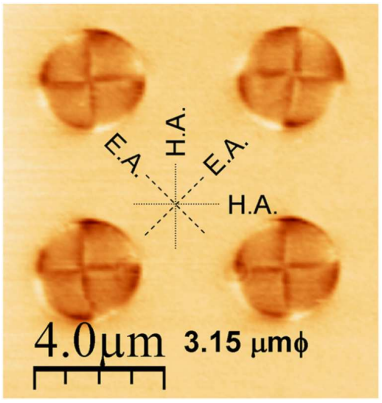

Figure 6.3: Standard MFM image at remanence of Fe-V discs of diameter 3.15 microns and thickness 26.7 nm from reference [95]. The easy (E.A.) and hard (H.A.) axis of the fourfold crystalline anisotropy of Fe-V are shown.

or impurities can be seen. Notice that the crystalline anisotropy of Fe-V is cubic, with two easy axes (E.A) at ninety degrees in the plane of the film. This is illustrated by the

deformation of the vortex structure in these images, showing four Landau domain walls aligned with the anisotropy hard axis. These walls are magnetic features of vortices in square elements and vanishes in soft magnetic discs because of the symmetry.

6.2.2 Single oscillator properties

In order to calibrate the properties of our magnetic oscillators, the individual 600 nm disc is first investigated as a reference. Its magnetisation is saturated out of the disc plane and a spectrum at a constant frequency ($\omega/2\pi = 7$ GHz), shown on the figure 6.4, was performed. Because of the magnetic confinement, magneto-static modes well separated in frequency are seen. The first bright mode, of fundamental importance in the following, is identified as the uniform spin wave mode ($l = 0, m = 0$). The other modes seen at higher energies are difficult to label. The microwave field is spatially uniform and should only couple to the radial spin wave modes. But the slight misalignment of the external perpendicular field could promote the excitation of combinations of azimuthal modes. Moreover, the fourfold anisotropy of the Fe-V should be taken into account in the calculation of the spin wave spectrum presented chapter 2.

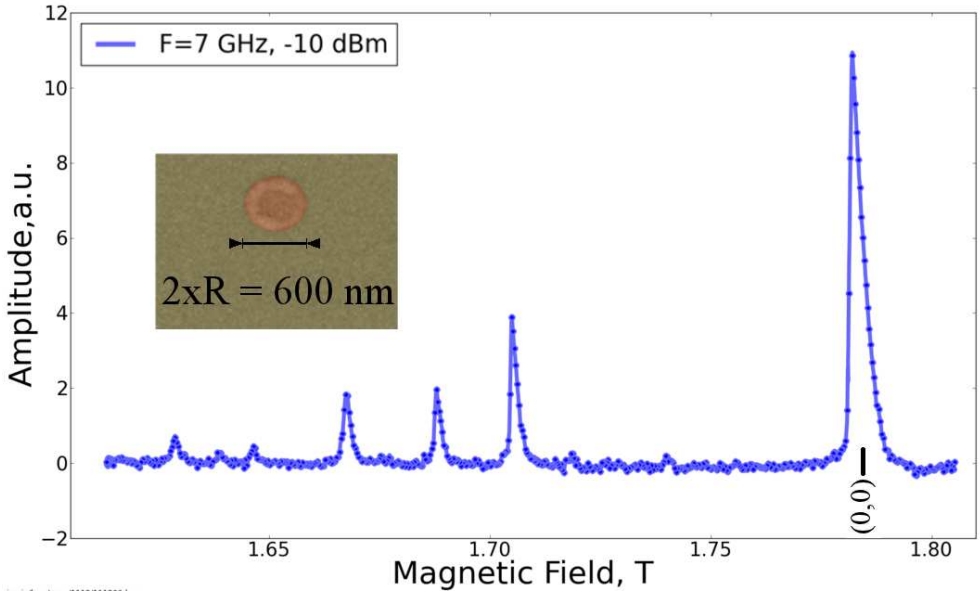

Figure 6.4: Spectrum of the Fe-V disc of 600 nm in diameter, perpendicularly magnetised. The field was varied at a constant frequency of $f = 7$ GHz. The first and bright mode corresponds to the uniform precession of the magnetisation.

Nevertheless, this spectrum confirms that the lateral confinement in discs of 600 nm in diameter is enough to achieve a significant separation of the spin wave modes energies.

6.2.2.1 A uniform spin-wave mode based oscillator

The lowest spin-wave mode ($l = 0, m = 0$) at $\simeq$17.8 kOe, corresponding to the uniform precession of the magnetisation, will be the base of our oscillator. The uniform modes of each disc constitute our oscillators and their coupled dynamics will be investigated experimentally.

This particular mode is chosen because of its simple geometry. Moreover, because in this mode all the magnetisation is precessing in-phase around the equilibrium field, the dipolar stray field radiated by the dynamical part of the magnetisation is enhanced. As explained earlier, this dynamical dipolar stray field is the driving force of the coupled dynamics.

The frequency of this mode, around 5 GHz for the fixed field of 17.2 kOe is ideally situated regarding the efficiency of our broadband microwave excitation. Furthermore, the theoretical description of the uniform mode, developed in the chapter 2, allows us to understand and calculate with high accuracy its eigen-frequency in any environment. In particular an analytical formula is available for the dynamical cross term $h_{i\to j}$ in this geometry.

6.2.2.2 Continuous tuning of the oscillator eigen-frequency

A crucial point is to find an external knob to couple and uncouple our pairs of oscillators, i.e., to be able to tune continuously, and differentially, the frequency of the uniform mode in each disc of the pair. This is even more important since the eigen-frequency of the uniform oscillation depends strongly on the disc diameter. From the nano-fabrication point of view, it is rather impossible to reach a nanometre precision for the discs diameter, and the ability to tune the frequency externally is very important.

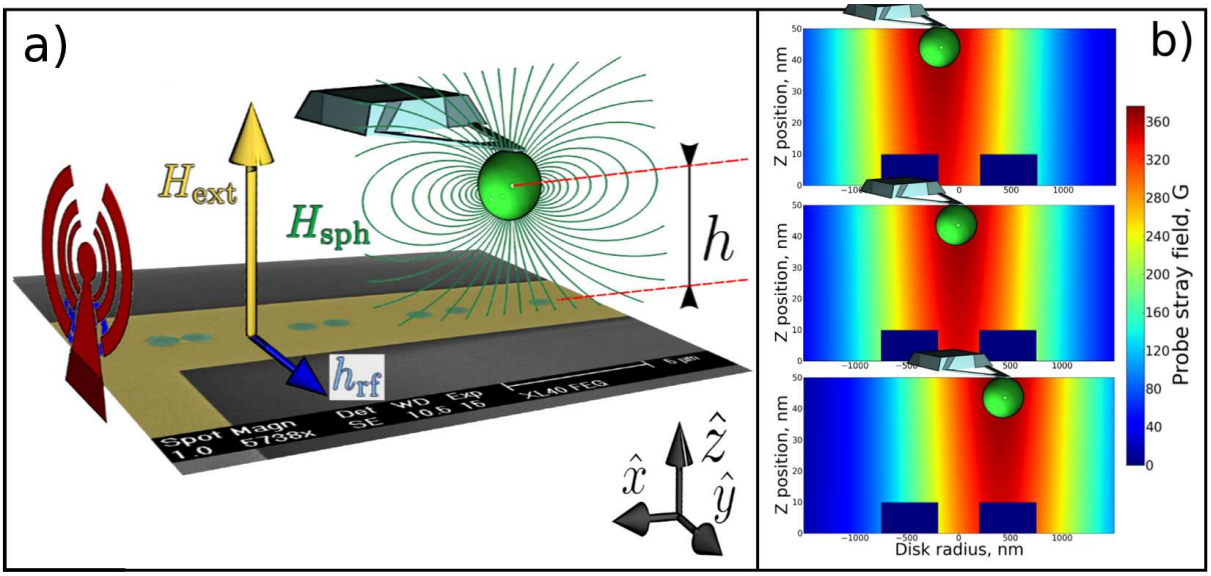

Figure 6.5: a) The MRFM probe (green sphere) is sketched over the Fe-V sample. The probe produces a stray field on the discs that is inhomogeneous in the radial direction x. b) Dipolar field maps of the z-component of the probe stray field, few tens of nanometres over over two discs, calculated considering the iron sphere as a magnetic dipole. Three probe radial x positions are considered.

In Magnetic Resonance Imaging (MRI), the physical information is spatially coded by localising the resonance frequency in space using a strong field gradient. The key idea is to take advantage from our scanning probe measurement technique, sketched on the figure 6.5a, to copy the MRI method [83]. The f-MRFM probe, placed 1.8 μm over the discs, produces its own stray field $H_{sph}(\boldsymbol{r})$ since this is a magnetic iron particle, perpendicularly

magnetised and saturated as well, see figure 6.5a. We will consider in the following that the stray field of the tip approximately reduces to the dipolar field created by a punctual magnetic moment $m_{sph} = 4 \times 10^{-10}$ emu placed at its centre. This approximation is valid since the global shape of the iron magnetic particle is spherical, as confirmed by the SEM image of the figure 4.5a. Moreover, its magnetisation is well saturated at 17.2 kOe. The saturation field of a magnetic sphere is indeed $4\pi M_s/3$ which gives approximately 6.5 kOe for iron with 3 % of silicon.

Following this assumption, the stray field from the probe at the position $\boldsymbol{r}$ is given by:

$$\boldsymbol{H}_{sph}(\boldsymbol{r}) = \frac{3(\boldsymbol{m}_{sph}.\boldsymbol{u}_r)\boldsymbol{u}_r - \boldsymbol{m}_{sph}}{r^3} \tag{6.2}$$

where the norm of the distance between the sphere centre (X_s, Y_s, Z_s) and $\boldsymbol{r}$ is r and $\boldsymbol{u}_r = \boldsymbol{r}/r$ is the unit vector in the same direction.

This dipolar field is added to the external uniform field H_z at the sample, but it is strongly non-uniform in the radial direction. As in the MRI setup, the role of the sphere is to create a lateral field gradient $g_{zx} = \partial \boldsymbol{H}_{sph}.\boldsymbol{u}_z/\partial x$ on the sample. By scanning the cantilever/tip at constant height over the sample, the total magnetic field applied on each disc can be modulated differentially, while providing a local MRFM detection.

In the figure 6.5b, a calculation of the z-component of the probe stray field over the discs for three cantilever lateral positions demonstrates that the total external magnetic field $H_z + H_{sph}(\boldsymbol{r})$ applied on each disc can be varied and even continuously and differentially tuned.

Using this procedure allows us to spatially code the oscillation frequency. Indeed, the uniform mode frequency is given by $\omega_{0,0} = \gamma H_{eff}$ where the effective field H_{eff} explicitly contains H_{sph}.

To confirm the role of the f-MRFM probe as a field gradient, the following experiment is performed. The tip is scanned in the x direction (with 100 nm steps) at an altitude $h = 1.7$ μm over the the isolated 600 nm disc, placed at $(x = 0, y = 0, z = 0)$. At each probe position, a spectrum is acquired by sweeping the microwave field frequency ω_{rf} produced by the antenna. The frequency and relative amplitude of the uniform mode are then measured by the f-MRFM. The result is shown on the figure 6.6a in a density plot, the f-MRFM amplitude being displayed in colour code.

Two main observations can be made:

1. The frequency shift is maximum when the probe is at the vertical of the disc centre and then decreases. The slope is proportional to the lateral field gradient g_{zx} produced by the sphere. For $h \gg 2R$, it is maximum at about $x \approx 0.39h$. At this location, the gradient is about $g_{zx} \approx 2.7 m_{sph}/h^4$. For our settings, this corresponds to a slope of about 0.3 GHz/μm. The total shift produced by the tip stray field is about 0.5 GHz, which is enough to compensate the nano-fabrications imperfections. For comparison, a 0.3 GHz variation of the eigen-frequency is equivalent to a change by 10% of the disc diameter.

2. The f-MRFM amplitude, in colour code, depends on the probe position as well. The sensitivity of the measurement is indeed a function of the probe-sample absolute distance r. If ΔM_z is the variation of the sample magnetisation induced by the FMR resonance, the force acting on the cantilever is given by: $g_{zz}(r)\Delta M_z$. Thus

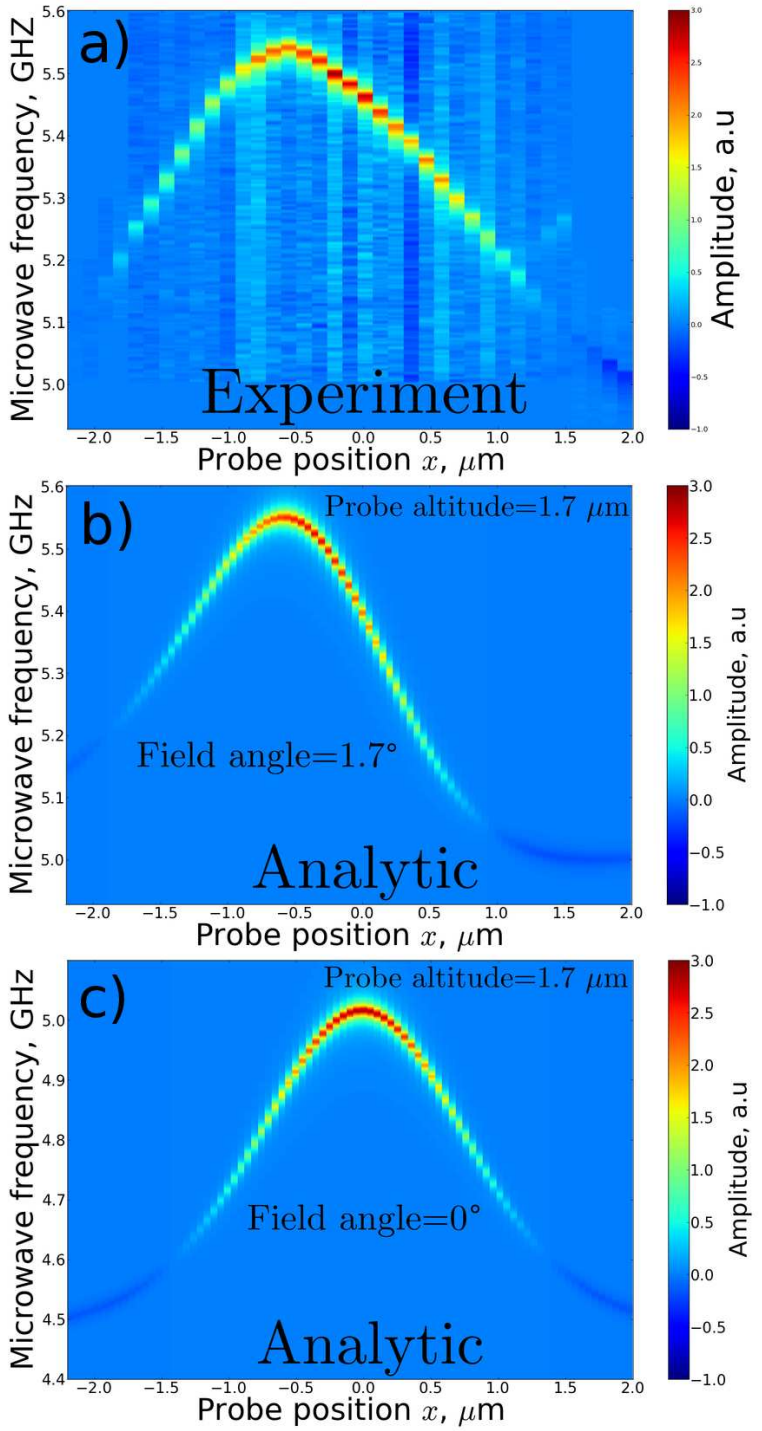

Figure 6.6: a) Uniform spin-wave mode frequency of the single disc of 600 nanometres in diameter as a function of the f-MRFM probe lateral position. The mode amplitude is displayed in colour code. The probe, of magnetic moment $m_{sph} = 4 \times 10^{-10}$ emu, is placed at an altitude of 1.7 μm. b) Calculation using the theory of chapter 2 performed with the same experimental parameters. The angle of the perpendicular field was set to $\theta_H = 1.7\hat{A}^\circ$ to reproduce the data c) Result of the same calculation without field angle.

the maximum of the amplitude is also found when the probe is just over the disc. The gradient g_{zz} decays as the power $1/x^5$ for large lateral displacement x, and the

measured amplitude decreases as well. Experimentally, the signal decreases by one order of magnitude when the probe is displaced by 1.2 μm laterally. The 3 μm gaps let between pairs of discs can then be considered sufficient to avoid parasite cross-talks between different sets of discs.

Nevertheless, these preliminary observations are incomplete regarding the real experiment of the figure 6.6a. The observed behaviour of the uniform spin wave frequency is more complicated. In particular, the bell shape of the curve is not symmetric and the maximum frequency shift is not aligned with the sample location. Moreover, the maximum of the f-MRFM amplitude does not coincides with the maximum frequency shift.

Experimentally, the disc is nearly perfectly cylindrical (see the SEM image of figure 6.2) and the tip is scanned symmetrically at constant height over the disc, passing exactly over its centre. Indeed, the f-MRFM acts also as a standard MFM and the cantilever frequency shift allows to find precisely the centre of the disc.

The asymmetry observed experimentally is then attributed to the slight misalignment of the external field with the disc normal $\boldsymbol{u}_z$. In order to confirm this assumption, we have performed calculations of the uniform mode frequency shift under the influence of the magnetic probe. For the single 600 nm disc placed in $x = 0$, the uniform mode frequency taking into account the f-MRFM probe placed in the position ($\boldsymbol{x} = (X_s, Y_s, Z_s)$ is given by [102]:

$$\omega_{0,0}(\boldsymbol{x}) = \omega_{\mathrm{FMR}} + \gamma\{\boldsymbol{H}_{sph}(\boldsymbol{x}).\boldsymbol{u}_z\} \tag{6.3}$$

where the first term is the resonance frequency in the absence of the sphere and the second term is the gyromagnetic ratio γ times the spatial average of the z-component of the stray field of the sphere over the disc volume:

$$\gamma\{\boldsymbol{H}_{sph}(\boldsymbol{x}).\boldsymbol{u}_z\} = \gamma\frac{\langle J_0^2(k_0\sqrt{x^2+y^2}/R)\boldsymbol{H}_{sph}(\boldsymbol{r}).\boldsymbol{u}_z\rangle_V}{V J_1^2(k_0 R)} \tag{6.4}$$

Here $k_0 = 2.4048/R$ is the uniform mode wave vector, R is the disc radius and J are the zero-th and first-th order Bessel functions of the first kind. In this formula, the field produced by the f-MRFM probe is averaged over the disc volume V taking into account the uniform mode profile (see chapter 2).

Because the probe is spherical, it has no shape anisotropy and we will consider that its magnetisation follows the external field. The external field is tilted from the normal by the polar angle θ_H. Even if the single disc experiment presents an axial symmetry, an azimuthal angle ϕ_H has to be introduced because the direction of the probe scan breaks that symmetry. Therefore, the probe magnetisation is given by:

$$\boldsymbol{m}_{sph} = m_{sph}\left|\begin{array}{l}\cos\phi_H \sin\theta_H \\ \sin\phi_H \sin\theta_H \\ \cos\theta_H\end{array}\right. \tag{6.5}$$

For each probe lateral position $x = X_s$, the equilibrium configuration of the disc magnetisation is calculated. The norm $H_{tot} = ||\boldsymbol{H}_{ext} + \boldsymbol{H}_{sph}||$ and orientation $\theta_{tot} = \cos^{-1}[H_{tot}/((\boldsymbol{H}_{ext} + \boldsymbol{H}_{sph}).\boldsymbol{u}_z)]$ of the total external field are used to calculate the equilibrium angle θ_M of the magnetisation. The uniform spin wave frequency $f_{0,0} = \omega_{0,0}/2\pi$ is then calculated using the formula (2.44) of chapter 2.

The amplitude $A(x)$ is proportional to the force acting on the f-MRFM cantilever. This force is proportional to the field gradient created by the precessing magnetisation in the disc at the probe centre [76]:

$$A(x) \propto F_z = \int_V \Delta M_z(\boldsymbol{r}) g_{zz}(\boldsymbol{r}) d^3\boldsymbol{r} \tag{6.6}$$

where ΔM_z is the dynamical variation of the longitudinal component of the magnetisation. This equation also allows a better understanding of the f-MRFM amplitude. The variation with the probe position is given by the radial profile of the field gradient $g_{zz}(x)$. It becomes eventually negative which leads to the negative amplitude measured on the figure 6.6a far from the disc, and reproduced in the calculation figure 6.6b.

In our case, we are interested in the variation of this amplitude with the radial probe position. The spin wave amplitude, proportional ΔM_z, is constant since the microwave excitation is constant. Therefore the amplitude is simply proportional to:

$$A(x) \propto \frac{\partial(\widehat{\boldsymbol{N}}.\boldsymbol{M}(x))}{\partial z}.\boldsymbol{u}_{\perp cant} \tag{6.7}$$

where $\widehat{\boldsymbol{N}}$ is the demagnetising tensor of the single 600 nm disc projected along the magnetisation equilibrium position $\boldsymbol{M}$ at the probe position x. To be more realistic, the force is also projected perpendicular to the cantilever beam $\boldsymbol{u}_{\perp cant}$, which is tilted by $15\hat{A}^\circ$ with respect to the xy plane. In the figure 6.6b, the spectra are simply displayed using Lorentzian functions of frequency $f_{o,o}(x)$, amplitude $A(x)$ and linewidth $\Delta f_{0,0} = 2\alpha_{FeV} f_{0,0}$.

In this calculation, all the experimental parameters were used: probe magnetisation and altitude, disc diameter and magnetic properties from the table 6.2.1.2. The only free parameters were the two polar angle (θ_H, ϕ_H) describing the external field. The best agreement with the experiment was found with $\theta_H = 1.7\hat{A}^\circ, \phi_H \simeq 0\hat{A}^\circ$: the external field is tilted by 1.7 degrees in the direction of the scan.

All the characteristic features of the experimental diagram are well reproduced by the calculation: the asymmetry in frequency and amplitude as well as the position of the maximum frequency shift. Thus the ingredient introduced by the external field angle seems to be sufficient to explain the experimental behaviour. To support this statement, the result of the symmetric calculation ($\theta_H = 0\hat{A}^\circ, \phi_H \simeq 0\hat{A}^\circ$) is plotted figure 6.6c. The asymmetry disappears and the frequency of the spin wave mode could not be reproduced quantitatively.

Moreover, the frequency shift calculated with the formula (6.3) corresponds to an averaged additional field from the probe of 14 mT at the maximum. Such variation is small compared to the static perpendicular field of 1.72 T, thus the tuning of the spin wave frequency is done without significant deformation of the uniform mode profile.

6.2.3 Experimental results on a pair of discs

All the ingredients for the experiment, field gradient and sensitivity, have been calibrated on the single disc. The experiment of the figure 6.6a can now be performed with a pair of discs.

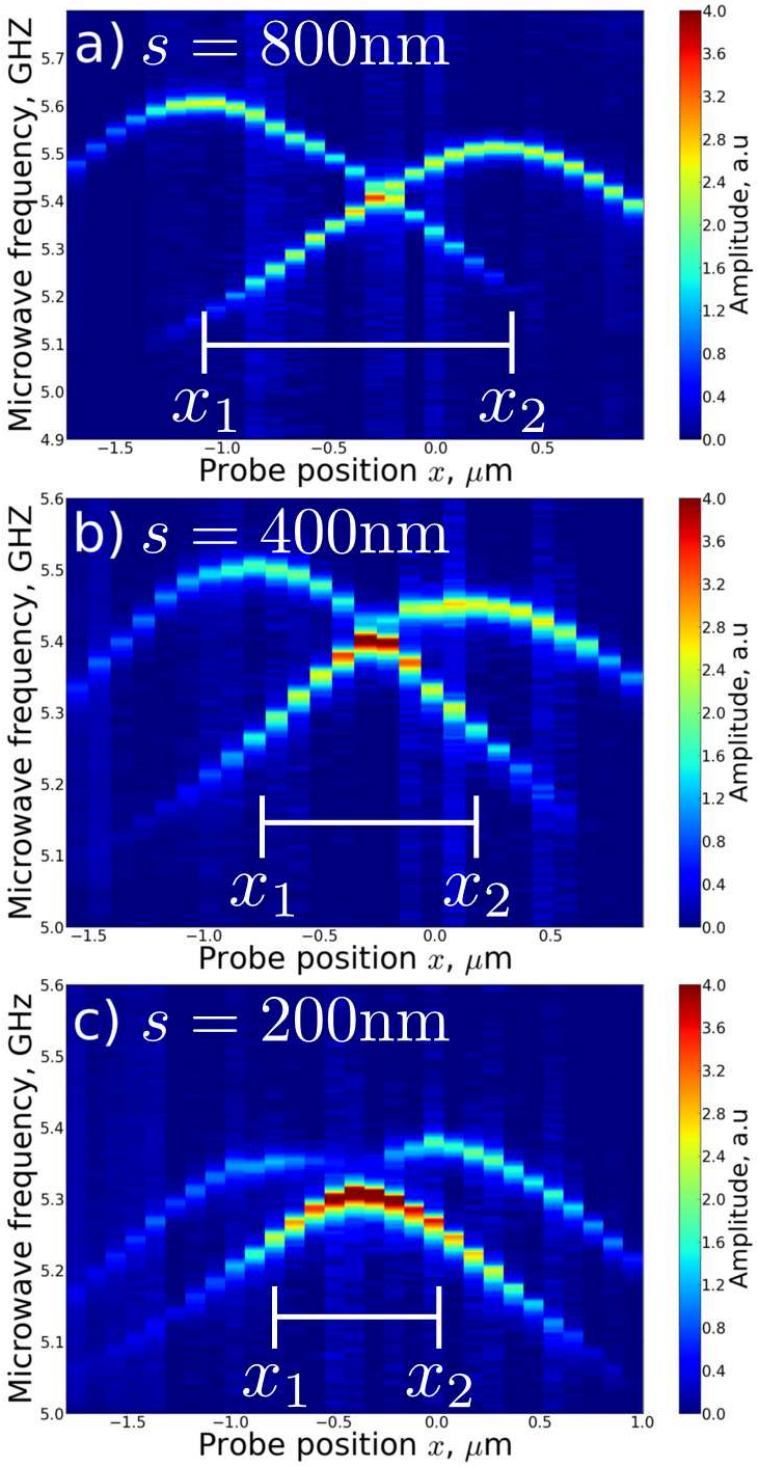

Figure 6.7: Frequencies of the uniform/coupled spin wave modes for pairs of discs of 600 nm in diameter as a function of the f-MRFM probe radial position. The tip is 1.7 µm above the discs and the edge-to-edge separation is a) 800 nm, b) 400 nm and c) 200 nm.

6.2.3.1 Measurement of Ω

Let us first begin with the pair of discs separated by $s = 800$ nanometres edge-to-edge. Since the dipolar interaction decays rapidly in the radial direction, the strong coupling

regime is not achieved for such large separation. Nevertheless, the experiment, presented in figure 6.7a provides an interesting result. The field gradient $g_{zx}(x)$ created by the tip is able to tune the uniform mode frequency, as seen for a single disc, but differentially in each discs depending on their relative positions. This diagram is simply the superposition of two bell-shaped curves from a single disc (see figure 6.6a), shifted radially by $x = s+2R = 1400$ nm. The difference between the two maxima in frequencies is attributed to the differences of nominal diameter between the two discs. This point will be discussed in detail in a following section.

Moreover, these frequencies eventually cross when the probe is close to the middle of the pair ($x = 0$ here). We demonstrate here the ability to continuously tune and detune the frequencies of our coupled oscillators as well as the possibility to reach the compensation point $\omega_1 = \omega_2$.

Once this crucial demonstration is done, the strong coupling regime can be investigated with the pair separated by only $s = 200$ nm. The resulting diagram, shown on the figure 6.7c, also presents two frequency maxima at $x_{i,j} = \pm 400$ nm, whose spatial separation corresponds to the centre-to-centre distance between disc i and disc j. But unlike in the figure 6.7a, the two bell shape curve do not cross but instead anti-cross. This is the first evidence of a coupled dynamics. The two modes observed here could not be attributed any more to individual uniform modes in each discs. They correspond to the coupled modes of this system, whose frequencies are given by the formula (B.1).

The upper branch, with the highest frequency ω_A, is the anti-binding mode. The magnetisation is precessing uniformly in both discs but with a π phase difference: this is an optical mode. The lower branch, with the lowest frequency ω_B, is the binding mode. The magnetisation is also precessing uniformly but in phase in both discs: this is an acoustic mode.

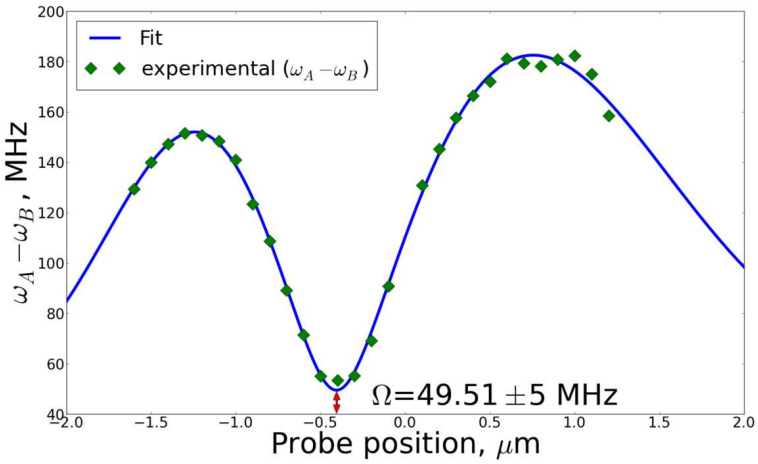

Figure 6.8: Procedure to measure the experimental dynamical splitting Ω, in the case of the pair separated by $s = 200$ nm.

At the expected crossing between ω_i and ω_j, the experimental splitting $\omega_A - \omega_B$ exactly measures Ω:

$$\omega_A - \omega_B = 2\sqrt{\left(\frac{\omega_1 - \omega_2}{2}\right)^2 + \left(\frac{\Omega}{2}\right)^2} \quad \text{reduces to} \quad \Omega \quad \text{if} \quad \omega_1 = \omega_2 \tag{6.8}$$

For each pair separation s, the coupling strength is accurately measured with the procedure illustrated in the figure 6.8. The frequencies of the coupled modes are extracted from the experiment by fitting the spectra with Lorentzian functions. Their difference $\omega_A - \omega_B$, plotted as green dots on figure 6.8, is then fitted with the equation (6.8) with Ω as an adjustable parameter. In this experiment, only the frequency shift $\Delta\omega_{1,2}$ induced by the tip field gradient is relevant. The individual frequencies $\omega_{1,2}$ are calculated using the same analytical expression as in equation (6.3): $\omega_{1,2} = \omega(x - x_{1,2})$. The result of such fitting procedure for the pair with $s = 200$ nm is shown by the blue curve in the figure 6.8. The fitted values are the data points of figure 6.13.

6.2.3.2 The mode amplitudes: a signature of the collective dynamics

The other striking effect revealed in the figure 6.7c is the strong variation of the signal amplitude near the optimum coupling. In order to perform a more quantitative analysis of this phenomenon, we have plotted the f-MRFM amplitude (for the pair $s = 200$ nm) measured for both coupled modes as a function of the tip position on the figure 6.9d. Close to the region of optimal coupling, the anti-binding mode (A) amplitude nearly vanishes, while the amplitude of the binding mode (B) is strongly enhanced.

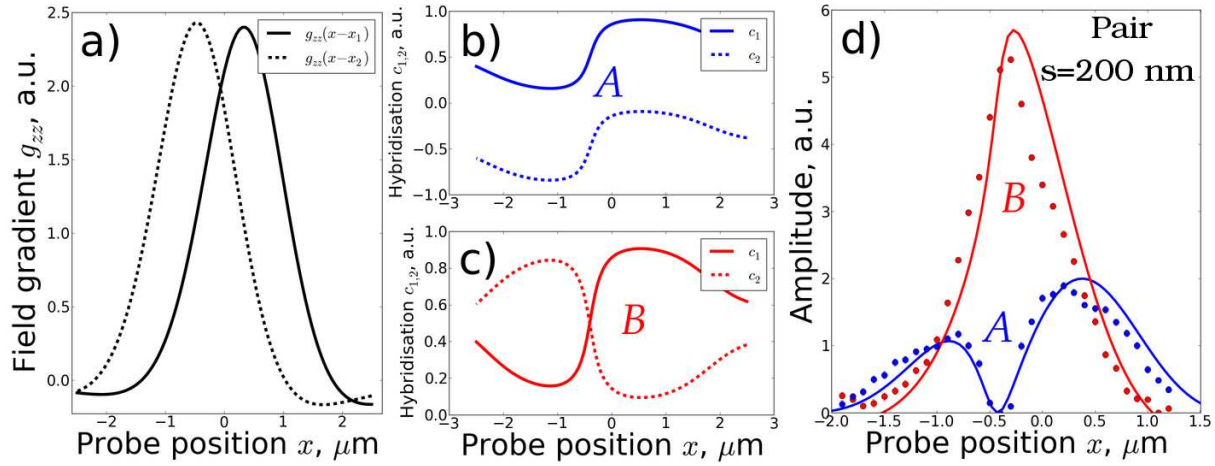

Figure 6.9: a) Stray field g_{zz} at the probe location from two uncoupled discs separated by 200 nm. b) and c) Coupled spin wave amplitude in each discs of the pair $s = 200$ nm versus probe position for the binding B and anti-binding A coupled modes. d) Amplitude of the coupled modes measured by f-MRFM (dots) and calculated (solid lines) as a function of the tip position for the pair separated by $s = 200$ nm. A corresponds to the optical mode while B is the acoustic mode.

First of all, the behaviour of the intrinsic coupled modes amplitudes has to be understood. If the two discs were uncoupled, a force proportional to the field gradient G_{zz} created by both discs at the probe centre would be applied on the cantilever. This force was calculated for one disc by the equations (6.6) and (6.7). In the figure 6.9a, the field gradients arising from two uncoupled discs separated by 200 nanometres are plotted versus the probe lateral position. The resultant measured amplitude would be proportional to the sum of these two contributions.

In our case, the two discs experience a coupled dynamics, which modifies the f-MRFM amplitude. In the case of a single disc, the real spin wave amplitude had no dependence on the probe position and was only a function of the microwave excitation strength, the signal

being only given by the f-MRFM sensitivity at the position x. For the coupled modes, the spin wave amplitudes are given by the eigen-vectors of the coupled system presented equation (2.59) of chapter 2. The amplitude is distributed with a certain weight between both discs, while the magnetisation precesses in or out-of-phase for each modes. We recall that the ratio of this hybridisation in each disc is given for both coupled modes by:

$$\left.\frac{c_1}{c_2}\right|_{\omega_{A,B}} = \left(\frac{(\omega_1-\omega_2) \mp \sqrt{(\omega_1-\omega_2)^2+\Omega^2}}{\Omega}\right)^{\mp 1} \tag{6.9}$$

where $c_{1(2)}$ is the amplitude of the magnetisation precession in the disc 1(2). Notice that the ratio depends on the intrinsic frequencies of each discs $\omega_{1,2}(x)$. These frequencies are a function of the probe position. Consequently, the ration of hybridisation of the coupled modes amplitudes will depend on the probe lateral position.

The spin wave amplitude in each disc corresponding to the coupled modes are plotted on the figure 6.9b and c for the anti-binding and binding modes. These curves are calculated with the equation (6.9) using a normalisation imposed by the phase of the precession: $(c_1 + c_2) = 1$ for the binding mode (B) and $(c_1 - c_2) = 1$ for the anti-binding mode (A).

Taking into account the ratio of hybridisation of the coupled modes in the two discs, we have:

$$A(x) \propto h_{rf}^2 |c_1 + c_2|^2 [c_1^2 G_{zz}(x - x_1) + c_j^2 G_{zz}(x - x_2)] \tag{6.10}$$

By using explicitly this equation, the dependence of the amplitude versus the tip position x can be calculated. The result (solid lines) is compared to the experimental values (dots) in the figure 6.9a.

The overlap of the uniform microwave field with the coupled mode is determined by the the selection rule $|c_1 + c_2|$. The curve B of the binding mode is easily understandable: at the optimum of the coupling, equation (6.9) leads to $c_1 = +c_2$. The binding amplitudes presented on the figure 6.9c highlight this fact: at the anti-crossing the precession is equally distributed in the two discs with the same phase. Therefore, this coherent coupling represents and enhancement of the amplitude by a factor of 4 compared to the single disc amplitude.

In the opposite, at the anti-crossing, the anti-binding mode A has $c_1 = -c_2$. The precession has also the same weight in both discs, but occurs out-of-phase, as can be seen on figure 6.9b. The vector sum of the precessing magnetisation in the two disks vanishes at this point and the overlap integral between the rf excitation field and this collective mode is zero. In other words, the spatial symmetry of the rf field is not appropriate to couple to this spin wave symmetry: the mode is not physically excited. Therefore, the amplitude of this optical mode vanishes.

In conclusion, the behaviour of the mode amplitudes measured by f-MRFM and presented on the figure 6.9d is a strong evidence of the collective dynamics of our pair of discs.

6.2.3.3 Effect on the mode linewidth

One of the goal of building arrays of spin transfer oscillators is to reduce the linewidth of the microwave emission. In the case of STNOs, the magnetisation auto-oscillation is the result of a strongly non linear process, which usually increases the linewidth of the

modes by enhancing the thermal noise [122]. As pointed out in the introduction, the phase locked emission of an STNOs array is a promising way to reduce the noise, thanks to improved coherence.

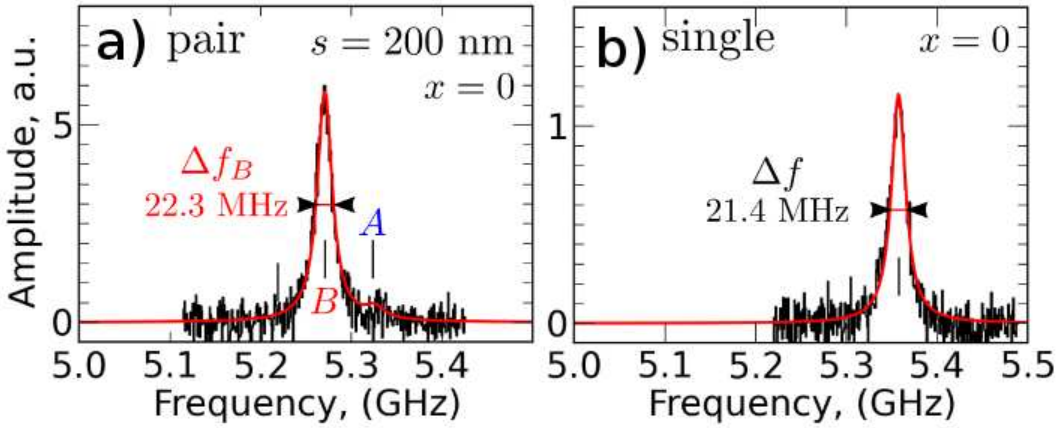

Figure 6.10: Effect of the dipolar coupling on the modes linewidths. The uniform mode in the single disc b) and the acoustic mode at the coupling maximum in the $s = 200$ nm pair a) are compared.

In our experiment, we are looking to the coupled eigen-modes of the system, using a small linear rf excitation. Therefore, the measured linewidth should not differ too much from the intrinsic Gilbert damping α: $\Delta f/2f \simeq \alpha$.

Nevertheless, the comparison between the linewidths of the coupled mode of a pair and the uniform mode of the single disc reveals some differences. In the figure 6.10a, the linewidth of the binding mode in the pair $s = 200$ at the optimal tuning is found to be $\Delta f = 22.3 \pm 0.5$ MHz. It becomes even slightly larger $\Delta f = 23.1 \pm 0.5$ MHz at the maximum detuning $x = x_{1,2}$. In figure 6.10b, the linewidth of the single disc uniform mode is $\Delta f = 21.4 \pm 0.5$ MHz.

A small increase of the ratio $\Delta f/2f$ is thus observed. It is expected for the dynamically coupled modes. As explained previously about the dissipation in the vortex state (see chapter 5, section 5.5) the quality factor of a resonance equals the damping α in the case of the uniform spin wave mode in a perpendicularly magnetised thin disc, where the magnetisation precession is circular. This is the case of the single disc, for which we recover $\Delta f/2f \simeq 2 \times 10^{-3} = \alpha$. Any deviation from the circularity causes an increase of the linewidth, since the minimum is found for a circular precession.

In the case of the collective modes in a pair of discs, the driving field of the coupling is the dynamical dipolar field $h_{i,j} = 2\pi M_s\big(\{N_{xx}^{i,j}\}+\{N_{yy}^{i,j}\}\big)$. The key point is the asymmetry $\beta = \{N_{xx}^{i,j}\}/\{N_{yy}^{i,j}\} = -2$ that reveals a ratio of two between the demagnetising tensor cross elements. This formula reflects that the magneto-dipolar cross interaction is anisotropic and thus, it induces an elliptical precession in the two discs. An analogy can be done between the binding mode in a pair of dipolarly coupled discs and the uniform mode in an ellipsoidal ferromagnet. In this case, two asymmetric stiffness fields H_x and H_y are introduced, characterising the torque exerted on the magnetisation when it is tipped along the x- or y-axis. The inverse quality factor of the resonance is given by [48]:

$$\Delta f/f = \alpha \frac{(H_x + H_y)}{\sqrt{H_x H_y}} \tag{6.11}$$

For the collective acoustic mode B, measured in the figure 6.10a, the induced ellipticity $\mathcal{E}$ is maximum at the anti-crossing and directed along the long axis x of the pair. To put numbers, the ellipticity, given by $\mathcal{E} = \frac{\beta-1}{\beta+1}\frac{\Omega}{\omega_B}$, is about 3%. An increase of ellipticity induces an increase of the linewdith, a behaviour which is consistent with the small additional broadening measured in our experiment.

6.2.4 Theoretical analysis

Using the theory of the collective dynamics developed in the chapter 2, the calculation performed for a single disc on the figure 6.6b can be extended to the case of a pair of discs. Performing such calculation will allow a precise understanding of the coupled diagrams presented figure 6.7. Indeed they present different kinds of asymmetries that must be interpreted physically.

The frequencies $\omega_{A,B}$ of the coupled modes is simply given by the equation (B.1). The individual frequencies of each oscillators $\omega_{1,2}$ must take into account the static demagnetising field created by the neighbouring disc, as explained in the last section of chapter 2. The same external field tilt of $\theta_H = 1.7\hat{A}^\circ$ is considered here and the magnetic parameters remains unchanged compared to the single disc calculation. The only free parameters are the diameters of the discs that are adjusted to fit the asymmetries present in the data.

The new ingredients are the dynamical cross demagnetising fields responsible for the dipolar coupling. Because the correction is very small, the calculation of the dynamical splitting Ω does not take into account the deviation of the field from the perpendicular. With $\{N^{i\to j}_{xx,yy}\}$ the cross demagnetising tensor elements, it reduces to:

$$\Omega = 4\pi\gamma M_s\sqrt{(\{N^{1\to 2}_{xx}\} + \{N^{1\to 2}_{yy}\})(\{N^{2\to 1}_{xx}\} + \{N^{2\to 1}_{yy}\})} \tag{6.12}$$

Aside from the saturation magnetisation M_s and gyromagnetic ratio γ, this is a pure geometrical factor, only dependent on the discs aspect ratio L/R and the pair separation s. This factor was calculated for the three disc separations considered in the experiment. It was introduced with the intrinsic frequencies in the equation (B.1) to calculate the coupled frequencies. In order to have a better understanding of the influence of the geometry, the coupling strength was also calculated for a pair of discs of 600 nm in diameter versus the edge-to-edge separation s. The obtained values are reported on the red line in the figure 6.13.

The amplitude of the coupled modes $A_{A,B}(x)$ are calculated with equations (6.10) and (6.9), the factor of proportionality being given by the microwave excitation strength.

Finally, the diagrams presented on the figure 6.11 are displayed using using double-Lorentzian functions for each probe lateral positions, with the frequencies ω_A and ω_B , amplitudes $A_A(x)$ and $A_B(x)$ and linewidths corresponding to the damping α of the Fe-V.

A good agreement is found with the experimental diagrams by taking into account:

1. The tilt ($\theta_H = 1.7\hat{A}^\circ, \phi_H = 0\hat{A}^\circ$) of the external field with respect to the normal of the disc plane. It reproduces the asymmetries already presented for the single disc: maximum of the frequencies not aligned with the maximum of the amplitudes and optimal coupling shifted from $x = 0$.

2. Small differences between the nominal diameters in a pair of discs. A difference of at most 4% between the diameters in a pair is able to explain the difference between

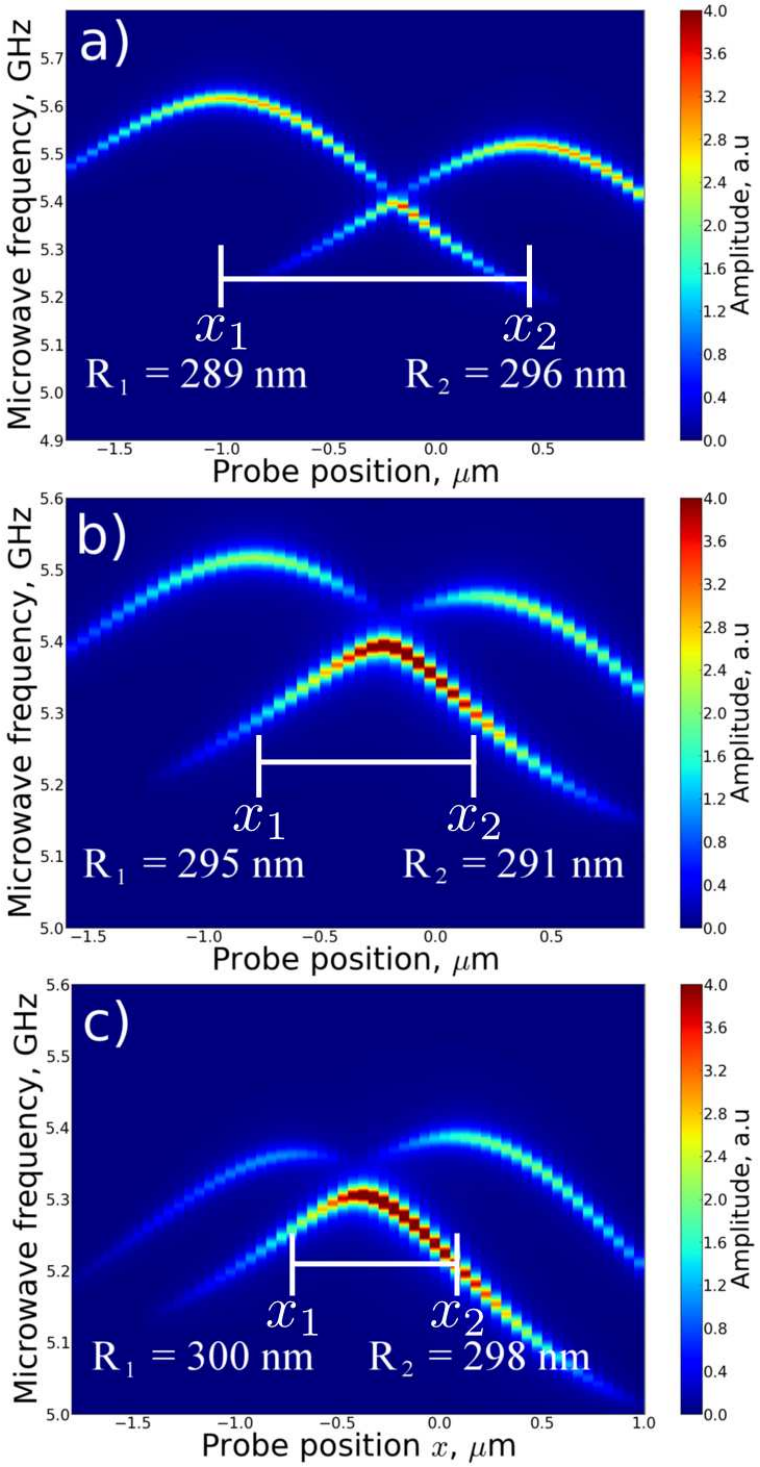

Figure 6.11: Calculation of the collective modes frequency and amplitude for the three pairs of discs presented figure 6.7. The separation is $s = 800$ a) 400 b) and 200 nm c). The radius of each discs used in the model are indicated. For each diagram, the probe altitude is $h = 1.8\mu m$ and the angle of the bias field is $(\theta_H = 1.7\hat{A}^\circ, \phi_H = 0\hat{A}^\circ)$

the two frequency maxima. The nominal diameters used in the calculations are given for each pair in the figure 6.11.

6.2.5 Numerical simulations

The analytical model used above to analyse the data assumes a uniform magnetisation throughout the magnetic body and does not take the elliptic precession of the magnetisation into account. Moreover, it is assumed that the mode profiles are not affected by the coupling, which is not exact in the strong coupling regime. To take more precisely into account the 3D texture of the magnetisation, as well as the real influence of the magnetic probe, micromagnetic simulations have been performed.

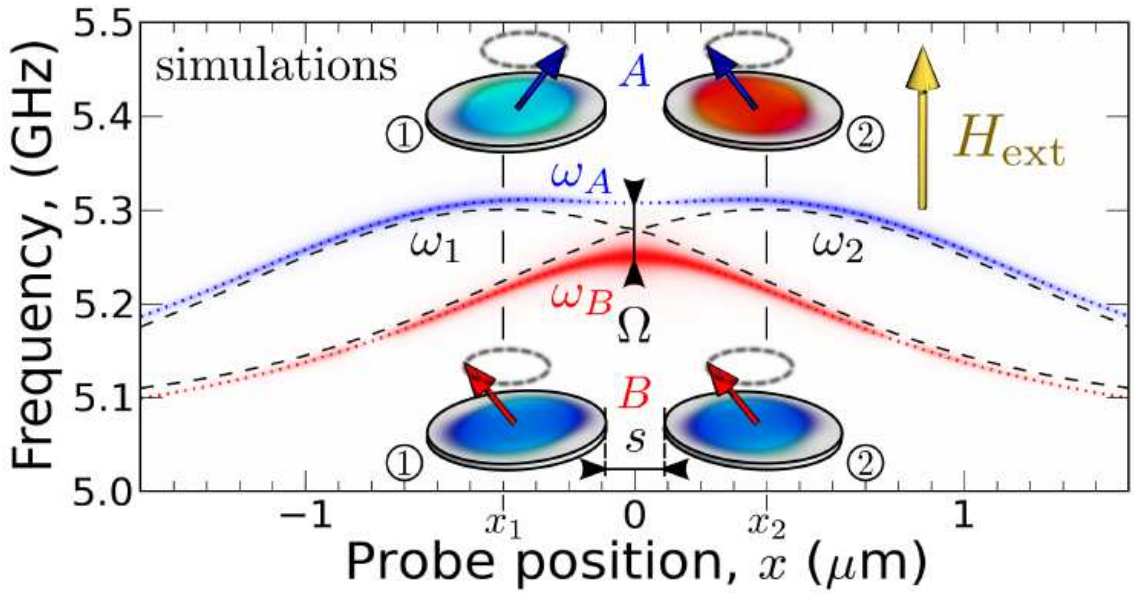

Figure 6.12: a) Simulation of the collective mode frequency as a function of tip position x for the pair separated by $s = 200$ nm. The amplitude is displayed in colour code. The calculation for two uncoupled discs is shown in dashed lines for comparison. The in-phase A and out-of-phase B modes dynamical magnetisation configuration is shown at the anti-crossing.

We have used the software SpinFlow3D, a finite element solver developed by In Silicio [132]. The discs are discretised with a mesh size of 10 nm using a Delaunay mesh construction. This mesh size allows to take adequately the dipolar pinning and the static/dynamical deformation of the magnetisation into account. At each position of the probe, we first calculate the magnetisation equilibrium configuration in the discs, which is in reality slightly distorted by the static dipolar interaction between the two discs and the real probe stray field. The Arnoldi algorithm is then used to compute the lowest eigen-values of the problem as well as the associated eigen-vectors, corresponding to the collective dynamics.

The experimental parameters, such as Fe-V magnetic constants, probe magnetisation and altitude, disc geometry... are introduced in the simulation. The result for the discs pair separated by $s = 200$ nm is shown on the figure 6.12, to be compared with the figure 6.7c. The frequencies and amplitude of the binding and anti-binding modes are well reproduced as well as their frequency splitting Ω. Notice that the field angle $\theta_H = 1.7\hat{A}^\circ$ was not taken into account in this simulation.

For comparison, the frequencies of the single discs are shown as dashed lines. The two analytical frequencies $\omega_{i,j}$, calculated using the spin wave theory of the chapter 2, are superimposed on the simulated coupled modes frequencies. It highlight the anti-crossing

of the coupled modes.

Within this simulation, it is possible to extract the phase of the magnetisation precession as well as the mode profile in each disc. In the figure 6.12, these profile are presented for both optical A and acoustical B modes at the anti-crossing. As expected, the phase between discs is π and 0, while the amplitude is equally distributed.

If the tip is shifted from $x = 0$, the discs are in a partial hybridisation state but the phase between discs in each modes remains unchanged: this "rigidity" is the signature of the collective motion. However, as the individual frequencies $\omega_{i,j}$ are different, the amplitude is distributed in each disc with a different weight.

Finally, the same simulation is reproduced by varying the disc separation s and the simulated coupling strength Ω is reported on the simulated curve of the figure 6.13.

6.2.6 Geometrical influence

The measurement and calculations of the dynamical coupling strength Ω as a function of the separation s between the nano-oscillators is presented in the figure 6.13. The experimental values (black dots) corresponding to the three pairs of disc of the figure 6.2 are compared with values predicted by both simulations (blue dashed curve) and analytical calculations (red curve). The linewidth of the binding coupled mode Δf at 5 GHz is shown to highlight the experimental "visibility" of Ω.

The general agreement between our three different analysis of the problem is rather good. The similar decay with s shown by the three sets of results supports this statement. Nevertheless, the slight discrepancies that remains can be explained qualitatively:

1. For small disc separation s, the simulation and the analytical theory deviate from each other, while showing a perfect agreement at larger s. At such small separation, the dipolar interaction between discs changes the static configuration of the magnetisation which is no longer perfectly uniform throughout the magnetic body. Moreover, the spin wave modes profiles are significantly distorted: they can no longer be modelled by Bessel functions. These effects are not taken into account in the analytical calculations, leading to an underestimated value of Ω.

2. The experimental values are systematically slightly below the predicted ones. The horizontal error bars illustrate the assumption that the disc could be slightly smaller than their nominal diameter, leading to an increase of the separation s. This is confirmed by the calculation of figure 6.11 where the diameters used in the calculations are always below 300 nm. This could be explained by some oxidation at the periphery of the discs.

In conclusion, the main result is that, within our experimental parameters, s needs to be less than the diameter of the discs in order to have Ω larger than the linewidth Δf. The geometry chosen is of course very simple, but this result showing the clear evidence of a collective dynamics is promising in order to realise more complicated arrays of oscillators.

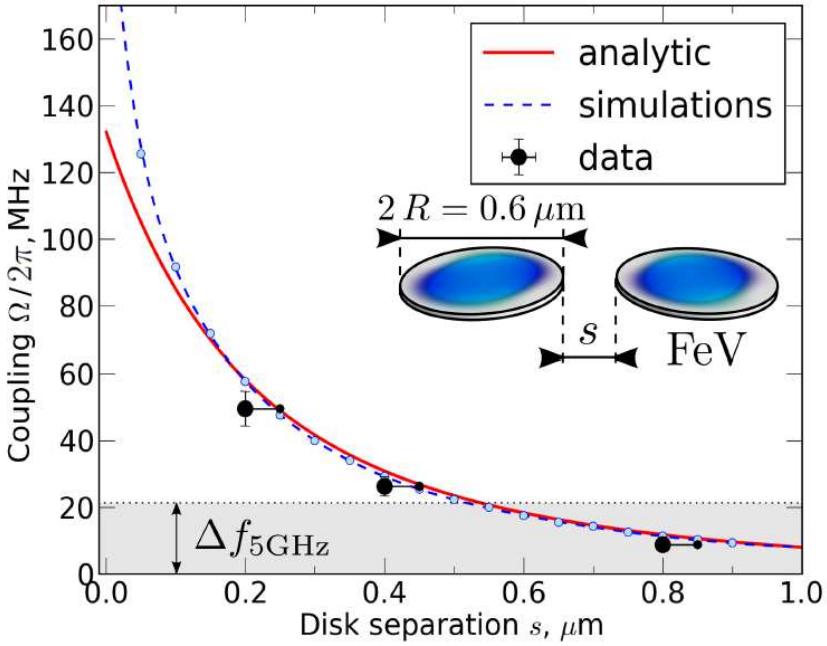

Figure 6.13: Coupling strength Ω as a function of the separation s between two discs. The experimental measurements (black points), are compared with the analytical calculations (red curve) and the micro-magnetic simulations (dashed blue curve).

6.3 Dipolar coupling: towards more complex geometries

Now that the possibility to couple two magnetic nano-oscillators through the dipolar interaction has been demonstrated, more complicated geometries can be investigated. Two preliminary experiments have been performed. The first one with a set of four identical discs placed in a square lattice. The second is with a pair of discs placed nearby but with very different diameters.

6.3.1 Four discs test

It is of course natural to try the same experiment with more oscillators, since our goal is to study wide arrays of them. The Fe-V sample, presented on the figure 6.2, contains a set of four discs arranged in square, on the left. The diameter of the discs is the same (600 nanometres) and they are separated by 200 nanometres edge-to-edge, on the sides of the square (283 nm for the diagonal).

The figure 6.14a displays the four coupled eigen-modes of this system at the exact tuning. The phase of the precession in each discs was extracted from SpinFlow3D simulations, performed in the same way as for the pairs of discs. The lowest energy mode is an acoustic mode: it exhibits a uniform in-phase precession of the magnetisation in the four discs. In the three other modes, the precession phase varies from disc to disc around the square. The highest energy mode is composed of two discs precessing with a π phase difference with respect to the two others. In between, two degenerated modes exhibit a phase varying by $\pi/2$ between each disc. Interestingly this mode arrangement follows the same hierarchy as the azimuthal modes of a single disc. We can introduce the inter-discs

indices (L, M) in analogy with the intra-discs indices (l, m). The mode corresponds to the uniform mode $(L = 0, M = 0)$, the degenerated ones have the symmetry of the azimuthal mode $(L = \pm 1, L = 0)$ and finally, the last mode is similar to $(L = 2, L = 0)$. Regarding the dynamical splitting Ω, values as high as 90 MHz could be achieved in this strongly coupled geometry.

An experiment similar to the previous one is performed in order to measure the collective dynamics, and the coupling strength, of this system. The experimental parameters, external field, probe composition and altitude, are kept the same. The resulting diagram, shown on the figure 6.14b, is expected to be more complex. The f-MRFM probe is scanned over the discs parallel to the square edges (x direction, see yellow arrows on the sketch), starting from the middle (y=0). By performing several scans at different position y, we tried to find the compensation point, were the four frequencies may cross.

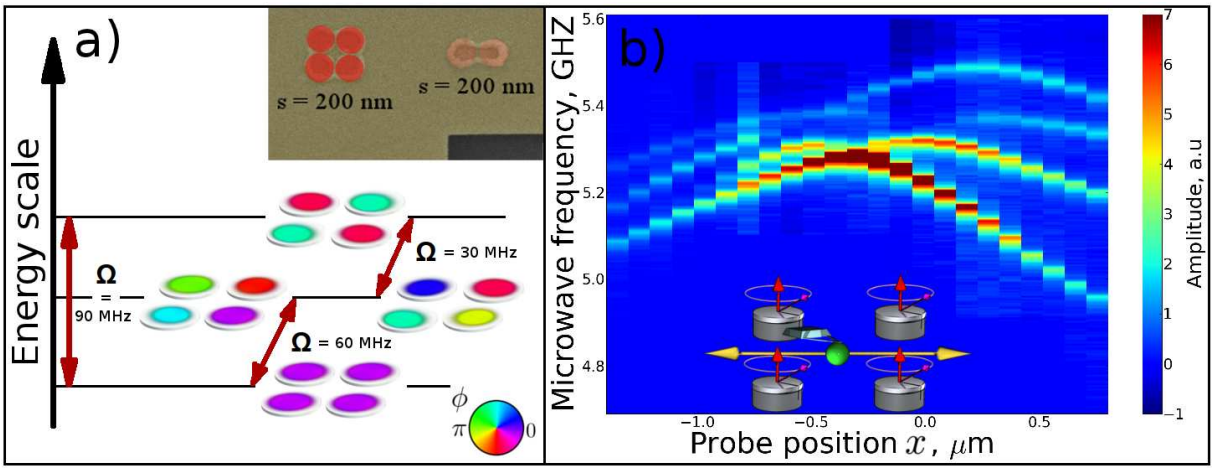

Figure 6.14: a) Phase symmetry of the magnetisation precession of the four collective modes, corresponding to the exact tuning of the four discs shown in the inset. b) Experimental frequencies of the coupled modes of this system while the probe position is varied along x.

Unfortunately, the geometrical problem is experimentally slightly more complex than before. With two discs, it is always possible to find a probe/field gradient position that compensates the uniform mode frequencies $\omega_{1,2}$ of both discs, even if their diameter are slightly different. In the case of four discs, it would have worked if the discs were perfectly identical, the compensation point being at the centre of the square.

The diagram presented on the figure 6.14b is the best we could achieve experimentally. At high detuning, the four different uniform modes can be seen, but we managed to make cross only three of them. We believe that at this point, three modes are really coupled, since the amplitude of the in-phase mode increases drastically while the amplitudes of the two others vanish. Indeed, all the excited collective modes doesn't couple to the uniform microwave field, because of their wrong "azimuthal" symmetry.

As a conclusion, because the strong coupling regime was reached with such small inter-disc separations, a collective dynamics was observed in this geometry. However, the slight difference of diameter between the discs prevents us two reach the exact tuning point of the four discs. Therefore, it was difficult to extract quantitative information from this experiment. For further development, it could be interesting to try the same with only three discs placed on a equilateral triangle, for which it should be easier to find the compensation point.

6.3.2 Coupled dynamics of a strongly asymmetric pair of discs

This particular study is a good way to confirm the ability of our technique to compensate the fabrication imperfections with the tip field gradient. Here, the diameters of the discs have been chosen to be very different on purpose. We have used the 20 nanometres thick NiMnSb sample presented in the section 5.2 of chapter 5. Indeed, the left of the sample, reproduced on the figure 6.15a, is composed of three discs of nominal diameter 700, 500 and 400 nanometres, separated by 800 nanometres centre-to-centre. The discs are saturated by a perpendicular field of 10 kOe.

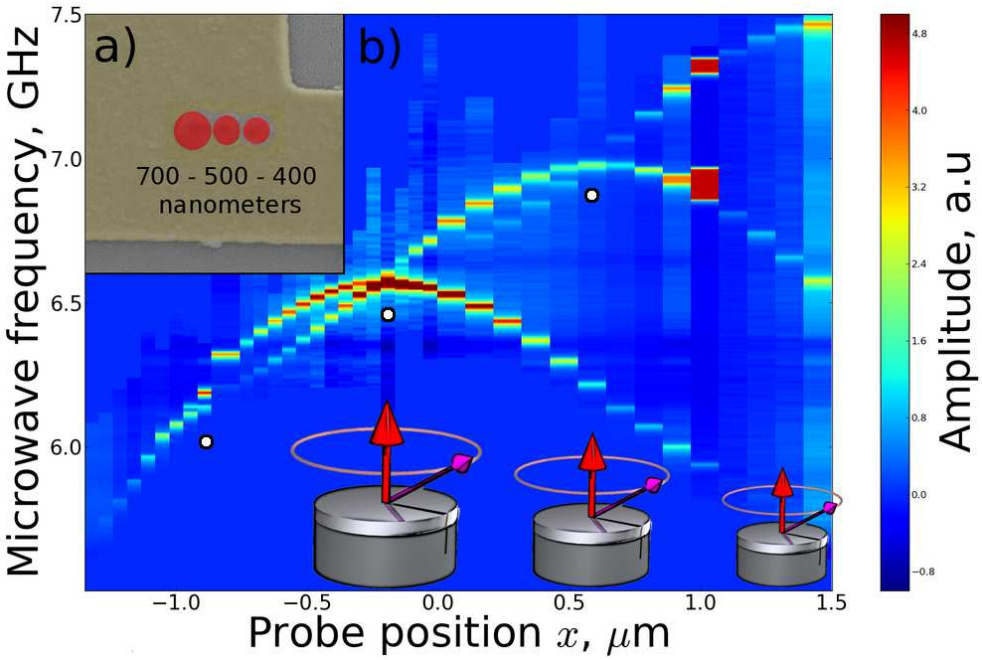

Figure 6.15: a) Set of 3 NiMnSb discs of 700, 500 and 400 nm in diameter and 20 nm thick. They are separated by 800 nm centre-to-centre. b) Diagram of the uniform mode frequencies in each disc as a function of the f-MRFM tip position. The tip was scanned 1.6 microns above the sample.

By using the measurement technique used previously, we will try to see the signature of the uniform modes collective dynamics of the two largest discs. The f-MRFM probe is scanned 1.6 microns above the sample and the uniform spin wave mode frequencies are measured. The resulting diagram is presented on the figure 6.15b.

A rapid comparison with the two discs diagram of figure 6.7 reveals two main differences. First of all, three bell-shaped curves are detected whose frequency maxima corresponds to the three discs locations, as sketched at the bottom: these frequencies are very different, which is the signature of the differences in diameter (the larger the diameter, the lower the frequency).

Nevertheless, the gradient g_{zx} introduced by the tip is able to overcome these frequency differences, and make them cross three times in the diagram (see the white dots on the figure). Notice that to compensate the frequency difference, the total magnetic field has to be very different in each disc and the crossing point is no longer in between a pair. In the following, we will concentrate on the second crossing, which happens when the tip is just over the largest disc.

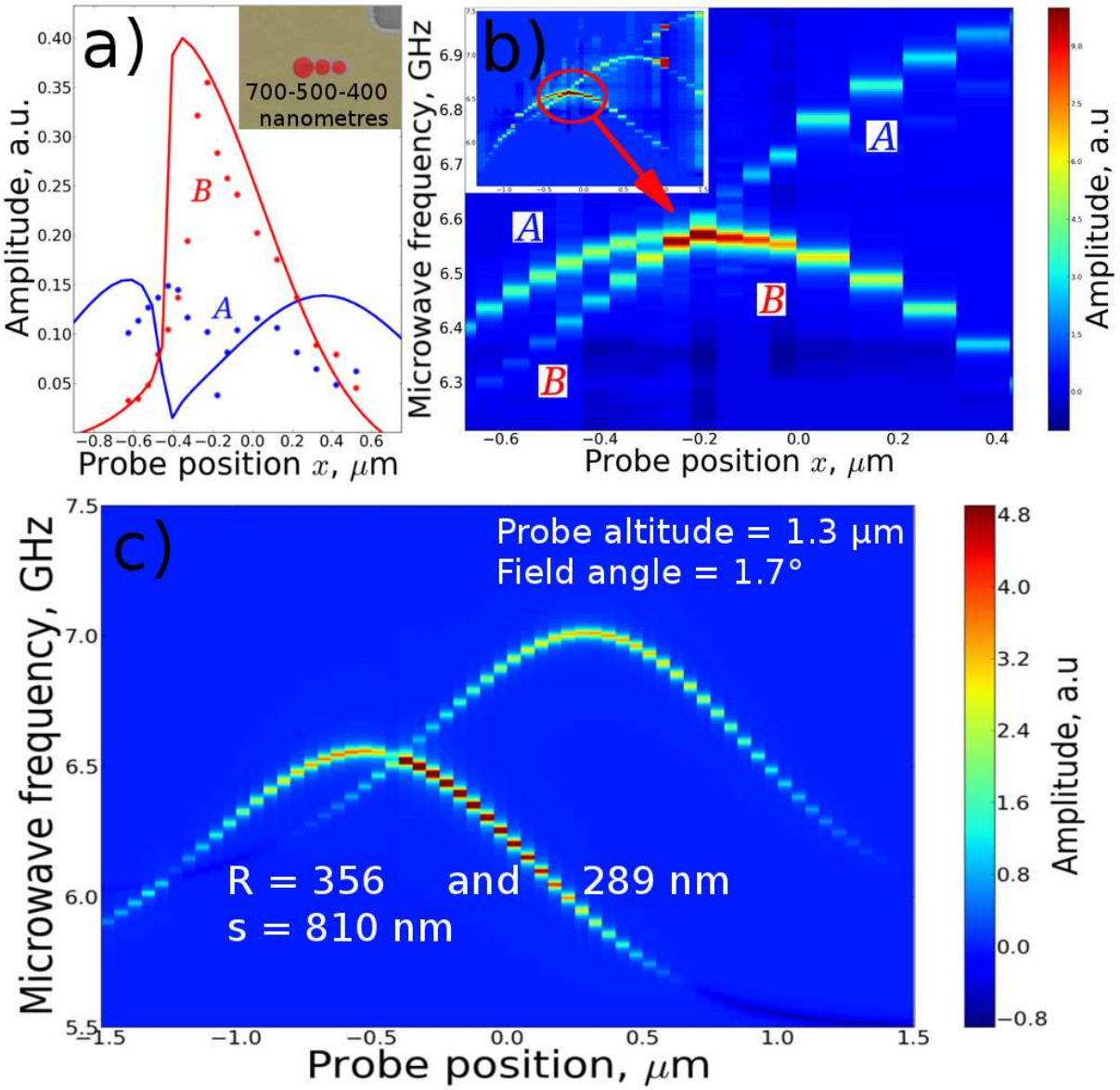

Figure 6.16: a) Coupled mode amplitudes corresponding to the two largest NiMnSb discs around the compensation point. b) Zoom of the figure 6.15 showing the region of maximum coupling above the 700 nm disc. c) Calculation of the coupled frequencies corresponding to figure 6.15.

The figure 6.16b displays a zoom of this interesting crossing region. The anti-crossing is difficult to identify at this point, because the coupling strength is smaller than in the case of Fe-V. The dynamical splitting depends strongly on the saturation magnetisation M_s, which is here three times smaller than Fe-V. Using the formula for Ω developed in the previous section, a value of $\Omega \simeq 10.5$ MHz is found in the case of the two largest discs. This is well below the linewidth of the resonance, corresponding roughly to $\Delta f = 2\alpha f \approx 30$ MHz. The anti-crossing of the coupled frequencies is therefore "buried" into the linewidth

Nevertheless, the measured amplitudes of the coupled modes, presented as coloured dots on the figure 6.16a, provide the signature of a collective dynamics. As depicted in the figure 6.9 for the Fe-V sample, the binding mode B amplitude increases drastically at the anti-crossing, while the anti-binding mode A amplitude is decreased. Notice that

the latter does not vanish completely. This is due to the fact that the hybridisation state of the collective modes is here partial at the anti-crossing, the compensation point being displaced from the middle of the discs due to the difference of diameters. The two magnetic oscillators are different in volume, and the magnetisation precession has a different weight in each one, even at the anti-crossing.

Following the analysis of the coupled discs of Fe-V, the behaviour of the coupled modes was calculated for the two largest NiMnSb discs. The diagram of the coupling is presented figure 6.16c with the fitting parameters used, while the calculated amplitudes are superimposed to the data points on the figure 6.16a. The qualitative agreement found with the experiment allows to validate the occurrence of a coupled dynamics in this asymmetric system.

Even if the collective dynamics of this asymmetric oscillator pair has been demonstrated, the interest for potential applications is limited. An array of identical discs is indeed more simple to realise and control because of the well defined hybridisation state at the anti-crossing. Moreover, the maximum of the coupling should be reached without any external field or gradient sources.

6.4 Conclusion

The problem of the collective dynamics of two neighbouring discs dipolarly coupled, modelled in chapter 2, was explored experimentally. It was first shown that the f-MRFM is a relevant tool in order to measure such tiny signal. We demonstrated how to take advantage of the slight perturbation introduced by the probe stray field to tune and detune continuously the frequencies of our coupled oscillators. This experimental trick allowed us to measure accurately the dynamical splitting between the two collective modes, which gives the strength of the dipolar coupling in the system. The influence of the geometry was demonstrated, firstly by varying the edge to edge separation between disc in a pair. And then by varying the shape of the discs, as well as their numbers. In particular the hybridisation of the collective dynamics in each oscillator was discussed.

This study is rather interesting in the way to demonstrate the ability of the f-MRFM to measure accurately the coupling strength Ω of any kind of coupled magnetic systems. This interesting advantage could be for instance very useful to the field of magnonics. The aim of this field is to engineer magnetic materials at the nanoscale in order to use spin waves for data storage applications and information processing [81, 35]. For this purpose, the spin wave dispersion of periodic magnetic nanostructures are studied and a particular attention is focused on the band gaps that forms due to the collective spin wave dynamics.

Once this precise analysis done on a well characterised magnetic state, we should try to apply the same method to the vortex state. Indeed, the vortex state is also a promising candidate as a microwave generator in new kinds of spin transfer torque devices [109]. The choice of the magnetic state of the two magnetic layers in an STNO is crucial for the efficiency of the spin transfer torque, and it was recently demonstrated that the vortex state has a lot of advantages [86, 38]. In particular, if one or both layers are in the vortex state, the linewidth of the microwave emission is substantially reduced.

Nevertheless, the emitted power of such an individual pillar is very small taken individually, typically in the nano-watt range. To overcome this difficulty, the concept of

coupled spin torque oscillators arranged in array and emitting in phase was proposed [46, 10]. In such an ideal array, the emitted power goes like N^2, where N is the number of coupled oscillators. Moreover, the linewidth of the emission is improved.

The goal of a future study is indeed to be able to couple the gyrotropic modes of several discs in the vortex state through the dipolar interaction. Even if the expected strength of the dipolar interaction is similar to the saturated case, our preliminary experiments revealed the real complexity of this unsaturated state. Experiments similar to these presented here in the saturated state have been performed in the vortex state with the same sample and clear evidences of a collective dynamics have been seen. But the f-MRFM probe is now in a strongly perturbative regime which affect the static and dynamic structure of the vortex. This regime has now to be controlled to explore the coupling between vortices.

Conclusion

The main goal of this thesis was to contribute to a better understanding of the spin wave spectra of magnetic nano-discs, involved in spintronic devices like STNOs. The study was particularly focused on the vortex state that has been found to be the stable remanent ground state of these nanostructures.

Our first original contribution was to study the dependence of the vortex dynamics versus a perpendicular bias field. In particular, the low-frequency gyrotropic mode experienced by the vortex core was found to be bi-stable. The degeneracy in frequency of this mode between the two core polarities is lifted by the bias field in a Zeeman like effect. The frequency of the mode increases linearly with the field if the core polarity is oriented in the same direction and decreases for the opposite polarity. This splitting could be properly explained using simple theoretical arguments to describe the deformation of the vortex structure by the bias field.

The gyrotropic mode driven in the non linear regime leads to the dynamical core reversal, which was extensively studied. The way to optimise the resonant core switching in an individual disc using a single microwave pulse was shown. The f-MRFM was of great interest for this study since we could perform accurate statistics of the reversal events in a reasonable acquisition time. The influence of the perpendicular field on the reversal statistics was also investigated. Interestingly, the minimal pulse power needed to reverse the core was found to be independent of the bias field. We used the analogy with the microwave assisted switching of a nanoparticle to describe the phenomenon. But we could only give simple assumption and further work is needed to have a better understanding of the physics involved.

We have taken advantage of the non linear dynamics experienced by the vortex core near the reversal threshold to study the relaxation of the gyrotropic mode far from equilibrium. It was found that the relaxation time, linked with the magnetic damping, could be increased by a factor of three in this non linear regime. The physical origin of this effect is the non linear coupling between the gyrotropic mode and the higher order spin wave modes, in particular the azimuthal modes. Nevertheless, a full microscopic and even phenomenological description of this phenomenon is missing at this time.

On this purpose, we have studied the azimuthal spin waves developing in the plane of the vortex. The predicted splitting between modes of opposite indices ($l = \pm 1, \pm 2...$) due to the dynamical interaction with the core was observed. With our f-MRFM setup, we could even measure their frequency dispersion under a perpendicular field. But the interpretation, done by comparison with numerical simulations is incomplete since a reliable theoretical description is missing.

From a practical point of view, it was demonstrated that the stability of the vortex state as well as its core polarity could be exploited in a full solid-state magnetic memory.

The combination of the resonant core switching and the bi-stability of the gyrotropic mode under a perpendicular field led to a proposal for an efficient read/write process for this future memory.

The second main achievement of this thesis is the demonstration of the collective dynamics inside nano-discs coupled by the dipolar interaction. Before addressing the problem of coupled vortices, for which no complete theoretical description is available, we have studied the case of perpendicularly saturated disc pair placed nearby laterally. The f-MRFM probe was used to provide a local field gradient needed to tune differentially the frequency of the spin wave modes in each disc. It also provides a local detection of the dynamics. This experimental control of the system at the nanoscale allowed us to measure accurately the coupling strength, or dynamical splitting, which is the frequency splitting between the two coupled modes. The influence of the geometry on the dipolar interaction has also been investigated. In particular the influence of the pair separation as well as the asymmetry between discs was measured. Moreover, the theoretical analysis and the numerical simulations developed here could explained satisfactorily the collective modes frequencies as well as their relative amplitude.

We would like to emphasise that these studies were possible thanks to new high quality ferromagnetic materials having ultra low damping: NiMnSb and FeV. The search for novel materials with improved properties is of course of fundamental importance in designing new spintronic devices. In that sense, we participated in the evaluation of these materials towards their integration in real STNOs.

As perspectives, two main directions can be given to extend this thesis work. As the samples are already available, the study of the collective dynamics should be continued and understood in the vortex state. This is of fundamental importance for the promising vortex based STNO. The problem is much more complicated since this is an unsaturated state. The vortex is easily deformable by applied field of any kind and new idea are needed to be able to control the gyrotropic frequency of each disc in a pair.

Then the problem of the coupled dynamics, restricted to the dipolar interaction, could be open to other coupling mechanism. For instance, the discs of a pair can be linked by a metallic stripes, which will allow the transfer of angular momentum between discs by conduction electrons. An interesting insight in the spin pumping phenomena could be given by such experiments.

Appendix A

Calculation of the gyrotropic frequency

A.1 The Thiele equation

The gyrotropic mode, wich is a circular motion of the vortex core around its equilibrium position, is well described by the Thiele equation:

$$\bar{\bar{M}}\ddot{\boldsymbol{X}} - \boldsymbol{G} \times \dot{\boldsymbol{X}} - \bar{\bar{D}}\dot{\boldsymbol{X}} + \frac{\partial W(\boldsymbol{X})}{\partial \boldsymbol{X}} = 0 \tag{A.1}$$

Here $\boldsymbol{X}$ is the position of the vortex core, $\bar{\bar{M}}$ is a mass term that can be neglected, $\boldsymbol{G} = -G.\boldsymbol{u}_z$ is the gyrofield created by the shifted vortex and $\bar{\bar{D}} = -d.G$ is a diagonal tensor describing the damping.

The vortex potential energy, in the linear approximation has an harmonic form: $W(\boldsymbol{X}) = W(0) - \frac{\kappa \boldsymbol{X}^2}{2}$. The Zeeman energy has to be added, which lead to the form:

$$W(\boldsymbol{X}) = W(0) + \frac{\kappa \boldsymbol{X}^2}{2} + \mu(\boldsymbol{u}_z \times \boldsymbol{h}).\boldsymbol{X} \tag{A.2}$$

The Thiele equation then becomes:

$$-\boldsymbol{G} \times \dot{\boldsymbol{X}} - \bar{\bar{D}}\dot{\boldsymbol{X}} + \kappa \boldsymbol{X} + \mu(\boldsymbol{u}_z \times \boldsymbol{h}) = 0 \tag{A.3}$$

Let expand it:
$$G \begin{vmatrix} -\dot{Y} \\ \dot{X} \\ 0 \end{vmatrix} - D \begin{vmatrix} \dot{X} \\ \dot{Y} \\ 0 \end{vmatrix} + \kappa \begin{vmatrix} X \\ Y \\ 0 \end{vmatrix} + \mu \begin{vmatrix} -h_y \\ h_x \\ 0 \end{vmatrix} = 0$$

The convenient complex coordinates $\boldsymbol{Z} = X + iY$ is introduced. Then by adding line 1 plus i times line 2, we get:

$$iG\dot{\boldsymbol{Z}}(t) - D\dot{\boldsymbol{Z}}(t) + \kappa \boldsymbol{Z}(t) + i\mu(h_x + ih_y) = 0 \tag{A.4}$$

The more convenient is to use the Green's function formalism, in order to consider any kind of excitation field $\boldsymbol{h}$. We first make a Fourier transform on the equation:

$$\boldsymbol{Z}(\omega) = \frac{-i\mu}{\kappa - \omega(G + iD)} . \int_{-\infty}^{+\infty} (h_x(t) + ih_y(t)) e^{i\omega t} dt \tag{A.5}$$

The Green function of the "Thiele operator" is then:

$$\mathcal{G}(w) = \frac{1}{\kappa - \omega(G + iD)} \tag{A.6}$$

To get the Green's function in the real space, we do another Fourrier transformation:

$$\mathcal{G}(t) = \frac{1}{2\pi}\int_{-\infty}^{+\infty} \frac{e^{-i\omega t}}{\kappa - \omega(G+iD)} d\omega = \frac{1}{2\pi}\int_{-\infty}^{+\infty} \frac{e^{-i\omega t}}{(\frac{\kappa}{G+iD} + \omega)(G+iD)} d\omega \tag{A.7}$$

This function has a singularity at $\omega = \frac{\kappa}{G+iD}$. Using Jordan's and the residues theorems, we calculate:

$$\mathcal{G}(t) = \frac{2i\pi}{2\pi}.Res(\frac{e^{-i\omega t}}{\kappa + \omega(G+iD)}, \frac{\kappa}{G+iD}) = \frac{i}{G+iD}\ e^{i(\frac{\kappa}{G+iD})t} \tag{A.8}$$

The singularity can be decomposed in real and imaginary part as: $\omega = \frac{\kappa G}{G^2+D^2} - \frac{i\kappa D}{G^2+D^2}$. The real part then corresponds to the gyrotropic frequency: $\omega_G(0) = \frac{\kappa G}{G^2+D^2}$. We have now the Green's fonction in time domain:

$$\mathcal{G}(t) = \frac{i}{G+iD}\ e^{i\omega_G t} e^{-d\omega_G t} \tag{A.9}$$

A.2 Response to a circularly polarized excitation

We consider here a microwave excitation field circularly polarized: $\boldsymbol{h} = h_0[cos(\omega_0 t).\boldsymbol{u}_x + sin(\omega_0 t).\boldsymbol{u}_y]$. By definition of the Green's function:

$$\boldsymbol{Z}(t) = \int_{-\infty}^{+\infty} \mathcal{G}(t-t').[h_x(t') + ih_y(t')]\ dt' \ +\ \textit{homogeneous solution} \tag{A.10}$$

The excitation goes from 0 to t and $[h_x(t) + ih_y(t)] = cos(\omega_0 t) + i\ sin(\omega_0 t) = e^{i\omega_0 t}$, so that:

$$\boldsymbol{Z}(t) = \frac{\mu h_0}{G+iD} e^{i(\frac{\kappa}{G+iD})t} \int_0^t e^{-i(\frac{\kappa}{G+iD})t'}\ e^{i\omega_0 t'} dt' = \frac{\mu h_0}{G+iD} e^{i(\frac{\kappa}{G+iD})t} \left[\frac{e^{-i(\frac{\kappa}{G+iD} - \omega_0)t'}}{-i(\frac{\kappa}{G+iD} - \omega_0)}\right]_0^t \tag{A.11}$$

$$\boldsymbol{Z}(t) = \frac{i\mu h_0}{\kappa - \omega_0 G - i\omega_0 D}\left(e^{i\omega_0 t} - e^{i\omega_G t} e^{-d\omega_G t}\right) \tag{A.12}$$

As the homogeneous solution only gives:

$$\boldsymbol{Z}(t) = \boldsymbol{Z}(0) e^{i\omega_G t} e^{-d\omega_G t} \tag{A.13}$$

We have the entire solution in the form:

$$\boldsymbol{Z}(t) = (\boldsymbol{Z}(0) - \boldsymbol{Z}(\infty)) e^{i\omega_G t} e^{-d\omega_G t} + \boldsymbol{Z}(\infty) e^{i\omega_0 t} \quad with: \quad \boldsymbol{Z}(\infty)) = \frac{i\mu h_0}{\kappa - \omega_0 G - i\omega_0 D} \tag{A.14}$$

Appendix B

Résumé substantiel en Français

B.1 Introduction

Les récents progès réalisés dans la croissance de couche minces de matériaux ferromagnétiques de haute qualité, ainsi que les progrès des techniques de nano-lithographie modernes ont renouvelé l'intéret porté à la dynamique de l'aimantation. D'un point de vue fondamental, la dynamiques des ondes de spin d'états de base magnétique non uniforme spatiallement peut maintenant être étudiée. Ces progrès rendent aussi possible le contrôle et la manipulation de l'aimantation dans des objets microscopiques.

Ces petits objets sont d'un grand intérêt pour le stockage de données et le traitement d'informations binaires, applications pour lesquelles il est crucial de contrÃ´ler efficacement l'état magnétique de nano-structures. Le problème du retournement de l'aimantation implique un compromis entre consommation d'énergie et vitesse. C'est pourquoi la mise à profit de processus résonants peut être intŕessante pour amener efficacement l'aimantation hors d'équilibre [7, 1, 117]. Il est alors essentiel d'identifier les modes propres d'onde de spin du système qui gouvernent la dynamique de l'aimantation. Plus récemment, il a été démontré que les ondes de spins elles-mêmes peuvent être utilisées pour manipuler l'information. L'idée est alors de transférer et manipuler l'énergie stockée dans chaque modes propres du système. Ce nouveau champ d'étude, appelé "Magnonics", étudie les propriétées collectives de nanostructure magnétique périodique et tente de comprendre la propagation et les intéractions entre ondes de spin, de manière a les manipuler de façon controllée [81, 73].

parallélement à ces dévellopements, l'idée d'utiliser le degré de liberté de spin dans les propriétées de transport à émergée. La découverte de l'effet de magnéto-résistance géante [8, 14] en 1988 (Nobelisée en 2007 avec Albert Fert et Peter Grünberg) suivie de la découverte de la magnéto-résistance tunnel a lancé la "Spintronique". Ces dćouvertes ont motivées le dévellopement puis la commercialisation de nombreuses applications, particulierement pour le stockage d'informations et les capteurs de champ [97, 3, 36, 103], les capteurs bio-compatible [45], et plus recemment les MRAM (magnetic random access memories) [24]. Dans un dispositif typique de la spintronique, les éléctrons sont polarisés en passant au travers d'une couche magnétique dont les propriétées de transport sont anisotropes par rapport à la direction des spins éléctronique. Le éléctrons ainsi polarisés sont diffusés par une seconde couche éléctronique, dite "couche libre", produisant un couple sur son aimantation. Au lieu d'utiliser des champs magnétiques, il devient possible de manipuler l'aimantation avec un courant polarisé en spin. La tendance actuelle est

d'exploiter ce transfert du moment angulaire de spin des éléctrons de conduction vers l'aimantation de nano-objets magnétiques metalliques [13, 123]. Ce transfert de moment angulaire induit un couple qui excite efficacement des auto-oscillations de grande amplitude de l'aimantation [75, 64] pouvant générer des signaux mico-onde dans la gamme de fréquence 0.28 à 65 GHz [38, 17]. Ces nano-oscillateurs à transfert de spin sont prometteurs en terme d'applications grâce à leur large spectre d'emission et leur vitesse de balayage en fréquence ainsi que leur intégration facile dans les processus de fabrication en couches minces. Pour exploiter le potentiel de ces oscillateurs, leur cohérence spéctrale doit être améliorée ainsi que leur puissance d'émission. Dans ce but, leur spectre d'onde de spin doit être précisement compris.

Dans le cas de nanostructures, l'état magnétique de base est souvent non uniforme spatiallement à cause de la compétition entre énergies d'échange et dipolaire. L'état magnétique dépend de la nature du matériau utilisé (principalement au travers de l'aimantation à saturation M_s et de la constante d'échange A) et de facteurs géométriques: rayon R et épaisseur L de la nanostructure. Une grande variété d'états magnétiques ont été décrit ainsi que leur stabilité gométrique dans le plan épaisseur/rayon.

Du point de vue de la dynamique, l'état vortex est particulièrement intéressant. L'état vortex est la configuration magnétique stable de structures en fines plaquettes ou disques de matériaux doux. Il existe pour une certaine gamme de tailles, avec $L > l_{ex}$ et $R \gg l_{ex}$ relativement à la longueur d'échange l_{ex} du matériau dont le disque est fait [54, 29]. La dynamique de l'aimantation de la plupart des états non uniformes est généralement très compliquée [9], mais la dynamique de l'état vortex est grandement simplifié par les symmétries du système. En particulier, le mode de plus basse énergie, isolé à basse fréquence, correspond à une rotation du coeur de vortex autour de sa position d'équilibre au centre du disque. La fréquence typique de ce mode peut être infrérieure de plusieurs gigahertz à celle des autres modes d'ondes de spin. Cette large séparation en énergie s'avère importante lorsque l'on considère l'excitation ou l'amplification d'un mode unique par transfert de spin [109]. De plus, les oscillateurs à transfert de spin basés sur l'état vortex présentent une largeur de raie d'émission sufisamment faible pour envisager de potentielle applications. Malgré tout, un effort important est encore à faire pour comprendre et modéliser la dynamique de l'aimantation de nano-disques dans l'état vortex.

Une autre approche prometteuse pour améliorer la cohérence de phase des oscillateurs à transfert de spin est de les coupler de manière cohérente lorsqu'ils sont arrangés en large réseaux [122]. Plusieurs méchanismes ont été proposés pour les coupler: un courant micro-onde [46], la propagation d'ondes de spin [70, 88], l'effet de pompage de spin [143] ou encore l'intéraction magnéto-dipolaire [10]. Cette dernière est la plus simple car elle elle est toujours présente naturellemnt, mais elle a été peu étudiée dans le cas d'états magnétiques complexes. L'état le plus simple pour cette étude de la dynamique collective de l'aimantation sous l'influence du couplage dipolaire est une paire de nano-disques dans l'état saturé. C'est en effet un des rares systèmes pour lequel le couplage dipolaire dynamique peut être calculé analytiquement.

Enfin nous mettons l'accent sur le point suivant: cette é'tude s'interesse à des processus résonant, de plus, améliorer la largeur de raie d'émission des oscillateurs à transfert de spin est crucial pour réaliser des applications pratiques. A cet effet nous avons utilisé des matériaux ferromagnétiques ayant les ammortissements magnétiques les plus bas parmis les métaux. Le premier est semi métal, alliage ordonné de NiMnSb: c'est un composé de la famille des Heusler. Le second matériau utilié est un alliage ordonné de FeV. Comme

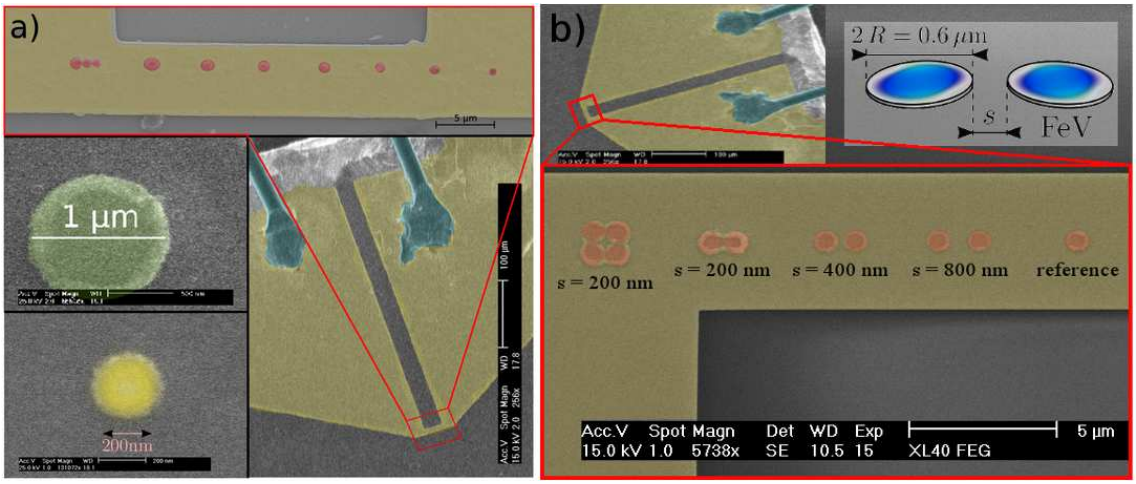

Figure B.1: Echantillons utilisés pendant cette thèse. Ils sont constitués de disques de NiMnSb a) et de FeV b) de différentes tailles sur lesquels est déposés une antenne micro-onde, après une fine couche isolante.

pour le NiMnSb, son ammortissement de Gilbert se situe autour de $\alpha \simeq 2 \times 10^{-3}$. Dans chaque cas, les études sont réalisées sur des films minces nanostructurés, dont la croissance est faite par épitaxie par jet moléculaire.

B.2 Méthode expérimentale

Une technique expérimentale appropriée doit maintenant être choisie pour mesurer le spectre d'onde de spin de ces nano-disques. Plusieurs options sont actuellement disponibles:

1. Dans des hétéro-structures métalliques, il est possible de mesurer la dynamiqe de l'aimantation grace aux effets GMR/TMR. Dans un oscillateur à transfert de spin, le produit d'un courant micro-onde avec les ondes de spin à hautes fréquences produit une tension continue [115, 131]. De manière compl'ementaire, la réistance micro-onde associée aux auto-oscillations d'ondes de spin produit une tension haute fréquence si elle est mixée avec un courant continu [75]. Il es même maintenant possible de détćter la dynamiqe grâce à l'effet Hall de spin [40, 111]. La sensibilité de ces techniques est grande et adaptée aux nano-structures. Mais d'un point de vue fondamental, il est toujours intéressant de comprendre la dynamique en l'abscence de courant de charges, qui introduit une nouvelle intéraction.

2. Les techniques inductives calssiques de résonance férromagnétique. Les ondes de spin sont détéctées grace à l'énergie micro-onde qu'elle absorbent dans une cavité résonnante. La précision spéctroscopique est grande, mais le rapport signal sur bruit dépend de manière critique du facteur de remplissage, qui est le rapport du volume de l'échantillon sur celui de la cavité. Cela restreint généralement cette technique à des échantillons macroscopiques, même si il est à noter que le développement de micro-antennes ouvre la voie à l'étude de nanostructures.

3. Les méthodes optiques. Les propriétées d'un faisceau lumineux cohérent, fréquence ou polarisation, sont modifiées aprés l'intéraction avec une onde de spin.

La premiére méthode est la microscopie kerr résolue en temps qui réalise une analyse vectorielle tridimentionnelle de la partie transverse de l'aimantation dynamique [1, 63]. La seconde méthode est la diffusion Brillouin [106, 69], qui mesure directement les modes d'onde de spin dans l'éspace des vecteurs d'ondes. En balayant le faisceau lumineux, ces deux techniques peuvent atteindre une résolution de spatiale de l'ordre de la centaine de nanomètres. Une troisième méthode est le dichroisme circulaire des rayons X sur la matière magétique [2]. Le faisceau de rayons x monochromatique pulsés d'un synchrotron est utilisé pour mesurer l'aimantation hors d'équilibre. Les méthodes optiques sont intéressantes car non perturbatives, mais elles requièrent un accès optique à l'échantillon. De plus, la mesure temporelle de l'aimantation transverse réduit la précision spéctroscopique, particulirement dans le cas de modes à basse fréquence et faible largeur de raie.

Pour ces travaux de thèse, nous avons choisi d'utiliser une détéction mécanique de la résonance férromagnétique [113, 150, 76]. Un microscope/spéctromètre de force à résonance magnétique a été construit au laboratoire. L'idée de base est de coupler la technique de champ proche (microscopie de force atomique/magnétique) avec la spéctrométrie.

Le champ de fuite fortement non homogène d'une nanostructure férromagnétique produit une force sur une moment magnetique, une particule sphérique de fer (en vert sur la figure B.2a), placée dans le champ proche de l'échantillon. Cette particule est collée au bout d'un résonnateur mécanique, un simple levier extrememement souple, qui transforme cette force en déplacement mesurable. Lorsque la dynamique de l'aimantation est excitée dans l'échantillon par un champ micro-onde (produit par une antenne, représentée en doré sur la figure B.2a), la composante longitudinale de l'aimantation (ΔM_z) varie sous l'effet de sa précession. La force appliquée sur la particule est modifiée et le déplacement du levier, proportionnel à cette variation, peut être mesuré par interférométrie.

Cette technique expérimentale présente de nombreux avantages pour réaliser les expériences spéctroscopiques envisagées plus tôt:

1. C'est une technique de champ proche qui permet de détécter la résonance férromagnétique localement. En utilisant le gradient de champ crée par la particule de fer, il est aussi possible de localiser la résonance spatiallement, à la manière des techniques d'IRM (imagerie par résonance magnétique). De plus, ce champ de fuite inhomogène peut être utilisé pour ajuster de manière continue la fréquence de résonance de nano-objets.

2. Le facteur de remplissage peut aisement être optimisé en choisissant une taille de particule comparable à celle de l'échantillon. Cette détection de la résonance par un transformateur force-déplacement est une des plus sensible existante. A température ambiante avec un levier commercial, une résolution de $100\mu_B$ est facilement atteinte. Cette sensibilité est suffisante pour mesurer les oscillations d'un coeur de vortex.

3. La dynamique de l'aimantation est mesurée dans le domaine fréquenciel avec un dispositif en onde continue. La résolution spéctroscopique est alors arbitrairement élevée, étant seulement limitée par la résolution spéctrale de la source micro-onde. Cette configuration est bien adaptée a la dynamique basse fréquence du vortex ainsi q'aux faibles largeurs de raie des modes considérés. C'est aussi une méthode appropriée 'à la résolution spéctroscopique de mode très proche en fréquence.

4. La dynamique de l'aimantation est révélée par la mesure statique de la variation longitudinale de l'aimantation ΔM_z. Cette technique donne donc directement accès au temps de relaxation T_1. Cela donne un point de vue expérimental complementaire de la plupart des autres techniques qui mesurent la composante transverse de l'aimantation, et donc T_2.

5. L'étude de l'état saturé de nanostructures magnétiques requiert l'application d'un fort champ magnétique (jusqu'a 2 Tesla dans notre cas). Le microscope utilisé dans cette thèse a été conu en matériaux mon magnétiques autorisant l'utilisation de champ intense.

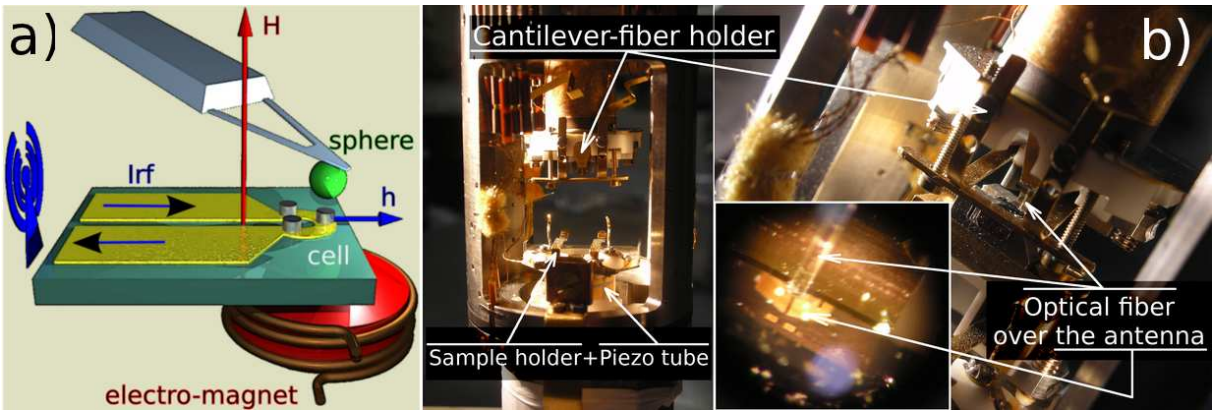

Figure B.2: a) Schema de principe du fonctionnement d'un microscope de force à résonance magnétique. b) Photos du dispositif expérimental construit au laboratoire.

Le dispositif expérimental réel est detaillé sur la figure B.2b. On peut y voir le coeur du microscope avec le dispositif de champ proche: tubes et scanners piezo-éléctriques, interféromètre avec fibre optique et résonateur mécanique. On voit aussi l'antenne micro-onde large bande utilisée pour la spéctroscopie.

B.3 L'état saturé

Du point de vue de la dynamique de l'aimantation, un état saturé uniforme constitue une bonne référence. Nous avons donc choisi de commencer notre étude en saturant perpendiculairement nos nano-disqes de (voir figure B.1b).

Le spectre d'ondes de spin de peut être calculé analytiquement dans ce cas précis [76, 137, 99]. Le confinement due à la taille réduite des disques discrétise les vecteurs d'ondes. La symétrie axiale permet de définir une bonne base de fonctions propres pour diagonaliser le système: les fonctions de Bessels. Les modes sont décomposés en mode radiaux, présentant m noeuds de précession selon le rayon du disque, et azimuthaux, ayant l noeuds de précession autour de la circomférence du disque. Ils sont numérotés par un couple (l, m) et leur fréquence peut être calculées avec une grande précision.

Ces modes sont mesurés sur des disques de NiMnSb de diffŕents diamt̀res sur la figure B.3. Le mode de plus basse énergie est le mode uniforme, pour lequel l'aimantation

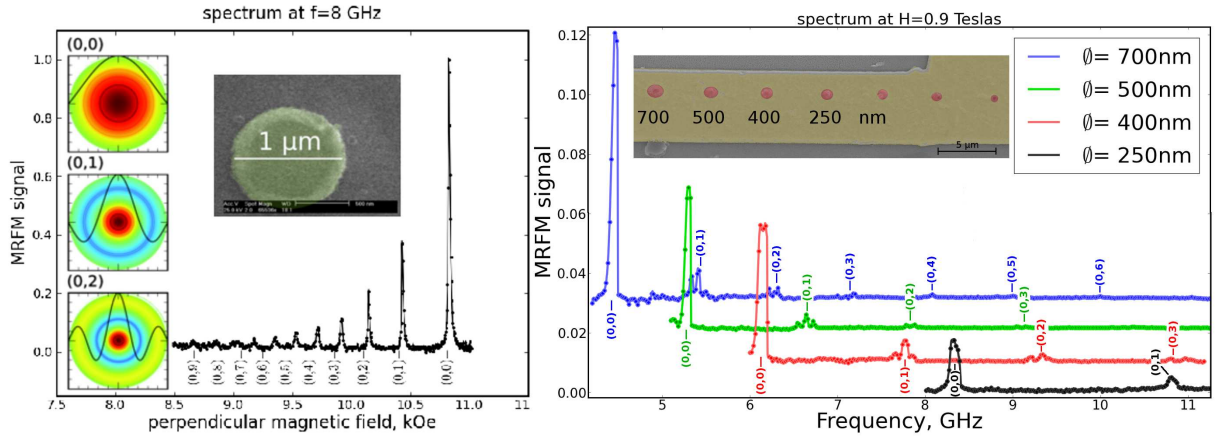

Figure B.3: Spectre d'onde de spin dans létat saturé perpendiculairement d'un disque de NiMnSb de 1 micron de diamètre a) et de quatre disques de diamètre compris entre 700 et 250 nanomètres. Leurs fréquences (tirets et indices) sont calculées analytiquement.

précesse en phase dans tout le disque. On voit sur la figure B.3 à droite l'influence du confinement sur la fréquences de ces modes.

De manière à comprendre la dynamique de l'aimantation dans des réseaux denses de disques magnétiques, nous avons réalisé une étude préliminaire sur un système de deux disques de FeV de 600 nanomètres de diamètre couplés par l'intéraction magnéto-dipolaire. Si on considére deux disques dont l'onde de spin à une fréquence ω_1 et ω_2 proche spatiallement l' un de l'autre, une dynamique couplés va apparaitre et réveler deux modes couplés de fréquences:

$$\omega_{A,B} = \frac{\omega_1 + \omega_2}{2} \pm \sqrt{\left(\frac{\omega_1 - \omega_2}{2}\right)^2 + \left(\frac{\Omega}{2}\right)^2} \tag{B.1}$$

Ces deux modes s'anti-croisent lorsque $\omega_1 = \omega_2$ et Ω est l'écart en fréquence des deux modes à cet endroit. Le couplage est médié par le champ magnéto-dipolaire dynamique rayonné par un disque sur son voisin.

Nous avons utilisé le gradient de champ de la particule magnétique du microscope pour ajuster différentiellement la fréquence de chaque disque en la déplaąnt latéralement au dessus de ceux-ci. La figure B.4 présente les diagrammes d'onde de spin couplées pour trois séparations décroissantes. En abcisses, la position de la sonde est une mesure relative du désaccord de fréquences entre les deux disques, tandis que l'ordonnée donne la fréquence des modes couplés. On voit bien apparaitre deux modes couplés, correspondant à une précession en phase et en opposition de phase, qui s'enticroisent lorsque les fréquences de chaque disques coincident.

En utilisant la thórie des ondes de spin et la formule des fréquences couplées, il est possible de calculer le comportement des modes couplés. Les diagrammes calculés sont comparés aux expériences sur la figure B.4.

Nous avons ainsi pu comprendre la dynamiques des modes couplés sur ce systéme simple. La mesure de Ω fournit de précieux renseignements sur la manière d'optimiser la géométrie de futures réseaux de disques. Enfin, nous avons démontré la perti-

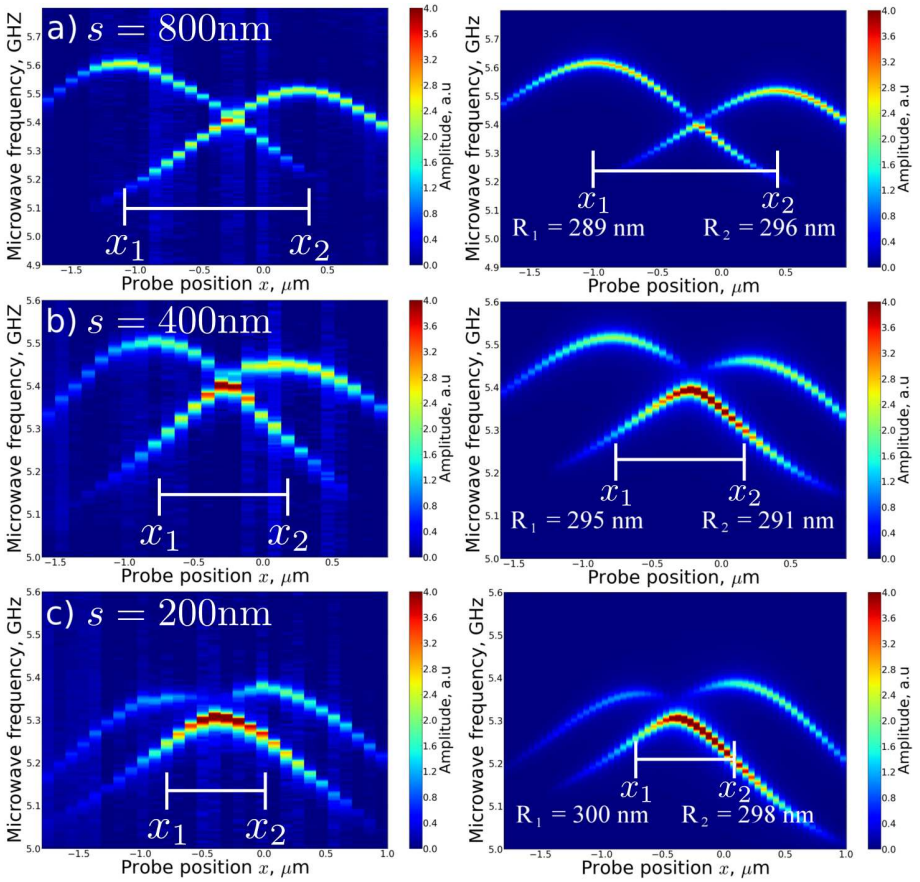

Figure B.4: Diagrammes expérimentaux (gauche) et calculés théoriquement (droite) des modes d'onde de spin couplés pour trois séparation diffŕentes entre disque de FeV de diamètre 600 nanomètres.

nence de notre technique de mesure pour détécter les effets du couplage de manière précise.

B.4 L'état vortex

L'état magnétique rémanent de nos nano-disques est une structure vortex. L'aimantation forme une boucle dans le plan du disque de manière à minimiser l'énergie magnéto-dipolaire, tandis qu'au centre l'aimantation est orientée hors du plan sur un rayon de l'ordre de la longueur d'échange, de manière à régulariser la singularité due à l'énergie d'échange. La caractéristique principale du vortex est la préscence de cette structure centrale, où coeur de vortex, dont l'orientation relative est définie par la polarité $p = \pm 1$.

La structure statique du vortex a été décrite par plusieurs models analytiques. La difficulté étant de reproduire correctement le coeur de vortex, dont la taille est calculée en minimisant l'énergie magnétique totale du système. Le calcul de la susceptibilité statique permet alors de comprendre la réponse du vortex á un champ magnétique exterieur.

Dans cette thse nous nous sommes intéressés à la dynamique de l'aimantation dans

l'état vortex. Plus particulièrement, le mode de plus basse énergie, ou mode gyrotropique, à été étudié en détail. Ce mode consiste en une rotation à basse fréquence (100 MHz - 1GHZ) du coeur de vortex autour du centre du disque. Sa fréquence de résonance a été calculée à partir de l'equation de Thiele [128], qui au premier ordre décrit la dynamique d'une paroi de domaine rigide se déplaçant sur un fond magnétique. En première approximation on trouve la formule [50] $\omega_G = 20/9\gamma M_s L/R$ à champ nul. Nous avons alors étudié l'influence d'un champ magnétique appliqué perpendiculairement au plan du disque sur ce mode. L'aimantation se trouvant dans le plan du vortex à champ nul est deviée hors du plan, d'un angle linéairement proportionnel au champ magnétique. L'expression précédente doit être modifiée pour tenir compte du champ perpendiculaire H_z [32]: $\omega_G(H_z) = \omega_G(0)[1 + pH_z/H_S]$; où H_s est le champ de saturation du disque magnétique. Ce mode subit l'équivalent d'un effet Zeeman, sa féquence de résonance ayant une dépendance avec le champ opposée pour chaque polarite p.

Les modes d'onde de spin à plus haute fréquence sont de nature comparable à ceux observés dans l'état saturé. Ils consistent en une combinaison d'ondes radiales et azimuthales, notées (l, m) se développant dans le plan du vortex, la différence étant la présence du coeur de vortex au centre du disque.

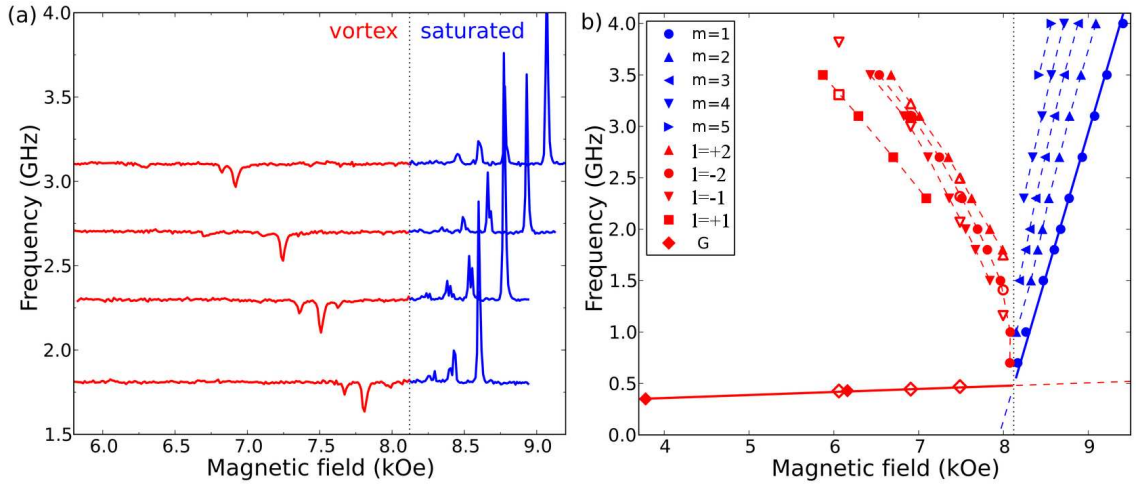

Figure B.5: Spectre d'onde de spin en fonction du champ perpendiculaire dans l'état vortex puis saturé. Le mode gyrotropique est noté G, puis on voit les modes azimuthaux $l = \pm 1, 2$ dans l'état vortex et $m = \pm 1, 2$ dans l'état saturé.

Expérimentallement, ces modes sont excités par un champ micro-onde, polarisé linéairement, appliqué dans le plan du disque. Le diagramme d'onde de spin général est présenté figure B.6. Sur la partie de droite, le mode de plus basse énergie est le mode gyrotropique (noté G) de polarité $p = +1$ (parallèle au champ appliqué). Sa dépendance en champ est bien décrite par la théorie. A plus haute fréquence, on identifie les premiers modes azimuthaux, qui ont une dépendance en champ inversée.

Le mode gyrotropique est d'un intérêt particulier car il est isolé à basse fréquence. Cela en fait un candidat potentiel pour réaliser un oscillateur à transfert de spin dans l'état vortex [86]. De plus, le régime non linéaire de ce mode est particulièrement riche. Lorsque le coeur de vortex est excité à grande amplitude, il se déforme dynamiquement, et si sa vitesse radiale dépasse une valeur universelle [85] $V_c =$

$1.66\sqrt{A_{ex}}$ (où A_{ex} est la constant d'échange du matériau) la polarité du coeur se renverse [134]. Nous avons étudié en détail ce retournement dynamique du coeur de vortex. Nous avons en particulier montré que le retournement peut-être efféctué à l'aide d'une courte impulsion micro-onde, dont nous avons optimisé la durée, la fréquence et la puissance.

La combinaison de l'effet Zeeman observé sur chaque polarité du mode gyrotropique en champ perpendiculaire associé au retournement dynamique de la polarité du vortex nous a menée à proposer un nouveau type de mémoire magnétique. L'information binaire est codée par la polarité du coeur de vortex: elle est stable thermiquement et au regard des champs appliqués. Le mécanisme d'écriture se fait grâce au retournement dynamique: il est rapide et énergétiquement favorable car il n'implique le retournement que d'un faible partie de l'aimantation du disque. La lecture se fait en discriminant entre chaque polarité par l'application d'un petit champ prependiculaire, ce qui lève la dégénérésence en fréquence du mode gyrotropique. Une mesure spéctroscopique de la fréquence du mode dans le régime linéaire révèle la polarité.

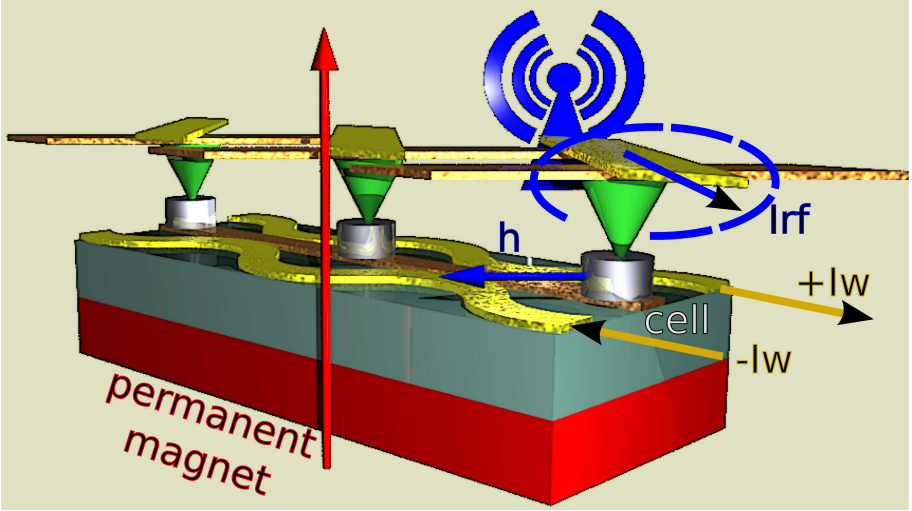

Figure B.6: Shéma de principe d'une mémoire magnétique utilisant la polarité de l'état vortex. Le processus de lecture/écriture se fait grace à un réseau de ligne de courant qui adresse un seul élément spécifique.

B.5 Conclusion

Notre technique de résonance férromagnétique détéctée mécaniquement à été appliquée à l'étude de nano disques de métaux magnétique à très bas ammortissement, FeV et NiMnsB. Le spectre d'onde de spin de ces échantillons à été mesuré dans l'état saturé pour calibration, puis dans l'état vortex. Il ont révelés une dynamique riche, qui peut-être décrite puis utilisé en é"léctronique de spin.

Bibliography

[1] Y. Acremann, C. H. Back, M. Buess, O. Portmann, A. Vaterlaus, D. Pescia, and H. Melchior, *Imaging precessional motion of the magnetization vector*, Science, 290 (2000), pp. 492–495.

[2] Y. Acremann, J. P. Strachan, V. Chembrolu, S. D. Andrews, T. Tyliszczak, J. A. Katine, M. J. Carey, B. M. Clemens, H. C. Siegmann, and J. Stohr, *Time-resolved imaging of spin transfer switching: Beyond the macrospin concept*, Phys. Rev. Lett., 96 (2006), p. 217202.

[3] J. Akerman, *Toward a universal memory*, Science, 308 (2005), p. 508.

[4] P. W. Anderson and H. Suhl, *Instability in the motion of ferromagnets at high microwave power levels*, Phys. Rev., 100 (1955), pp. 1788–1789.

[5] A. A. Awad, K. Y. Guslienko, J. F. Sierra, G. N. Kakazei, V. Metlushko, and F. G. Aliev, *Precise probing spin wave mode frequencies in the vortex state of circular magnetic dots*, Appl. Phys. Lett., 96 (2010), p. 012503.

[6] P. Bach, A. S. Bader, C. Rüster, C. Gould, C. R. Becker, G. Schmidt, L. W. Molenkamp, W. Weigand, C. Kumpf, E. Umbach, R. Urban, G. Woltersdorf, and B. Heinrich, *Molecular-beam epitaxy of the half-heusler alloy nimnsb on (in,ga)as/inp(001)*, Appl. Phys. Lett., 83 (2003), pp. 521–523.

[7] C. H. Back, R. Allenspach, W. Weber, S. S. P. Parkin, D. Weller, E. L. Garwin, and H. C. Siegmann, *Minimum field strength in precessional magnetization reversal*, Science, 285 (1999), pp. 864–867.

[8] M. N. Baibich, J. M. Broto, A. Fert, F. N. V. Dau, F. Petroff, P. Etienne, G. Creuzet, A. Friederich, and J. Chazelas, *Giant magnetoresistance of (001)fe/(001)cr magnetic superlattices*, Phys. Rev. Lett., 61 (1988), pp. 2472–2475.

[9] M. Bailleul, R. Hollinger, and C. Fermon, *Microwave spectrum of square permalloy dots: Quasisaturated state*, Phys. Rev. B, 73 (2006), p. 104424.

[10] A. D. Belanovsky, N. Locatelli, P. N. Skirdkov, F. A. Araujo, J. Grollier, K. A. Zvezdin, V. Cros, and A. K. Zvezdin, *Phase locking dynamics of dipolarly coupled vortex-based spin transfer oscillators*, Phys. Rev. B, 85 (2012), p. 100409.

[11] A. A. Belavin and A. M. Polyakov, *Metastable states of two-dimensional isotropic ferromagnets*, JETP letters, 22 (1975), p. 245.

[12] M. Beleggia, S. Tandon, Y. Zhu, and M. D. Graef, *On the magnetostatic interactions between nanoparticles of arbitrary shape*, J. Magn. Magn. Mater., 278 (2004), pp. 270 – 284.

[13] L. Berger, *Emission of spin waves by a magnetic multilayer traversed by a current*, Phys. Rev. B, 54 (1996), p. 9353.

[14] G. Binasch, P. Grunberg, F. Saurenbach, and W. Zinn, *Enhanced magnetoresistance in layered magnetic structures with antiferromagnetic interlayer exchange*, Phys. Rev. B, 39 (1989), pp. 4828–4830.

[15] M. Bolte, G. Meier, B. Krüger, A. Drews, R. Eiselt, L. Bocklage, S. Bohlens, T. Tyliszczak, A. Vansteenkiste, B. V. Waeyenberge, K. W. Chou, A. Puzic, and H. Stoll, *Time-resolved x-ray microscopy of spin-torque-induced magnetic vortex gyration*, Phys. Rev. Lett., 100 (2008), p. 176601.

[16] F. Bonell, S. Andrieu, C. Tiusan, F. Montaigne, E. Snoeck, B. Belhadji, L. Calmels, F. Bertran, P. Le Fèvre, and A. Taleb-Ibrahimi, *Influence of misfit dislocations on the magnetoresistance of mgo-based epitaxial magnetic tunnel junctions*, Phys. Rev. B, 82 (2010), p. 092405.

[17] S. Bonetti, P. Muduli, F. Mancoff, and J. Akerman, *Spin torque oscillator frequency versus magnetic field angle: The prospect of operation beyond 65 ghz*, Appl. Phys. Lett., 94 (2009), p. 102507.

[18] F. Boust and N. Vukadinovic, *Micromagnetic simulations of vortex-state excitations in soft magnetic nanostructures*, Phys. Rev. B, 70 (2004), p. 172408.

[19] K. S. Buchanan, P. E. Roy, M. Grimsditch, F. Y. Fradin, K. Y. Guslienko, S. D. Bader, and V. Novosad, *Magnetic-field tunability of the vortex translational mode in micron-sized permalloy ellipses: Experiment and micromagnetic modeling*, Phys. Rev. B, 74 (2006), p. 064404.

[20] M. Buess, T. Haug, M. R. Scheinfein, and C. H. Back, *Micromagnetic dissipation, dispersion, and mode conversion in thin permalloy platelets*, Phys. Rev. Lett., 94 (2005), p. 127205.

[21] M. Buess, R. Höllinger, T. Haug, K. Perzlmaier, U. Krey, D. Pescia, M. R. Scheinfein, D. Weiss, and C. H. Back, *Fourier transform imaging of spin vortex eigenmodes*, Phys. Rev. Lett., 93 (2004), p. 077207.

[22] M. Buess, T. P. J. Knowles, R. Hollinger, T. Haug, U. Krey, D. Weiss, D. Pescia, M. R. Scheinfein, and C. H. Back, *Excitations with negative dispersion in a spin vortex*, Phys. Rev. B, 71 (2005), p. 104415.

[23] V. Castel, J. Ben Youssef, F. Boust, R. Weil, B. Pigeau, G. de Loubens, V. V. Naletov, O. Klein, and N. Vukadinovic, *Perpendicular ferromagnetic resonance in soft cylindrical elements: Vortex and saturated states*, Phys. Rev. B, 85 (2012), p. 184419.

[24] C. Chappert, A. Fert, and F. Nguyen Van Dau, *The emergence of spin electronics in data storage*, Nature materials, 6 (2007), p. 813.

[25] V. Charbois, *Détection Mécanique de la Résonance Ferromagnétique*, thèse de doctorat, Université Paris 7, Paris, France, 2003.

[26] T.-Y. Chen and P. Crowell, *Non-linear dynamics of a magnetic vortex*, Magnetics, IEEE Transactions on, 46 (2010), pp. 1457 –1459.

[27] H.-J. Chia, F. Guo, L. M. Belova, and R. D. McMichael, *Nanoscale spin wave localization using ferromagnetic resonance force microscopy*, Phys. Rev. Lett., 108 (2012), p. 087206.

[28] S.-B. Choe, Y. Acremann, A. Scholl, A. Bauer, A. Doran, J. Stohr, and H. A. Padmore, *Vortex Core-Driven Magnetization Dynamics*, Science, 304 (2004), pp. 420–422.

[29] R. P. Cowburn, D. K. Koltsov, A. O. Adeyeye, M. E. Welland, and D. M. Tricker, *Single-domain circular nanomagnets*, Phys. Rev. Lett., 83 (1999), pp. 1042–1045.

[30] M. Curcic, B. Van Waeyenberge, A. Vansteenkiste, M. Weigand, V. Sackmann, H. Stoll, M. Fähnle, T. Tyliszczak, G. Woltersdorf, C. H. Back, and G. Schütz, *Polarization selective magnetic vortex dynamics and core reversal in rotating magnetic fields*, Phys. Rev. Lett., 101 (2008), p. 197204.

[31] G. de Loubens, *Spectroscopie micro-onde d'une nanostructure metallique magnetique hybride*, PhD thesis, Universite Paris Sud - Paris XI, 2005.

[32] G. de Loubens, A. Riegler, B. Pigeau, F. Lochner, F. Boust, K. Y. Guslienko, H. Hurdequint, L. W. Molenkamp, G. Schmidt, A. N. Slavin, V. S. Tiberkevich, N. Vukadinovic, and O. Klein, *Bistability of vortex core dynamics in a single perpendicularly magnetized nanodisk*, Phys. Rev. Lett., 102 (2009), p. 177602.

[33] C. L. Degen, M. Poggioa, H. J. Mamin, C. T. Rettner, and D. Rugar, *Nanoscale magnetic resonance imaging*, Proceedings of the National Academy of Sciences of the United States of America, 106 (2009), pp. 1313–1317.

[34] V. E. Demidov, M. Buchmeier, K. Rott, P. Krzysteczko, J. Münchenberger, G. Reiss, and S. O. Demokritov, *Nonlinear hybridization of the fundamental eigenmodes of microscopic ferromagnetic ellipses*, Phys. Rev. Lett., 104 (2010), p. 217203.

[35] S. O. Demokritov, V. E. Demidov, O. Dzyapko, G. A. Melkov, A. A. Serga, B. Hillebrands, and A. N. Slavin, *Bose-einstein condensation of quasi-equilibrium magnons at room temperature under pumping*, Nature, 443 (2006), pp. 430–433.

[36] B. Dieny and al., *Spin-transfer effect and its use in spintronic components*, International Journal of Nanotechnology, 7 (2010), p. 591.

[37] O. Dmytriiev, T. Meitzler, E. Bankowski, A. Slavin, and V. Tiberkevich, *Spin wave excitations of a magnetic pillar with dipolar coupling between the layers*, Journal of Physics: Condensed Matter, 22 (2010), p. 136001.

[38] A. Dussaux, B. Georges, J. Grollier, V. Cros, A. Khvalkovskiy, A. Fukushima, M. Konoto, H. Kubota, K. Yakushiji, S. Yuasa, K. Zvezdin, K. Ando, and A. Fert, *Large microwave generation from current-driven magnetic vortex oscillators in magnetic tunnel junctions*, Nature Communications, 1 (2010), p. 8.

[39] A. Dussaux, A. V. Khvalkovskiy, P. Bortolotti, J. Grollier, V. Cros, and A. Fert, *Field dependence of spin-transfer-induced vortex dynamics in the nonlinear regime*, Phys. Rev. B, 86 (2012), p. 014402.

[40] M. Dyakonov and V. I. Perel, *Possibility of orienting electron spins with current*, JETP letters, 13 (1971), p. 467.

[41] D. Evans, *Direct observation of static nuclear susceptibilities at room temperature*, Phil. Mag., 1 (1956), pp. 370–373.

[42] E. Feldtkeller and H. Thomas, *Struktur und energie von blochlinien in dA$\tilde{1}$4nnen ferromagnetischen schichten*, Phys. Kond. Mat., 4 (1965), p. 8.

[43] Y. Gaididei, T. Kamppeter, F. G. Mertens, and A. R. Bishop, *Switching between different vortex states in two-dimensional easy-plane magnets due to an ac magnetic field*, Phys. Rev. B, 61 (2000), pp. 9449–9452.

[44] T. Gilbert, *A phenomenological theory of damping in ferromagnetic materials*, Magnetics, IEEE Transactions on, 40 (2004), pp. 3443 – 3449.

[45] D. L. Graham, H. A. Ferreira, and P. P. Freitas, *Magnetoresistive-based biosensors and biochips*, Trends in Biotechnology, 22 (2004), p. 455.

[46] J. Grollier, V. Cros, and A. Fert, *Synchronization of spin-transfer oscillators driven by stimulated microwave currents*, Phys. Rev. B, 73 (2006), p. 060409.

[47] G. Gubbiotti, M. Kostylev, N. Sergeeva, M. Conti, G. Carlotti, T. Ono, A. N. Slavin, and A. Stashkevich, *Brillouin light scattering investigation of magnetostatic modes in symmetric and asymmetric nife/cu/nife trilayered wires*, Phys. Rev. B, 70 (2004), p. 224422.

[48] A. G. Gurevich and G. A. Melkov, *Magnetization Oscillations and Waves*, CRC Press, 1996.

[49] K. Guslienko, R. Heredero, and O. Chubykalo-Fesenko, *Nonlinear vortex dynamics in ferromagnetic dots*, Phys. Rev. B, 82 (2010), p. 014402.

[50] K. Guslienko, B. Ivanov, V. Novosad, Y. Otani, H. Shima, and K. Fukamichi, *Eigenfrequencies of vortex state excitations in magnetic submicron-size disks*, J. Appl. Phys., 91 (2002), pp. 8037–8039.

[51] K. Guslienko and K. L. Meltov, *Evolution and stability of a magnetic vortex in a small cylindrical ferromagnetic particle under applied field*, Phys. Rev. B, 63 (2001), p. 100403.

[52] K. Guslienko and V. Novosad, *Vortex state stability in soft magnetic cylindrical nanodots*, J. Appl. Phys., 96 (2004), p. 4451.

[53] K. Y. Guslienko, *Low-frequency vortex dynamic susceptibility and relaxation in mesoscopic ferromagnetic dots*, Appl. Phys. Lett., 89 (2006), p. 022510.

[54] K. Y. Guslienko, *Magnetic vortex state stability, reversal and dynamics in restricted geometries*, Journal of Nanoscience and Nanotechnology, 8 (2008), p. 2745.

[55] K. Y. Guslienko, G. R. Aranda, and J. M. Gonzalez, *Topological gauge field in nanomagnets: Spin-wave excitations over a slowly moving magnetization background*, Phys. Rev. B, 81 (2010), p. 014414.

[56] K. Y. Guslienko, S. O. Demokritov, B. Hillebrands, and A. N. Slavin, *Effective dipolar boundary conditions for dynamic magnetization in thin magnetic stripes*, Phys. Rev. B, 66 (2002), p. 132402.

[57] K. Y. Guslienko, K.-S. Lee, and S.-K. Kim, *Dynamic origin of vortex core switching in soft magnetic nanodots*, Phys. Rev. Lett., 100 (2008), p. 027203.

[58] K. Y. Guslienko, V. Novosad, Y. Otani, H. Shima, and K. Fukamichi, *Magnetization reversal due to vortex nucleation, displacement, and annihilation in submicron ferromagnetic dot arrays*, Phys. Rev. B, 65 (2001), p. 024414.

[59] K. Y. Guslienko, W. Scholz, R. W. Chantrell, and V. Novosad, *Vortex-state oscillations in soft magnetic cylindrical dots*, Phys. Rev. B, 71 (2005), p. 144407.

[60] K. Y. Guslienko, A. N. Slavin, V. Tiberkevich, and S.-K. Kim, *Dynamic origin of azimuthal modes splitting in vortex-state magnetic dots*, Phys. Rev. Lett., 101 (2008), p. 247203.

[61] D. Herranz, F. Bonell, A. Gomez-Ibarlucea, S. Andrieu, F. Montaigne, R. Villar, C. Tiusan, and F. G. Aliev, *Strongly suppressed 1/f noise and enhanced magnetoresistance in epitaxial fev/mgo/fe magnetic tunnel junctions*, Appl. Phys. Lett., 96 (2010), p. 202501.

[62] R. Hertel and C. M. Schneider, *Exchange explosions: Magnetization dynamics during vortex-antivortex annihilation*, Phys. Rev. Lett., 97 (2006), p. 177202.

[63] W. K. Hiebert, A. Stankiewicz, and M. R. Freeman, *Direct observation of magnetic relaxation in a small permalloy disk by time-resolved kerr microscopy*, Phys. Rev. Lett., 79 (1997), p. 1134.

[64] D. Houssameddine and al., *Spin-torque oscillator using a perpendicular polarizer and a planar free layer*, Nature materials, 6 (2007), p. 447.

[65] D. L. Huber, *Dynamics of spin vortices in two-dimensional planar magnets*, Phys. Rev. B, 26 (1982), pp. 3758–3765.

[66] B. A. Ivanov, H. J. Schnitzer, F. G. Mertens, and G. M. Wysin, *Magnon modes and magnon-vortex scattering in two-dimensional easy-plane ferromagnets*, Phys. Rev. B, 58 (1998), pp. 8464–8474.

[67] B. A. Ivanov and G. M. Wysin, *Magnon modes for a circular two-dimensional easy-plane ferromagnet in the cone state*, Phys. Rev. B, 65 (2002), p. 134434.

[68] B. A. Ivanov and C. E. Zaspel, *High frequency modes in vortex-state nanomagnets*, Phys. Rev. Lett., 94 (2005), p. 027205.

[69] J. Jersch, V. E. Demidov, H. Fuchs, K. Rott, P. Krzysteczko, J. Münchenberger, G. Reiss, and S. O. Demokritov, *Mapping of localized spin-wave excitations by near-field brillouin light scattering*, Appl. Phys. Lett., 97 (2010), p. 152502.

[70] S. Kaka, M. R. Pufall, W. H. Rippard, T. J. Silva, S. E. Russek, and J. A. Katine, *Mutual phase-locking of microwave spin torque nano-oscillators*, Nature, 437 (2005), pp. 389–392.

[71] B. A. Kalinikos and A. N. Slavin, *Theory of dipole-exchange spin wave spectrum for ferromagnetic films with mixed exchange boundary conditions*, Journal of Physics C: Solid State Physics, 19 (1986), pp. 7013–7033.

[72] M. Kammerer, M. Weigand, M. Curcic, M. Noske, M. Sproll, A. Vansteenkiste, B. V. Waeyenberge, H. Stoll, G. Woltersdorf, C. H. Back, and G. Schuetz, *Magnetic vortex core reversal by excitation of spin waves*, Nature Communications, 2 (2011), p. 279.

[73] A. D. Karenowska, J. F. Gregg, V. S. Tiberkevich, A. N. Slavin, A. V. Chumak, A. A. Serga, and B. Hillebrands, *Oscillatory energy exchange between waves coupled by a dynamic artificial crystal*, Phys. Rev. Lett., 108 (2012), p. 015505.

[74] A. V. Khvalkovskiy, A. N. Slavin, J. Grollier, K. A. Zvezdin, and K. Y. Guslienko, *Critical velocity for the vortex core reversal in perpendicular bias magnetic field*, App. Phys. Lett., 96 (2010), p. 022504.

[75] S. I. Kiselev, J. C. Sankey, I. N. Krivorotov, N. C. Emley, R. J. Schoelkopf, R. A. Buhrman, and D. C. Ralph, *Microwave oscillations of a nanomagnet driven by a spin-polarized current*, Nature, 425 (2003), pp. 380–383.

[76] O. Klein, G. de Loubens, V. V. Naletov, F. Boust, T. Guillet, H. Hurdequint, A. Leksikov, A. N. Slavin, V. S. Tiberkevich, and

N. Vukadinovic, *Ferromagnetic resonance force spectroscopy of individual submicron-size samples*, Phys. Rev. B, 78 (2008), p. 144410.

[77] O. Klein, G. De Loubens, and B. Pigeau, *U.s. patent: Magnetic vortex storage device*, 2012.

[78] J. M. Kosterlitz and D. J. Thouless, *Ordering, metastability and phase transitions in two-dimensional systems*, Journal of Physics C: Solid State Physics, 6 (1973), p. 1181.

[79] A. Koveshnikov, G. W. znd J. Q. Liu, B. Kardasz, O. Mosendz, B. Heinrich, K. L. Kavanagha, P. Bach, A. S. Bader, C. Schumacher, C. Ruster, C. Gould, G. Schmidt, L. W. Molenkamp, and C. Kumpf, *Structural and magnetic properties of nimnsb/ingaas/inp001*, J. Appl. Phys., 97 (2005), p. 073906.

[80] V. P. Kravchuk, D. D. Sheka, Y. Gaididei, and F. G. Mertens, *Controlled vortex core switching in a magnetic nanodisk by a rotating field*, J. Appl. Phys., 102 (2007), p. 043908.

[81] V. V. Kruglyak, S. O. Demokritov, and D. Grundler, *Magnonics*, Journal of Physics D: Applied Physics, 43 (2010), p. 264001.

[82] L. Landau and E. Lifschitz, *On the theory of the dispersion of magnetic permeability in ferromagnetic bodies*, Phys. Z. Sov. Union, 8 (1935), p. 153.

[83] I. Lee, Y. Obukhov, G. Xiang, A. Hauser, F. Yang, P. Banerjee, D. Pelekhov, and P. Hammel, *Nanoscale scanning probe ferromagnetic resonance imaging using localized modes*, NATURE, 466 (2010), pp. 845–848.

[84] K.-S. Lee, K. Y. Guslienko, J.-Y. Lee, and S.-K. Kim, *Ultrafast vortex-core reversal dynamics in ferromagnetic nanodots*, Phys. Rev. B, 76 (2007), p. 174410.

[85] K.-S. Lee, S.-K. Kim, Y.-S. Yu, Y.-S. Choi, K. Y. Guslienko, H. Jung, and P. Fischer, *Universal criterion and phase diagram for switching a magnetic vortex core in soft magnetic nanodots*, Phys. Rev. Lett., 101 (2008), p. 267206.

[86] N. Locatelli, V. V. Naletov, J. Grollier, G. de Loubens, V. Cros, C. Deranlot, C. Ulysse, G. Faini, O. Klein, and A. Fert, *Dynamics of two coupled vortices in a spin valve nanopillar excited by spin transfer torque*, Appl. Phys. Lett., 98 (2011), p. 062501.

[87] H. J. Mamin, M. Poggio, C. L. Degen, and D. Rugar, *Nuclear magnetic resonance imaging with 90-nm resolution*, Nature Nanotechnology, 2 (2007), p. 301.

[88] F. B. Mancoff, N. D. Rizzo, B. N. Engel, and S. Tehrani, *Phase-locking in double-point-contact spin-transfer devices*, Nature, 437 (2005), p. 393.

[89] W. P. Mason, *Electromechanical transducers and wave filters*, Van Nostrand, New York, 1942.

[90] K. Meltov and K. Guslienko, *Stability of magnetic vortex in soft magnetic nano-sized circular cylinder*, J. Magn. Magn. Mater., 242-245 (2002), p. 1015.

[91] N. D. Mermin, *The topological theory of defects in ordered media*, Rev. Mod. Phys., 51 (1979), pp. 591–648.

[92] F. Mertens and A. Bishop, *Nonlinear Science at the Dawn of the 21st Century: Dynamics of Vortices in Two-Dimensional Magnets*, vol. 542 of Lecture Notes in Physics, P. L. Christiansen and M. P. Sorensen and A. C. Scott, 2000. 10.1007/3-540-46629-0-7.

[93] M. M. Midzor, *Ferromagnetic Resonance Force Microscopy*, PhD thesis, California Institute of Technology, Pasadena, California, 2001.

[94] C. Miramond, C. Fermon, F. Rousseaux, D. Decanini, and F. Carcenac, *Permalloy cylindrical submicron size dot arrays*, J. Magn. Magn. Mater., 165 (1997), pp. 500–503.

[95] K. Mitsuzuka, D. Lacour, M. Hehn, S. Andrieu, and F. Montaigne, *Magnetic vortices in single crystalline fe-v disks with four folds magnetic anisotropy*, Appl. Phys. Lett., 100 (2012), p. 192406.

[96] T. Miyazaki and N. Tezuka, *Giant magnetic tunneling effect in fe/al2o3/fe junction*, J. Magn. Magn. Mater., 139 (1995), pp. L231 – L234.

[97] J. S. Moodera, L. R. Kinder, T. M. Wong, and R. Meservey, *Large magnetoresistance at room temperature in ferromagnetic thin film tunnel junctions*, Phys. Rev. Lett., 74 (1995), pp. 3273–3276.

[98] O. Mosendz, G. Woltersdorf, B. Kardasz, B. Heinrich, and C. H. Back, *Magnetization dynamics in the presence of pure spin currents in magnetic single and double layers in spin ballistic and diffusive regimes*, Phys. Rev. B, 79 (2009), p. 224412.

[99] V. V. Naletov, G. de Loubens, G. Albuquerque, S. Borlenghi, V. Cros, G. Faini, J. Grollier, H. Hurdequint, N. Locatelli, B. Pigeau, A. N. Slavin, V. S. Tiberkevich, C. Ulysse, T. Valet, and O. Klein, *Identification and selection rules of the spin-wave eigenmodes in a normally magnetized nanopillar*, Phys. Rev. B, 84 (2011), p. 224423.

[100] J. M. Nichol, E. R. Hemesath, L. J. Lauhon, and R. Budakian, *Nanomechanical detection of nuclear magnetic resonance using a silicon nanowire oscillator*, Phys. Rev. B, 85 (2012), p. 054414.

[101] V. Novosad, F. Y. Fradin, P. E. Roy, K. S. Buchanan, K. Y. Guslienko, and S. D. Bader, *Magnetic vortex resonance in patterned ferromagnetic dots*, Phys. Rev. B, 72 (2005), p. 024455.

[102] Y. Obukhov, D. V. Pelekhov, J. Kim, P. Banerjee, I. Martin, E. Nazaretski, R. Movshovich, S. An, T. J. Gramila, S. Batra, and P. C. Hammel, *Local ferromagnetic resonance imaging with magnetic resonance force microscopy*, Phys. Rev. Lett., 100 (2008), p. 197601.

[103] M. Pannetier, C. Fermon, G. Le Goff, J. Simola, and E. Kerr, *Femtotesla magnetic field measurement with magnetoresistive sensors*, Science, 304 (2004), pp. 1648–1650.

[104] J. P. Park and P. A. Crowell, *Interactions of spin waves with a magnetic vortex*, Phys. Rev. Lett., 95 (2005), p. 167201.

[105] J. P. Park, P. Eames, D. M. Engebretson, J. Berezovsky, and P. A. Crowell, *Imaging of spin dynamics in closure domain and vortex structures*, Physical Review B, 67 (2003), p. 020403.

[106] K. Perzlmaier, M. Buess, C. H. Back, V. E. Demidov, B. Hillebrands, and S. O. Demokritov, *Spin-wave eigenmodes of permalloy squares with a closure domain structure*, Phys. Rev. Lett., 94 (2005), p. 057202.

[107] B. Pigeau, G. de Loubens, O. Klein, A. Riegler, F. Lochner, G. Schmidt, and L. W. Molenkamp, *Optimal control of vortex-core polarity by resonant microwave pulses*, Nature Physics, 7 (2011), pp. 26–31.

[108] B. Pigeau, G. de Loubens, O. Klein, A. Riegler, F. Lochner, G. Schmidt, L. W. Molenkamp, V. S. Tiberkevich, and A. N.

Slavin, *A frequency-controlled magnetic vortex memory*, Appl. Phys. Lett., 96 (2010), p. 132506.

[109] V. S. Pribiag, I. N. Krivorotov, G. D. Fuchs, P. M. Braganca, O. Ozatay, J. C. Sankey, D. C. Ralph, and R. A. Buhrman, *Magnetic vortex oscillator driven by d.c. spin-polarized current*, Nature Physics, (2007).

[110] L. Ritchie, G. Xiao, Y. Ji, T. Y. Chen, C. L. Chien, M. Zhang, J. Chen, Z. Liu, G. Wu, and X. X. Zhang, *Magnetic, structural, and transport properties of the heusler alloys* co_2MnSi *and nimnsb*, Phys. Rev. B, 68 (2003), p. 104430.

[111] O. Rousseau and M. Viret, *Interaction between ferromagnetic resonance and spin currents in nanostructures*, Phys. Rev. B, 85 (2012), p. 144413.

[112] D. Rugar, R. Budakian, H. J. Mamin, and B. W. Chui, *Single spin detection by magnetic resonance force microscopy*, Nature, 430 (2004), pp. 329–332.

[113] D. Rugar, C. S. Yannoni, and J. A. Sidles, *Mechanical detection of magnetic resonance*, Nature, 360 (1992), p. 563.

[114] D. Rugar, O. Züger, S. Hoen, C. S. Yannoni, H. M. Vieth, and R. D. Kendrick, *Force detection of nuclear magnetic resonance*, Science, 264 (1994), p. 1560.

[115] J. C. Sankey, P. M. Braganca, A. G. F. Garcia, I. N. Krivorotov, R. A. Buhrman, and D. C. Ralph, *Spin-transfer-driven ferromagnetic resonance of individual nanomagnets*, Phys. Rev. Lett., 96 (2006), p. 227601.

[116] E. Schlomann, *Ferromagnetic resonance at high power levels*, tech. rep., Raytheon company, 1959.

[117] H. W. Schumacher, C. Chappert, P. Crozat, R. C. Sousa, P. P. Freitas, J. Miltat, J. Fassbender, and B. Hillebrands, *Phase coherent precessional magnetization reversal in microscopic spin valve elements*, Phys. Rev. Lett., 90 (2003), p. 017201.

[118] C. Serpico, *Notes on vortex dynamics ferroresonance due to nonlinear vortex damping.* private communication.

[119] T. Shinjo, T. Okuno, R. Hassdorf, K. Shigeto, and T. Ono, *Magnetic Vortex Core Observation in Circular Dots of Permalloy*, Science, 289 (2000), pp. 930–932.

[120] J. A. Sidles, *Noninductive detection of single-proton magnetic resonance*, Appl. Phys. Lett., 58 (1991), pp. 2854–2856.

[121] J. A. Sidles, J. L. Garbini, K. J. Bruland, D. Rugar, O. Züger, S. Hoen, and C. S. Yannoni, *Magnetic resonance force microscopy*, Rev. Mod. Phys., 67 (1995), pp. 249–265.

[122] A. Slavin and V. Tiberkevich, *Nonlinear auto-oscillator theory of microwave generation by spin-polarized current*, IEEE Transactions on Magnetics, 45 (2009), p. 1875.

[123] J. C. Slonczewski, *Current-driven excitation of magnetic multilayers*, J. Magn. Magn. Mater., 159 (1996), p. 1.

[124] S. Sugimoto, Y. Fukuma, S. Kasai, T. Kimura, A. Barman, and Y. Otani, *Dynamics of coupled vortices in a pair of ferromagnetic disks*, Phys. Rev. Lett., 106 (2011), p. 197203.

[125] O. Sukhostavets, J. Gonzalez, and K. Guslienko, *Magnetic vortex excitation frequencies and eigenmodes in a pair of coupled circular dots*, Applied Physics Express, 4 (2011), p. 065003.

[126] S. Tandon, M. Beleggia, Y. Zhu, and M. De Graef, *On the computation of the demagnetization tensor for uniformly magnetized particles of arbitrary shape. part i: Analytical approach*, J. Magn. Magn. Mater., 271 (2004), pp. 9–26.

[127] A. Thiaville, J. M. Garcia, R. Dittrich, J. Miltat, and T. Schrefl, *Micromagnetic study of bloch-point-mediated vortex core reversal*, Phys. Rev. B, 67 (2003), p. 094410.

[128] A. A. Thiele, *Steady-state motion of magnetic domains*, Phys. Rev. Lett., 30 (1973), pp. 230–233.

[129] C. Thirion, W. Wernsdorfer, and D. Mailly, *Switching of magnetization by nonlinear resonance studied in single nanoparticles*, Nature Materials, 2 (2003), p. 524.

[130] S. P. Timoshenko and J. N. Goodier, *Theory of Elasticity*, McGraw-Hill, New York, 1970.

[131] A. A. Tulapurkar, Y. Suzuki, A. Fukushima, H. Kubota, H. Maehara, K. Tsunekawa, D. D. Djayaprawira, N. Watanabe, and S. Yuasa, *Spin-torque diode effect in magnetic tunnel junctions*, Nature, 438 (2005), pp. 339–342.

[132] T.Valet, *http://www.insilicio.fr/pdf/spinflow$_3$d.pdf*.

[133] N. Usov and S. Peschany, *Magnetization curling in a fine cylindrical particle*, J. Magn. Magn. Mater., 118 (1993), p. L290.

[134] B. Van Waeyenberge, A. Puzic, H. Stoll, K. W. Chou, T. Tyliszczak, R. Hertel, M. Fahnle, H. Bruckl, K. Rott, G. Reiss, I. Neudecker, D. Weiss, C. H. Back, and G. Schutz, *Magnetic vortex core reversal by excitation with short bursts of an alternating field*, Nature, 444 (2006), pp. 461–464.

[135] A. Vansteenkiste, K. Chou, M. Weigand, M. Curcic, V. Sackmann, H. Stoll, T. Tyliszczak, G. Woltersdorf, C. Back, G. Schutz, and B. V. Waeyenberge, *X-ray imaging of the dynamic magnetic vortex core deformation*, Nature physics, 5 (2009), p. 332.

[136] A. Vansteenkiste, B. V. de Wiele, M. Weigand, H. Stoll, K. W. Chou, T. Tyliszczak, G. Woltersdorf, C. H. Back, G. Schutz, and B. V. Waeyenberge, *Observation of non-linear magnetic vortex gyration by x-ray microscopy and micromagnetic simulations*, Arxiv cond-mat, arXiv:1110.0828v1 (2011).

[137] R. Verba, G. Melkov, V. Tiberkevich, and A. Slavin, *Collective spin-wave excitations in a two-dimensional array of coupled magnetic nanodots*, Phys. Rev. B, 85 (2012), p. 014427.

[138] V. Vlaminck and M. Bailleul, *Current-induced spin-wave doppler shift*, Science, 322 (2008), pp. 410–413.

[139] J. Vogel, W. Kuch, M. Bonfim, J. Camarero, Y. Pennec, F. Offi, K. Fukumoto, J. Kirschner, A. Fontaine, and S. Pizzini, *Time-resolved magnetic domain imaging by x-ray photoemission electron microscopy*, Appl. Phys. Lett., 82 (2003), pp. 2299–2301.

[140] K. Vogt, O. Sukhostavets, H. Schultheiss, B. Obry, P. Pirro, A. A. Serga, T. Sebastian, J. Gonzalez, K. Y. Guslienko, and B. Hillebrands, *Optical detection of vortex spin-wave eigenmodes in microstructured ferromagnetic disks*, Phys. Rev. B, 84 (2011), p. 174401.

[141] A. Wachowiak, J. Wiebe, M. Bode, O. Pietzsch, M. Morgenstern, and R. Wiesendanger, *Direct observation of internal spin structure of magnetic vortex cores*, Science, 298 (2002), pp. 577–580.

[142] S. A. Wolf, D. D. Awschalom, R. A. Buhrman, J. M. Daughton, S. von Molnar, M. L. Roukes, A. Y. Chtchelkanova, and D. M. Treger, *Spintronics: A spin-based electronics vision for the future*, Science, 294 (2001), pp. 1488–1495.

[143] G. Woltersdorf, O. Mosendz, B. Heinrich, and C. H. Back, *Magnetization dynamics due to pure spin currents in magnetic double layers*, Phys. Rev. Lett., 99 (2007), p. 246603.

[144] G. M. Wysin, *Magnetic vortex mass in two-dimensional easy-plane magnets*, Phys. Rev. B, 54 (1996), pp. 15156–15162.

[145] K. Yamada, S. Kasai, Y. Nakatani, K. Kobayashi, H. Kohno, A. Thiaville, and T. Ono, *Electrical switching of the vortex core in a magnetic disk*, Nature Materials, 6 (2007), pp. 269–273.

[146] K. Yamada, S. Kasai, Y. Nakatani, K. Kobayashi, and T. Ono, *Switching magnetic vortex core by a single nanosecond current pulse*, Appl. Phys. Lett., 93 (2008), p. 152502.

[147] M.-W. Yoo, J. Lee, and S.-K. Kim, *Radial-spin-wave-mode-assisted vortex-core magnetization reversals*, Appl. Phys. Lett., 100 (2012), p. 172413.

[148] M.-W. Yoo, K.-S. Lee, D.-E. Jeong, and S.-K. Kim, *Origin, criterion, and mechanism of vortex-core reversals in soft magnetic nanodisks under perpendicular bias fields*, Phys. Rev. B, 82 (2010), p. 174437.

[149] C. E. Zaspel, E. S. Wright, A. Y. Galkin, and B. A. Ivanov, *Frequencies of radially symmetric excitations in vortex state disks*, Phys. Rev. B, 80 (2009), p. 094415.

[150] Z. Zhang, P. C. Hammel, and P. E. Wigen, *Observation of ferromagnetic resonance in a microscopic sample using magnetic resonance force microscopy*, Applied Physics Letters, 68 (1996), pp. 2005–2007.

[151] O. Züger and D. Rugar, *First images from a magnetic resonance force microscope*, Appl. Phys. Lett., 63 (1993), p. 2496.

Résumé

Dynamique de vortex magnétique dans une nanostructure

Cette thèse à pour objet l'étude expérimentale de la dynamique de l'aimantation de disques de taille sub-micronique fait de matériau ferromagnétiques à faible amortissement . Pour cela, nous avons utilisé une technique spectroscopique extremement sensible qui sera préalablement présentée: la résonance férromagnétique détéctée mécaniquement. Une première partie est consacré à la mesure des modes propres dans des disques de NiMnSb dans leur état rémanent: le vortex. L'influence d'un champ magnétique, aplliqué perpendiculairement, sur les ondes de spin du vortex est détaillé. L'accent est ensuite mis sur l'interaction du coeur de vortex avec ces ondes de spin, qui mène à son retournement dynamique. Un cadre théorique de l'état vortex est présenté, permettant de modéliser les mesures expérimentales. Dans une deuxième partie, le problème de la dynamique collective de plusieurs disques de FeV dont l'aimantation est saturée perpendiculairement est étudiée. La mesure des modes couplés par l'intéraction dipolaire dynamique y est présentée, associée à une modélisation théorique qui explique quantitativement les résultats observés.

Mots-clefs: Ondes de spin; MRFM-microscopie de force à résonance magnétique; état vortex magnétique; couplage dipolaire.

Abstract

Magnetic vortex dynamics nanostructures

This thesis is aimed at studying experimentally the magnetisation dynamics of discs in the sub-micron range made of low damping ferromagnetic materials. For this purpose, an extremely sensitive technique has been used: the ferromagnetic resonance force microscopy. A first part is devoted to the measurement of the eigenmodes of NiMnSb discs taken in their remanent state: a vortex. The influence of a perpendicular magnetic field on the spin wave modes in the vortex state will be detailed. Then, the coupling mechanism between the vortex core and these spin wave, eventually leading to its dynamical reversal, is highlighted. A theoretical framework of the vortex state is presented, allowing to model the experimental observations. In a second part, the problem of the collective magnetisation dynamics in several FeV discs is addressed. Measurements of the collective modes coupled by the dynamical dipolar interaction are presented, associated with a theoretical model which explain quantitatively the experimental results.

Keywords: Spin waves; MRFM-magnetic resonance force microscopy; magnetic vortex state; dipolar coupling.